1
Light-Emitting Diodes and Lighting

Introduction

Owing to nitride semiconductors primarily, which made possible emission in the green and blue wavelengths of the visible spectrum, light-emitting diodes (LEDs) transmogrified from simple indicators to high-tech marvels with applications far and wide in every aspect of modern life. LEDs are simply p–n-junction devices constructed in direct-bandgap semiconductors and convert electrical power to generally visible optical power when biased in the forward direction. They produce light through spontaneous emission of radiation whose wavelength is determined by the bandgap of the semiconductor across which the carrier recombination takes place. Unlike semiconductor lasers, generally, the junction is not biased to and beyond transparency, although in superluminescent varieties transparency is reached. In the absence of transparency, self-absorption occurs in the medium, which is why the thickness of this region where the photons are generated is kept to a minimum, and the photons are emitted in random directions. A modern LED is generally of a double-heterojunction type with the active layer being the only absorbing layer in the entire structure inclusive of the substrate. Such LEDs have undergone a breathtaking revolution that is still continuing, since the advent of nitride-based white-light generation for solid-state lighting (SSL) applications. Essentially, LEDs have metamorphosed from being simply indicator lamps replacing nixie signs to highly efficient light sources featuring modern technology for getting as many photons as possible out of the package. In the process, packaging has changed radically in an effort to collect every photon generated within the structure. Instead of just employing what used to be the standard 5 mm plastic dome to focus the light, the device package is now a high-tech marvel with even holographically generated (employing laser lithography, which is maskless and convenient for periodic patterns) polymeric photonic crystals placed on top or flip-chip mounts (after peeling the GaN structure from the sapphire substrate) with the blackened N-polarity surface for maximum light collection. Furthermore, the area of the device as well as the shape of the chip is designed for maximum étendue, a measure of the optical size of the device. Furthermore, device packaging also had to adopt strategies not only to remove the heat generated by

Handbook of Nitride Semiconductors and Devices. Vol. 3. Hadis Morkoç
Copyright © 2009 WILEY-VCH Verlag GmbH & Co. KGaA, Weinheim
ISBN: 978-3-527-40839-9

the process but also to deal with the thermal mismatch between the chip and the heat sink owing to the Joule heating effect resulting from the current levels in the vicinity of 350 mA.

It should be pointed out that nitride LEDs are fabricated on the polar Ga-face of GaN. Therefore, the quantum wells (QWs) used are subjected to quantum-confined Stark shift (red) due the electric field induced by spontaneous and piezoelectric polarization. The latter is severe for increased InN mole fraction in the lattice, in particular, for green LEDs. This results in reduced emission efficiency because of reduced matrix element (lowered overlap integral between the electron and hole wave functions that are pushed to the opposing sides of the quantum well). In fact, the carrier lifetime increases from some 10 ns in bulk InGaN to as high as about 85 ns in a quantum well corresponding to green wavelength. While the same situation is present in lasers, much lower InN compositions and much higher injection levels mitigate the situation to some extent. A quick fix that helps to some extent is to use vicinal substrates even with tilt angles as small as 1° to reduce the polarization-induced field. To really combat this issue, nonpolar surfaces such as the *a*-plane GaN is explored. However, the quality of the films is much inferior to those on the *c*-plane GaN, owing in part to the severe structural mismatch between the *r*-plane sapphire and *a*-plane GaN and small formation energy of stacking faults. An additional, aggravating issue is that not much In can be incorporated on this plane, preventing the achievement of blue and green wavelength emission. Research on other orientations such as growth of *m*-plane GaN has begun. For further information, growth of *a*- and *m*-plane GaN is discussed in Volume 1, Chapter 3, and the issue of polarization is discussed in Volume 1, Chapter 2.

Elaborating further, as LEDs became brighter and white light generating varieties became available, the role of LEDs shifted from being simply indicator lights to illuminators. The advent of nitride LEDs made white light possible with perfect timing, just when handheld electronic devices such as cell phones and digital cameras became popular, and energy cost increased. In these gadgets, LEDs are used not only for background illumination but also as flashlights, particularly in cell phones. Additionally, LEDs penetrated the automotive industry (aircraft industry is going to follow) in a major way with every indicator and/or background light source, with the exception of headlights, being of LEDs. In the year 2002, with nearly $2 billion in sales worldwide, about 40% accounted for mobile electronics, 23% for signs, and 18% for automotive. The mobile electronics market is mainly of the white-LED type, which is made possible solely by nitride LEDs. The market continues to experience rapid growth. Retail lighting, shelf lighting, flashlights, night lighting, traffic signaling, highway moving signs, outdoor displays, landscape lighting, and mood lighting have all gone the way of LEDs. The power savings made possible by LEDs in the year 2002 amounted to nearly 10 TW year^{-1} with potential savings approaching 35 TW year^{-1}, which will ease the tax on the environment by reducing the greenhouse gas emission. The next frontier for LEDs is to conquer the general illumination, which is underdeveloped, with fierce competition that will bring the best out of those who are going to make this possible. Nitride-based LEDs with InGaN

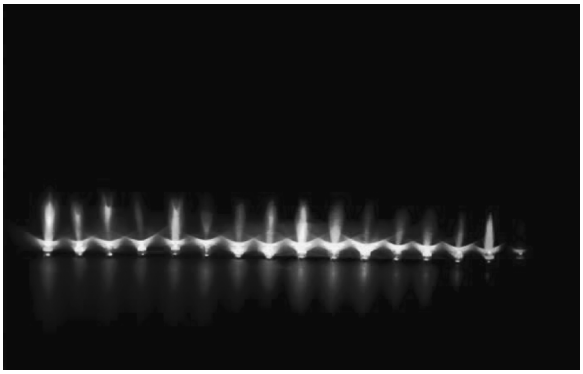

Figure 1.1 InGaN LEDs spanning the spectral range from violet to orange. Courtesy of S. Nakamura, then with Nichia Chemical Co. Ltd. (Please find a color version of this figure on the color tables.)

active regions span the visible spectrum from yellow to violet, as illustrated in Figure 1.1.

The three types of LEDs are *surface emitters*, which are divided into those with plastic domes and those with varieties of flat surface-mount, lacking the dome, *edge emitters*, generally intended for fiber-optic communications, and *superradiant* or *superluminescent* devices, which are biased not quite to the point of lasing but biased enough to provide some gain and narrowing of the spectrum. Antireflection coatings or some other measures are taken to ensure that the device does not lase.

Among the applications of LEDs are displays, indicator lights, signs, traffic lights, printers, telecommunications, and (potentially) lighting, which requires emission in the visible part of the spectrum. While saturated-color red LEDs can be produced using semiconductors such as GaP, AlGaAs, and AlGaInP, the green and blue commercial LEDs having brightness sufficient for outdoor applications have so far been manufactured with nitride semiconductors. Figure 1.2 exhibits the various ternary and quaternary materials used for LEDs with the wavelength ranges indicated. The color bar corresponds to the visible portion of the spectrum. We should also mention that another wide-gap semiconductor, ZnO, with its related alloys is being pursued for light emission, as it is a very efficient light emitter. However, lack of convincingly high p-type doping in high concentration has kept this approach from reaching its potential so far [1].

Even though there is still some discussion of the fundamentals of radiative recombination in InGaN LEDs, the basics of LEDs will be treated first, assuming that the semiconductors of interest are well behaved. This will be followed by the performance of available nitride LEDs and their characteristics. The discussion is completed with succinct treatments of the reliability of nitride-based LEDs, and of organic LEDs (OLEDs), which have progressed to the point that indoor applications are being considered.

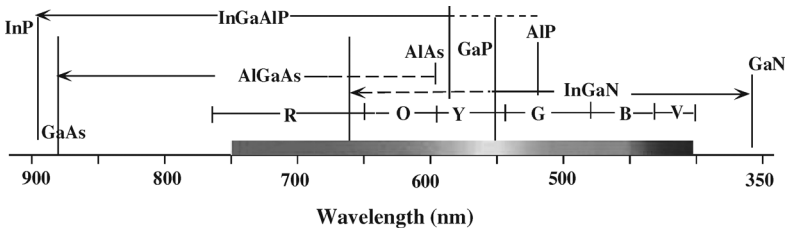

Figure 1.2 The LED materials and range of wavelength of the emission associated with them. The color band indicates the visible region of the spectrum. (Please find a color version of this figure on the color tables.)

1.1 Current-Conduction Mechanism in LED-Like Structures

Consider an AlGaN(p)/GaN(p)/AlGaN(n) double-heterojunction device that is forward biased. The carrier and light distribution in the active layer are depicted schematically in Figure 1.3. For simplicity, let us assume that a double-heterojunction device is one in which all the carriers recombine in the smaller bandgap active region. In reality, recombination takes place in the active layer, some fraction of the recombination is nonradiative, and at the two heterointerfaces on both sides of the active layer that is nonradiative. Here, the larger bandgap AlGaN n- and p-layers are doped rather heavily so that no field exists in these regions. The treatment here will be developed in a manner similar to that of Lee *et al.* [2] and Wang [3].

Because the active layer is p-type, we will be dealing with minority electron carriers. The continuity equation for electrons can be written as

$$D\frac{\partial^2 n}{\partial x^2} - \frac{n-n_0}{\tau} + g = \frac{\partial n}{\partial t}, \tag{1.1}$$

where n and n_0 represent the minority-carrier concentration and the equilibrium minority-carrier concentration, respectively. The terms D, g, and τ represent the electron diffusion length, the generation rate, and the carrier lifetime, respectively, and x and t have their usual meaning. If the active layer were n-type, the same equations would apply with the minority electron parameters replaced with the minority hole parameters.

Under steady-state conditions and high injection levels, such as the case for LEDs, the time dependence vanishes, the generation rate and the equilibrium minority carrier concentration can be neglected, and the continuity expression reduces to

$$D\frac{\mathrm{d}^2 n}{\mathrm{d}x^2} - \frac{n}{\tau} = 0. \tag{1.2}$$

This second-order differential equation can be solved with appropriate boundary conditions that can be arrived at by considering the rate of change in the carrier

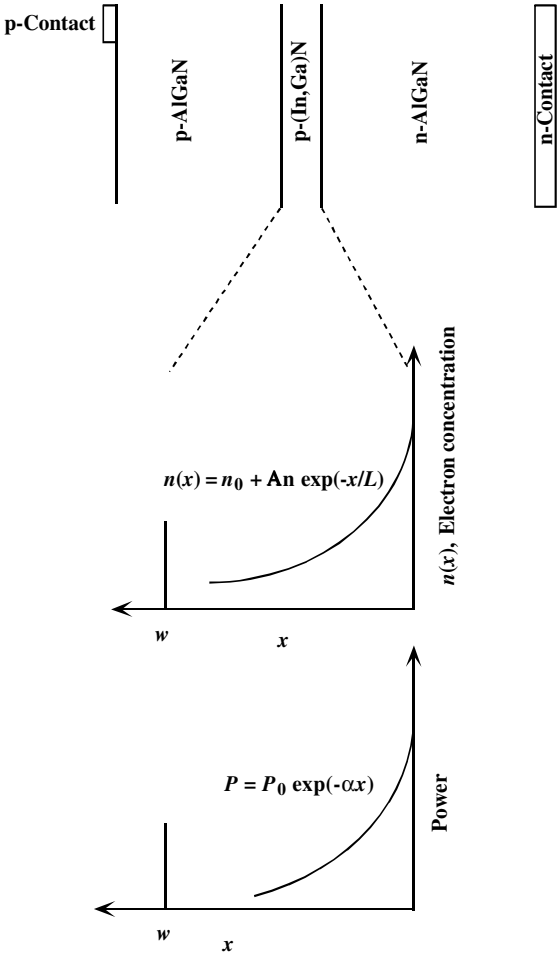

Figure 1.3 The spatial carrier and light distribution in a double-heterostructure LED structure.

concentration at each side of the active p-layer. The general solution of the continuity equation is given by

$$n(x) = A\exp\left(\frac{-x}{L}\right) + B\exp\left(\frac{x}{L}\right) \tag{1.3}$$

or in the p-region

$$n(x) = A\sinh\left(\frac{w-x}{L}\right) + B\cosh\left(\frac{w-x}{L}\right). \tag{1.4}$$

Here, L is the diffusion length $L = (D\tau)^{1/2}$, and the constants A and B can be found subject to the boundary conditions as described below.

The rate of change in carrier concentration at $x = 0$ is the difference between the injection rate and the interface recombination rate. The rate of change in carrier concentration at $x = w$ is the difference between the injection rate at $x = w$ and the interface recombination rate at $x = w$:

$$-\left.\frac{\mathrm{d}n}{\mathrm{d}x}\right|_{x=0} = \frac{J_{\mathrm{diff}}(0)}{qD} - \frac{v_{\mathrm{s}}n(0)}{D} \quad \text{at} \quad x = 0 \tag{1.5}$$

and

$$-\left.\frac{\mathrm{d}n}{\mathrm{d}x}\right|_{x=W} = \frac{J_{\mathrm{diff}}(w)}{qD} - \frac{v_{\mathrm{s}}n(w)}{D} \quad \text{at} \quad x = W, \tag{1.6}$$

where q is the electronic charge, J_{diff} is the diffusion current density, and v_{s} (cm s^{-1}) is the interface recombination velocity. It is assumed that $J_{\mathrm{diff}}(w)$ is negligible in the case when the p-layer is thicker than the diffusion length. One must keep in mind that the rate of change in the minority carrier is always negative.

The solution to the continuity equation subject to the above boundary conditions is

$$n(x) = \frac{J_{\mathrm{diff}}(x=0)}{q}\sqrt{\frac{\tau}{D}}\left\{\frac{\cosh[(w-x)/L]+v_{\mathrm{s}}\sqrt{\tau/D}\sinh[(w-x)/L]}{\left[v_{\mathrm{s}}^2(\tau/D)+1\right]\sinh(w/L)+[2v_{\mathrm{s}}\sqrt{\tau/D}\cosh(w/L)]}\right\}. \tag{1.7}$$

Here, J_{diff} $(x = 0)$ can be assumed to be the terminal current as the hole injection is negligible, given the very small intrinsic carrier concentration.

The average electron concentration in the active region can then be calculated from the integral:

$$n_{\mathrm{ave}} = \frac{1}{w}\int_0^w n(x)\mathrm{d}x = \frac{J\tau_{\mathrm{eff}}}{qw}. \tag{1.8}$$

Substitution of the electron concentration (Equation 1.7) into Equation 1.8 leads to an effective carrier lifetime, which reduces to

$$\tau_{\mathrm{eff}}^{-1} = \tau^{-1} + 2\frac{v_{\mathrm{s}}}{w} = \tau_{\mathrm{rad}}^{-1} + \tau_{\mathrm{nrad}}^{-1} + 2\frac{v_{\mathrm{s}}}{w} \tag{1.9}$$

if $w/L < 1$ and $v_{\mathrm{s}}^2(\tau/D) \ll 1$. In addition, in the absence of interface recombination, the effective lifetime would reduce to τ, which is related to radiative and nonradiative recombination times through $\tau^{-1} = \tau_{\mathrm{rad}}^{-1} + \tau_{\mathrm{nrad}}^{-1}$.

1.2 Optical Output Power

As seen by the electron-density expression, the electron density and thus the photon density are reduced in the area away from the junction. Consequently, increasing the

active layer thickness does not lead to a continually increasing optical power. In addition, the light generated in the active layer itself is self-absorbed in the active layer. Here, it is assumed that the rest of the structure is a larger bandgap semiconductor, which would not be absorbing. The photon flux density can be approximated by a Gaussian function of the form

$$S(\lambda) = S_0 \exp\left[\frac{-4(\lambda-\lambda_0)^2}{(\Delta\lambda)^2}\right], \tag{1.10}$$

where S is the number of photons per unit time per unit volume with S_0 representing the same at the center of the spectrum.

At a given point x, in the active layer, $S_0 = \Delta n(x)/\tau_{\text{rad}} \approx n(x)/\tau_{\text{rad}}$, with τ_{rad} being the radiative lifetime. Recognizing that the photon energy equals $h\nu = hc/\lambda$, the power is given by

$$P = Ahc \int_0^\infty \frac{S(\lambda)}{\lambda} \mathrm{d}\lambda, \tag{1.11}$$

where A is the cross-sectional area.

With further manipulation and substitutions connecting the photon density to the carrier density in the form of $S(\lambda) = \tau_{\text{rad}}^{-1} \int_0^w n(x)\exp[-\alpha(\lambda)x]\mathrm{d}x$, we obtain

$$P = Ahc \int_0^\infty \frac{\mathrm{d}\,\lambda}{\lambda} \int_0^w \frac{n(x)\exp[-\alpha(\lambda)x]}{\tau_{\text{rad}}} \mathrm{d}\,x, \tag{1.12}$$

with $\alpha(\lambda)$ being the absorption coefficient, which is of course a function of wavelength, λ.

1.3 Losses and Efficiency

One must grapple with the fact that the photons generated in the active layer are emitted in all directions with only a fraction of them escaping the device to reach the human eye. To combat this loss of photons, which relates to the collection efficiency, various packaging designs have been developed. For example, in 5 mm (the epoxy dome diameter) LEDs, the mounting scheme also involves a back-reflector to reflect the light back into the epitaxial composite and then out of the surface for collection. In this regard, the transparent nature of sapphire substrates is very advantageous in that the wavelength of interest is not absorbed as it traverses the structure as shown in Figure 1.4. The backside of the sapphire substrate must be thinned by polishing to facilitate breaking of the wafer into the LED chips and, in the context of this discussion, to eliminate absorption at the otherwise rough surface. Thus, absorption of photons emitted down into the semiconductor structure can be reduced by utilizing layers and substrates transparent to the radiant wavelength. This is coupled with a highly reflective back at the bottom face (substrate in the case of normal mount

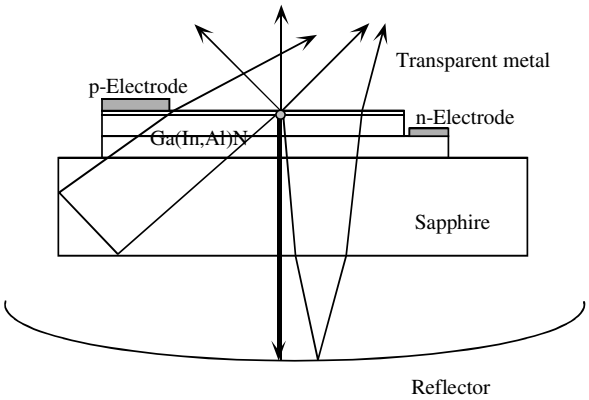

Figure 1.4 Schematic diagram of an LED intended for as much light extraction as possible with a back-reflector and a transparent substrate as is employed in some InGaN-based devices.

and top epitaxial layer in the case of flip-chip mount). The absorption by the metal ohmic contact in the way of the light ray can be reduced by using transparent contacts such as indium tin oxide (ITO). Absorption within the LED (η_A in terms of efficiency), critical-angle loss (η_c), and reflections (η_F) (*Fresnel* loss) represent the main sources of loss. These loss factors are not yet considered in the derivation of Equation 1.12. It should be noted that in hot intensity LEDs designed for illumination, the substrate is completely removed and the flipped chip is mounted on metal alloy that plays a dual role as reflector and heat sink, as discussed in Section 1.5. In GaAs diodes with a GaAs substrate, about 85% of the photons generated are absorbed. If transparent substrates are used, such as GaP, only about 25% of the photons are lost. In the case of InGaN diodes, the entire structure with the exception, of course, of the active layer itself, is transparent, and therefore, absorptive losses are almost eliminated.

As for the reflection at the semiconductor–air interface, when light passes from a medium with refractive index n_2, which is the active layer here, to a medium with refractive index n_1, being air in this case, a portion of the radiation is reflected at the interface. This loss, which is called the *Fresnel loss*, is given in the case of normal incidence by

$$R = \left(\frac{n_2 - n_1}{n_2 + n_1}\right)^2. \tag{1.13}$$

The *Fresnel loss efficiency* [4] can be defined as $\eta_F = 1 - R$.

The *critical angle for total reflection* ϑ_c – total reflection taking place above this angle – is determined by *Snell's law*

$$\vartheta_c = \sin^{-1}\left(\frac{n_1}{n_2}\right). \tag{1.14}$$

For GaAs and GaP, these angles are 16° and 17°, respectively. For GaN–air interface, the critical angle is about 21°, 24°, and 25° at the wavelengths of 365, 450, and 520 nm, respectively. The *critical loss efficiency* can be expressed as $\eta_c = \sin^2\theta_c$ or $1 - \cos\theta_c$.

If the efficiency term associated with internal losses including interface recombination and self-absorption is denoted by η_A, then $\eta_{opt} = \eta_F \eta_c \eta_A$ would represent the efficiency of the total power extraction.

The optical power at the central wavelength λ_0 can be obtained as

$$P_0 = \frac{Ahc}{\lambda_0 \tau_{rad}} \int_0^w n(x) \exp(-\alpha_0 x) \mathrm{d}\, x = \frac{Ahc}{q\lambda_0 \tau_{rad}} J \tau_{eff}. \tag{1.15}$$

Recognizing that hc/λ_0 represents the photon energy and if the photon energy is ξ_{ph} given in electron volts, one can define the internal quantum efficiency as

$$\eta_{int} = \frac{P_0}{I \xi_{ph}}. \tag{1.16}$$

Utilizing Equation 1.15 for the power, we obtain

$$\eta_{int} = \left(\frac{hc}{q\lambda_0}\right)\left(\frac{I}{\tau_{rad}\tau_{eff}^{-1}}\right)\left(\frac{1}{I\xi_{ph}}\right) = \frac{\tau_{eff}}{\tau_{rad}}. \tag{1.17}$$

Multiplying the internal quantum efficiency by the combined loss and efficiency factors, the external quantum efficiency becomes

$$\eta_{ext} = \eta_{opt}\eta_{int} = \eta_{opt}\frac{\tau_{eff}}{\tau_{rad}}, \tag{1.18}$$

which is about 10% for UV and blue GaN-based diodes. In the case where there are ohmic losses, the term ξ_{ph} must be replaced by the energy corresponding to the applied voltage qV_{appl}. Then, the external quantum efficiency will assume the form

$$\eta_{ext} = \eta_{opt}\left(\frac{\tau_{eff}}{\tau_{rad}}\right)\left(\frac{\xi_{ph}}{qV_{app}}\right). \tag{1.19}$$

The optical power extracted from the LED is given by

$$P_0 = \eta_{opt}\left(\frac{hc}{q\lambda_0}\right)\frac{I}{\tau_{rad}\tau_{eff}^{-1}}. \tag{1.20}$$

For a double-heterojunction LED, where the active layer is the only absorbing layer in the entire structure on a transparent substrate, the internal absorption term, η_A, including interface recombination, has been determined to be [2]

$$\begin{aligned}\eta_A = &\left\{2\left[\left(V_s^2+1\right)\sinh\left(\frac{w}{L}\right)+2V_s\cosh\left(\frac{w}{L}\right)\right]\right\}^{-1}\\ &\times\left\{\left[\frac{1+V_s}{1+\alpha L}\right]\left[1-\exp w\left(\frac{1+\alpha L}{L}\right)\exp\frac{w}{L}\right]-\left[\frac{1-V_s}{1-\alpha L}\right]\right.\\ &\times\left.\left[1-\exp w\left(\frac{1-\alpha L}{L}\right)\exp\frac{-w}{L}\right]\right\},\end{aligned} \tag{1.21}$$

with $V_s = v_s L/D$.

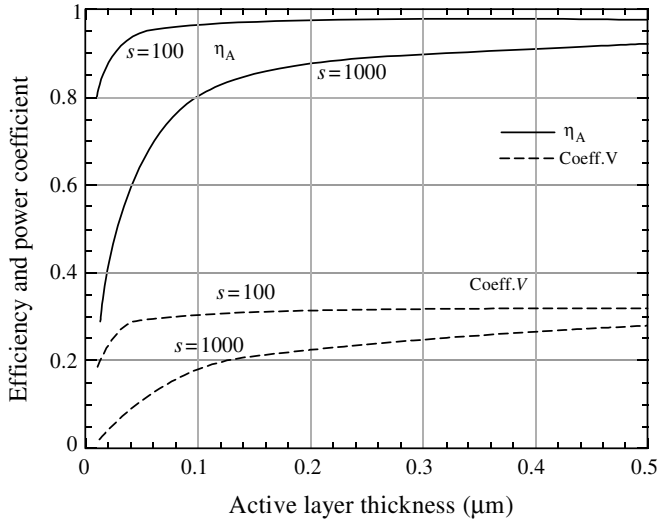

Figure 1.5 The efficiency reduction term caused by interface recombination and bulk absorption in an otherwise ideal GaN-based LED for surface-recombination velocities of 100 and 1000 cm s^{-1}. The coefficient term relates the output power to the injection current.

Figure 1.5 exhibits η_A as a function of the active layer thickness for two surface-recombination velocities (100 and 1000 cm s^{-1}). The other parameters used are for GaN, even though all the LEDs are made of InGaN (center wavelength: 450 nm; electron mobility: 600 $cm^2 V^{-1} s^{-1}$). The effective carrier lifetime is as indicated (radiative lifetime $= 2 \times 10^{-9}$ s, absorption coefficient $\alpha = 10^5$ cm^{-1}, and refractive index = 2.6). Moreover, the coefficient in front of the injection current in Equation 1.15 relating the power to the injection is also plotted. In the absence of available data, what would be plausible was chosen based on the assertion that the GaN surface is reasonably inert. Further consideration was given to the observation that the Schottky barrier height seems to become higher with an increased work function of the metal. Figure 1.6 displays the same parameters as a function of the surface-recombination velocity in the range of 1–10 000 cm s^{-1} for several thicknesses of the active layer ranging from 3.5 to 20 nm.

Having done the analysis, we must recognize that the underlying assumption made is that the carrier motion in the active layer is driven by conventional diffusion. However, the InGaN active layer utilized in an LED is highly clustered and textured, and far from ideal for the diffusion-limited current to be applicable. In fact, these clusters may be responsible for the carrier localization and therefore the enhanced radiative recombination, which may explain the efficient light emission even in the presence of extremely high concentrations of defects. The expressions above are meant to provide the reader with a guide to which parameters are important and what role they play in the device operation. Appropriate carrier lifetimes, when available,

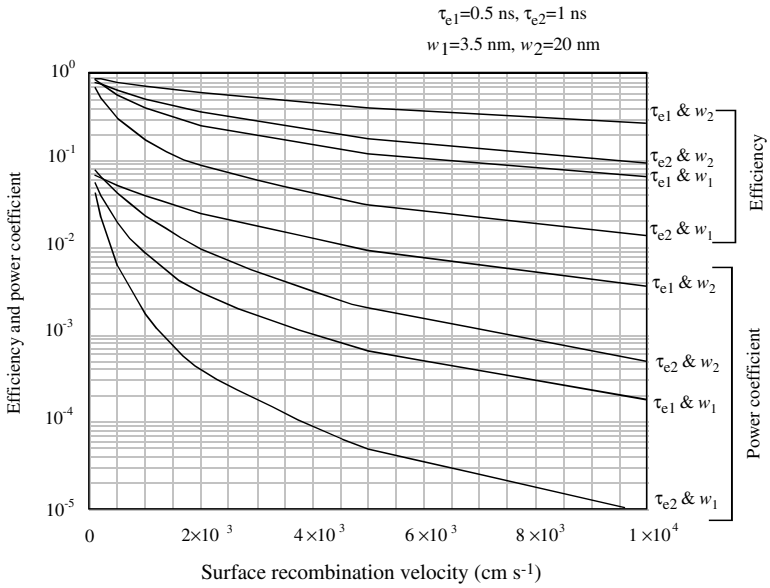

Figure 1.6 The parameters of Figure 1.5 as a function of the surface-recombination velocity for active layer thicknesses ranging from 3.5 to 20 nm. Here, τ_e and w represent the lifetime and active layer thickness, respectively.

can be used in conjunction with the expressions provided here to arrive at characteristics representative of devices available today.

1.4 Current Crowding

Current spreading is prevalent in many semiconductor devices including bipolar transistors, which provided impetus for investigations leading to the understanding of the phenomenon and the means to combat it, and of particular interest LEDs and laser diodes fabricated on insulating substrates. Current crowding robs the device of its optimum performance, as well as causing premature breakdown, and as such it is an important and complex process [5, 6]. Most GaN-based light-emitting diodes are grown on insulating sapphire substrates and thus employ mesa structures with lateral contact geometries of the anode and cathode electrodes. The uniform current spreading in such mesa structures can be expected when the p- and n-cladding layers are thick and highly conductive [5]. However, the growth of thick and highly conductive p-type AlInGaN films is more difficult, compared to that of the n-type films. Thus, it is intuitively expected that the current in the mesa structure will crowd near the edge of the p-type metal electrode. Nakamura and Fasol [7] used a Ni/Au transparent electrode on the p-type cladding layer to help uniformly spread the current in the mesa structure of GaN-based

LEDs. To date, the p-transparent electrode is generally used for GaN-based LEDs. It can be, in turn, expected that the highly conductive p-transparent electrode may cause a current crowding at the edge of p-type mesa near the n-type electrode when the sheet resistance of n-type GaN cladding layer is larger than that of the p-transparent electrode. In 1999, Eliashevich *et al.* [8] demonstrated experimentally that the insufficient n-GaN conductivity in InGaN LEDs caused current crowding near the edge of the mesa adjacent to the n-contact pad, resulting in a degradation of the LED performance. This kind of current crowding, which can be caused by employing the highly conductive p-transparent electrode, can be minimized by (i) adjusting the device parameters related to the current-spreading length, L_s [9], (ii) optimizing the configuration of p- and n-metal electrodes [10], or (iii) a combination of the methods.

Calculations of current crowding in lateral p-side-up mesa structures utilizing GaN/InGaN grown on insulating substrates have been carried out by Guo and Schubert [11] using an equivalent circuit model shown in Figure 1.7. The model includes the p-type contact resistance and the resistances of the n-type and p-type cladding layers with the assumption that the p-type metal contact has the same electrostatic potential at every point. The p–n-junction region was approximated by an ideal diode. The developed model revealed an exponential decrease of the current density with distance from the mesa edge. That is, the model could quantitatively explain the current crowding effect near the mesa edge when the sheet resistance of the p-type transparent electrode is zero. Later, an advanced model to explain the current crowding phenomenon was presented by Kim *et al.* [9]. The model included the lateral resistance component of the p-type transparent electrode in the equivalent circuit of the LED, which is different from the earlier model developed by Guo and Schubert [11]. The expanded model revealed that the current distribution of the LED was critically dependent on the sheet resistance of p-type transparent electrode, that is, the film thickness of the p-transparent electrode, and that theoretically uniform current spreading would be possible when the sheet resistances of the p-transparent electrode and

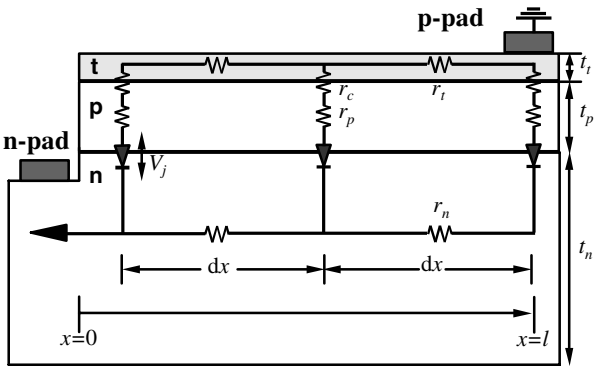

Figure 1.7 Equivalent LED circuit, with a p-pad as the physical ground that can be used to model current crowding [9].

n-type layer are identical. The expanded model developed by Kim *et al.* [9] is introduced as follows.

Figure 1.7 shows the schematic LED structure with lateral injection geometry. In this structure, important distributed components of the total series resistance can be categorized into the lateral resistance component of the n-layer, r_n, and the transparent electrode, r_t, and the vertical component of the p-layer, r_p, and the p-contact, r_c. It is noted that the nontransparent p-pad and the transparent p-electrode layer are discriminate. Applying the assumption that the p-pad is grounded, the current continuity equation applied to the circuit in Figure 1.7 leads to the following two basic equations:

$$\frac{d^2 V_n}{dx^2} = \frac{\rho_n}{t_n} J, \qquad \frac{d^2 V_t}{dx^2} = \frac{\rho_t}{t_n} J. \tag{1.22}$$

The relation between V_n and V_t can also be expressed as follows:

$$V_n = V_j + R_v I_0 \exp\left(\frac{eV_j}{kT}\right) + V_t. \tag{1.23}$$

The parameters V_n, V_t and ρ_n, ρ_t are the lateral voltage drops and the electrical resistivities of the n-layer and p-transparent electrode, respectively, and J is the current density across the p–n-junction region. V_j is the junction voltage drop, I_0 is the reverse saturation current, and R_v is the vertical resistance of the area element $w\,dx$.

Using the above three equations, Kim *et al.* [9] derived the following diode equation:

$$J(x) = J(0)\exp\left[\pm x \Big/ \left(\sqrt{(\rho_c + \rho_p t_p)\left|\frac{\rho_n}{t_n} - \frac{\rho_t}{t_t}\right|^{-1}}\right)\right]; \quad -, \text{ p-pad}; \quad +, \text{ n-pad}, \tag{1.24}$$

where $J(0)$ is the reverse saturation current density at the mesa edge, and the $(-)$ sign holds for the p-pad and the $(+)$ sign for the n-pad as physical grounds, respectively. As a result, the current-spreading length, L_s, can be expressed as follows:

$$L_s = \sqrt{(\rho_c + \rho_p t_p)\left|\frac{\rho_n}{t_n} - \frac{\rho_t}{t_t}\right|^{-1}}. \tag{1.25}$$

Figure 1.8 shows the calculated current distribution of the LED, indicating that it is possible to achieve a perfectly uniform current distribution at the critical condition of $\rho_t/t_t = \rho_n/t_n$.

The current-spreading length equation given above illustrates that the current distribution in the LED structure can be controllable by adjusting the device parameters included in the expression, which is fruitful in designing efficient high-power III-nitride LEDs.

Because the conductivity of the p-layer is relatively low, which is the crux of the current-spreading problem, coupled with all on-top contact configuration, attempts have been made to reduce the current crowding effect. However, it must be mentioned that vertical device structure thin-film LEDs, including the top and

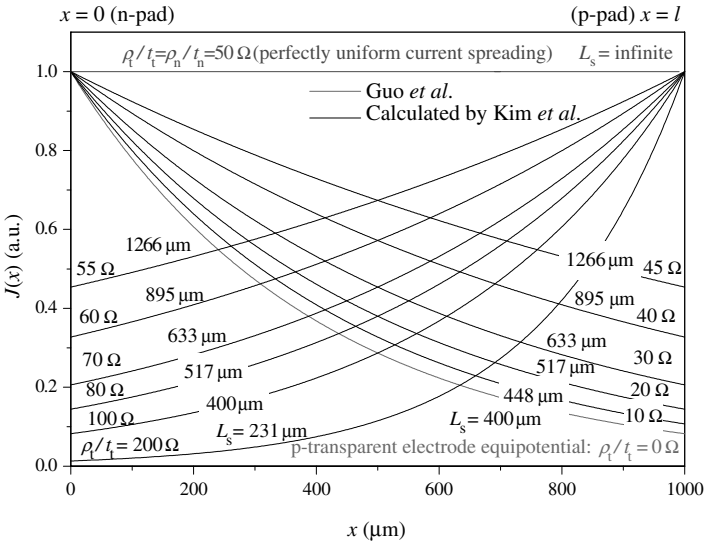

Figure 1.8 Calculated current distributions versus the lateral length x in a LED. The parameters used in the calculation $\rho_n = 0.01\,\Omega\,\text{cm}$, $t_n = 2\,\mu\text{m}$ [9].

bottom contact configurations, have been developed for high-efficiency and highly luminous devices that obviate the current-spreading problem to a large extent. Nevertheless, for completeness and instructional value, a few approaches that have been used to help alleviate current spreading in surface oriented devices are discussed here. For example, Jeon *et al.* [12] have shown that p^+/n^+ GaN tunnel junctions (TJs) inserted into the upper cladding layers of conventional devices allow the use of an n-type GaN in place of a p-type GaN as the top contact layer. The reverse-biased tunnel junction helps with lateral current spreading without semitransparent electrode and spatially uniform luminescence exhibiting an improved radiative efficiency. With the same goal in mind, an n^+ short-period superlattice [13] and a p-InGaN tunneling contact layer on low conductive p-GaN [14] have been employed for uniform current distribution. Again, in the same vein an undoped GaN spacer layer [15] and a modulation-doped AlGaN/GaN heterostructure [16] have also been inserted.

The current crowding effect, which can be reduced by employing a p-transparent electrode, can also be minimized by improving the metal contact configuration. This is especially important in high-power AlInGaN LEDs with a large chip size. Krames *et al.* [10] reported an interdigitated contact geometry, wherein each set of p-metal contacts is surrounded by two n-metal contact fingers. The interdigitated configuration reduces the spreading distance required by the current in the n-GaN layers, resulting in a more uniform current distribution on a large-area LED chip [17]. Figure 1.9 shows the schematic (a) planar and (b) cross-sectional views of a large-area LED structure employing the interdigitated contact geometry, which shows symmetric current paths below the p-metal pads.

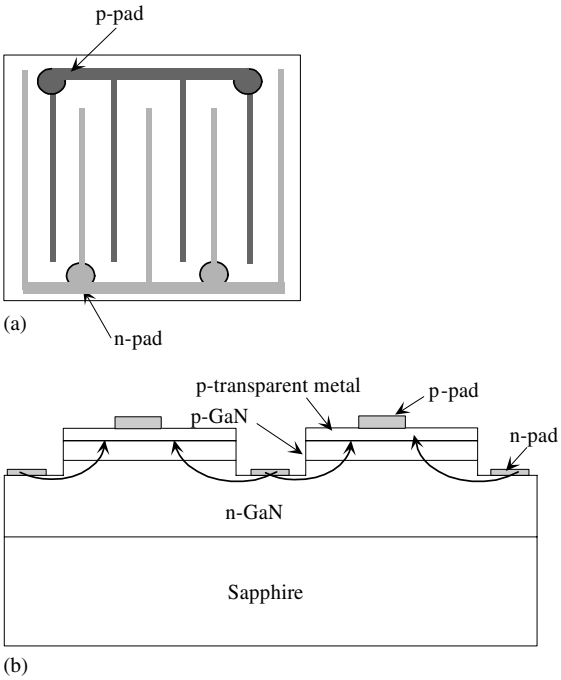

Figure 1.9 Schematic (a) plane and (b) cross-sectional views of a $1 \times 1\,mm^2$ power AlInGaN LED employing interdigitated contact geometry [10].

1.5 Packaging

Packaging plays multiple roles in that it mechanically interfaces the LED chip to its operating interface, inclusive of electrical connections; in many cases, it focuses and increases the light extracted from the LED, dissipates the heat generated, and provides protection, both in physical terms and against stray fields. Packaging is configured for a given device design. It should be pointed out, however, that LEDs are nowadays competing in areas that are not traditional for them and as such the standard packaging design may not be appropriate for all devices. The standard LED package is the 5 mm diameter epoxy dome with which everyone is familiar.

Device design and packaging go hand in hand. To increase light extraction from a p–n-junction, the active layer is placed close to the surface; the entire layer structure outside of the active layer is made of a transparent (larger bandgap) semiconductor that transmits the emission wavelength. Moreover, a dome of lower refractive index (lens) is placed on top of the device, which increases the collection cone and causes the photons entering it to strike the domed surface at or near a normal angle with an escape certainty of unity (Figure 1.10). For extracting as much of the light generated

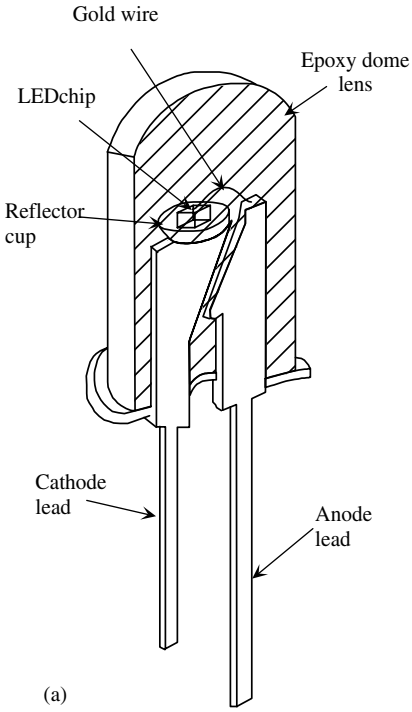

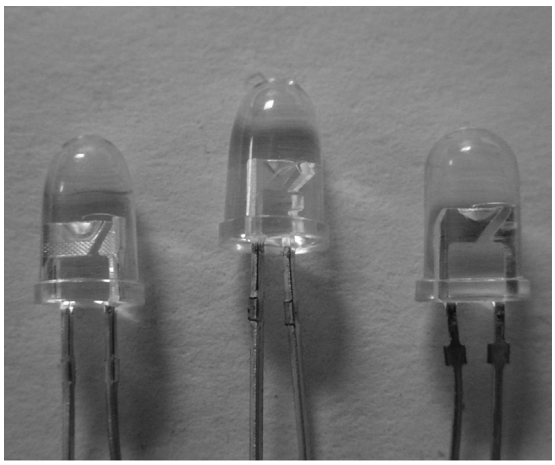

(b) "5 mm" LEDs

Figure 1.10 (a) Schematic representation of a standard 5 mm epoxy domed LED for enhanced light collection as well as focusing of the emitted light (circa 1970). This cross-sectional schematic also identifies the various important components in the package. (b) A photograph of three 5 mm domed packaged LEDs. The longer lead represents the anode and is connected to the positive terminal of the battery for light emission. This package could be used at current levels of 30 mA with the LED producing 2–3 lm. Courtesy of Lumileds/Phillips.

as possible, a transparent top ohmic contact coupled with, when applicable, a high-reflectivity back contact is also employed. The dome increases the efficiency by about twice the square of the refractive index of the semiconductor. The dome also serves to focus the light, concentrating the radiation within the field of view. Various dome approaches are available, among which are hemispheres, truncated spheres, and paraboloidal types with narrowing radiation patterns. The cone defined by the total reflection angle in larger bandgap semiconductors, such as GaN, is larger and increases the light collection. In 5 mm LEDs, only about 60% of the light flux is captured within a 120° cone in air.

For higher power LEDs, as compared to the 5 mm devices, the chip design must be improved [18]. For high-luminance LEDs, flip-chip mounting combined with Ag-based back-reflector techniques has been utilized [19, 20], an example of which, developed by Lumileds, is shown in Figure 1.11. These high-power devices are much larger than the conventional chip, with dimensions of $1 \times 1\,\mathrm{mm}^2$ (i.e., $\approx 10\times$ larger active area) or larger. The large area of the chip puts stringent requirements on the current spreading in the GaN:Si layers beneath the active region. It is impossible to spread current uniformly over the full distance of the chip through a GaN:Si layer that is only a few microns in thickness, but an interdigitated contact design is employed to separate the large area of the chip into segmented areas, or cells, wherein uniform current spreading and low series resistance is achieved. The flip-chip design described below addresses the issues pertinent to this high-power device.

There are many advantages to the flip-chip LED (FCLED) design among which is the fact that light exits through the polished transparent sapphire substrate instead of an absorbing Ni/Au contact layer as for the case of top-emitting power and conventional AlGaInN LEDs [19]. Also, downward-propagating light is reflected up, increasing the light extraction, as shown in Figure 1.11. A second benefit is that the heat generated in the LED flows directly from the p–n-junction out through the Si submount, which forms the base of the package and has a thermal conductivity that is at least three times better than that of sapphire. This is important because under standard operating conditions, the power dissipation in the high-power chip is approximately 1 W (350 mA at $\approx$3.5 V), which is more than 10 times that for conventional LEDs in 5 mm LEDs [18]. The Si submount also contains two back-to-back semiconductor diodes for electrostatic discharge (ESD) protection to which LEDs on sapphire are prone. Third, current spreading on the p-side of the device is handled by a thick p-contact, instead of the standard thin Ni/Au contact in conventional mounting schemes, reducing spreading resistance. In conventional mounting schemes, the Ni/Au contact must be made thin enough for light propagation. Thinner metal allows greater light transmission at the expense of increased current crowding, which lowers the injection efficiency of the devices by preferentially favoring the edges of the device and forcing the area in the middle to be pumped at lower injection currents. Finally, the outer housing, which provides support for a plastic lens, contains a concave recess that forms a cavity surrounding the chip. This cavity is backfilled with a soft silicone encapsulant ($n \approx 1.5$), which provides increased light extraction while minimizing thermal expansion/contraction stress on the chip and wire bonds during operation.

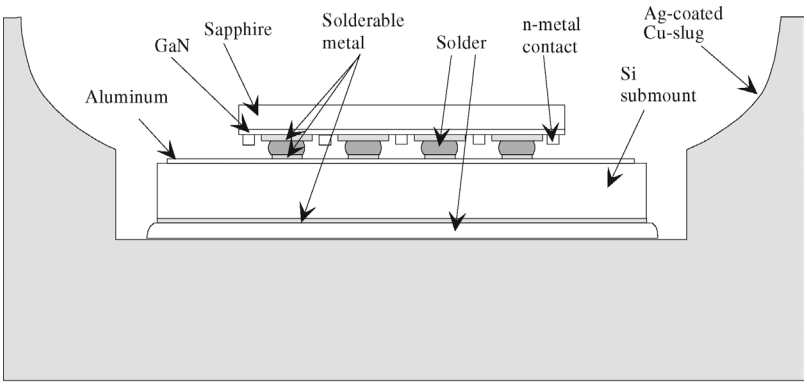

(a)

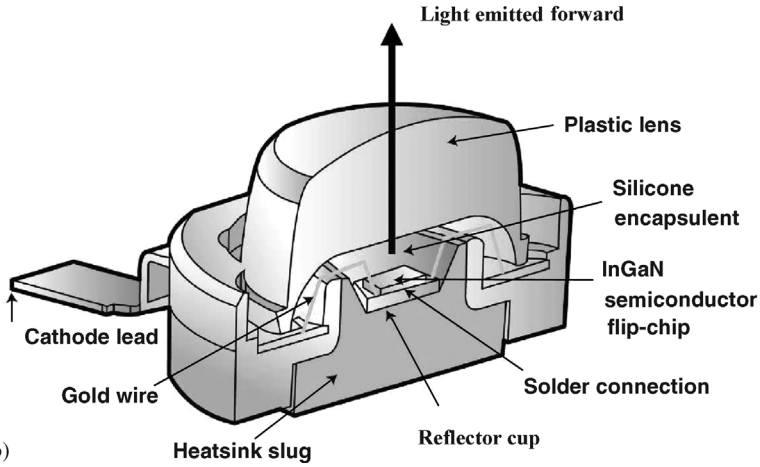

(b)

Figure 1.11 (a) Cross-sectional schematic flip-chip mounted high-luminance LED package with Ag back-reflector. Electrostatic discharge protection is integrated into the Si submount (circa 1997). The package is able to handle power dissipation associated with 350 mA current injection with resulting LED lumens of 20–40 lm. (b) Artistic rendition of the package inclusive of plastic lens. In this flip-chip model, the substrate can be removed and the exposed N-polarity GaN can be made dark by chemical etching or a polymeric photonic crystal can be placed on what is now the top surface for better photon collection. Polymeric photonic crystal can be produced by laser lithography (holography) to reduce the cost of fabrication. Courtesy of Lumileds/Phillips. (Please find a color version of this figure on the color tables.)

The improved extraction efficiency of the flip-chip LED provides 1.6 times more light when compared to top-emitting power LEDs and 10 times more light than conventional small-area ($\sim$0.07 mm^2) LEDs. The design also features low spreading resistance, mitigating current crowding. Additional attributes are low thermal

resistance, stable and soft gel inner encapsulant, and controlled radiation patterns. As has been reported, this improved packaging led to output powers greater than 250 mW ($1 \times 1\,mm^2$ device) and 1 W ($2 \times 2\,mm^2$ device) at standard operating current densities ($\approx 50\,A\,cm^{-2}$), corresponding to "wall-plug" efficiencies of 22–23% in the blue wavelength regime. Employing phosphors for the generation of white light, these same devices achieve luminous efficiencies higher than $30\,lm\,W^{-1}$. This package is well suited for the high-power Luxeon LEDs developed by Lumileds with electrical input power levels up to 5 W.

For enhancing the light extraction efficiency, a thin-film LED structure, in which the substrate is removed, has been reported [21]. This particular technique employs a combination of laser liftoff (LLO) and photoelectrochemical (PEC) etching to produce a roughened top surface with cone-like features, from which the light emerges. The output power of an optimally roughened surface LED showed a twofold to threefold increase as compared to that of an LED without surface roughening.

The combination of the thin-film LED concept with flip-chip technology can provide surface brightness and flux output advantages over the conventional flip-chip and vertical-injection thin-film LEDs [22]. An encapsulated thin-film flip-chip blue LED (TFFC-LED) ($\sim$441 nm) exhibited an external quantum efficiency of 38% at a forward current of 350 mA. A white-LED lamp based on a YAG:Ce phosphor-coated device exhibited a luminous efficacy of $60\,lm\,W^{-1}$ at 350 mA with a peak efficiency of $96\,lm\,W^{-1}$ at 20 mA and a luminance of $38\,Mcd\,m^{-2}$ for 1 A drive current. Green ($\sim$517 nm) LED devices exhibited a luminance of $37\,Mcd\,m^{-2}$ at 1 A.

In the world of LEDs, it is clear that there are three guiding principles: convert all the electron–hole pairs into photons to the extent possible; collect all the photons, again to the extent possible, from the emitting surface; and minimize the Joule heating (heat loss). The former relies on device designs, such as the use of heterojunction, and material quality and is commonly measured by internal quantum efficiency. The second is addressed by the use of transparent layers, contacts, and substrates with the exception of the emitting region of the semiconductor that can be made thin by using double heterojunctions. In addition, the plastic lens, which not only focuses the light somewhat but also increases the collection angle from within the semiconductor, helps in this respect. Essentially, the optical size of a component, which is termed the étendue, must be increased. As the need to extract more light from LEDs became more critical with the advent of LEDs being used not just for displays but illumination also, the shape of the semiconductor chip has also taken a central role. The third item can be addressed by reducing the series resistances arising from both the semiconductors and ohmic contacts. The evolution of chip designs within the framework of light extraction is shown in Figure 1.12. In the Lambartian design of Figure 1.12d, the étendue that is given (in terms of $mm^2\,sr$) by.

$$E = \pi A n^2 \sin(\theta/2) \tag{1.26}$$

is maximized. Here, A is the emission area of the optical component (in mm^2), n is the refractive index of the medium surrounding the optical component, and θ is the angle of emission. In the Lambartian design, the angle $\theta = \pi$, maximizing $E = \pi A n^2$.

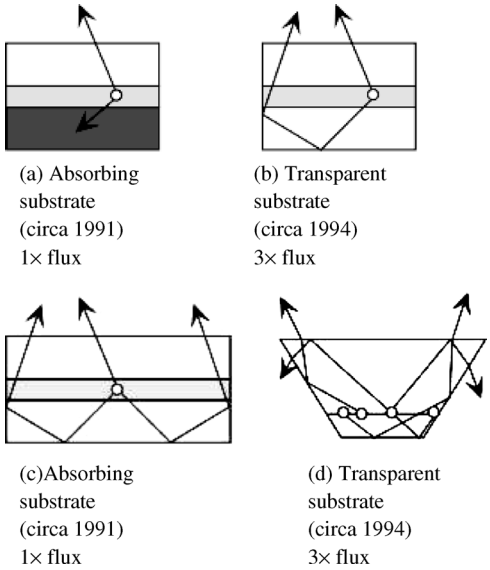

Figure 1.12 Evolution of LED chip and chip shapes in the pursuit of extracting more of the photons generated within the chip. The circle represents the point of photon generation. Part (a) depicts the early designs with absorbing substrates, (b) indicates transition to the transparent substrates with back-reflectors, (c) depicts increased area for better collection of photon (larger étendue), and (d) indicates reshaping of the LED package for even more enhanced collection of photons. In the Lambartian design (d), the use of a thin quantum well emitting layer as opposed to a thick emitting layer has also been incorporated. From (a) to (d), an enhancement by a factor of 30 in the light flux has been realized. Courtesy of Lumileds/ Phillips.

Once the chip is removed from the substrates, the chip can be mounted on a metal alloy substrate, which has a very high thermal conductivity of $400\,\mathrm{W\,m^{-1}\,K^{-1}}$ and therefore allows high-current operation (see Figure 1.13 for a schematic) [23]. The chip has a patterned surface with "photon-injecting nozzle" microstructures to

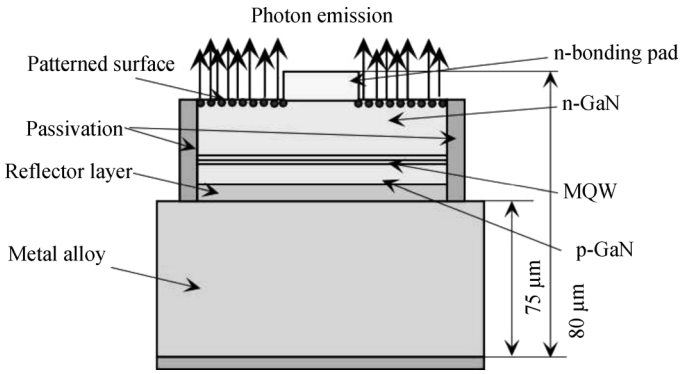

Figure 1.13 A MVP-LED structure from Semi-LEDs. Courtesy of C. A. Tran [23].

enhance light extraction in the forward direction. Eight LED chips packed together could provide 460 lm white light with a luminous efficacy of 58 lm W^{-1} at 470 mA. The metal vertical photon LED (MVP-LED) has a p-down epitaxial structure mounted on a reflector layer that is attached to a metal alloy substrate.

Even with the thin flip-chip package, one must still deal with the top-emitting surface, namely, the semiconductor–air interface reflection and the associated collection cone angle. Unless this is countered, only a fraction of photons headed toward the top surface would actually escape the semiconductor. To eliminate the above-mentioned internal loss issue of GaN LEDs and to extract more light from the device surface, GaN-based photonic crystal (PC)-LEDs fabricated using a laser holography (LH) method have been reported [24]. These structures are suitable for high-throughput and large-area processing. There are two kinds of PC-LEDs reported: top-loaded and bottom-loaded. For the top-loaded PC-LEDs [25], a conventional LED structure was grown first. Then using laser holography method, the photonic crystal pattern was generated, as shown in Figure 1.14. The resultant LEDs exhibited significant improvements in light extraction, up to 1.5 times that of planar LEDs without PC integration. Similar results were obtained for the bottom-loaded

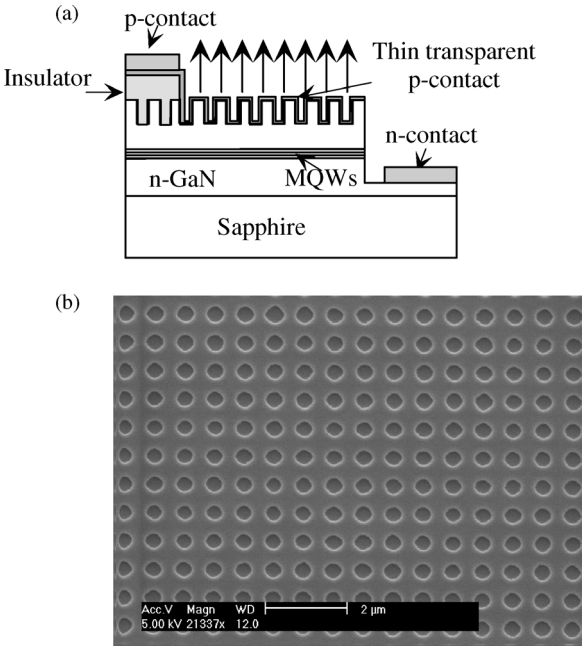

Figure 1.14 (a) Schematic view of a top-loaded PC-LED, illustrating the vertical layer structure of the device. (b) Scanning electron microscope image for a top-loaded PC-LED device surface. The square-lattice air–hole array pattern was generated by the holographic double-exposure method. The lattice period of this specific example is ~700 nm. Courtesy of H. Jeon [24].

PC-LEDs, in which the photonic crystal was formed between the substrate and the epilayer.

Another approach to reduce the internal optical loss is to employ a so-called "sidewall deflector" to reflect out the photons that are trapped between the air–GaN–sapphire waveguide. Typically, angles of 20–40° between the mesa sidewalls and the substrate were achieved by a photoresist reflow method [26]. Experimental results, including photoluminescence and near- and far-field patterns, show a strong additional emission along the sidewall edge, and the proposed LED structure enhanced the overall surface emission intensity by a factor of 2 for a sidewall angle of 30°. When a combination of photonic crystal and angled sidewall was employed, three times higher emission power was achieved.

1.6 Perception of Visible Light and Color

Human vision is a complex process, the understanding of which is still an evolving matter. It involves the simultaneous interaction of the eyes and the brain through a network of neurons, receptors, and other specialized cells. The initial steps in vision are the stimulation of light receptors in the retina, which lines the back of the eyeball, and transmission of electrical signals containing the vision information to the brain through the optic nerves. This information is processed in several stages, ending at the visual cortex of the brain.

The human eye is equipped with a variety of optical elements including the cornea, iris, pupil, aqueous and vitreous fluids, variable-focus lens, and the retina, as illustrated in the schematic shown in Figure 1.15. Together, these elements work

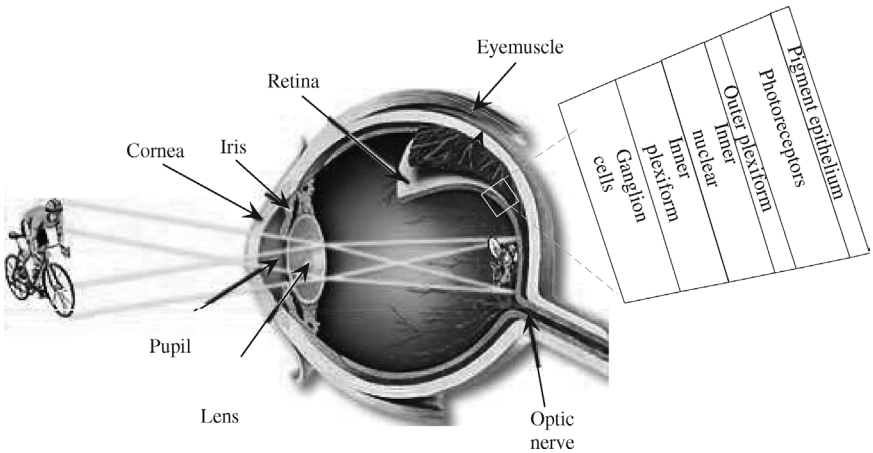

Figure 1.15 Diagram of a human eye showing its various structures along with the optical path of vision. (Please find a color version of this figure on the color tables.)

to form images of the objects in our field of view. The iris, which opens wide at low light levels and closes to protect the pupil and retina at very high levels, controls the amount of light entering the eye. As the light enters, it is first focused through the cornea and lens onto the retina, a filmy, multilayered membrane that contains millions of light-sensitive cells that detect the image and translate it into a series of electrical signals. These image-capturing receptors, which are termed *rods* and *cones*, are connected with the fibers of the optic nerve bundle through a series of specialized cells and tissues that coordinate the transmission of signals to the brain. It is interesting to note here that these tissues develop from a pouch of the embryonic forebrain, and therefore the retina is considered part of the brain.

The basic structure of the retina can be compared to a three-layer cake, with the bodies of nerve cells arrayed in three rows separated by two layers packed with synaptic connections. The back of the retina contains the photoreceptive sensory cells, and being there, light rays must pass through the entire retina before reaching photoreceptive molecules to excite. The retina in mammals contains at least two types of photoreceptors, namely, rods and cones, but rods dominate. Rods are utilized for low-light vision and cones for daylight. At dusk, dawn, and in dimly lit places, rods provide gray vision without color. The cones are responsible for bright-colored vision. Most mammals have two types of cones, green-sensitive and blue-sensitive, but primates have three types of cones: red-sensitive, green-sensitive, and blue-sensitive. With our cone vision, we can see from gray dawn to the dazzling conditions of high noon.

Most fish, frog, turtle, and bird retinas have three to five types of cones and consequently very good color vision. In cats and dogs, images focus to a central specialized area, appropriately called the area centralis, where the cones predominate. The retinas of mammals such as rabbits and squirrels, as well as those of nonmammals such as turtles, have a long, horizontal strip of specialized cells called a visual streak, which can detect the fast movement of predators. Primates as well as some birds have front-projecting eyes allowing binocular vision and thus depth perception; their eyes are specialized for good daylight vision and are able to discriminate color and fine details. Primates and raptors, such as eagles and hawks, have a fovea, a tremendously cone-rich spot devoid of rods where images focus. The fovea contains most of the cones, packed together as tightly as physically possible, and allows good daylight vision. More peripheral parts of the retina can detect the slightest glimmer of photons at night.

Initially, the cone photoreceptors themselves can adapt to the surrounding brightness, and circuitry through the retina can further modulate the eye's response. Similarly, the rod photoreceptors and the neural circuitry to which they connect can adapt to lower intensities of light. An artistic rendering of retina with photoreceptors is shown in Figure 1.16, where the photoreceptors are at the top of the schematic. Both rods and cones respond to light with a slow hyperpolarizing response, but report quite different image properties. Rods, detecting dim light, usually respond to relatively slow changes. Cones, dealing with bright signals, can detect rapid light fluctuations. As photons strike these photoreceptors, retinal molecules become fixed in the photoreceptors' scotopsin (rods) or photopsin (cones) proteins, and these

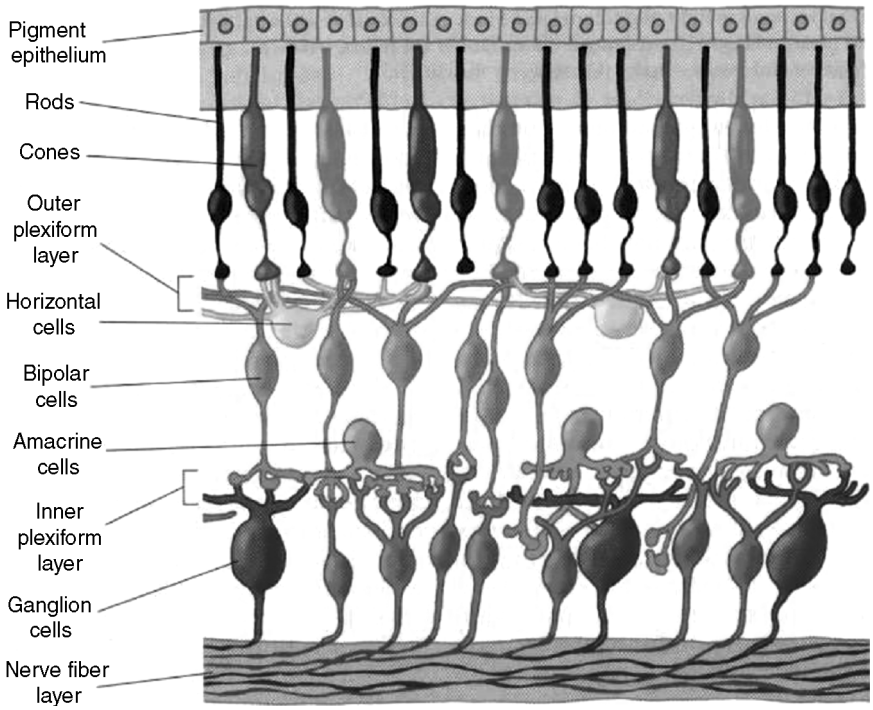

Figure 1.16 A schematic showing rods that are sensitive to low-level gray light and cones that are sensitive to color. In this rendering, light enters the eye from the bottom. The photons travel through the vitreous fluid of the eyeball and penetrate the entire retina, which is about half a millimeter thick, before reaching the photoreceptors: the cones and rods that respond to light (the colored and black cells attached to the epithelium on top). Signals then pass from the photoreceptors through a series of neural connections toward the surface of the retina, where the ganglion cell nerve fiber layer relays the processed information to the optic nerve and then to the brain [27]. (Please find a color version of this figure on the color tables.)

molecules change their conformation in response to the photons. Once retinal molecules are exposed to light and undergo their conformational change, they are recycled into the dark row of cells at the back of the retina called the pigment epithelium [27, 28].

This tissue behind the retina is usually very dark because its cells are full of melanin granules. The pigment granules absorb stray photons, preventing their reflection back into the photoreceptors, which would cause images to blur. They also protect the cells from too much exposure to light radiation.

The image continues to be broken into component elements at the first synapses of the visual pathway, those between photoreceptors and what are called the bipolar cells. Different bipolar cells have different types of receptors for the neurotransmitter glutamate, allowing the cells to respond to photoreceptor input differently. Some bipolar cells are tuned to faster changes and some to slower ones in the visual signal; some glutamate receptors resensitize rapidly and others more gradually.

Consequently, the cells fire either quickly in succession or relatively slowly in response to the same amount of stimulation. Some receptors respond to glutamate by activating what is known as an OFF pathway in the visual process, detecting dark images against a lighter background. Other bipolar cells have inhibitory glutamate receptors, which prevent the bipolar cell from firing when the cell is exposed to the neurotransmitter. These receptors activate the ON pathway, detecting light images against a darker background [19].

Intricately wired neurons in the retina allow a good deal of image assembly to take place in the eye itself. The parallel sets of visual channels for the ON (detecting light areas on dark backgrounds) and OFF (detecting dark areas on light backgrounds) qualities of an image are fundamental to our seeing. Parallel bipolar channels transmit inputs to ganglion cells. In early stages of development, the architecture of the inner plexiform layer, which is full of synapses between bipolar and ganglion cells, shows that synaptic connections become segregated in distinct and parallel pathways. Connections occur between ON bipolar cells and ON ganglion cells and also between OFF bipolar cells and OFF ganglion cells in delineated portions of the inner plexiform layer. If the retina were simply to transmit opposite-contrast images directly from the photoreceptors to the brain, the resulting vision would probably be coarse, grainy, and blurred. Further processing in the retina defines precise edges to images and provides the means to focus on fine details. The fine-tuning of image perception starts at the first synaptic level in the retina, where horizontal cells receive inputs from many cones. Horizontal cells' receptive fields become even broader because their plasma membranes fuse with those of neighboring horizontal cells at gap junctions. The membrane potentials of a whole sheet of cells become the same; consequently, horizontal cells respond to light over a very large area. Meanwhile, a single bipolar cell receives inputs from a handful of cones and thus has a medium-sized receptive field. Whereas a single bipolar cell with its OFF or ON light response would carry a fairly blurred response to its ganglion cell, horizontal cells add an opponent signal that is spatially constrictive, giving the bipolar cell what is known as *center surround* organization [27].

At the anatomical level, imaging techniques ranging from silver staining to electron microscopy and modern-day antibody staining have been applied to reveal the shapes and sizes of the retina's cell types and how the different cells connect to form synapses. The optic nerve fibers could be stimulated to give traditional depolarizing action potentials, like those observed in other neurons. These "S potentials" are now known to originate with the photoreceptors and to be transmitted to horizontal cells and bipolar cells. The membrane hyperpolarization starts on exposure to light, follows the time course of a light flash, and then returns to the baseline value when the light is off. This reflects the counterintuitive fact that both rods and cones release neurotransmitters during the dark, when the membrane is depolarized and sodium ions flow freely across the photoreceptors' cell membranes. When exposed to light, ion channels in the cell membranes close. The cells go into a hyperpolarized state for as long as the light continues to shine on them and do not release a neurotransmitter [28]. In the brain, the optic nerves from both eyes join at the optic chiasma where information from both retinas is

correlated. From here, the visual information travels to the lateral geniculate nucleus where the signals are distributed to the visual cortex located on the lower rear section of each half of the cerebrum. The fovea centralis is located in an area near the center of the retina located on the optical axis of the eye. This area contains exclusively high-density tightly packed cone cells and is the area of sharpest vision. The density of cone cells decreases outside of the fovea centralis, and the ratio of rod cells to cone cells gradually increases. At the periphery of the retina, the total number of both types of light receptors decreases substantially, causing a dramatic loss of visual sensitivity at the retinal borders. This is offset by the fact that we constantly scan objects in the field of view, giving a perceived image that is uniformly sharp.

Rod cells have peak sensitivity to green light (about 550–555 nm), although they display a broad range of responses throughout the visible spectrum. They are the most populous visual receptor cells, with each eye containing about 130 million cells. The light sensitivity of rod cells is about a thousand times that of cone cells. However, as mentioned above, the images generated by rod stimulus alone are relatively blurred and confined to shades of gray, similar to those found in a black-and-white soft-focus photographic image. Rod vision is commonly referred to as *scotopic* or twilight vision because in low light levels, it allows us to distinguish the shapes and relative brightness of objects, but not their colors. When all three types of cone cells are stimulated equally, we perceive the light as being *achromatic* or white. As an example, noon sunlight appears to us as white light because it contains approximately equal amounts of red, green, and blue light. An excellent demonstration of the color spectrum of sunlight is interception of the light by a glass prism, which refracts (or bends) different wavelengths to varying degrees, spreading out the light into its component colors. Our color perception is dependent upon the interaction of all receptor cells with light and this combination results in nearly trichromic stimulation. There are shifts in color sensitivity with variations in light levels, so blue colors look relatively brighter in dim light and red colors look brighter in strong light. This effect can be observed by pointing a flashlight onto a color print under dim ambient light, which will result in the red suddenly appearing much brighter and more saturated.

In daylight, the human eye is most sensitive to the wavelength of 555 nm, with a maximum sensitivity of 683 $\mathrm{lm\,W^{-1}}$. This is called *photopic vision*. In low-light and night situations, when *scotopic vision* is used the peak sensitivity changes, blueshifting to 507 nm. The maximum sensitivity for scotopic vision is 1754 $\mathrm{lm\,W^{-1}}$. At the red and blue extremes, the sensitivity of the human eye drops dramatically [29–32]. Figure 1.17 shows the *luminous efficacy*, $K(\lambda)$, which represents the effectiveness of the radiant power of a monochromatic light source in stimulating the visual response for daylight vision (*photopic vision*) and night vision (*scotopic vision*). As seen in Figure 1.17, the efficacy curve falls drastically at both ends of the visual spectrum. This increases the requirements for the output power and the external quantum efficiency for emitters in the blue and red regions to achieve the same brightness or luminous performance offered by green-light sources and for practical visual displays.

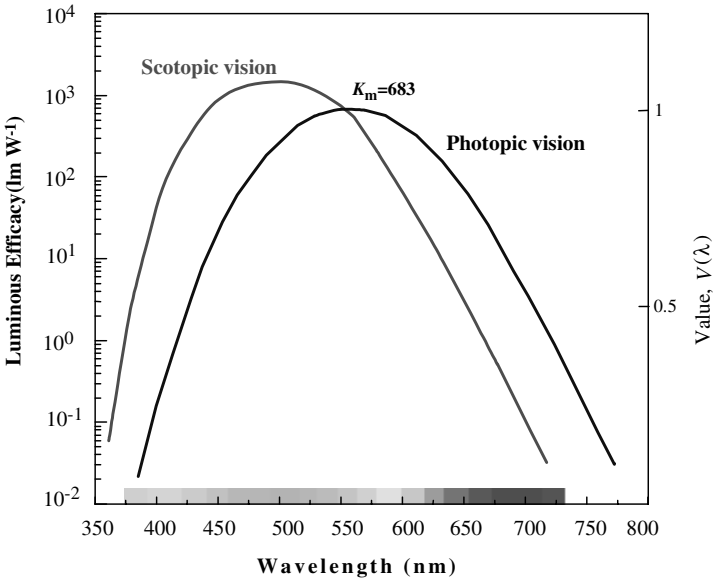

Figure 1.17 Luminous efficacy of monochromatic radiation, $K(\lambda)$, for the human eye under light (photopic vision) and dim (scotopic vision) conditions. The band indicates the color at visible wavelengths. The maximum luminous efficacy, K_m, for photopic vision is 683 lm W^{-1} and occurs at 555 nm. (Please find a color version of this figure on the color tables.)

Another interesting feature of human eye is that it is extremely good at delineating edges. This manifests itself, for example, in two patterns having the same spectral power distribution appearing different depending on the background. In other words, the photopigment response in a small area does not determine the color perceived by human eye. The color appearance then depends on the shape of the image as a whole that is being viewed. This brings about an added complexity to the meaning of color and thus the illumination needed to bring it to being.

1.7 Visible-Light Terminology

The optical power generated by a light-emitting diode must excite the human eye. This brings into the discussion the color perception of the human eye, which has been standardized by the *Commission Internationale de l'Éclairage or International Commission on Illumination* (CIE) [33]. This commission produces charts used by the display society to define colors. Detection and measurement of radiant electromagnetic energy is called *radiometry*, which when applied to the visible portion of the spectrum involving the human eye is termed *photometry*. The nomenclature for the latter delineates itself from the former by adding the adjective luminous to the terms

used for the former. For example, energy in the former is called the *luminous energy* in the latter. The former can be converted to the latter, and vice versa, if the perception of color by the human eye is understood.

The terms employed to describe LED performance in terms of photometric terms are as follows:

Brightness: A subjective term used to describe the perception of the human eye, ranging from very dim, on the one hand, to blinding, on the other. The relationship between brightness and luminance is very nonlinear.

Luminance: The luminous intensity per unit area projected in a certain direction in SI units ($\mathrm{cd\,m^{-2}}$).

Luminous efficiency: The power in photometric terms, measured in lumens per watt, divided by the electric power that generates it. In short, it is lumens output divided by electric power input. To avoid confusion, *luminous efficacy* is used in the display field. In the LED literature, one finds the reference *luminous performance* for this term ($\mathrm{lm\,W^{-1}}$).

Wall-plug efficiency (power efficiency): Optical power output divided by the electrical power provided to the device, irrespective of the spectrum of that output. The electrical *efficacy* of a device is the product of the wall-plug efficiency and the spectral or optical efficacy. This is the most appropriate term when it comes to figuring out the energy usage.

Electrical efficiency ($\eta\nu$): Represents the conversion of electrical energy to photon energy and is defined by photon energy divided by forward voltage multiplied by electronic charge, qV_{appl} ($\%|_{\mathrm{el}}$). The forward voltage applied is determined by the diode characteristics and should be as low as possible for the photon-emitting medium, which ideally is the bandgap of the medium if radiative recombination is through conduction band electrons with holes in the valence band. Resistive losses and electrode injection barriers add to the forward voltage.

Luminous flux: Power of visible light in photometric terms.

Luminous intensity: The luminous flux emitted from a point per solid angle. The unit is lumens per steradian, or candela (cd). This term is dependent on the package and the angle of measurement, and as such is not reliable.

Other definitions having to do with the power efficiency, which are becoming increasingly relevant and important, are the following:

Internal quantum efficiency (IQE): Ratio of the photons emitted from the active region of the semiconductor to the number of electrons *injected* into the p–n-junction LED.

Extraction efficiency (χ)*:* Ratio of photons emitted from the encapsulated chip into air to the photons generated in the chip. This includes the effect of power reflected back into the chip due to index of refraction difference between air and the device surface but excludes losses related to phosphor conversion.

External quantum efficiency (EQE): Ratio of extracted photons to the injected electrons; as such, it is the product of the internal quantum efficiency, IQE, and the extraction efficiency, χ.

Color-mixing efficiency (η_{color}): Losses incurring during mixing the discrete colors for white-light generation (not the spectral efficacy but just optical losses only). Color mixing could also be achieved in the fixture and optics.

Scattering efficiency: Ratio of the photons emitted from the LED to the number of photons emitted from the chip, which accounts for the scattering losses in the encapsulant of the lamp.

The specified total luminous flux Φ of a LED is determined for photopic vision and can be calculated through the relation

$$\Phi = S(\lambda)K(\lambda)\mathrm{d}\lambda, \tag{1.27}$$

where $S(\lambda)$ is the spectral power output of the LED and $K(\lambda)$ is the luminous efficacy of monochromatic radiation at wavelength λ. A more relevant criterion to describe the performance of an LED is the luminous performance, which is the amount of electrical power converted to luminous power. This is to be contrasted to the *conversion efficiency*, which is the amount of electrical power converted to radiant power.

1.7.1
Luminous Efficacy

The luminous efficiency of light sources involves the efficiency of energy conversion from electrical power (W) to optical power (radiant flux in watts), followed by conversion by the eye sensitivity over the spectral distribution of light. The conversion by eye also accompanies a conversion of units, from radiant flux (W) to luminous flux (lumen = lm), and is called *luminous efficacy of radiation*, having units of $\mathrm{lm\,W^{-1}}$. The luminous efficacy of monochromatic radiation $K(\lambda)$ at wavelength λ is shown in Figure 1.17 and is defined by $K(\lambda) = K_\mathrm{m}V(\lambda)$, where $K_\mathrm{m} = 683\,\mathrm{lm\,W^{-1}}$ and $V(\lambda)$ is the spectral luminous efficiency of photopic vision defined by the CIE [34] and is the basis of photometric units. The value for K_m is a constant given in the definition of the candela and is referred to as the *maximum luminous efficacy of radiation*. No light source can exceed this efficacy value, as shown in Figure 1.17. It should be noted that $K(\lambda)$ peaks at 555 nm (depicted as K_m, which is equal to $683\,\mathrm{lm\,W^{-1}}$) and falls off at both ends of the visible region. The values of $K(\lambda)$ are the theoretical limits of light source efficacy at each wavelength. For example, monochromatic light at 450 nm has a luminous efficacy of only $26\,\mathrm{lm\,W^{-1}}$ (theoretical limit). For real light sources, including LEDs, the luminous efficacy of radiation, K, is calculated from its spectral power distribution $S(\lambda)$ by

$$K = \frac{K_\mathrm{m}\int_0^\infty S_\lambda(\lambda)V(\lambda)\mathrm{d}\lambda}{\int_0^\infty S_\lambda(\lambda)\mathrm{d}\lambda}, \tag{1.28}$$

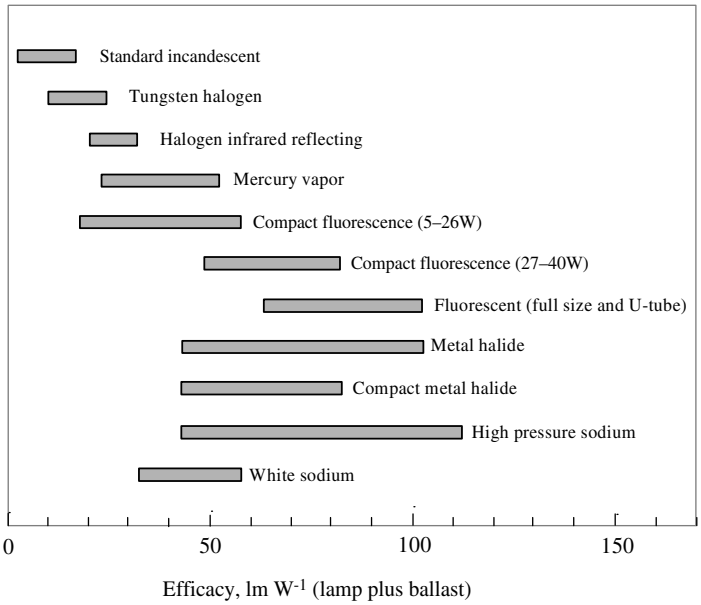

Figure 1.18 Efficacy of traditional light sources [129].

where $K_m = 683\,\mathrm{lm\,W^{-1}}$, which occurs at 555 nm for photopic vision, and $V(\lambda)$ is the spectral luminous efficiency of photopic vision being normalized to 1 at 555 nm.

The total efficacy (lumens per electrical power, including ballast losses) of traditional light sources is summarized in Figure 1.18 [35]. Within a lamp type, the sources having higher wattage are generally more efficient than the ones with lower wattage. High-pressure sodium (HPS), metal halide, and fluorescent lamps are the most efficient white-light sources. Obviously, the spectral power distribution of white light producing LEDs should be designed to have high luminous efficacy.

1.7.2
Chromaticity Coordinates and Color Temperature

All color spectra detectable by human eye can be represented in a number of different three-dimensional spaces. To convert the light spectrum to color space, the color matching functions of CIE colorimetric observer functions are used, which are shown in Figure 1.19. These plots of functions *X*, *Y*, and *Z* are representative of the sensitivity of the human eye versus wavelength over the entire visible spectrum. The common conversion splits the color space into two variables for color and one for luminance, paving the way for color representation by two dimensions, often neglecting the luminance term. This reduces the color space into two-dimensional color spaces such as CIE 1931 xy chromaticity diagram (or space), shown in Figure 1.20a, and CIE 1976 UCS (uniform color space) chromaticity diagram (or space), shown in Figure 1.20b.

The color of light is expressed by the CIE colorimetric system, which is a dynamic system in that improvements are made periodically to enhance its utility and render it

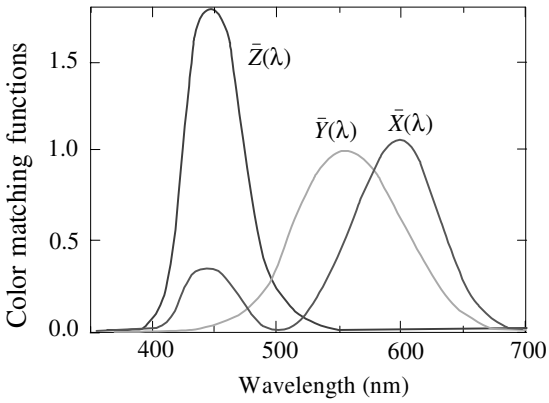

Figure 1.19 CIE 1931 *XYZ* color matching functions (standard colorimetric observer sensitivity plots for red (x), green (y), and blue (z) color perception cones of human eye. Courtesy of Lumileds/Philips. (Please find a color version of this figure on the color tables.)

more representative [36]. The spectrum of a given light is weighted by the *XYZ color matching functions* [37], as shown in Figure 1.19. From the resulting three weighted integral values (called *tristimulus values*, $\overline{X}$, $\overline{Y}$, $\overline{Z}$) the *chromaticity color coordinates* x, y are then calculated by $x = \overline{X}/(\overline{X}+\overline{Y}+\overline{Z})$, $y = \overline{Y}/(\overline{X}+\overline{Y}+\overline{Z})$.

The basic two-dimensional representation of visible colors is the CIE 1931 xy chromaticity space, as shown in Figure 1.20a, which is by far the most commonly used two-dimensional color representation. However, it has one major drawback that the distance between two points in this space (Δxy) does not correspond to the perceived color difference. In the revised CIE 1976 UCS chromaticity space, this drawback has been resolved to a large extent, as shown in Figure 1.20b. The newer chromaticity diagram, although not perfect, is the preferred two-dimensional color representation. In this revised color space, the distance between two points, usually called $\Delta u'v'$, is a reasonable indicator of the perception of color difference. A typical value for the visibility limit by human eye is $\Delta u'v' = 0.005$. Any color of light can then be expressed by the chromaticity coordinate (x, y) on the *CIE (x, y) chromaticity diagram*, as shown in Figure 1.21 (still using the 1931 CIE standard), with commonly used colors indicated by their abbreviations. The boundaries of this horseshoe-shaped diagram represent the plots of monochromatic light, called the *spectrum locus*, such as that expected from narrow bandwidth light source, which represents saturation color for that wavelength. Also plotted near the center of the diagram is the so-called *Planckian locus*, which is the trace of the chromaticity coordinate of a blackbody with its temperature ranging from 1000 to 20 000 K.

The colors on the Planckian locus can be specified by the blackbody temperature, which is called the *color temperature, expressed in kelvin*. The colors around the Planckian locus from about 2500 to 20 000 K are regarded as *white*. The 2500 K color temperature corresponds to reddish (soft white) white and 20 000 K to bluish white. The point labeled "Illuminant A" is the color of a typical incandescent lamp,

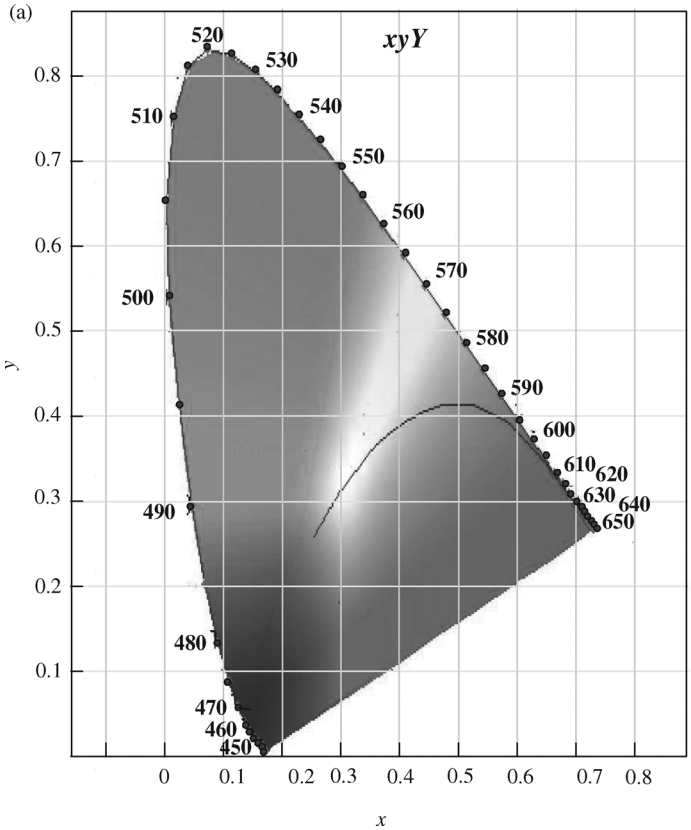

Figure 1.20 (a) The CIE 1931 *xy* chromaticity space (horizontal and vertical axes denote the *x* and *y* coordinates, respectively) and (b) the CIE 1976 UCS *u′v′* chromaticity space. Courtesy of Lumileds/Philips. (Please find a color version of this figure on the color tables.)

and "Illuminant D65" represents the typical daylight, as standardized by the CIE [38]. The colors of most traditional lamps for general lighting fall in the region between the points from 2850 to 6500 K. The color shift along the Planckian locus is generously accepted or purposely varied for general lighting for desired mood. But the color shift away from the Planckian locus (greenish meaning toward green or purplish meaning toward purple) is hardly acceptable. For illustrative purposes, the chromaticity coordinates of a few common fluorescent lamps are shown in Figure 1.22 [39].

The color temperature is not used for color coordinates (x, y) off the Planckian locus. In this case, the term *correlated color temperature* (CCT) is used. CCT is the temperature of the blackbody whose perceived color most resembles that of the light source in question. Due to the nonuniformity of the (x, y) diagram, the ISO-CCT lines are not perpendicular to the Planckian locus on the (x, y) diagram shown in Figure 1.22. To calculate CCT, an improved chromaticity diagram, namely, the CIE

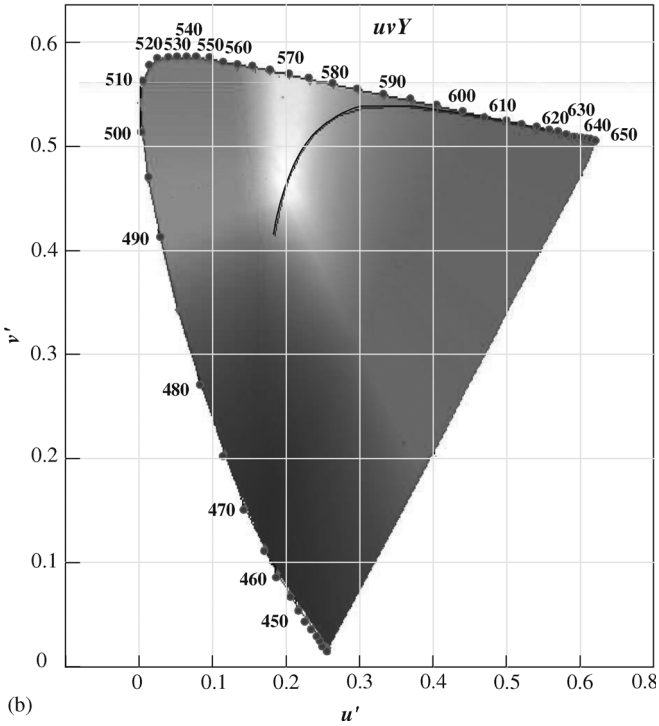

Figure 1.20 (*Continued*)

1960 (eV) diagram, later replaced by 1976 (u', v') diagram [36], is used where the ISO-CCT lines are perpendicular to the Planckian locus by definition.

An important characteristic of the chromaticity diagram is that light stimuli on the diagram are additive. A mixture of two colors will produce a chromaticity coordinate falling on the line between their respective chromaticity coordinates. For example, the mixture of two sources of light with wavelengths at 485 nm (blue) and 583 nm (yellow–orange) each with a half-bandwidth of 20 nm results in an (x, y) value of (0.38, 0.38). This value is very close to the spectrum locus, producing a soft white color with a temperature of about 4000 K. This idea is the basis of the phosphor conversion LED (pcLED) in which a yellow-emitting yttrium aluminum garnet (YAG) phosphor is pumped with a blue LED, generating white light, as discussed in Section 1.15.3.

1.8
Inroads by LEDs

LEDs are coming! Though we have lived in the domain of fluorescent and incandescent bulbs for a long time, the brightness and efficiency of LEDs have come so far that they have begun to replace incandescent bulbs in special applications and to cause

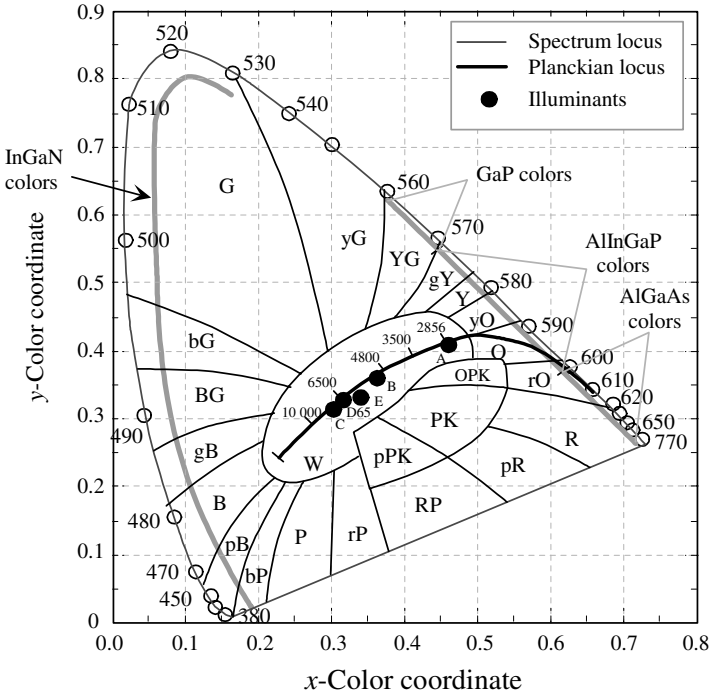

Figure 1.21 CIE (*x*, *y*) chromaticity (color coordinate) diagram, commonly known color domain, Planckian blackbody radiation locus with its temperatures, several available white-light illuminants, and the wavelength range achievable with various LED semiconductor materials. Courtesy of Lumileds/Philips.

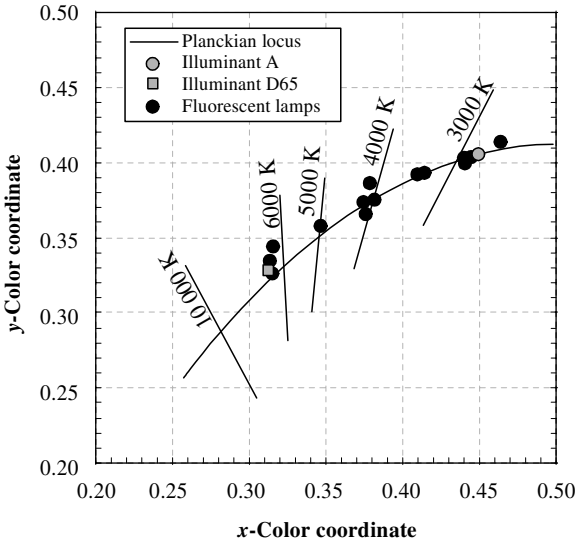

Figure 1.22 Chromaticity coordinates of common fluorescent lamps along with illuminants A and D65 [129].

many to project that LEDs could have applications not just in low-level lighting, but in general lighting. If so, the savings in fuel and pollutants would be tremendous, as LEDs are very efficient and environmentally green, unlike fluorescent bulbs that contain Hg and cannot be disposed off safely. For a detailed description of potential energy savings and related issues, the reader is referred to a report by Arthur D. Little, Inc., conducted for the US Department of Energy [40]. These devices have come a long way and are no longer just for low signal applications. They have had a "colorful" history, continually pushed by technological advances and pulled by key applications. The General Electric Corporation first demonstrated an LED in 1962, and LED products were first introduced in 1968 as indicator lights by Monsanto and then as electronic displays by Hewlett-Packard. Within a few years, LEDs replaced incandescent bulbs for indicator lamps, and LED displays made the Nixie tube obsolete. The initial performance of these LEDs was poor by today's standards, around 1 mlm at 20 mA, and the only color available was deep red.[1)] Steady progress in efficiency made LEDs viewable in bright ambient light, even in sunlight, and the color range was extended to orange, yellow, and yellow/green and with the advent of nitrides was followed by blue and green. The evolution of LEDs over the years in terms of their efficiency is shown in Figure 1.23.

Not only the efficiencies but brightness as well has come a long way since the 1960s. In fact the flux per LED (lumens/package) has been doubling every 2 years since 1968, with this figure being higher in the later years. LED flux has progressed from millilumens in the late 1960s to over 300 lm in the first decade of the twenty-first century.

Until the timescale of about 1985, LEDs were limited to small-signal applications requiring less than 100 mlm of flux per indicator function or display pixel. Around 1985, LEDs started to enter the medium-flux power signaling applications, in the range of 1–100 lm (Figure 1.24). The first large-scale application of red LEDs was the newly required center high-mount stop lights in automobiles, but it took many more years for LEDs to conquer this application fully. The early versions had some 75 LEDs in a row or in a two-dimensional array. With increased brightness, the number of LEDs was reduced. By 1990, efficiencies reached 10 lm W^{-1} in the GaAlAs material system, exceeding for the first time an equivalent red-filtered incandescent lamp. Nevertheless, even higher efficiencies were desired to further decrease the number of LEDs required per vehicle. Moreover, the GaAlAs system was limited in color to deep red with wavelengths longer than 640 nm. Currently, conversion efficiencies of commercial LEDs emitting in the red (650–660 nm) stands at 21% at 400 nm and red LED are said to have a conversion efficiency of 50% (Section 1.16), which compares with 75% of higher for edge-emitting lasers.

These developments set the stage for the exploration of the GaAlInP quaternary material system with still higher efficiencies and a wider color range, encompassing the red to yellow/green region of the visible spectrum. The efficiency exceeded

1) For comparison, a 60 W incandescent lamp emits six orders of magnitude higher light flux (about 900 lm).

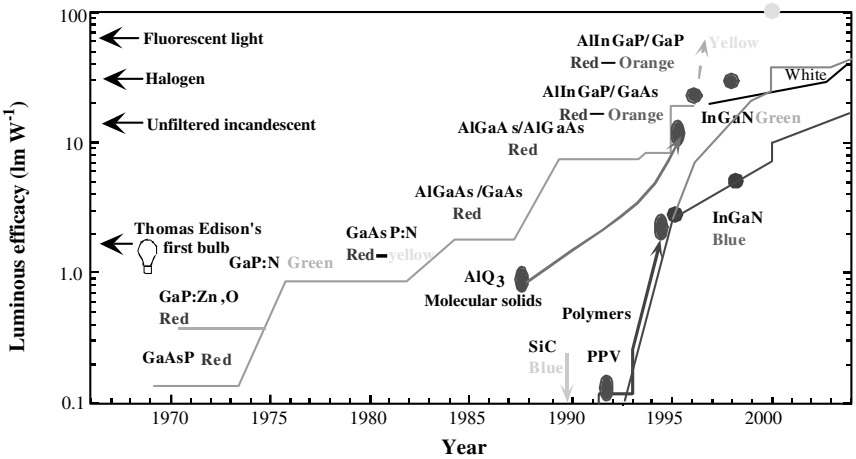

Figure 1.23 Evolution of all LED performance with some benchmarks against commonly used lamps. Both red and white LEDs were projected to produce luminous efficiencies of about 150 lm W^{-1} by about the years 2015–2020 as compared to the value of about 100 lm W^{-1} achievable by fluorescent bulbs and 10 lm W^{-1} by incandescent lamps. However, the figure for white LEDs was attained in 2007, well ahead of projections. Courtesy of Lumileds/Philips. (Please find a color version of this figure on the color tables.)

20 lm W^{-1} in the 620 nm red/orange part of the spectrum. If the maximum possible efficiency of 150 lm W^{-1} is nearly realized, LEDs could challenge even the very efficient yellow low-pressure sodium lamps. However, the lack of blue and true green prevented LED-based full-color displays from reality until the advent of GaN and related heterostructures, which paved the way for full-color displays, accent lighting,

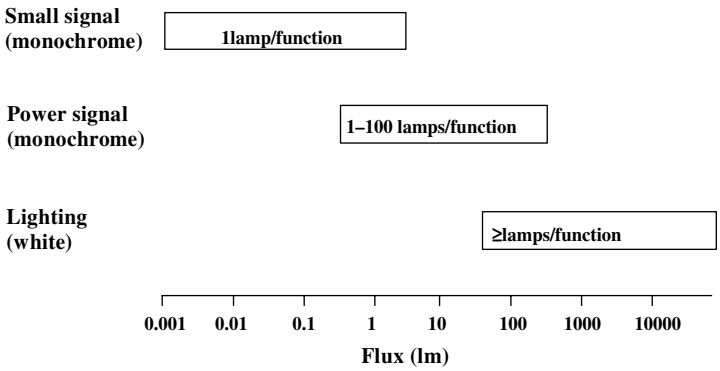

Figure 1.24 Flux and numbers of lamps required for various classes of LED applications: low–medium-flux "signaling" applications in which lamps are viewed directly and medium–high-flux "lighting" applications in which lamps are used to illuminate objects. Current LED lamps emit 0.01–10 lm of light. Courtesy of Lumileds/Philips.

moving signs, traffic lights, and so on as well as demonstrations of 100 lm W^{-1} white-light performance, which is considered illumination class.

1.9 Nitride LED Performance

Light-emitting diodes have undergone a tremendous advancement in performance and are now used in nearly every aspect of life. The future of many technologies including printing, communications, displays, and sensors depends profoundly on the development of compact, reliable, and inexpensive light sources. A primary goal of GaN research is to efficiently harness its direct energy bandgap for optical emission. Though the band-edge emission in GaN occurs at about 362 nm, which is in the UV, by appropriately alloying GaN with its cousins AIN and InN, the energy bandgap of the resulting Al(In)GaN can be altered for emission in the range of ultraviolet (UV) to yellow or even red. The first GaN LEDs were reported more than nearly three decades ago by Pankove *et al.* [41]. Due to difficulties in doping GaN p-type at that time, these LEDs were MIS LEDs, rather than p–n-junction LEDs. The electroluminescence (EL) of these LEDs could be varied from blue to yellow, depending on the doping of the insulator layer. Unfortunately, the measured efficiencies of these preliminary MIS LEDs were not sufficient to compete with the commercially available LEDs of that time.

With the achievement of p-type doping, see Volume 1, Chapter 4, followed by the improvement in the quality of InGaN with its compositionally dependent tunable bandgap, blue (430 nm), green (530 nm), and later white LEDs became available. Now, LEDs cover practically the entire visible spectrum, enabling their entry into additional power signaling applications, such as traffic lights [42]. Nitride LED performance on sapphire and SiC substrates associated with large area and standard die sizes for UV-, blue-, green-, and white-light emission is tabulated in Table 1.1. Efficiencies for green and white LEDs stood at 60 and 80 lm W^{-1} with white LEDs are beginning to exceed 150 lm W^{-1} for high injection levels and still improving. These high-efficiency devices sport features for extracting the photons efficiently from the device employing flip-chip mounts, photonic crystals, and so on.

It should be pointed out that due to the large In mole fraction in green LEDs, the strain-induced polarization is relatively large and thus the quantum-confined Stark shift is large. Consequently, the emission efficiency due to the reduced overlap of the electron and hole wave functions is lower than it would otherwise be. Naturally, this effect is reduced as the injection level is increased. Furthermore, the light intensity in green LEDs saturates as the injection current is increased for maximum power. This is attributed to the loss of localization, allowing the nonradiative recombination manifold to be available, and efficiency droop due to relatively large hole mass and the resultant electron leakage. When higher quality layers with reduced clustering/localization are produced coupled with better device designs, this effect is expected to be reduced in which case the saturation would be due to thermal effects. The increased sensitivity of human eye to green cannot compensate for the inferior

Table 1.1 Nitride LED performance for both commercial and developmental devices as of 2007.

High-power LEDs	Wavelength (nm)	Output power (mW)	Flux/LED (lm)	Luminous efficiency (lm W^{-1})	Drive current (mA)	Drive voltage (V)	Die size (mm^2)	Lifetime (h)	Company
UV	365	250			500	3.8	1×1		Nichia
	385	310			500	3.7	1×1	100 000	Nichia
Blue	470		35	9.4	1000	3.72	1×1	50 000	Lumileds
	460	385			700	4.5	0.9×0.9	50 000	Cree
Green	530		55	52.3	300	3.5			Nichia
	530[a]		100	26.9	1000	3.72	1×1	50 000	Lumileds
White	Blue + phosphor[a]		170	69.4	700	3.5	1×1	50 000	Lumileds
			84	75	350	3.2	0.9×0.9	50 000	Cree

[a]Commercial.

absolute quality of green LEDs versus the blue and in particular violet LEDs. In spite of this, efficiencies of about 60 lm W^{-1} were achieved in the year 2005. For white LEDs that feature a blue LED and a yellow phosphor, efficiencies of 80 lm W^{-1} are obtained in the flip-chip mount configuration with darkened surface for optimum light extraction out of the top surface. With multiple chips (4), the efficiency figure has been increased to 100 lm W^{-1}. Because the power level and the number of chips used could be variables in this figure of merit, it is more instructive to use and compare the total output power for a fixed chip size of, say, $1 \times 1\ mm^2$.

1.9.1
LEDs on Sapphire Substrates

The first GaN p–n-junction LED was demonstrated by Amano *et al.* in 1989 [43]. The fabricated device consisted of a Mg-doped GaN layer grown on top of an undoped n-type ($n = 2 \times 10^{17}\ cm^{-3}$) GaN film with the chemical Mg concentration estimated to be $2 \times 10^{20}\ cm^{-3}$. The electroluminescence of the devices was dominated by near-band-edge emission at 375 nm, which was attributed to transitions involving injected electrons and Mg-associated centers in the p-GaN region. Additionally, a small shoulder extending 20 nm, due to defect levels, was also observed.

One of the timely advancements in the nitride effort has been the exploitation of double heterostructures (DHs) for light emission devices [44–46]. The advantage of DH LEDs over homojunction LEDs is that the entire structure outside of the active region where the light is generated is transparent, reducing the internal absorption losses. Furthermore, this cladding region serves as an interface for scattering light, thus minimizing the probability of total internal reflection within the device. Together, these two factors enhance the probability of escape for the light out of the device.

In order to achieve other desired colors, InGaN alloys for emission media are required. While an increased InN mole fraction in GaN redshifts the spectrum, this

would be at the expense of introducing additional structural defects unless InGaN is made sufficiently thin, because it is not lattice matched to GaN. This is the picture in classical semiconductors whose properties are not dominated by inhomogeneities. In homogeneous semiconductors, lattice-mismatched films can be grown up to a certain thickness called the critical thickness for a given composition. Larger compositions correspond to smaller critical thicknesses. In view of this, there should be substantial effort devoted to optimization. In this vein, near-band-edge emission was also obtained for LEDs employing Si-doped InGaN quantum wells as the active region in a GaN/InGaN DH LED [47]. The In mole fraction content of the active layer was varied and resulted in a shift of the peak wavelengths of the device's electroluminescence spectra from 411 to 420 nm. Impressively, researchers at Nichia Chemical [48] were later successful in reducing the thickness of InGaN emission layers to about 30 Å. With this achievement, InGaN quantum wells with InN mole fractions up to a maximum of 70% have been obtained, and light-emitting diodes with commercial capabilities are possible even in amber color, in addition to the blue and green. The amber LED is desirable owing to its performance being less temperature sensitive than that of the AlInGaP varieties. It should be mentioned, however, thinner quantum wells particularly with relatively thick barriers are prove to efficiency droop.

A schematic representation of a typical early variety of nitride-based Nichia LED is illustrated in Figure 1.25. The light generated in the active InGaN layer traverses the chip without any appreciable absorption, as the entire LED chip is transparent to the radiation wavelength except for the self-absorption in the thin active layer. Due to

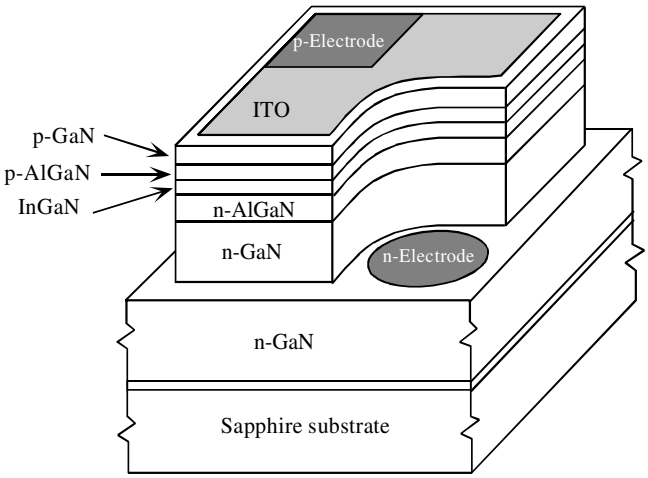

Figure 1.25 Artist's view of an LED with a transparent and conductive large-area contact made of ITO to the top p-type GaN for better light transmittance. In the wavelength range of interest, the transmittance through ITO is about 80%. In the early versions, semitransparent AuNi was used in place of ITO. Demand for better performance caused the abandonment of the semitransparent metal approach.

the problematic nature of p-doping and the low hole mobility, the spreading resistance in the top layer is large. To combat this problem, only a small portion of the p-layer, where the wire bond is made, is covered with a thick metallization, with the rest being covered with a semitransparent metal contact, thin in this case. However, when the competition for getting the maximum number of photons became heated, a transparent top contact such as indium tin oxide (ITO) became popular. ITO can be e-beam evaporated on the partially processed chip layer. Followed by a quality-enhancing annealing step, transmission coefficients near 80% in the spectrum of interest can be obtained. The method naturally keeps the contact resistance to the p-layer low, by virtue of increased area of contact, and reduces current crowding and associated ill effects. It should be mentioned that in high-intensity applications, the flip-chip mount method is used in which the p-side is mounted face down on a metallic mirror and the light is collected from the n-side after the removal of the substrate, and therefore, there is no need for conducting oxides. A discussion of conducting oxides can be found in Volume 2, Chapter 1.

It should be pointed out that internal field induced by polarization on *c*-plane GaN reduces internal quantum efficiency due to carrier separation and ensuing increased carrier lifetime. To circumvent this obstacle, nonpolar surfaces of GaN have been explored for light emission. Among them are the $1\,1\,\bar{2}\,0$ *a*-plane and $(1\,\bar{1}\,0\,0)$ *m*-plane GaN growth. Some pertinent details can be found in Volume 1, Chapter 3.

1.9.1.1 **Blue and Green LEDs**

The blue and blue–green LEDs developed by Nichia Chemical initially relied on the transitions to Zn centers in InGaN (Figure 1.26). Although it was suggested [49] that Zn levels are deep, no direct evidence was provided as to whether the centers were direct Zn centers and/or deep levels produced due to the presence of Zn in the growth environment. Although the presence of Zn causes the film to be of high electrical resistivity, Zn centers situated about 500 meV above the valence-band edge of GaN are

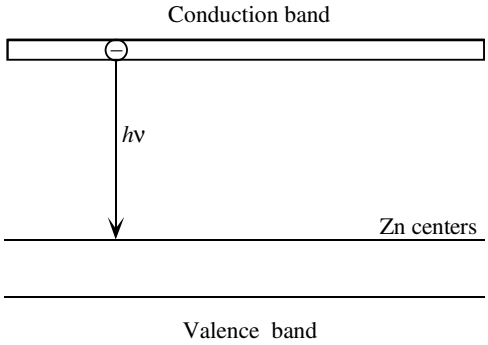

Figure 1.26 Schematic depicting transitions from states near the conduction band to Zn centers in the earlier versions of commercial nitride LEDs. The Zn centers were also used in the original GaN LEDs fabricated in the 1970s. A schematic representation of optical transitions in Zn-doped and unintentionally doped InGaN LEDs.

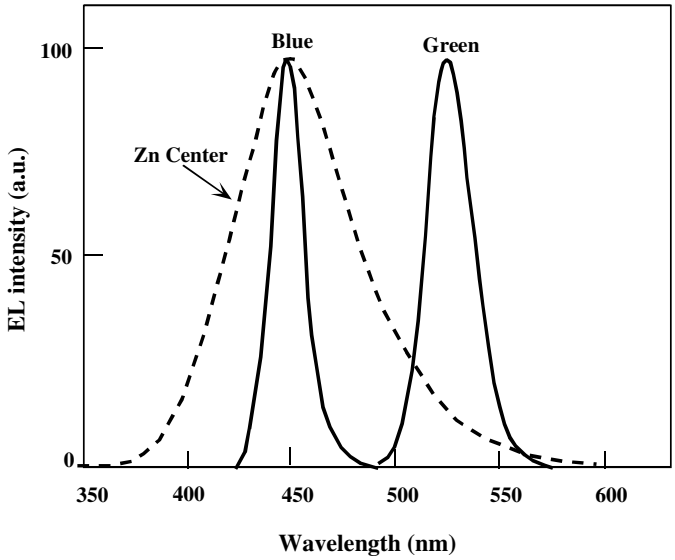

Figure 1.27 Electroluminescence spectra of the Nichia blue and green LEDs. By way of comparison to the one with Zn centers, the contrast is drawn to the improved spectrum in devices relying on near band-to-band transitions.

very efficient centers for recombination. The addition of Zn was originally necessitated by the need to increase the wavelength to the desired values, and the limitation deemed present in the amount of In that could be added while maintaining a good crystalline quality. These LEDs had the undesirable characteristics of wide spectral widths and a saturation of the light output with injection current accompanied by a blueshift. Figure 1.27 plots the electroluminescence spectrum of one such blue LED, whose radiative transitions are from near the conduction band to the Zn centers, along with the electroluminescence of so-called quantum well devices not containing Zn centers. The large spectral width of the Zn devices spoiled the color saturation with the undesirable outcome that not all the colors could be obtained through color mixing. It should be noted that, in the quantum well approach, the term quantum well has been used very loosely, and in many cases, the InGaN layers are not thin enough for carrier confinement and the transitions rely on band-tail states near the conduction and/or valence bands. With the so-called quantum well approach, the In mole fraction can be extended to about 70%, which paves the way for excellent violet, blue, green, and yellow/amber InGaN LEDs. The commercial LEDs exhibit power levels of 5 and 3 mW at 20 mA injection currents for the wavelengths of 450 and 525 nm, respectively.

Elimination of the Zn centers immediately led to the very important consequence that the FWHMs of the emission spectra were reduced to 20, 45, and 90 nm for blue, green, and yellow LEDs, respectively (Figure 1.28). For yellow, the InN molar fraction approaches 40% (70% has been reported in the past, on the assumption that the bandgap of InN is 1.9 eV). It should be stressed that an accurate determination of the

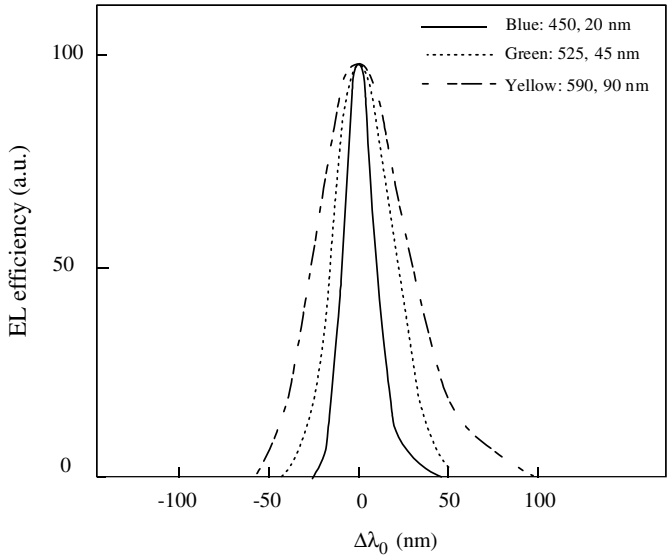

Figure 1.28 Spectral linewidth of blue, green, and yellow InGaN-based LEDs, the so-called quantum well types. The increasing line broadening, due to strain and compositional inhomogeneities, is noticeable according to an increase in the InN mole fraction, as one goes successively from blue to yellow.

InN molar fraction is difficult due to inhomogeneities in composition and strain. This is even more so when the InN bandgap was not accurately known. The In mole fractions deduced from using the large-bandgap value of InN are 15–20, 40–45, and about 60% for the 450, 525, and 590 nm emission, respectively. However, with downward correction of the bandgap of InN, these figures are actually, in the same order, under 15, 25, and 40% (Volume 1, Figure 1.44). In Zn-free blue LEDs, the linewidth has a temperature-dependent as well as a temperature-independent term. The latter is dominant and is attributable to inhomogeneities in the semiconductor such as compositional and strain variations. The behavior in green LEDs is similar, but to a different extent. With advances in technology, the linewidths have been narrowed, which bodes well for accessing more of the colors defined in the CIE diagram. Despite the advances, the not so narrow linewidths of InGaN-based LEDs, particularly that of green, make it nearly impossible to achieve the full range of colors or true white with high color rendering index (CRI) by using the three-LED solution. In part, it is for this reason, a 3-phosphor and UV LED pump solution is being pursued with development effort focusing on producing phosphors that can be efficiently pumped with the near-violet UV LEDs afforded by InGaN, and perhaps GaN, emitting active layers.

Figure 1.29a and b shows the dependence of EL spectra on injection current and ambient temperature of green InGaN LEDs, respectively. The blueshift observed with increasing current is attributed to band filling of the localized energy states caused by compositional fluctuations in the InGaN well layer.

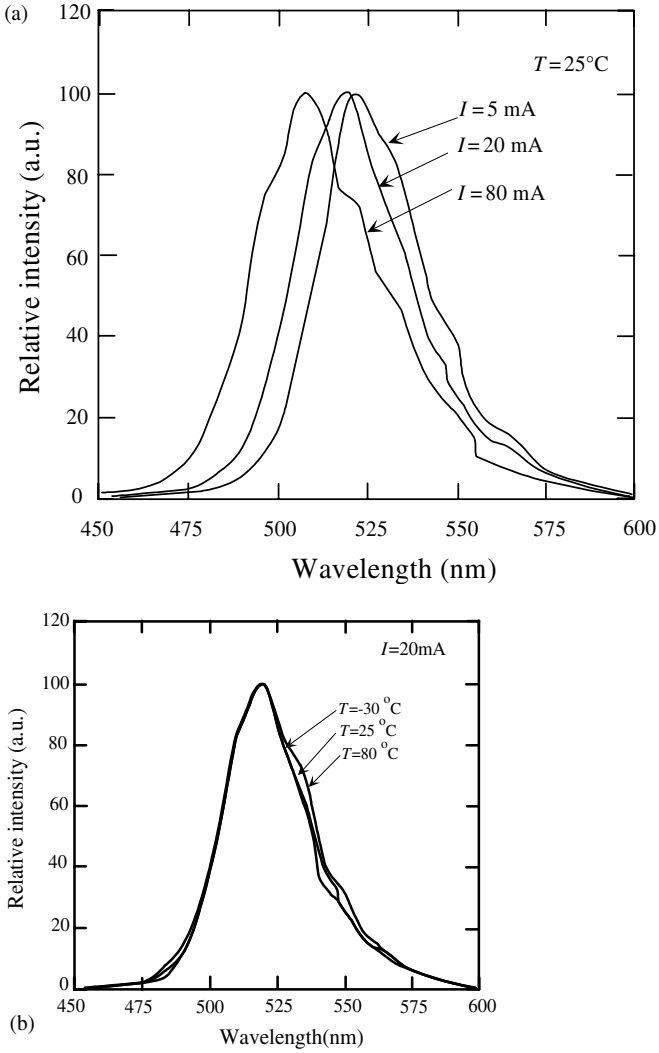

Figure 1.29 (a) The spectral dependence on operating current in an InGaN green LED at room temperature; note the blueshift caused by filling of the extended band-edge states or localized energy states. (b) Spectral dependences of InGaN green SQW structure on temperature at an injection current of 20 mA indicative of good temperature stability [42].

Contrary to injection current dependence, there is no discernable change of the EL with ambient temperature; additionally, these observations are consistent with those for blue LEDs. Comparing these observations to the InGaAlP red multiquantum well (MQW) LEDs (Toshiba TLRH 157P) could shed some light on the matter. The InGaAlP red LEDs show no dependence of the emission wavelength on injection

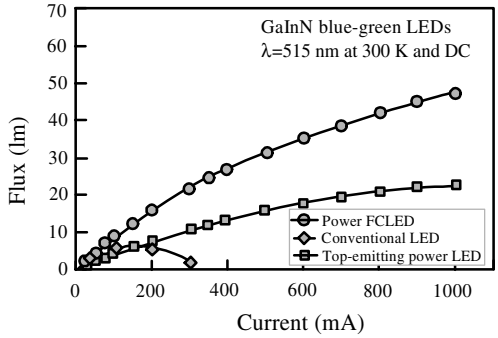

Figure 1.30 Flux (lm) versus current (mA) for a conventional LED, top-emitting power LED, and a power FCLED operated with DC drive currents. The power LED easily operates above 200 mA while the conventional LED fails. The FCLED operates at a higher efficiency than the top-emitting power LED exhibiting ~48 lm at 1.0 A. Courtesy of Lumileds/Philips.

current due to the lack of localized states induced by compositional fluctuations. The same LEDs do show a redshift with increasing temperature, indicative of bandgap narrowing. The lack of a redshift in InGaN LEDs would imply that the temperature dependence of the transition energy or the bandgap of InGaN is not as pronounced as that for InGaAlP and/or carrier confinement is stronger.

Much work has been done of late to increase the efficiency and the amount of light extracted from blue and green LEDs. Utilization of the flip-chip method discussed in Section 1.5 has ushered in considerable advantages over traditional LEDs. Figure 1.30 shows a plot of flux versus the drive current for a power FCLED with an area of ~0.7 mm^2 and a conventional LED with an area of ~0.07 mm^2. The flux for both LEDs is for CW operation at a peak wavelength of ~515 nm. The output flux of a conventional LED peaks at ~150 mA, where the epoxy-based 5 mm lamp package degrades dramatically in a few hours, eventually leading to catastrophic failure [50]. The performance of the conventional 5 mm package LED is limited at high currents caused by the smaller chip size and the high thermal resistance of the package, which is typically ~145 °C W^{-1}. In contrast, the flip-chip LED can be operated up to 1.0 A without significant power degradation or failure and sports a thermal resistance of approximately 14 °C W^{-1}. Moreover, the flip-chip LED has higher efficiency, producing 16 lm with about 27 lm W^{-1} efficiency at an injection current of 200 mA, which corresponds to a current density of about 30 A cm^{-2}. When the drive current of the flip-chip LED is increased to 1 A, a flux value of 48 lm at 445 nm is produced [19]. The forward voltage of the power flip-chip LED is 2.95 V at 200 mA, as compared to 3.15 V for the top-emitting power LED.

Figure 1.31 is a plot of normalized external quantum efficiency versus peak wavelength (nm) for a top-emitting power LED and a flip-chip LED fabricated from the same wafer and subjected to a 350 mA pulse (10% duty factor), circa 2001. Pulsed operation was employed to eliminate effects associated with different thermal resistances between the top-emitting power LEDs and power flip-chip LEDs [19].

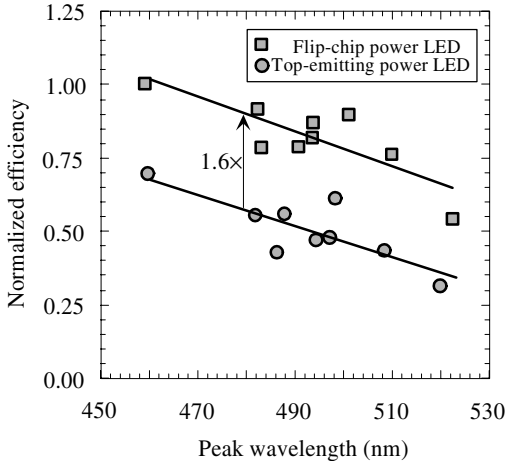

Figure 1.31 Comparison of flip-chip mount conventional top-emitting mount LEDs (operated at 350 mA pulsed (10% duty factor) and from the same wafer) in terms of efficiency over the wavelength range covering blue and green. The flip-chip is 1.6 times brighter. Courtesy of Lumileds/Philips.

The flip-chip LED external quantum efficiency was shown to be 1.6 times greater than that of the top-emitting power LED, from the blue to the green region of the visible spectrum. The improvement in efficiency is also approximately constant from a drive current range of 25–1000 mA.

Luminous efficiency for two different wavelengths, 502 and 527 nm, versus the drive current in $2 \times 2\ mm^2$ Lumiled LEDs is given in Figure 1.32, where efficiencies

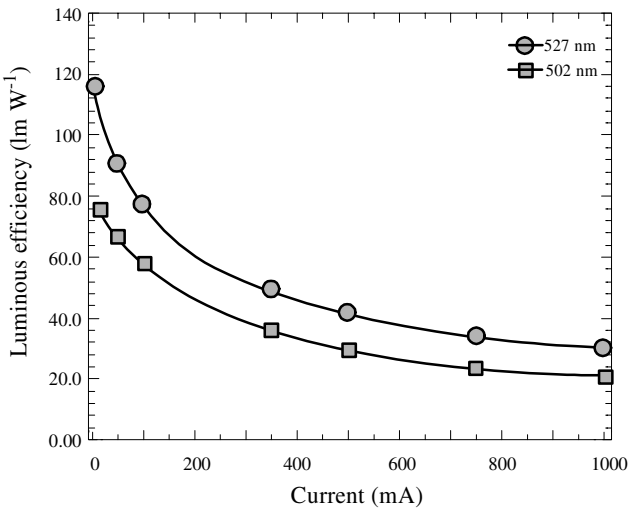

Figure 1.32 Luminous efficiency for two different $2 \times 2\ mm^2$ Lumiled flip-chip LEDs operative at 502 and 527 nm as a function of the drive current. Courtesy of Lumileds/Philips.

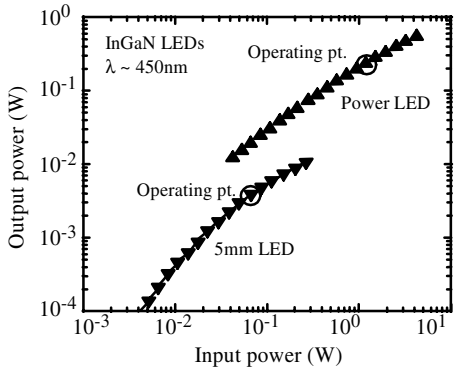

Figure 1.33 Optical output power versus input power for conventional and flip-chip mount LEDs operative at 450 nm. Courtesy of Lumileds/Philips.

are about 120 lm W^{-1} for 527 nm and 80 lm W^{-1} for 502 nm devices, at low injection levels; at higher injection levels, the efficiency drops to between 20 and 40 lm W^{-1}.

Luxeon LEDs deliver average lumen maintenance of 70% through 50 000 h under typical conditions. Output power for a conventional top-emitting diode and a flip-chip mount LED versus input power [51] operating at 450 nm is shown in Figure 1.33. External quantum efficiency versus drive current and luminous flux versus drive for a 5 mm conventional LED and a flip-chip LED emitting at 530 nm are shown in Figure 1.34.

To summarize, typical conventional LED indicator lamps are 0.25 mm^2 in chip size and are mounted in packages that can handle about 0.1 W electrical input power. High-performance LEDs have an output of 1–2 lm per device. Larger chips, up to about 4 mm^2 in size, when packaged appropriately such as with flip-chip mounting, are capable of handling several watts of electrical input power and are available with optical outputs of tens of lumens and hundreds of milliwatts, as tabulated in Table 1.2.

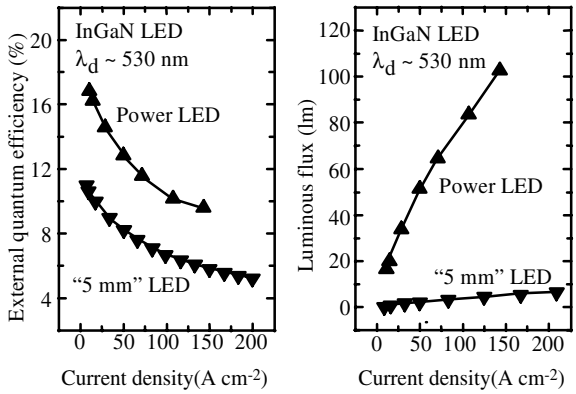

Figure 1.34 External quantum efficiency versus drive current and luminous flux versus drive for a 5 mm conventional LED and a flip-chip LED emitting at 530 nm. Courtesy of Lumileds/Philips.

Table 1.2 High-power InGaN LED performance for blue, cyan, and green.

Color and wavelength	Chip area (mm^2) flip-chip mount	Drive J ($A\,cm^{-2}$)	Efficiency ($lm\,W^{-1}$)	Flux output (lm)
Blue, 473 nm	2×2	50	9.4	46
Cyan, 506 nm	2×2	50	41.4	175
Green, 519 nm	2×2	50	36	170

[a]Keep in mind that this is a moving target with results improving daily. Therefore, the results represent a snapshot at a given time. Courtesy of Lumileds/Philips.

When the LEDs are driven at high currents, nearly 100 lm performance is obtained. Specifically, 108 lm intensity was obtained for a drive current of 700 mA for green LEDs. Similar results, even better of late, are available for white LEDs also. Such packages, which also feature photonic crystals in p-face-up mounts, are increasingly used for red, amber, and green traffic signaling lights. Even larger chips, emitting hundreds or even thousands of lumens at higher current densities per package, may be required for general illumination. Typically, high-performance devices are obtained in the laboratory followed by reproduction in development and production facilities. Values similar to the aforementioned one, or slightly lower, are made mention of in this book, representing variation among the laboratories. One thing is certain that improvements in epitaxial layer quality as well as packaging are vigorously pursued in the industry.

The light output for green LEDs (which features the largest InN mole fraction) saturates at very high injection levels possibly due in part to the loss of localization, which renders the nonradiative recombination paths to be active. Heating effect of the junction may also increase the nonradiative recombination. When higher quality layers with reduced clustering/localization are produced, this effect is expected to be reduced. Also complicating the issue, albeit more so at the lower end of injection levels, is the polarization charge and associated Stark shift, which reduces the emission intensity by reducing the overlap of electron and hole wave functions, manifested as the increase of carrier lifetime by as much as a factor of 10, gets to be rather severe as the InN mole fraction is increased for green emission with its associated piezoelectric polarization induced by strain. Nonpolar surface orientations such as the *a*-plane, see Volume 1, Chapter 3 for a discussion of growth with this polarity, and also *m*-plane, again see Volume 1, Chapter 3 for growth details, are beginning to be explored. The *a*-plane variety suffers from low quality as it is produced on *r*-plane sapphire with highly mismatched interfaces, and In incorporation has proved to be difficult. High-quality *a*-plane growth can be obtained on *a*-plane bulk GaN and to some extent on SiC and ZnO. The former is discussed in terms of it optical performance in Volume 2, Chapter 5.

1.9.1.2 **Amber LEDs**

Amber-colored LEDs are the domain of the InGaAlP material system. However, because the bandgap of the emitting layer is not very different from the larger bandgap carrier-confining layers, carrier leakage occurs. The small barrier

is exacerbated by the temperature dependence of the output light of the amber LEDs. Because plenty of band discontinuity is available in the InGaN/GaN, the carrier leakage is not the major problem in this context. The main issue becomes one of whether high-quality InGaN layers with large In concentration could in fact be grown. If so, temperature stability of these amber LEDs would be superior to those based on the InGaAlP system. In this section, the properties of InGaN-based amber LEDs [42, 52] are described. Similar to blue and green LEDs, the amber InGaN LED device structure developed by Nichia consists of a 300 Å thick GaN nucleation buffer layer grown at low temperature (550 °C), a layer of undoped GaN 0.7 μm thick, a layer of n-type GaN:Si 3.3 μm thick, a layer of undoped GaN (the current-spreading layer) 400 Å thick, an active layer of undoped InGaN 25 Å thick, a layer of p-type $Al_{0.2}Ga_{0.8}N$:Mg 300 Å thick, and a layer of p-type GaN:Mg 0.2 μm thick. It was not possible to determine the exact value of the mole fraction of indium in the InGaN active layer due to the weak signal intensity in X-ray diffraction and photoluminescence measurements. However, using a bandgap of 0.8 eV for InN bandgap and with the appropriate bowing parameter (1.43 eV), the predicted composition becomes nearly 30% for amber color. The n-type GaN:Si layer in blue and green LEDs was replaced with a combination of an undoped GaN and a n-GaN:Si. The purpose of the undoped GaN layer having a relatively high resistivity between the InGaN active and n-GaN layers was to uniformly spread the current in the InGaN active layer.

The characteristics of the LEDs were measured under direct current-biased conditions at RT, except for the measurement of the temperature dependence of the output power. The typical forward voltage was 3.3 V at a forward current of 20 mA. The peak wavelength and the FWHM of the emission spectra of the amber InGaN LEDs were 594 and 50 nm, respectively. Figure 1.35 shows the output power of amber InGaN and AlInGaP LEDs (type: HLMP-DL32, what was then Hewlett-Packard – now Lumileds) as a function of the ambient temperature from −30 to +80 °C. At 25 °C, the output powers of amber InGaN and AlInGaP LEDs shown are 1.4 and 0.66 mW, respectively. When the ambient temperature was increased from RT to 80 °C, the output power of amber AlInGaP LEDs decreased dramatically due to the carrier leakage or overflow caused by a small band offset between the active layer and cladding layers, which is dictated by the need to maintain lattice match between the layers of InGaAlP and the GaAs substrate on which they are grown [53]. Large bandgap discontinuity in the nitride system leads to very weak temperature dependence, as shown. When the ambient temperature is increased from RT to 80 °C, the output power of amber InGaN LEDs decreases only to 90% of the room-temperature value, possibly due to additional nonradiative paths becoming available.

1.9.1.3 **UV LEDs**

For many biological staining/imaging applications, biodetection, and even short-range communications, LEDs operating in the UV region of the spectrum are of interest. Because the wavelength of interest is comparable to, and in many cases, smaller than the one that can be attained with GaN, thin confined layers of GaN and AlGaN active emitting layers are used to reduce emission wavelength. However, any LED-emitting radiation above the energy of violet light is technically considered a UV

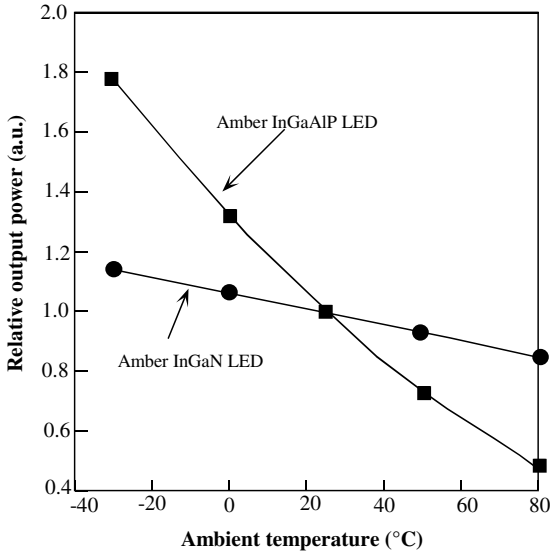

Figure 1.35 The normalized output power of amber InGaN and AlInGaP LEDs as functions of the ambient temperature from −30 °C to +80 °C. The output power of each LED was normalized to 1.0 at 25 °C, the crossing point in the figure [42].

LED, the fringe of which is accessible by low InN molar fraction InGaN. As mentioned throughout this book, some amount of In seems to be a requisite for localization-enhanced radiative emission. Because InGaN lends itself to composition fluctuations or clustering and thus reduced adverse effects of nonradiative recombination, the emission intensity goes down as the InN mole fraction is reduced near the GaN end of the binary, as shown in Figure 1.36 in the form of external quantum efficiency for Nichia LEDs as well as those that have been published by various groups and compiled by Kneissl *et al.* [54] with original data published in Refs [55–62]. Nevertheless, LEDs based on InGaN QW active layers just below the violet wavelengths have been developed and go under the nomenclature UV LEDs. Shorter wavelength LEDs deeper in the UV region rely on the quaternary, quantum wells with GaN, or AlGaN depending on the wavelength desired.

Lowering the sample temperature can provide a glimpse of improvements in the efficiency of LEDs that can be had by reducing the defect concentration. At lower temperatures, the carrier localization is more effective and manifold to nonradiative recombination centers as phonon interaction is made unlikely. In this vein, Figure 1.37 shows the temperature dependence of the output power of InGaN LEDs having a room-temperature emission peak wavelength of 400 nm. The efficiency is reduced by a factor of 2 at room temperature as compared to low temperatures. This implies that reducing the nonradiative recombination centers could lead to a twofold improvement in LED performance.

The LED structures utilizing low mole fractions of InGaN, GaN, or AlGaN emission layers are similar in fabrication geometry to those of the longer wavelength

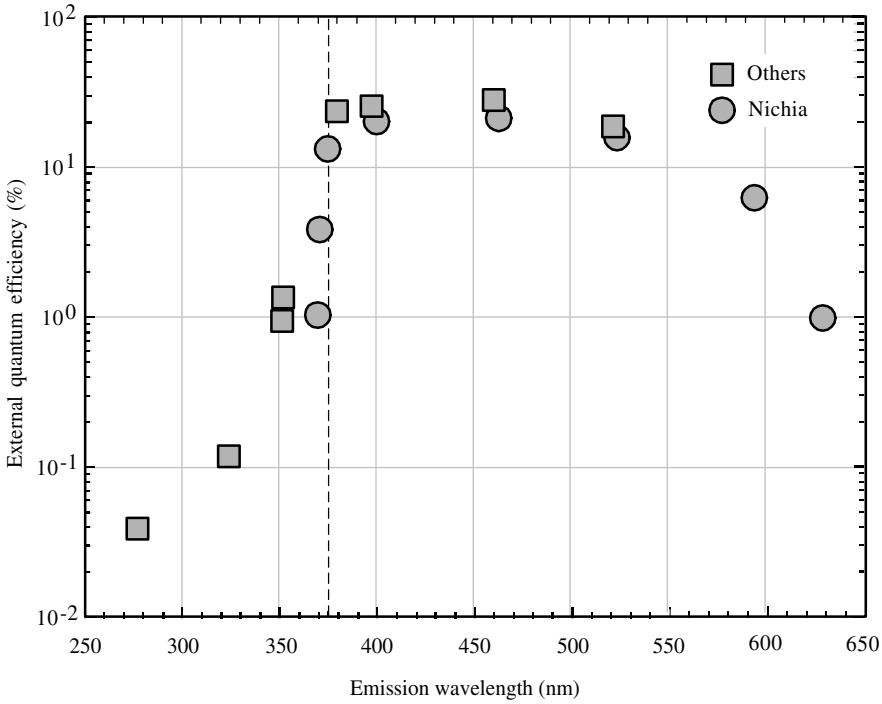

Figure 1.36 The wavelength dependence of the external quantum efficiency in the GaN-based LEDs grown on sapphire substrates. One should keep in mind that the data improve in time. The point is clear that there is a precipitous drop in efficiency approximately below 375 nm corresponding to about 10% InN mole fraction. Compiled from data presented in Refs [42, 54].

InGaN varieties, of course with the exception of the composition of the emitting medium. The varieties possessing low mole fractions of InGaN [63], GaN, GaN/AlGaN quantum well, AlGaInN quantum well [64], AlGaInN [65], and AlGaN [66] emission layers have been reported.

By reducing the InN mole fraction in the lattice, the wavelength of operation can be shifted to the UV region of the spectrum. Because the InN mole fraction is lower, as indicated above, the emission intensity degrades. However, the low InN concentration also means that compositional fluctuation-induced localization is not as severe. Consequently, the injection current-induced blueshift should not be a serious problem. Figure 1.38 shows the EL spectral dependence of UV InGaN LEDs (having an emission peak wavelength of 380 nm at a current of 20 mA) on current and temperature. The reduced blueshift of the emission peak wavelength with increasing current (compared to InGaN green LED) confirms reduced localization energy of the carriers. Figure 1.38 also shows only slight shift of the emission peak wavelength with temperature, as compared to the stable case of the green and blue LEDs. As one reduces the InN content slightly to reduce the wavelength merely by another 5 nm, the picture changes substantially. Figure 1.39 shows the EL of a UV LED with an

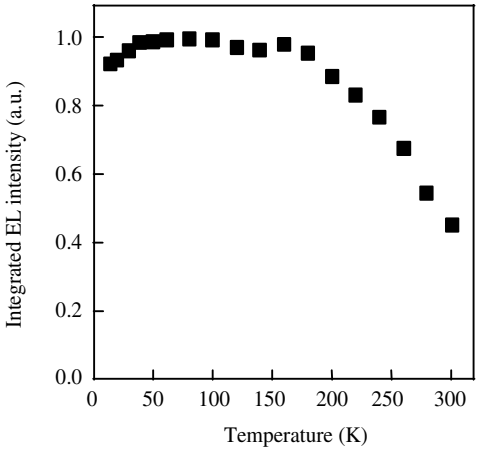

Figure 1.37 The temperature dependence of the output power of InGaN LEDs with an emission peak wavelength of 400 nm [42].

emission peak wavelength of 375 nm. Contrary to the case of 380 nm LED, the emission peak wavelength does not show any change with increasing current. However, a more noticeable redshift of the emission peak wavelength, as compared to the 380 nm LED, is observed with increasing temperature. This spectral shift with temperature is comparable to the conventional AlInGaP LEDs, which could be explained by reduced barrier discontinuity. The UV LEDs with an emission peak wavelength of 375 nm have small, localized energy states resulting from small fluctuations in In composition. This means that the emission mechanism is dominated by a conventional band-to-band emission, as in AlInGaP LEDs. It should also be mentioned that the possibility of the bandgap narrowing with increased temperature should be considered as well. A discussion of the dependence of the

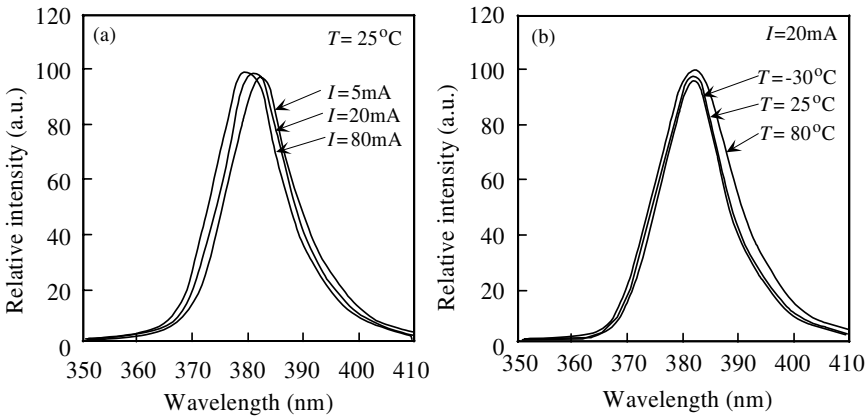

Figure 1.38 The operating current (a) and ambient temperature (b) dependences of the EL of InGaN UV SQW structure LEDs with an emission peak wavelength of 380 nm [42].

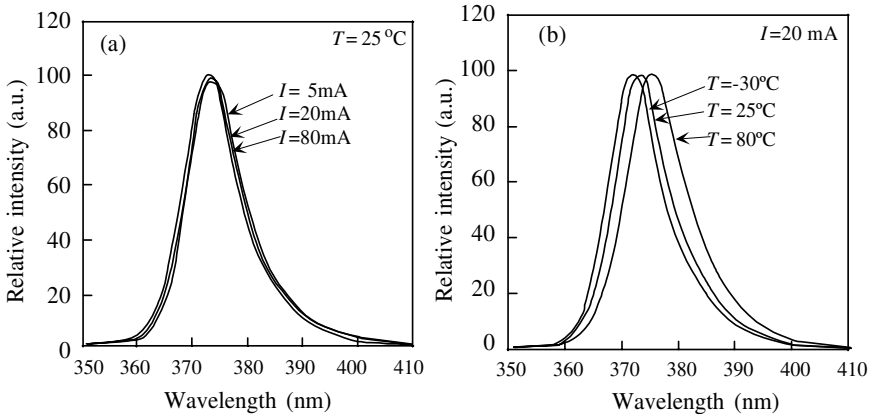

Figure 1.39 The operating current (a) and ambient temperature (b) dependences of the EL of InGaN UV SQW structure LEDs with an emission peak wavelength of 375 nm [42].

bandgap of nitride semiconductors on temperature can be found in Volume 2, Chapter 5.

Large area, $1 \times 1\,mm^2$ GaN- and InGaN-based UV LEDs with optical power levels of 250 and 310 mW at 365 and 385 nm, respectively, with operating lifetimes of 100 000 have been achieved at Nichia Chemical. The forward current to attain this power level is 500 mA and the forward voltage is around 3.8 and 3.7 V, respectively.

As mentioned above, deleterious effects of threading dislocations, through the nonradiative recombination centers that they introduce, increase with reduced InN mole fraction in an attempt to obtain UV emission. In this vein, investigations with reduced threading dislocation counts have been undertaken [57]. UV LEDs with InGaN multiquantum wells were fabricated on a patterned sapphire substrate (PSS) using a single growth process of metalorganic vapor-phase epitaxy. In this investigation, the grooves were made along the $\langle 1\ 1\ \bar{2}\ 0\rangle$ direction of sapphire. The GaN layer grown by ELO on a patterned substrate (light-emitting polymers (LEPs)) has a dislocation density of $1.5 \times 10^8\,cm^{-2}$. The LEDs fabricated using ELO on patterned sapphire substrates were flip-chip mounted on Si templates and exhibited power levels of about 15 mW at 382 nm for an injection current of 20 mA at room temperature. When the injection current increased to 50 mA, a power level of 38 mW resulted.

To reduce the wavelength further, GaN, AlGaN, the quaternary, or the quantum wells of these emission layers must be used. Because the effect of dislocations is expected to be more severe, approaches such as incorporation of GaN templates for substrates have been explored. In one such investigation [66], an output power exceeding 3 mW at the peak wavelength of 352 nm for injection current of 100 mA under a bare-chip geometry was reported. The internal quantum efficiency was estimated at more than 80%. The maximum power exceeded 10 mW for a large current injection of 400 mA, with an operation voltage below 6 V.

As the AlGaN mole fraction is increased for shorter wavelength operation, the energy barrier height at the junction of the emission and cladding layers must be

maintained to the fullest extent possible. Otherwise, carrier spillover and leakage reduces the quantum efficiency as is the case in conventional compound semiconductor systems based on As and P. Theoretically, the AlN mole fraction in barriers can be increased, but quality degrades as well as Mg doping becoming more difficult for p-type layer. One approach is to introduce a carrier-blocking layer between the p-type AlGaN layer and the active layer, which would allow one to get by without so high an Al mole fraction in the p-type AlGaN barrier layer. By doing so, Nishida *et al.* [67] improved the output power of an AlGaN-based UV LEDs by one order of magnitude to 1 mW at the emission peak wavelength of 341–343 nm.

The quaternary alloy that allows lattice-matching conditions while providing bandgap variability is attractive for UV LEDs for its higher quantum efficiency. This may have the genesis in In-causing compositional fluctuations or impeding dislocation propagation. The UV emission is considerably enhanced by the In-segregation effect upon introducing 2–5% of In into AlGaN. Room-temperature intense UV emission in the wavelength range of 315–370 nm from quaternary $In_xAl_yGa_{1-x-y}N$ alloys grown by metalorganic vapor-phase epitaxy has been obtained [68]. The In incorporation in quaternary $In_xAl_yGa_{1-x-y}N$ is enhanced with the increase of Al content when using a relatively high growth temperature in the range of 830–850 °C. Maximally efficient emission was obtained at around 330–360 nm from the fabricated quaternary $In_xAl_yGa_{1-x-y}N$ ($x = 2.0$–4.8%, $y = 12$–34%). The intensity of the 330 nm emission from quaternary $In_{0.034}Al_{0.12}Ga_{0.85}N$ was as strong [68]. By using $In_{0.05}Al_{0.34}Ga_{0.61}N/In_{0.02}Al_{0.60}Ga_{0.38}N$ three-layer MQWs with approximately 1.4 nm well thickness, the EL emission was lowered to 320 nm [68]. The authors observed emission fluctuations of submicron size in cathodo luminescence images of $In_{x1}Al_{y1}Ga_{1-x1-y1}N/In_{x2}Al_{y2}Ga_{1-x2-y2}N$ single QWs, which might be due to In segregation effect. The temperature dependence of photoluminescence emission for InAlGaN-based QWs was greatly improved in comparison with that of GaN- or AlGaN-based QWs. These quaternary structures have been used in UV LEDs in the form of multiple quantum wells, as discussed below.

Almost all nitride-based LEDs have quantum wells or at least one in the active emission medium. In this section, devices utilizing multiple quantum wells for confinement-induced blueshift or growth regimes facilitated/mitigated by quantum wells are discussed. Quantum wells provide an efficient medium for carrier recombination; therefore, efficiency in a device can be improved. Moreover, the blueshift obtained by narrow quantum wells allows increasing the emission energy beyond the bulk bandgap of the emitting medium and tuning of the emission wavelength. The emission energy versus quantum well thickness in $Al_{0.4}Ga_{0.6}N/GaN$ quantum wells is shown in Figure 1.40, which indicates that no matter how small the quantum well thickness is made, the maximum energy obtainable is about 3.84 eV, which corresponds to a wavelength of about 320 nm. This means that for wavelengths below this value, the active layer composition must be changed to either AlGaN or AlGaInN.

As seen in blue and green LEDs, the active medium of emission is made of InGaN quantum wells. The same holds true for shorter wavelength emission in that remarkable progress has been made in the field of MQW-based UV LEDs, primarily grown on sapphire and SiC substrates [57]. Output powers greater than 1 mW at

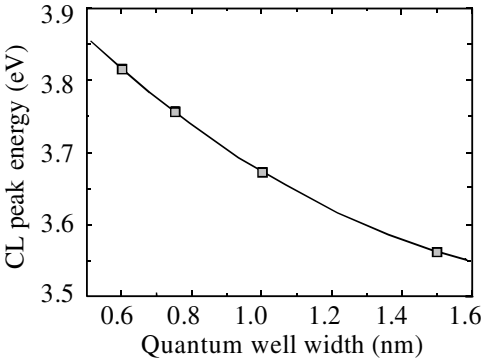

Figure 1.40 The emission energy versus quantum well thickness in $Al_{0.4}Ga_{0.6}N/GaN$ quantum wells as determined by cathodoluminescence. Courtesy of M. Holtz and H. Temkin.

emission wavelengths of 340–350 nm have been achieved [66]. LEDs with shorter emission wavelengths in the range of 280–330 nm are of much interest [64, 65, 69] and require bulk AlGaN, AlInGaN, or quantum wells of the two in some combination, since GaN quantum wells, no matter how thin they are made, barely reach the longer end of this range. Higher output powers and shorter wavelengths are limited by difficulties associated with attaining high-quality Al-rich AlGaN, reduction in Mg doping activation in p-type large-bandgap alloys, and design, which ironically is probably the easiest part of the entire problem. The high deposition temperatures associated with conventional MOVPE make it difficult to control the composition and thickness of AlGaInN quantum wells. However, the compositional fluctuations could be mitigated by use of quantum wells and/or pulsed epitaxy, which when done led to LEDs emitting at 340 nm [64]. The expanded description of pulsed epitaxy in the context of the quaternary alloy can be found in Volume 1, Chapter 3. In this particular structure, the epilayers were deposited on *c*-plane sapphire or n^+-SiC substrates using a pulsed atomic layer epitaxy process for a better control of the composition and thickness. The overall structure consists of a 0.8 μm thick n^+-$Al_{0.26}Ga_{0.74}N$ layer followed by a 30-period n^+-$Al_{0.2}Ga_{0.8}N/Al_{0.16}Ga_{0.84}N$ multiple short-period structures with periodicity of 30 Å. The device active layers consisted of a quaternary $Al_{0.15}In_{0.02}Ga_{0.83}N/Al_{0.1}In_{0.01}Ga_{0.89}N$ MQW, the barrier and well layer thickness of which were each kept at 15 Å and the number of wells was varied up to 10. A power level of 0.11 mW was achieved at a large bias current of 500 mA.

In another approach, AlN/AlGaInN superlattices (SLs) were employed to produce LEDs emitting at 280 nm, using reactive MBE with ammonia [70]. The device is composed of n- (doped with Si) and p-type (doped with Mg) superlattices of AlN (1.2 nm thick)/AlGaInN (0.5 nm thick) to mimic large bandgap bulk. With these superlattices, and despite the high average Al content, hole concentrations of $0.7–1.1 \times 10^{18}\,cm^{-3}$ with corresponding mobilities of $3–4\,cm^2\,V^{-1}\,s^{-1}$ and electron concentrations of $3 \times 10^{19}\,cm^{-3}$ with the mobilities of $10–20\,cm^2\,V^{-1}\,s^{-1}$ were obtained at room temperature. The barriers are 1.2 nm thick and the wells are 0.5 nm thick, as calculated from growth rates. The Al content in the well is 0.1. The

level of In incorporation, 0.05%, is estimated from the redshift of cathodoluminescence (CL) spectra of AlGaInN compared to a reference of AlGaN. The n-type dopant is introduced intermittently, during the growth of AlGaInN wells only. The n-type structure contains 150 barrier/well pairs for a total thickness of less than 300 nm. The p-type SL is intended to be structurally identical to the n-type structure. It is uniformly doped with Mg evaporated from an effusion cell. The growth is terminated with a 5 nm thick quaternary p-type contact layer. The barrier and well dimensions are below their critical thickness and no additional dislocations appear to be generated in the SL itself.

Electroluminescence results are strongly influenced by the design of the active region and the device fabrication procedure with Ni contacts of 70 and 500 μm diameter, the large diameter contact serving as the cathode. Light is collected with a UV-transparent fiber from the edge of the small dot, the p-type contact, and analyzed with a spectrometer. Although the spectrum has multiple peaks with the dominant emission occurring at ~330 nm, a second peak at 280 nm is also present. When driven with pulsed current, up to 350 mA, the intensity of the 280 nm begins to dominate. When mesas were etched, the 330 nm emission decreased to a shoulder with the predominant emission at 280 nm.

1.9.1.4 **Resonant Cavity-Enhanced LED**

The resonant cavity-enhanced (RCE) LEDs are interesting in that by use of Bragg reflectors, nearly monochromatic light (when single-mode operation is supported) can be obtained [71]. In addition, this device represents the first step toward the fabrication of vertical cavity lasers discussed in Section 2.14. Blue resonant cavity light-emitting diodes (RCLEDs) based on InGaN/GaN quantum well heterostructures have been reported [72]. Vertical microcavity devices with either one or both mirrors forming the cavity are patterned and high-reflectivity dielectrics, Bragg reflectors, have been fabricated. The active region in Ref. [72] was grown on 2.0 μm GaN buffer layer and was composed of 10 $In_xGa_{1-x}N$ quantum wells ($L_w = 30$ Å) with GaN barriers ($L_B = 50$ Å), surrounded by $Al_{0.07}Ga_{0.93}N$ upper and lower outer cladding layers (approximately 3600 Å and 0.5 μm, respectively). The In concentration was varied to span the wavelength range from about 430 to 480 nm. The structures were capped by a 1000 Å thick p-GaN contact layer. As could be expected, a good morphology is imperative for achieving a high-Q vertical cavity. Both one metallic and one dielectric distributed Bragg reflector (DBR) and two dielectric DBRs were employed to form the cavities. The schematic diagram of the latter is shown in Figure 1.41. The process begins with the deposition of a patterned 1000 Å thick layer of ITO, having a conductivity of $4 \times 10^{-4}\,\Omega$ cm and an absorption loss of approximately 2% in the 400–500 nm wavelength range, on the p-GaN cap layer of the as-grown nitride heterostructure for a transparent conducting layer [73]. Electron beam evaporation of a Cr/Al bilayer formed both the electrical contact to ITO and one optical reflector ($R \sim 0.8$).

Patterned SiO_2 was used to define a current injecting aperture of 15–35 μm diameter. A 20-pair SiO_2/HfO_2 multilayer DBR was deposited atop the ITO film to create a high-reflectivity mirror ($R > 0.999$). The electrical injection to p-type nitride

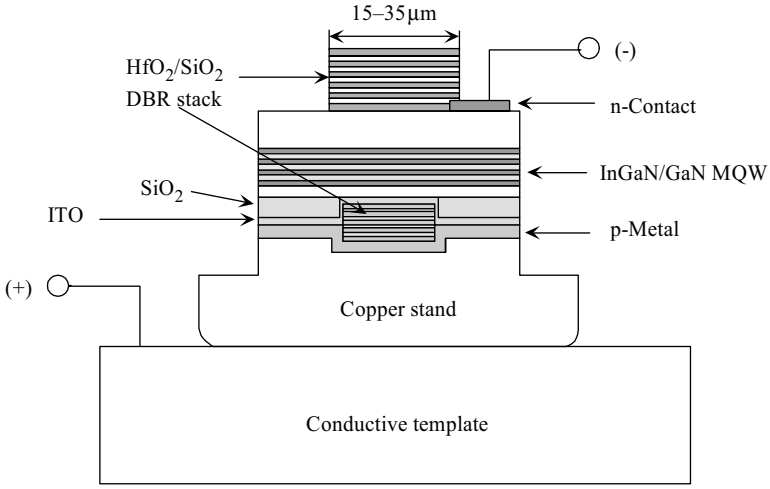

Figure 1.41 Schematic representation of a RCLED with two dielectric DBR mirrors. The device also features a low loss intracavity ITO p-current-spreading layer. Courtesy of A. Nurmikko [72].

was provided by the lateral current spreading via the ITO. A patterned multilayer metallization was applied to contact the ITO film outside the optically active area. Next, the entire structure was flip-chip mounted on a permanent host substrate (e.g., silicon or other electronically integrateable material). Pulsed excimer laser radiation at $\lambda = 308$ nm was directed through the backside of the sapphire substrate so as to induce its complete separation from the nitride heterostructure in a single 10 ns laser shot. Finally, a HfO_2/SiO_2 multilayer dielectric stack (DBR) was deposited directly onto the exposed n-AlGaN or n-GaN layer surface and patterned for completion of the optical resonator (consistent with the 15–35 μm effective aperture). Patterned Ti/Al contacts were used on the n-side of the junction.

Spectral response of the two-mirror RCLED described above is shown in Figure 1.42, for which the light emission was collected along the optical axis of the device, within an approximately 5° forward solid angle. The cavity for the device is relatively thick, approximately 16λ. The spectrum of the device encompassing two dielectric DBRs is centered at around $\lambda = 430$ nm and underscores the impact of a high-quality resonator on the definition of the cavity modes, with the inset (Figure 1.42) showing a particular mode. The modal linewidth is approximately 0.6 nm, implying a cavity Q-factor of approximately 750. This device, where the bottom reflector is made of a metallic mirror with an improved reflectivity of $R > 0.9$, is easier to fabricate and could be a good candidate for short-cavity blue RCLED. If higher power could ensue from a structure of this kind owing to better collection of photons, the structure with appropriate bandgap could be used to excite dyes for white-light generation discussed in Section 1.15.3.

A three-terminal tunnel junction employed in a monolithic, electrically segmented dual wavelength blue–green LED consisting of two electrically isolated InGaN QWs

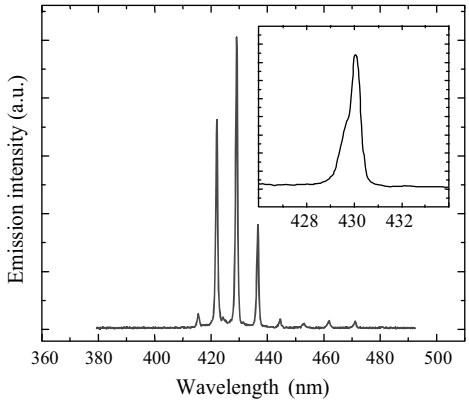

Figure 1.42 Emission spectrum of the RCLED device incorporating two dielectric DBR mirrors [72].

of different indium composition within a single vertical heterostructure has been demonstrated [74]. The device incorporated a p^{++}/n^{++} InGaN/GaN tunnel junction so as to operate a time-multiplexed two-color blue–green LED source operative at 470 and 535 nm (note that these are not necessarily consistent with the true definition of the color terminology, and the p^{++} is used figuratively to indicate doping as high as possible). The nitride heterostructure used, in the form of an artistic view of the fabricated device, is shown in Figure 1.43. The tunnel junction segment is inserted between the two active $In_xGa_{1-x}N$ QW emitter sections, having a quantum well thickness of $L_w = 30$ Å. Here, the tunnel junction (TJ), serves the purpose of electrically sectioning the nitride heterostructure into two independent LEDs and lateral current spreading for the bottom device. The diameters of the top and the bottom LEDs are 60 and 80 μm, respectively. In the LED injection regime for drive current levels of approximately 100 A cm^{-2} or less, the TJ in the bottom device typically added about 1 V to the forward turn-on characteristics.

Shown in Figure 1.44 are the spectral characteristics where the dashed curves depict the case for each LED being switched on in a time sequential manner and the solid line is for the LED operated as a simple two-terminal device with a constant voltage applied across the top p-GaN and lowest n-GaN. The electrical independence of the blue and green segments allows one to program the 470 and 535 nm LEDs for any time sequence up to speeds of 100 MHz.

1.9.1.5 Effect of Threading Dislocation on LEDs

As discussed in Volume 1, Chapter 3, the ELO process can be used to reduce the threading dislocation density in the GaN buffer layer. This would then allow one to determine the effect of threading dislocations on LED intensity, and other relevant features as they have been reported [42]. Figure 1.45 shows the relative output power of UV (380 nm) InGaN and GaN LEDs produced using sapphire and ELO substrates as functions of forward current. The ELO and GaN on sapphire were reported to have average dislocation densities of 7×10^6 and 1×10^{10} cm^{-2}, respectively. Here, the

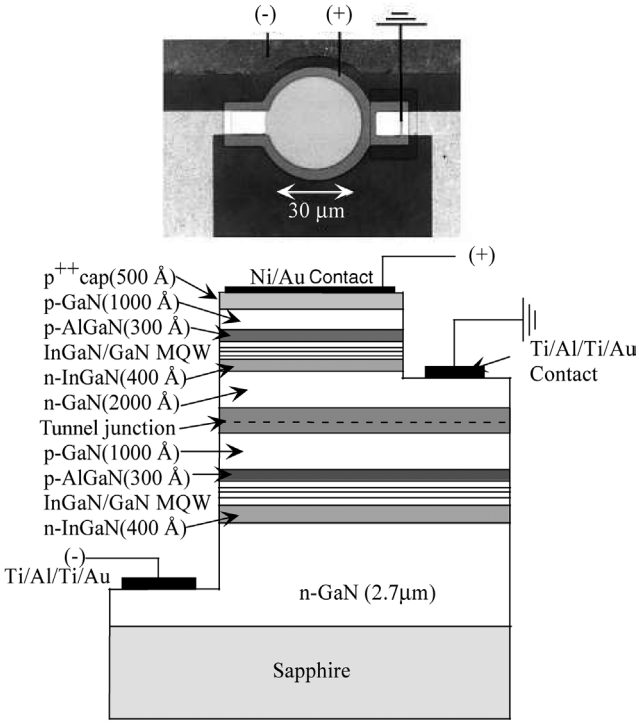

Figure 1.43 Schematic view of the two-wavelength blue–green LED, indicating the active regions, the tunnel junction, and the bias arrangement. A plan view photograph of a device is shown at the top. Courtesy of A. Nurmikko [74].

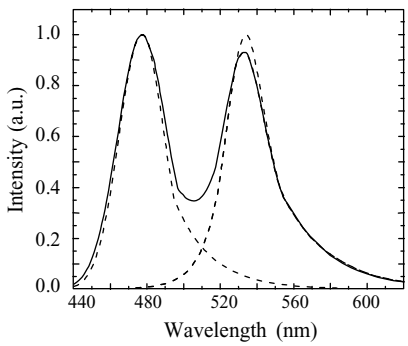

Figure 1.44 Superposition of the emission spectra from the blue and green LEDs when they are activated sequentially (dashed lines), and their simultaneous activation as a two-terminal LED (solid line). Courtesy of A. Nurmikko [74].

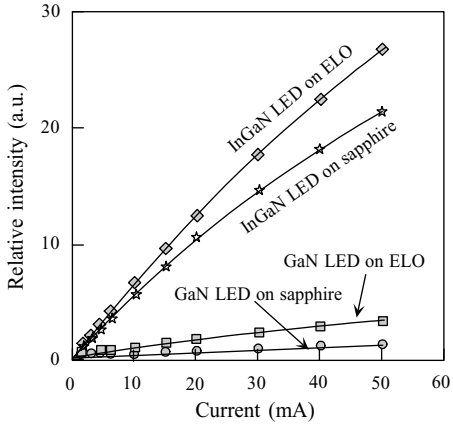

Figure 1.45 Relative output power of UV InGaN and GaN LEDs as functions of forward current for LED chip size as large as $350 \times 350\,\mu m^2$, which covers many ELO stripes covering both higher and lower dislocation density regions [42].

average dislocation density of the ELO on sapphire was obtained by dividing the dislocation density of $2 \times 10^7\,cm^{-2}$ on the window region by the ratio (stripe periodicity of 12 μm)/(window width of 4 μm) because the dislocation density on the SiO_2 stripe region was very small. The $350 \times 350\,\mu m^2$ LED chip size caused many windows and SiO_2 stripe regions to fall under each device, necessitating the use of a geometric average dislocation density for the ELO on sapphire. As the figure indicates, the UV GaN LED on ELO has a much higher (about twofold) output power than that on sapphire. This is because the magnitude of dislocation densities of a GaN LED on ELO is much smaller than that on sapphire. However, the 380 nm UV InGaN LED on ELO showed a smaller improvement in output power (25%) in comparison with that on sapphire at 20 mA. This is attributed to alloy composition fluctuation in InGaN and resultant carrier localization, which apparently does not occur to the same extent for GaN. This is consistent with the overall poorer performance of GaN emission layers as compared to InGaN discussed in Section 1.9.1.3. Therefore, any reduction in threading dislocation density is more effective for GaN emitting layer than the InGaN variety. Furthermore, radiative recombination is limited by hole injection and improvement of layer quality unless accompanied by enhanced hole injection in relation to electron injection, carrier leakage prevent attainment of improved light output.

This localization picture, which we also touched upon in Section 1.9.1.1, is also consistent with poorer performance as the InN mole fraction in the alloy is reduced. This reduced InN fraction causes a reduction in the depth of the localized energy states, which degrades the effectiveness of carrier localization and therefore opens manifolds to nonradiative recombination centers. However, when the InN mole fraction is increased past the point corresponding to a wavelength of about 470 nm, the efficiency degrades again presumably due to the increased lattice mismatch

between the GaN buffer layer and InGaN emitting layer. In addition, a combination of relatively high InN mole fraction and high temperatures used during growth, extensive compositional inhomogeneities and resultant localization may occur. This manifests itself as saturation in light output with increasing injection current as nonradiative recombination channels become available for recombination. The electron leakage also must be kept in mind. With reduced defects, increased pressure during MOCVD growth may be employed to reduce some of the aggravating conditions mentioned above. We should point out that InN is of special interest in light emission in that InN containing ternary has long radiative recombination lifetime compared to GaN and the emission intensity does not drop as much as that in GaN with increased temperature from low temperatures. Because of reduced or lack on InN in the lattice, the effect of InN in the emission process is of paramount importance in UV LEDs with very low InN mole fraction in the emission layer, GaN, or AlGaN emission layers depending on the emission wavelength. Somewhat relevant to the case is the fact that InN nanostructures have been prepared where the emission intensity shows little or no temperature dependence on temperature from low temperature to room temperature. This means that when and if InGaN active layers without defects and localization are available, one can expect much improved performance. We should mention that GaN layers are not as efficient light emitters at room temperature as InN containing active layers (providing that the InN mole fraction is not high). Naturally, the UV varieties do not feature InN in their active media. It is known that the PL efficiency for InN nanostructures do not degrade at room temperature in temperature-dependent PL measurement experiments. If the same would hold true due to confinement, one can then assume that if nanostructured GaN is used for the active medium for emission, much better performance of UV LEDs can be obtained [75].

1.9.2 LEDs on SiC Substrates

SiC substrates have some advantages. Among them are the conductive natures of the substrates, which simplify LED fabrication and in particular packaging; generally, SiC has better quality epitaxial layers and has better thermal conductivity compared to sapphire. Moreover, the LEDs on SiC are less sensitive to electrostatic fields whereas special packaging and handling methods must be employed in LEDs on sapphire. Some high-brightness LEDs produce optical power levels of 15, 14, 11, and 9 mW at 460 (deep blue), 470 (blue), 505 (for green traffic lights), and 527 (for display green) at a forward current of 20 mA, respectively, in production levels. The forward voltage at 20 mA drive is between 3.7 and 3.8 V, and the die size is $300 \times 300\,\mu m^2$. The 460 nm LEDs can produce 30 mW of power in selected production runs at a forward current of 30 mA, which is remarkable. When the die size is increased to $900 \times 900\,\mu m^2$, an optical power output level of 150 mW is available at 470 nm for a drive current of 350 mA. The same size die designed for UV operation at 405 nm produces 250 mW of optical power at a drive current of 350 mA. The forward voltage for both large die devices is 3.7 V. The electrostatic discharge threshold is about 1000 V.

1.9.3
LEDs on Si Substrates

Bringing down the price of semiconductor material by improving the quality and rate at which epitaxial reactors produce semiconductor wafers is crucial to reducing the overall cost of LEDs. Other keys to cost reduction include designing low-cost revolutionary packages with high reliability and low thermal impedance, and increasing the area of substrates while reducing their cost [76].

Silicon shows promise as a substrate for nitride-based LED devices that emit across the spectrum from green into the ultraviolet. The possibility of LEDs built on Si substrates is exciting, but high-performance devices have not yet been demonstrated due to problems such as differences in the thermal coefficient of expansion between the deposited semiconductor and substrate, and lattice mismatching wherein the lattice sizes of the deposited semiconductor and the substrate are different to the extent that lattice defects cause significant amounts of energy to be thermalized. Unlike lasers, which sport waveguides, the photons in LEDs are emitted in random directions. Having a substrate and a buffer layer structure that do not absorb these photons allows them to be emitted back through the surface by back-reflectors, and so on. However, Si absorbs all the visible and UV photons, which causes efficiency degradation even for identical quality layers, as compared to a transparent substrates. With ELO on Si, discussed in Volume 1, Chapter 3, the layer quality has been improved substantially. But the absorbance issue is a fundamental one.

Unless special precautions are undertaken, GaN and AlN films crack on Si substrates. Therefore, thick crack-free films become an important issue. With ELO and similar techniques, these problems have been somewhat assuaged. By using a low-temperature AlN:Si seed layer and two low-temperature AlN:Si interlayers for stress reduction in tandem, Dadgar *et al.* [77] reported crack-free GaN films of about 2.8 μm in thickness. Further, low turn-on voltages along with a series resistance of 55 Ω were observed for a vertically contacted diode. By *in-situ* insertion of a Si_xN_y mask, the luminescence intensity was significantly enhanced to the point of producing 152 μW at a current of 20 mA and a wavelength of 455 nm.

As in the case of sapphire and SiC substrates, the quaternary InGaAlN system, in the short-period multiple quantum well fashion, was applied to Si(1 1 1) substrates as well, for below 300 nm light emission [78]. The layers are composed of superlattices of AlGaN/GaN and AlN/AlGaInN and nearly identical to those reported on sapphire [70]. The LEDs show light emission between 290 and 334 nm. The room-temperature EL spectrum of the carrier injection structure, a homojunction-like LED based on n- and p-type superlattices of AlN/AlGaInN, obtained with a DC current of 100 mA and $V_f \sim 25$ V shows a well-defined peak at 290 nm, followed by a broader structure at 340 nm. This is in part due to the recombination region not being well defined and the entire structure being heavily doped. The translation is that more work needs to be done in the area of below 300 nm LEDs, in general, let alone whether Si is a viable substrate. However, even the discussion of this issue in itself is a mark of how remarkably the field has progressed. Exciting advances can, however, be made using orientations of Si which when etched allow the growing plane to be for example m-plane because growth takes place on the (1 1 1) surface of Si.

1.9.4
LEDs Utilizing Rare Earth Transitions

The basics behind tunable wavelength emission in rare earth (RE) doped GaN are discussed in Volume 2, Chapter 5. Here, only the device aspects of rare earth doped GaN light-emitting diodes are discussed. Recent success in fabrication of *electroluminescent devices* (ELDs) utilizing red, green, and blue (RGB) emission from REs in GaN, as shown in Figure 1.46, has made possible the realization of a new generation of flat panel displays (FPDs) [79–81]. The lateral integration of ELDs

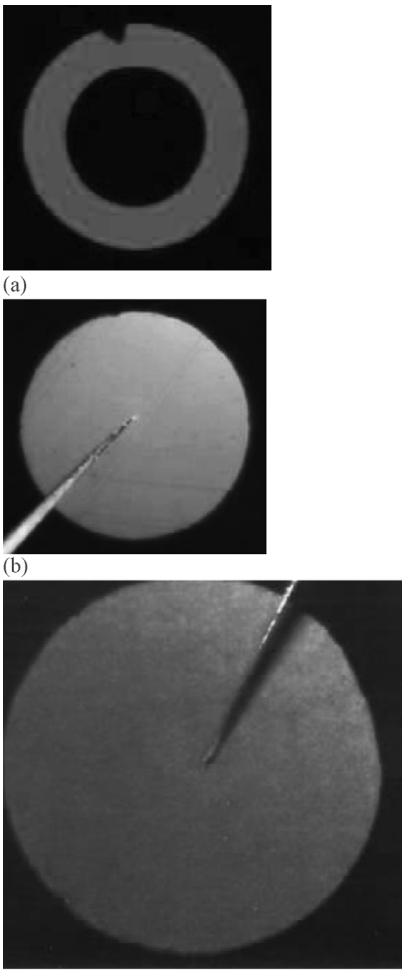

Figure 1.46 Photographs of red (a), green (b), and blue (c) emissions in LED fabricated from MBE-grown GaN doped with Eu (a), Er (b), and Tm (c) [79–81]. (Please find a color version of this figure on the color tables.)

doped with different REs has been recently demonstrated [82]. GaN:RE films were grown by radio-frequency plasma-assisted MBE on 2 in p-Si (1 1 1) substrates. The main fabrication steps for three-color integrated devices are as follows [83]:

(1) spin SOG on Si wafer twice, then coat with photoresist (PR) and expose the PR pattern;
(2) etch SOG with 0.1% diluted HF to form the SOG window for GaN:RE growth;
(3) grow GaN:Tm in MBE system after the SOG was sufficiently outgassed;
(4) SOG liftoff with HF revealing the GaN:Tm patterns;
(5) repeat twice the procedures from (1) to (4), using GaN:Eu and GaN:Er;
(6) produce PR patterns for ITO electrodes on GaN:RE pixels;
(7) sputter-deposit a thin film of ITO;
(8) liftoff PR and anneal samples in N_2 ambient to form good contacts.

Figure 1.47 shows a photograph of the laterally integrated three-color thin-film ELD from GaN:RE as well as the ELDs in operation under DC bias. The EL brightness

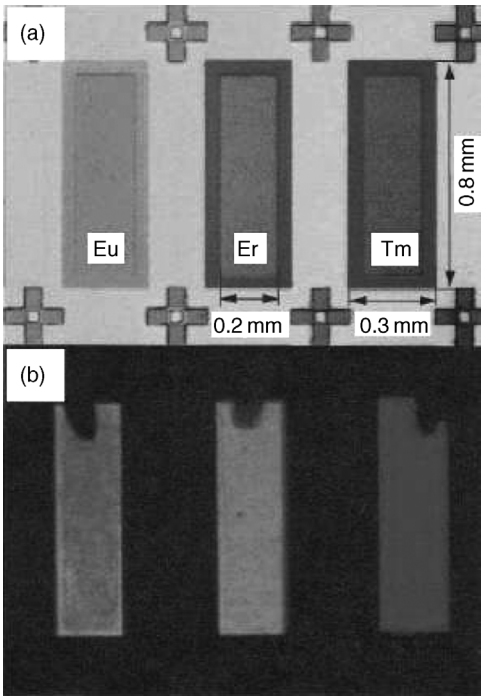

Figure 1.47 Laterally integrated GaN:RE thin-film ELD containing the three primary colors fabricated with the SOG liftoff technique: (a) optical microscopy photograph of the GaN ELD showing the three-color integration; (b) blue, green, and red emission under DC bias from ELD GaN devices doped with Tm, Er, and Eu, respectively [83]. (Please find a color version of this figure on the color tables.)

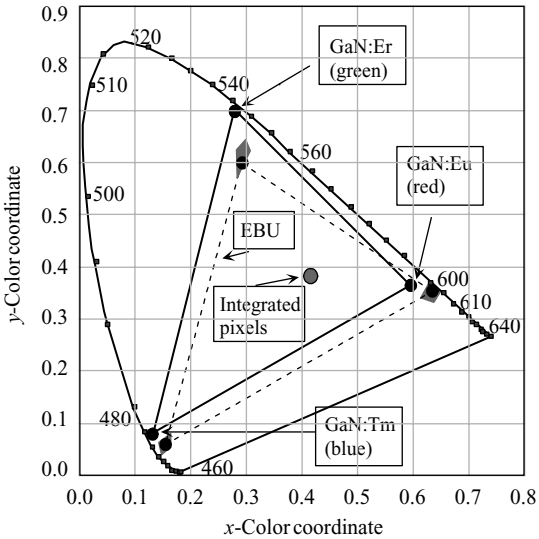

Figure 1.48 CIE *x*–*y* chromaticity diagram showing the locations of the blue, green, and red emission from the individually biased pixels in an integrated GaN:RE-based ELD and from simultaneously biasing all three pixels in the device. Also shown are the coordinates of the EBU-recommended phosphors [83].

values of the red, green, and blue pixels from the three-color integrated device are approximately 14, 45, and 3 cd m^{-2}, respectively. Figure 1.48 illustrates the full-color capability of RE-doped GaN integrated ELDs using the Commission International d'Eclairage (CIE) chromaticity diagram. The solid triangle in the diagram defines the full-color capability of emission from GaN doped with Eu (red), Er (green), and Tm (blue). The CIE triangle recommended by the European Broadcasting Union (EBU) is shown by a dashed line for comparison.

1.10
On the Nature of Light Emission in Nitride-Based LEDs

Although nitride LEDs were introduced as a commercial product in late 1993, there are still many unanswered questions regarding the optical emission processes responsible for their outstanding operation. One of the questions sending everyone to search for answers is the unusually high efficiency of light emission in the presence of large concentrations of defects in the material as well as a current-conduction mechanism that is inconsistent with band-to-band recombination. It is known that the radiative recombination in wide-bandgap semiconductors such as ZnS deposited on glass is very efficient. The mechanism responsible for this has been attributed to carrier localization and, of course, it is very enticing to make a parallel here.

1.10.1
Pressure Dependence of Spectra

In order to take a glimpse at the origin of the strong electroluminescence in nitride-based LEDs, and more importantly to understand the origin of light emission, Perlin *et al.* [84] examined the photoluminescence and electroluminescence emission in commercially available blue and green LEDs under hydrostatic pressure after they had been decapsulated. To complement the pressure experiments, Perlin *et al.* [85] also embarked on an extensive investigation of EL from blue and green LEDs over a broad current and temperature range in an effort to gain some insight into the genesis of radiative transitions. The blue and green LEDs exhibited similar behavior with the green ones accenting the anomalies mentioned. Consequently, the following discussion will be limited to the case of the green devices.

The green Nichia LED investigated has an undoped active layer consisting of a 30 Å thick $In_{0.45}Ga_{0.55}N$ layer sandwiched between n-GaN on the bottom and p-$Al_{0.2}$-$Ga_{0.8}N$ on the top layers. The lattice mismatch between the active layer and the barrier materials is about 6%, bringing into question whether the structure has a pseudomorphic character or the strain is relaxed by a large concentration of dislocations, on the order of $10^{10}\,cm^{-2}$ [86]. Another perplexing aspect of these diodes is the 2.28–2.33 eV photon energy that is somewhat smaller than the 2.50–2.68 eV expected from the bandgap of $In_{0.45}Ga_{0.55}N$, although the clustered nature of InGaN makes the reported compositional dependence of its bandgap a suspect [87]. Nakamura *et al.* [88] suggested that this discrepancy could be caused by tensile strain in the quantum well, which had been induced by differences in the thermal expansion coefficients of the quantum well and barrier materials. Other suggestions involve unidentified and elusive localized states [89] or localized excitons [90]. In any case, no definitive answer has been given yet as to the nature of the recombination in the so-called Nichia single quantum well LEDs.

Figure 1.49 exhibits the photoluminescence spectra of a green Nichia diode as a function of hydrostatic pressure. The observed Fabry–Perot interference fringes are

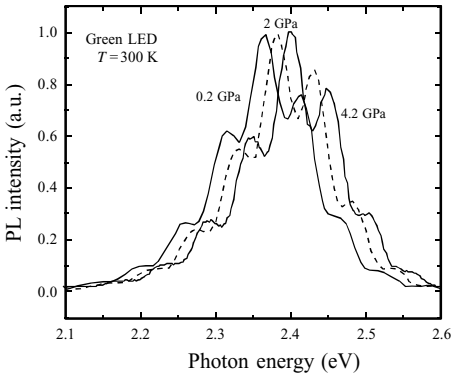

Figure 1.49 Photoluminescence spectra of a Nichia green LED at three indicated uniaxial pressures at 300 K obtained after decapsulation [84].

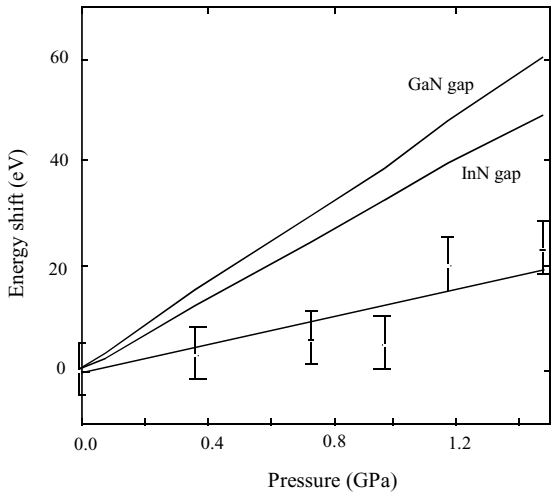

Figure 1.50 Shift of the EL peak position as a function of the hydrostatic pressure for a Nichia green LED. The data are shown along with error bars and the expected shifts of the band edge for GaN (*experimental*) and InN (*theory*) are the labeled solid lines. The solid line through the data points is a guide to the eye [84].

indicative of the fact that the structure is mostly transparent to the particular radiation. The distance between fringe maxima is close to 50 meV (500 cm^{-1}) and gives a total cavity thickness, sapphire on the one side and air on the other, of approximately 5 mm, which agrees well with the total thickness of these GaN/InGaN/AlGaN structures (4.6 mm). The presence of interference fringes can cause misidentification of the peak position, which is made worse as the fringe periodicity can change with pressure due to the pressure dependence of the refractive index (about 6 meV GPa^{-1}). For accuracy, the Gaussian peak profile and an oscillating function representing the interference fringes were fitted to the data, which paved the way to determine the peak shift in luminescence and electroluminescence with hydrostatic pressure, the latter of which is displayed in Figure 1.50 for a green LED. The observed linear shift with pressure was 12 meV GPa^{-1} for the green LED, compared with 40 meV GPa^{-1} (experimental) and 33 meV GPa^{-1} (theoretical) for GaN and InN, respectively, and this indicates that the transition energy is not of traditional band-edge origin. The contribution of pressure to any confinement due to an increasing effective mass has been determined to be about 2 meV GPa^{-1} [84]; it is very small. In short, one can conclude that the LED spectra do not follow the band edge.

A pressure coefficient lagging behind the band edge can be expected from deep states. For example, transitions between uncorrelated electrons and holes, meaning those with wave functions that do not overlap, trapped in band-tail states caused by indium clusters/compositional fluctuations lead to pressure coefficients smaller than the band-edge value. Band-tail states can extend deep into the forbidden gap, and deep states have a pressure coefficient that is an average across the entire Brillouin zone. This average coefficient is much lower than that at the r-point direct bandgap. Localized excitons have also been postulated as being responsible for the transitions

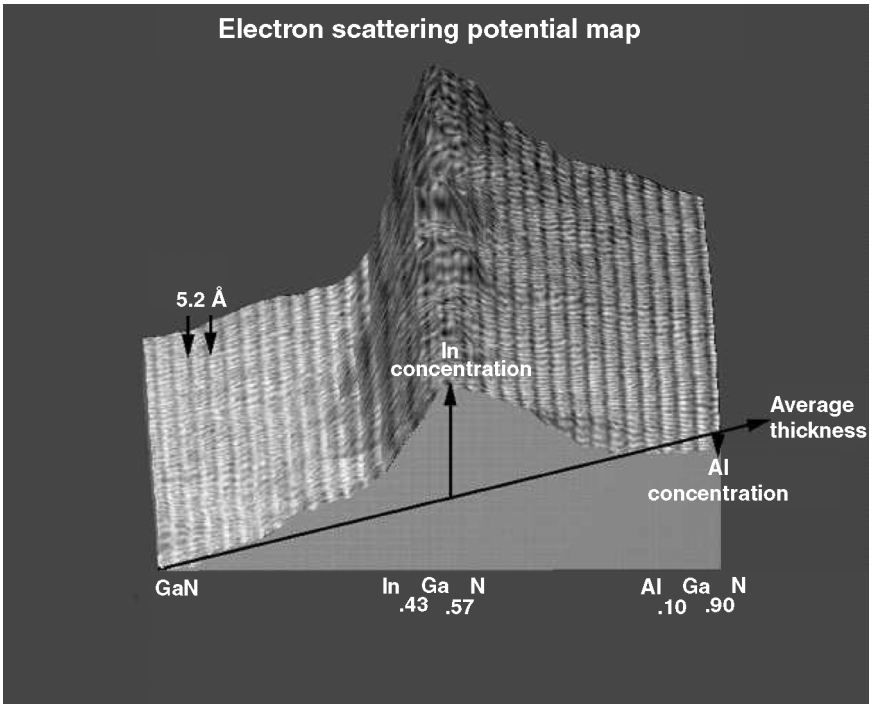

Figure 1.51 Out-of-plane and in-plane compositional variation of InGaN in a GaN/InGaN well structure similar to that used in the Nichia LEDs. Courtesy of C. Ksielowski, Lawrence Berkeley National Laboratory.

in InGaN LEDs [90]. However, the observed behavior retains the same trend at high current injection levels where excitons would certainly dissociate and would therefore not be responsible. Localization effects such as the postulated quantum dots (QDs) are so far limited to casual observations of compositional variations [91]. Shown in Figure 1.51 is the compositional variation of InN in an InGaN quantum well, which is similar to that used in LEDs, manufactured by Nichia Chemical Co. Clearly, the molar fraction varies in the growth direction and in the plane of growth leading to clusters. Moreover, dots of the kind postulated would have pressure coefficients similar to the band edge. In short, the available pressure dependence indicates that the transitions are due to uncorrelated electron–hole pairs localized deep in band tails, which are most likely caused by inhomogeneous InN mole fraction and strain. Ironically, we would not be too illogical if we were to argue that it is precisely the presence of these band tails that is responsible for the extraordinary performance .

1.10.2
Current and Temperature Dependence of Spectra

Figure 1.52 exhibits the peak position of the EL emission at several temperatures from the green LED discussed above, with a clear shift to higher energies as the injection

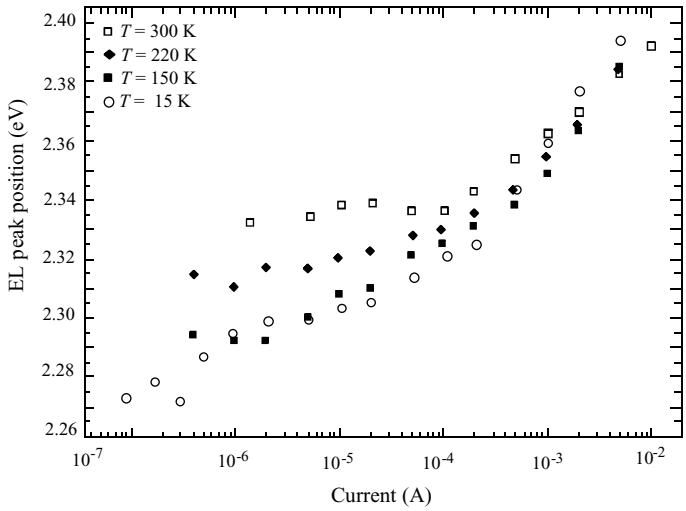

Figure 1.52 The peak position of the EL emission at several temperatures from a green Nichia LED indicating a clear shift to higher energies as the injection current exceeds 0.1 mA [85].

current approaches 0.1 mA. As the temperature is increased, the low-current plateau also shifts toward higher energies. This blueshift is about two orders of magnitude larger than what we would expect from the filling of the conduction band states. Consequently, the transition responsible must be due to states with very low density of states compared to the conduction band. This observation is also consistent with the premise that deeper states are the origin of the observed transitions. Deeper states here include band tails as well as other pseudocontinuous states. Interestingly enough, the energy of the emitted photons at the largest applied currents is quite close to the estimated separation between the confined states in a 3 nm thick $In_{0.45}Ga_{0.55}N$ quantum well. Figure 1.53 depicts the same shift at 300 K up to a pulsed-current level of 2 A and accentuates the blueshift very well with injection current.

Figure 1.54 plots the temperature dependence of the peak energy of the EL emission. The solid line depicts the expected trend of the band edge of GaN but shifted rigidly to represent the bandgap of InGaN. Figure 1.54 indicates that for a current level of 0.1 mA (preceding the band-tail filling), the EL emission undergoes a blueshift with increasing temperature. Between 15 and 300 K, this shift can be as large as about 70 meV, for the lowest applied current. It should also be stated that the emission bandwidth (≈130 meV at 1 mA, not shown) remains practically unchanged over the entire temperature range.

The data presented above suggest that the radiative recombination does not directly involve the conduction and valence bands and, in the case of quantization, quantum well subbands. Though radiative recombination has been suggested to relate to excitons localized in regions containing large InN molar fraction that are caused by fluctuations of the indium contents in the active layer material, the data of Perlin support the band-tailing effect. On the contrary, the same data on high carrier injection

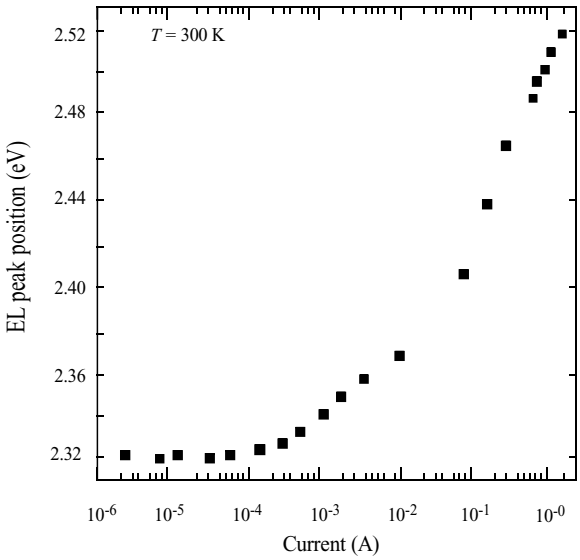

Figure 1.53 The peak position of the EL emission at room temperature from the same green LED as in Figure 1.52, showing the blueshift at 300 K up to a pulsed-current level of 2 A accenting very well the blueshift with injection current [85].

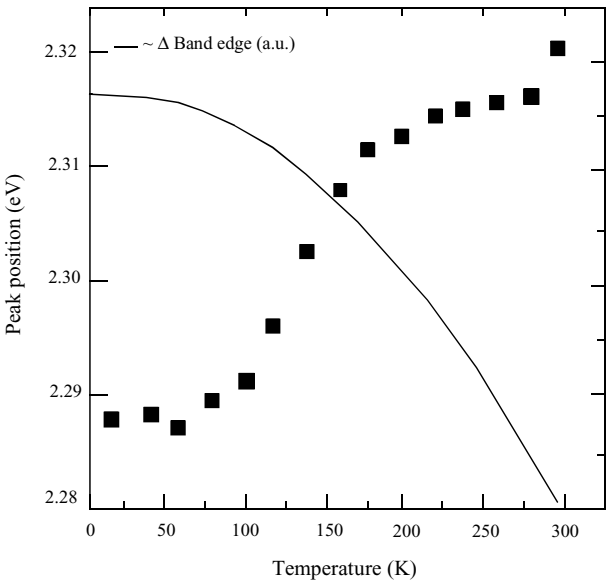

Figure 1.54 The PL peak position of the same green LED as in Figure 1.52 measured at different temperatures. The PL peak shifts to higher energies with increasing temperature. This is to be contrasted to the band-edge energy dependence on temperature, which is depicted by the solid line. This line is intended to show the trend only with no attention paid to the absolute values [85].

levels do not support the exciton premise. Particularly, the rapid blueshift of the electroluminescence with injection is indicative of a continuous density of states favoring band-tailing effects that are caused by strain and compositional fluctuations.

1.11 LED Degradation

Prior to the debut of GaN, the experience with all LED materials had been that acceptable quantum efficiencies can be obtained only when the defect concentration in the semiconductor is well below about $10^4\,cm^{-2}$. GaN, with defect concentrations about six orders of magnitude higher than this at the time of introduction of GaN-based LEDs, was not consistent with the trend of the time, and thus GaN was discounted by many LED manufactures. Even with large defect concentrations in the vicinity of $10^9\,cm^{-2}$, GaN LEDs, with longevity well over the minimum 10 000 h, required by the display society (CIE), were marketed in early 1994, which took many by surprise. In order to reduce the amount of InN employed in InGaN active emission layers, early devices utilized deep Zn centers in the 20 nm thick active layer to shift the wavelength to about 450 nm, which is defined as blue by CIE. These devices were shown to have more gradual and graceful aging than the AlGaAs diodes, particularly in steam tests. Nevertheless, degradation caused by p-metallization was notable. In the second wave of devices, the Zn centers were eliminated and the blue color was obtained by an increased InN mole fraction in the lattice, with an accompanying decrease in the active layer thickness to about 3–4 nm. These devices exhibit longevity well over that required by CIE.

In addition to manufacturers' own life testing, early independent life testing of Nichia LEDs was undertaken by Osinski *et al.* [92], Barton *et al.* [93], and Barton and Osinski [94]. This work was later extended to include improved single quantum well varieties with sufficient InN in the lattice so as to not rely on Zn centers [95]. In the initial degradation experiments of Osinski *et al.* [92], there were three types of devices, two containing Zn deep centers and wider InGaN layers, and a third set of devices that did not utilize Zn, but took advantage of the increased InN mole fraction to obtain the 450 nm blue radiation.

The general trend amongst the 18 LEDs measured was for the output intensity to decrease at a faster rate within the first 50–100 h, and then at a slower rate over the remainder of the test. The output intensity of the two earlier model LEDs containing Zn increased within the first 50 h and then decreased during the remainder of the test. After the first 1000 h, the drive currents of the LEDs were increased to accelerate the test.

The relative intensity of one of the older generation LEDs dropped to about one-half of its initial value after approximately 1200 h of testing. In this case, the high current (70 mA) had indeed caused a rapid failure. The cause of this premature degradation was a crack in the LED, which isolated a part of the junction area from the p-contact. The remaining devices driven at the same current level, however, have performed much better. The degradation rate slowed after a relatively fast drop in the output (10–15% over the first 750 h).

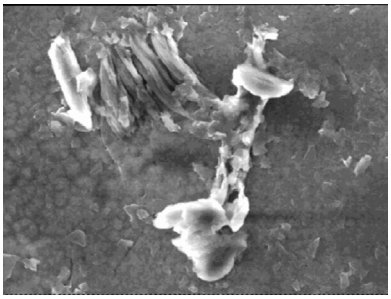

Figure 1.55 Secondary electron EBIC image of a shorted Nichia LED after the p-contact metal has been removed. Courtesy of M. Osinski, University of New Mexico.

To speed up the life test, electrical stress under high pulsed-current conditions was also applied, which resulted in a degradation of the *I–V* characteristics with some devices exhibiting a low-resistance ohmic short (40–800 Ω). Electron beam induced current (EBIC) imaging pointed to a conductive path extending from the surface (the p-contact metal) to the n-type side of the junction. The high forward current applied to this device caused metal from the p-contact to migrate across the junction, as is evident in the secondary electron EBIC image (Figure 1.55).

The use of low-resistance and thermally stable ohmic contacts to the p-GaN layer can mitigate indiffusion of the ohmic contact elements along dislocations in nitride-based epilayers, leading to an electrical short of the p–n-junction. The use of a diffusion barrier in Ni/Au-based contacts showed superior long-term stability of turn-on voltage, leakage current, and output power [96].

Double-heterojunction green LEDs without the deep Zn centers were also stressed with pulsed currents of approximately 5 A with a 1 kHz repetition rate and a 10^{-4}% duty cycle yielding an average power dissipation of 25 mW to eliminate heating. Three devices were stressed to failure with a sudden and complete loss of light output. The *I–V* characteristics were all linear with resistive shorts in the range 18–140 Ω.

In both blue and green failed LEDs, optical micrographs taken after decapsulation showed severe damage to the plastic encapsulation, which could not be completely removed even in hot acids due to damage. The opaque encapsulant is to a great extent responsible for the faster light output degradation, leaving the cause of the slow degradation to nonradiative recombination center generation. It has also been noted that as the material's quality improved, the high current-induced stress causes encapsulant damage earlier than the device [97].

The data presented above on the early vintage double-heterojunction LEDs indicate a possible connection between the large number of crystalline defects and a tendency for metal to migrate from the p-contact across the junction and short out the device. The newer generation, quantum well LEDs showed a significant improvement in resistance to this type of stress and revealed that the limitation may be in the plastic packaging material and not in the diode itself. The slow degradation in light output appears to be due to degradation in the transparency of the plastic package material

caused by high current pulses, not likely due to the creation of crystalline defects. Constant current life tests have shown that the plastic encapsulant can change in transparency due to Joule heating. The conditions in the final stage of the CW life test showed that the package would be adversely affected by prolonged exposure to temperatures around 140 °C. The analysis of LEDs subjected to pulsed-current stress showed that some regions on the LED may have exceeded 140 °C during a single pulse, thereby damaging the plastic in that region. The observed rapid degradation occurs when the plastic degrades to the point where its conductivity increases and facilitates the burnout of the LED. At this point of low resistance, ohmic shorts are observed across the LED.

Degradation testing of high-brightness green LEDs under high current electrical stress with current pulse amplitudes between 1 and 7 A, voltages between 10 and 70 V, a pulse length of 100 ns, and a 1 kHz repetition rate has been carried out [95]. When the current amplitude increased above 6 A, a fast degradation (on the order of 1 s), accompanied by a visible discharge between the p- and n-type electrodes occurred. Follow-up analysis revealed severe damage to the metal contacts, causing electrical shorts on the surface plane of the diode. Below 6 A, a slow degradation was observed in the form of a decrease in optical power and increase in the reverse current leakage. However, a rapid degradation, similar to that for higher current, occurred between 24 and 100 h. Overall analyses indicate that the degradation process begins with carbonization of the plastic encapsulation material on the diode surface, which leads to the formation of a conductive path across the LED and subsequently to the destruction of the diode itself.

Additional DC aging experiments, following a schedule of tests under 20, 50, and 100 mA current stress, were carried out on more improved, in terms of semiconductor properties, blue LEDs packaged with encapsulants, as well as LED chips mounted without encapsulants, in order to delineate the role of encapsulant degradation [98]. In the process, three distinct failure modes were identified:

(i) High current levels and, consequently, high junction temperatures, induce degradation of the epoxy encapsulant where it is in contact with the hot device surface, leading to opacity of the encapsulant. This degradation mechanism is faster, but does not apply to high intensity LEDs which do not employ epoxy encapsulant.

(ii) High current and thus temperature degrades the semitransparent p-ohmic contact and the top surface of the p-GaN layer, which leads to increased series resistance. This leads to current crowding, reducing the optical power, again this does not apply to flip chip mounts and their transparent contacts which could have their own reliability issues in terms of transparency retention.

(iii) Redistribution of electrically active deep levels, which already exist in control devices, and also generation of shallow traps, as probed by deep-level transient spectroscopy (DLTS). The decrease of optical power seems to correlate with reverse leakage current, which in turn is possibly due to an increase in the density of nonradiative recombination centers.

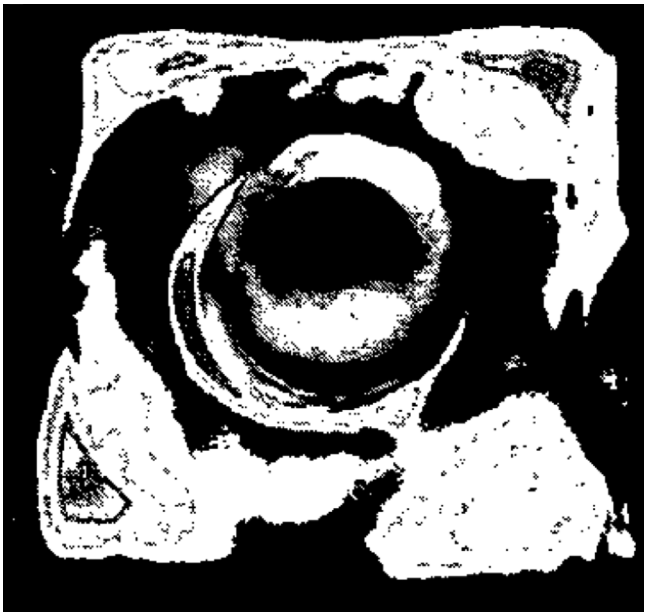

Figure 1.56 Emission micrograph of a failed LED after decapsulation with severe damage to the plastic encapsulation, which could not be removed completely, even in hot H_2SO_4 [98].

Figure 1.56 shows an emission image of a blue LED aged for 250 h at 100 mA after removal of the epoxy encapsulant in hot H_2SO_4. High temperature and short-wavelength irradiation have damaged the encapsulant and left an opaque layer, which could not be removed in hot sulfuric acid.

Comparative electrical measurements in control and stressed LEDs are shown in Figure 1.57. As mentioned earlier, the failure modes are as follows: (i) increase of the

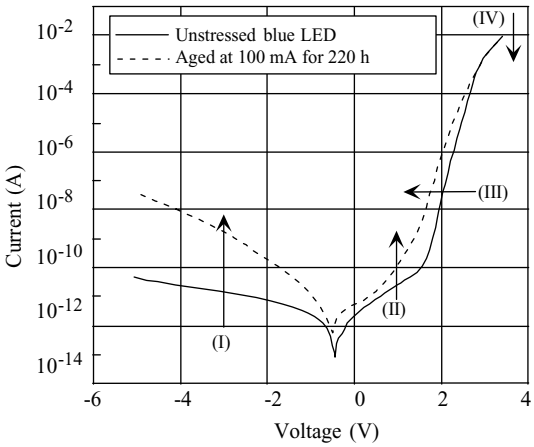

Figure 1.57 *I–V* characteristics of control and stressed (100 mA and 220 h CW) LEDs [98].

reverse leakage current accompanied with optical power degradation; (ii) increase of the generation–recombination current for low forward-bias voltages; (iii) degradation of the device ideality factor; and (iv) increase of the parasitic series resistance, most likely due to degradation of the semitransparent p-type ohmic contact when used. The increased resistance causes current crowding with increasing current exacerbating device performance [98].

Extending the issue of longevity to white-light LEDs, Narendran *et al.* [99] tested the lifetimes of two groups of white LEDs. The LEDs in one group had similar junction temperatures but different amplitudes for the short-wavelength emission, and the LEDs in the second group had similar amplitudes for the short-wavelength emission but different junction temperatures. In the experiment, both the junction temperature and the amplitude of short-wavelength emission were affected by the degradation rate of the white LEDs. However, the effect of the temperature on the degradation of the LEDs was much more extensive than the short-wavelength amplitude. Furthermore, they also showed that some portion of the light circulates between the phosphor layer and the reflector cup, potentially increasing the epoxy-yellowing issue.

In an effort to assure the reliability of the LEDs especially under the high temperature (>100 °C) and extreme photon fluence (>50 W cm^{-2}), several improvements in base material and chip attachment technologies have been undertaken. Among them is a package that can allow 150 °C (white) or higher (185 °C, nonwhite) junction temperature operation, as provided by the LUXEON K2 package, an artistic view of which is shown in Figure 1.58 for junction tempera-

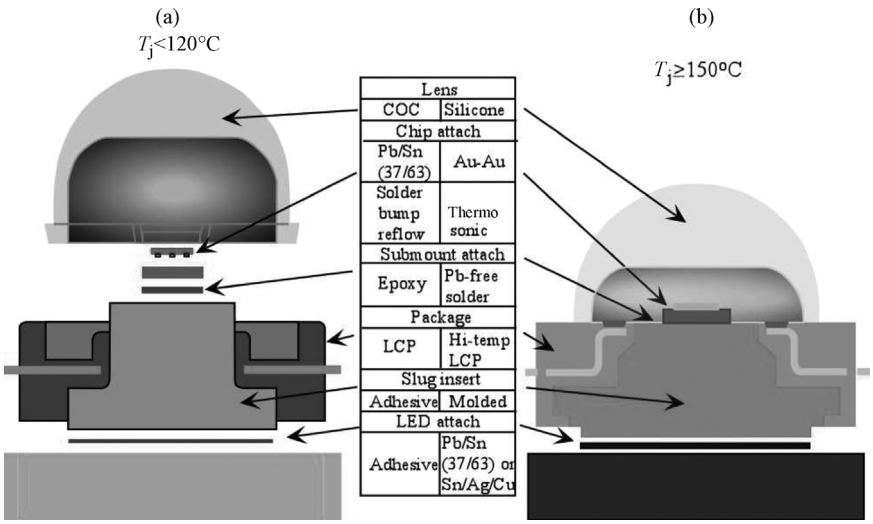

Figure 1.58 High-power LED packages for lighting applications. (a) LUXEON circa 1998. (b) LUXEON K2 circa 2006. Courtesy of Lumileds/Philips. (Please find a color version of this figure on the color tables.)

tures $T < 120\,^{\circ}C$ and $T \geq 150\,^{\circ}C$ [100]. While on the topic, we should mention that the epoxy used in some packages suffers from yellowing, a degradation mechanisms that can be mitigated by substituting it with silicon resins or silicon-epoxy resins with thermal stability and UV resistance for use in encapsulating LED [101].

The generation of additional nonradiative defect centers after aging was also confirmed in another investigation where electroluminescence, electron beam induced current, and cathodoluminescence investigations were brought to support this conclusion, albeit in early varieties of devices [102]. The aged InGaN/AlGaN DH LED exhibited formation and propagation of dark spots as well as a crescent-shaped dark patch, which were acting as nonradiative recombination centers, determined by cathodoluminescence images. The degradation rates of the relative optical power under an injected current density of $0.1\,kA\,cm^{-2}$ were determined to be 1.1×10^{-3}, 1.9×10^{-3}, and $3.9 \times 10^{-3}\,h^{-1}$ at ambient temperatures of 30, 50, and $80\,^{\circ}C$, respectively. The activation energy of degradation was also determined to be 0.23 eV. Having said this, the point of changing the deep-level picture is of some controversy, as earlier reports based on investigations utilizing deep-level transient spectroscopy, thermally stimulated capacitance, and admittance spectroscopy measurements performed on stressed (earlier version) devices showed no evidence of any deep-level defects that may have developed as a result of high current pulses [92]. This may be due to variability in stress testing or higher extended and point-defect concentration existing in devices before testing and thus earlier degradation than shown by more improved devices of later varieties.

High junction temperature limits the performance of GaN LED, with the main degradation mechanisms arising due to the emission crowding and series resistance. Pending confirmation, the degradation process has been attributed to the presence of hydrogen, which can diffuse in the p-layer and generate Mg–H bonds with the acceptor atoms, thus compensating the overall active, already low, hole concentration and reducing device performance. The likely source of hydrogen could be from the passivation layer [103] typically deposited by PECVD on the LEDs for chip encapsulation and surface leakage current reduction.

In phosphor conversion LEDs, in addition to degradation of LEDs themselves, the reliability of YAG and any encapsulant used enters into the picture. In the short history of pcLEDs, there have been speculation and some reports about lifetime threats. Especially for YAG:Ce, this appears strange, as this material has been proven to be extremely stable under most adverse conditions [104]. However, as the best argument is a reliability test, a meaningful ensemble of YAG-pcLEDs was put into a 60% relative humidity/85 °C test chamber and driven at $50\,A\,cm^{-2}$. After 3000 h, no significant degradation of the lumen output was observed. These studies were conducted on pcLED in a special package, which did not contain an epoxy encapsulant. Previous tests on 5 mm LEDs with epoxy dome lenses, which are still common in the industry, failed often because of "browning" (oxidation) of the epoxy, reducing the transmission. It is not unlikely that the previous reports relate to results that actually tested the package materials [105].

1.12 LED Efficiency

A rather important aspect in GaN LEDs in general is the reduction of output light with increasing injection current. The thermal component of the problem is reasonably well addressed with very advanced packaging technologies that not only effectively extract the photons generated but also dissipate the heat. However, all GaN LEDs suffer efficiency reduction when pumped at high injection currents, the absolute value of which depends on the layer quality and packaging, among others. Specifically, a good part of the reduction in efficiency in LEDs on *c*-plane sapphire with increasing injection current is due to reduction in the internal quantum efficiency, which in general involves opening up channels for nonradiative recombination. Carrier leakage when the band discontinuities in the quantum well regions are small can also contribute to such an effect. Consequently, the maximum internal quantum efficiencies are obtained at relatively low injection levels, sometimes as low as $10\,\mathrm{A\,cm^{-2}}$ (see Figure 5 of Ref. [108] and Figure 8 of Ref. [107]). This is in contrast to the observations made in LEDs based on relatively well-developed and high-quality conventional III–V semiconductor material systems such as (In, Al, Ga)As and (Al, Ga)InP. As the current density is increased beyond that point at which the maximum injection efficiency is attained, a monotonic drop in quantum efficiency is noted in blue and green InGaN/GaN QW LEDs, even under short-pulse, low-duty-factor, and constant-temperature injection [106, 107]. However, just about all the applications of these LEDs require them to retain high quantum efficiencies at larger current densities (e.g., $>50\,\mathrm{A\,cm^{-2}}$). As mentioned throughout this chapter, these applications include, but are not limited to, projection displays [108], automotive headlights [100], and general lighting.

The decay in quantum efficiency with increasing current for blue and particularly green InGaN/GaN LEDs has been attributed to many different mechanisms, among which are poor injection efficiency [109, 110], carrier delocalization from quantum dots [111], exciton dissociation [112], high plasma carrier temperatures (hot carriers) [113], and polarization effects together with electron-blocking layers [114]. Furthermore, the Auger nonradiative recombination [115] as well as methods to mitigate it [116] has been reported to cause the droop in efficiency at high injection levels. It should be noted the measurements performed at various laboratories, including that of the author, indicate that the intensity droop is not observed in PL experiments, but rather in EL experiments, indicating that reduction in the efficiency is not related to the MQW radiative recombination efficiency but to the loss of carriers by means such as recombination outside the quantum well region. This is generally termed as carrier leakage. The effect of heating due to increased current at high injection levels has been ruled out. The dependence of the efficiency droop on quantum well layer thickness has been investigated. Studies indicate that the droop is not as evident in wider quantum wells that have the downside of reduced overall intensity pointing to some unresolved issues [117].

In the case of the notion of Auger recombination, the Auger recombination coefficient that is estimated by fitting a third-order polynomial is on the order of

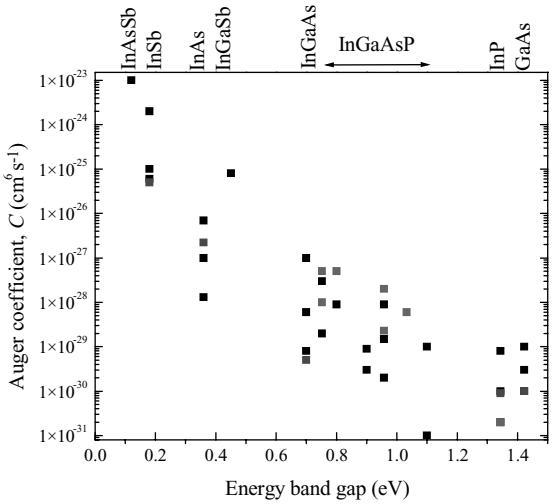

Figure 1.59 Auger coefficient *C* for direct-bandgap semiconductors in which it has been determined at room temperature. Data courtesy of J. Piprek.

1.4×10^{-30} to $2.0 \times 10^{-30}\,\mathrm{cm}^6\,\mathrm{s}^{-1}$, which is comparable to the one that has been measured for InP that has half the bandgap of InGaN emitting in the blue [115]. This is approximately four to five orders of magnitude larger than what can be expected of the bandgap of the blue of InGaN when extrapolated from the data shown in Figure 1.59 (also see Equation 1.29), in more conventional semiconductors ranging from InAsSb on the small-bandgap side to GaAs on the relatively large-bandgap side [118]. The four to five orders of magnitude disparity could in fact increase, considering that the dispersion between hole and electron masses in conventional III–V semiconductors is much smaller as compared to InGaN. We should mention that Auger recombination has been studied in the smallest bandgap triad of nitride semiconductors, InN [119]. Regardless, it is clear that the efficiency droop with increasing injection level points to carrier leakage or loss of some sort, which will take some time sort out.

All of the above-mentioned processes with the exception of *Auger recombination* [120–123] are discussed in Volume 2, Chapter 5. It should be recognized that Auger recombination is an intrinsic property of a given semiconductor and is determined by the conduction and valence bands as well as the bandgap and its type, meaning direct or indirect. Further, because Auger recombination involves carrier recombination across the band and also carrier excitation to higher energies, the process involves many carriers and as such it becomes more important at high carrier densities. To a first degree, if the Auger recombination, which is more dominant at high injection levels and as in its simplest treatment goes with the third power of the carrier concentration, were to take place in GaN-based LEDs at current densities dwarfed by those in effect in lasers, to be consistent one can surmise that lasers in GaN could not be obtained if the layer qualities were in the same ball park.

Because, this is not the case, it is more likely that the efficiency reduction with injection current is related to the material quality/particulars (e.g., localization, which at high injection levels would not be as effective) and heterojunction design (e.g., thin multiple quantum wells versus one relatively thick active layer considering the large hole effective mass) if the processing- and packaging-related issues are addressed effectively. It is likely that the Auger process involving defect levels could enter into the equation. One can then surmise that the current density at which the efficiency peaks would increase in time. Already preliminary results in author's laboratory indicate that large hole effective mass and relatively low p-doping form the genesis and that measures can be taken to increase the current at which the efficiency peaks.

Nevertheless, below we give a brief discussion of Auger recombination and how it is quantified for instruction purposes. In brief, Auger recombination depicts the process in which an electron in the conduction band recombining with a hole in the valence bands does not lose its energy radiatively. Instead, it gives off its energy to another electron, which is then excited to a higher energy level in the conduction band, or a hole, which is excited to a higher energy level in the valence band. As shown in Figure 1.60, the process naturally requires that both energy and momentum be conserved, necessitating indirect transitions to occur. Again, as shown in Figure 1.60, the process can also involve phonon participation. For example, if the process following the recombination is electron excitation to a higher energy, the process goes by the depiction of CCCH. The processes involving donor and acceptor states are not shown, for simplicity, but can be found elsewhere [124].

The dominant temperature dependence of the Auger recombination specific carrier lifetime (the inverse of Auger recombination rate) to a first extent is given by a modified expression of Beattie and Landsberg [120] by

$$\tau \propto \left[\frac{E_g(T)}{kT}\right]^{3/2} \exp\left[\frac{1+2M}{1+M}\frac{E_g(T)}{kT}\right] \tag{1.29}$$

for a nondegenerate and intrinsic semiconductor. The terms $E_g(T)$ and M represent the temperature-dependent bandgap and electron to hole mass ratio, respectively. For a semiconductor with a conduction band effective mass smaller than the valence band effective mass, the lifetime is determined by electron–electron collisions, namely, electron recombination with a hole followed by another electron excitation to a higher energy or electron excitation from the valence band to the conduction band coupled with hot electron relaxation to near the bottom of the conduction band with the entire process conserving energy and momentum. If the hole mass is smaller than the electron mass, which is not the case in GaN and related materials, the lifetime would be determined by hole–hole collisions, namely, electron recombination with a hole coupled with another hole excitation to a higher energy or electron excitation from the valence band to the conduction band, coupled with hot hole relaxation to near the bottom of the valence band, again with the whole process conserving both energy and momentum [120].

Typically, Auger recombination rate is higher, or the lifetime is smaller, for relatively small-bandgap materials, meaning the value of the ratio of energy gap/kT, in which

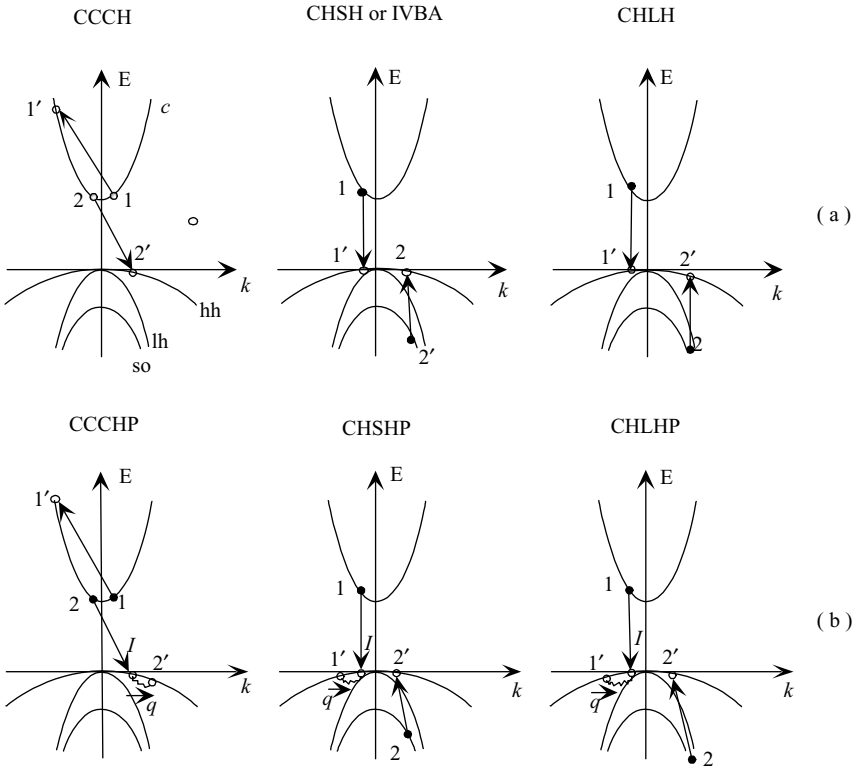

Figure 1.60 Auger processes involving the intraconduction band, interband, and intravalence band processes. Parameters c, hh, lh, and so represent the conduction band, heavy-hole valence band, light-hole valence band, and spin–orbit split-off band. Processes CCCH, CHSH, and CHLH indicate the conduction band–conduction band and conduction band–heavy-hole valence band, conduction band–heavy-hole valence band and split-off band–heavy-hole valence band, and conduction band–heavy-hole valence band and light-hole band–heavy-hole valence band transitions, respectively. These transitions conserve both momentum and energy (a). Processes similar to CHSH are also considered IVBA processes. Processes CCCHP, CHSHP, and CHLHP represent the conduction band–conduction band and conduction band–heavy-hole valence band with phonon interaction, conduction band–heavy-hole valence band and split-off band–heavy-hole valence band with phonon interaction, and conduction band–heavy-hole valence band and light-hole band–heavy-hole valence band with phonon interaction transitions, respectively. These latter transitions (b) conserve energy and momentum through the assistance of phonons. Patterned after Refs [125, 126].

case, electrons in the conduction band and holes in the valence band participate in the process. By the same token, Auger recombination is more important at high temperatures. To a first order, the traps do not participate in the process, although their taking part could be important in some cases. In large-bandgap semiconductors, the Auger process would depend on the doping level and become important in degenerate cases. At high doping concentrations, the electron wave function of adjacent impurities would overlap and delocalize the electrons (or holes), which

increase the likelihood of Auger recombination. The energy of the excited carrier in the process would be dissipated by a cascade of optical phonon emission while conserving energy and momentum.

The recombination process, in general, has been treated in Volume 2, Chapter 4. Here, we will extend the discussion to include the contribution to this process of Auger processes. Recall Volume 2, Equation 4.54 for a p-type semiconductor, repeated below for convenience:

$$U = \frac{\sigma v_{\mathrm{th}} N_{\mathrm{t}}(pn - n_i^2)}{n + p + 2n_i \cosh[(\xi_{\mathrm{t}} - \xi_i)/kT]} = \frac{1}{\tau_{\mathrm{r}}} \frac{(pn - n_i^2)}{n + p + 2n_i \cosh[(\xi_{\mathrm{t}} - \xi_i)/kT]}, \quad (1.30)$$

with $\tau_{\mathrm{r}}^{-1} = \sigma v_{\mathrm{th}} N_{\mathrm{t}}$, the average lifetime of the minority carriers.

As mentioned above, Auger recombination involves three particles, namely, an electron and a hole that recombine in a band-to-band transition and give off the resulting energy to another electron or hole. Naturally, the expression for the net recombination rate in Auger recombination is similar to that of band-to-band recombination but with the exception that it must include the density of the electrons or holes, which receive the released energy from the electron–hole annihilation. In the case of electron excitation to a higher level in the conduction band, the Auger recombination rate can be expressed as

$$U_{\mathrm{Auger}} = C_{\mathrm{n}} \left[n(pn - n_i^2) \right]. \quad (1.31)$$

In the case of a hole excited to a higher energy in the valence band, the Auger recombination is given by

$$U_{\mathrm{Auger}} = C_{\mathrm{p}} \left[p(pn - n_i^2) \right], \quad (1.32)$$

where C_{n} and C_{p} represent the Auger recombination coefficients for electrons and holes, respectively. If both of the above processes take place, then the sum of Equations 1.31 and 1.32 must be used.

In the case of high-level injection, the electron and hole concentrations, n and p, are nearly equal to each other and both are much larger than n_i. Consequently, the Auger recombination rate would be proportional to n^3. For comparison, the band-to-band radiative recombination rate ($U_{\mathrm{b-b}} = B(pn - n_i^2)$), which at high injection levels would be proportional to Bn^2, and the recombination by traps, Shockley, Hall, and Reed recombination ($U_{\mathrm{SHR}} \approx \tau_{\mathrm{n}}^{-1}(n_{\mathrm{p}} - n_{\mathrm{p0}})$), would be proportional to n. In simple terms, the total rate of change of electron concentration at high injection levels due to deep levels, band-to-band radiative recombination, and nonradiative Auger recombination can be expressed as

$$U = -\frac{\mathrm{d}n}{\mathrm{d}t} = B_{\mathrm{dl}} n + B_{\mathrm{b-b}} n^2 + B_{\mathrm{A}} n^3, \quad (1.33)$$

where B_{dl}, $B_{\mathrm{b-b}}$, and B_{A} represent the deep-level recombination, band-to-band recombination, and Auger recombination coefficients, respectively, in the units of s^{-1}, $\mathrm{cm}^3\,\mathrm{s}^{-1}$, and $\mathrm{cm}^6\,\mathrm{s}^{-1}$, respectively. If there is generation, for example, by photoexcitation, then a generation term G must be added to Equation 1.33. Time-resolved luminescence experiments have been conducted to determine the decay

rates. The term dn/dt can be written as $(dn/dI_{PL})(dI_{PL}/dt)$ wherein the first term can be obtained from time decay of the PL experiments in which the photogenerated carrier concentration before decay is known. Specifically [115], a fit of the dependence of the PL intensity on the absorbed photon density, I (in terms of $W\,cm^{-2}$), for the total recombination rate can be used to determine the internal quantum efficiency η_{int} through the relation $\eta_{int} = Bn^2/G$, albeit without a unique combination of B_{dl}, B_{b-b}, and B_A coefficients (popularly referred to as the A, B, and C coefficients). Luckily, the B coefficient can be uniquely determined by fitting a decay curve at a known I and η_{int} (I) in an iterative procedure. The carrier density n is determined from two points in a single light output intensity decay (L_1 and L_2 at time intervals t_1 and t_2) from

$$n = \frac{2G(t_2 - t_1)}{1-(L_2/L_1)}. \tag{1.34}$$

Knowledge, therefore, of n, η_{int}, and G would pave the way to calculate the B coefficient from $B = \eta_{int}G/n^2$, which in turn leads to the determination of the remaining coefficients, A and C.

Because of the cubic dependence, the Auger recombination would become relatively more effective at very high injection levels, such as those experienced in lasers, particularly in small-bandgap semiconductors. Having larger bandgaps reduces the Auger recombination rate in nitride semiconductors, which should inherently be the case (Equation 1.29). Still, the carrier leakage/loss issue, which causes the efficiency droop at high injection levels, particularly for green LEDs, would have to be addressed satisfactorily.

Another issue with the external quantum efficiency is that the external quantum efficiency drops sharply for wavelengths shorter than 360 nm [127], as shown in Figure 1.61. Typically, two reasons are thought to be responsible for the efficiency roll-off at longer peak wavelengths. First, a reduced crystal quality is expected for structures with higher In content as it is necessary to lower the bandgap of $Ga_xIn_{1-x}N$. Second, a higher piezoelectric field for $Ga_xIn_{1-x}N$ layers that are more highly strained with higher In content leads to a stronger separation of the electron and hole wave functions. On the shorter wavelength portion of the spectrum, the roll-off

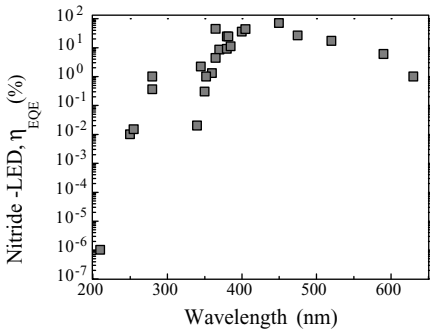

Figure 1.61 External quantum efficiency of GaN-based LEDs. Courtesy of H. Amano.

is associated with reduced localization due to relatively low In mole fraction. If and when the defect concentration in GaN is substantially reduced, for example, when inexpensive bulk GaN substrates are available, one can discern whether InGaN is inherently more efficient in radiative recombination. How to improve the external quantum efficiency without significantly increasing the processing costs is still a challenging problem.

1.13
Monochrome Applications of LEDs

LEDs have already penetrated many monochrome applications. Among the most notable is the traffic light [128], a schematic of which is shown in Figure 1.62. Estimates are that a 12 in traffic light in the United States usually employs a 135 W long-life light bulb in combination with a red, yellow, or green filter. The most advanced LED based red varieties use 12–18 LEDs per traffic light and consume a total of about 14 W, which will slide downward with time, including power supply losses. A single-LED traffic light sells for about $110 compared with a $30 cost of an incandescent variety. The operating cost for electricity is approximately $10 per year for the LED variety compared with $90 for the incandescent model, and LED model pays for installation costs in less than 1 year, not to mention the long operating lifetime of the LED further reduces maintenance and emergency repair costs. By some estimates, there are some 10 M red/yellow/green traffic lights in the United States consuming approximately 400 MW. On an average, red lights are lit 65% of the time, 90% in the case of red arrows. Just converting all red lights to LEDs would

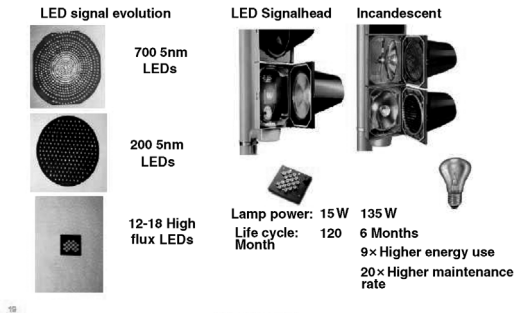

Figure 1.62 Evolution of LED-based traffic signals and a comparison of LED to incandescent traffic lights. Incandescent bulbs consume 135 W and must be replaced every 6 months. The LED alternatives, on the other hand, consume 15 W and would have to be replaced only every 120 months (2002 figures). Using red traffic lights as an example, because of their priority, the number of LEDs for each traffic light went down from 700 per traffic light in 1993 to 12–18 in 2003. The latest LED count is similar to the improvement experienced for green-LED-based traffic lights over the years. Courtesy of Lumileds/Philips. (Please find a color version of this figure on the color tables.)

reduce the US electricity consumption by approximately 250 MW. This would nearly double with green LED insertion.

All large buildings with public access must have lighted emergency signs assisting in evacuation during emergencies such as power failure. These "Exit" signs are designed with two incandescent or compact fluorescent lamps consuming 15–30 W. Using approximately 100 inexpensive LEDs (the number of LEDs needed declines with improved brightness) is comparable in cost to the conventional variety but uses only 5 W, saving somewhere between $10 and $25 in annual electricity cost per sign, while reducing the size and cost of the stand-by battery [128].

As mentioned in Section 1.8, LEDs started to be used on the taillight of cars shortly after the center high mount stop lights (CHMSL) was made a mandatory feature in the United States in 1982. As of 1999, LEDs have reached a penetration of 30–40% of those cars equipped with a CHMSL. In the model year 2000, the first rear combination lights (taillight, brake light, and turn indicator light) emerged as LEDs on high-end models in the United States and Europe. Other functions such as side markers and front turn indicators followed shortly thereafter. Shallow design that does not protrude into the trunk, styling freedom, reduced warranty cost, and reduced power consumption are among the reasons for preferring LED insertion. It is only a matter of time before the red taillights will fully convert from incandescent lighting to LEDs, with the yellow front beam indicators following in their footsteps. This will eventually give way to conversion of the white backup, license plate lights, background dashboard illumination. Estimates are that the average car will contain 1000 lm of LED flux, or even more: 300 red, 300 yellow, and 400 white. Operating these LED chips at $100\,\mathrm{A\,cm^{-2}}$ will require about $20\,\mathrm{mm^2}$ of LED material per car. The conversion of the passenger car market from incandescent lighting to LEDs is quite sensitive to the cost differential. However, the truck and bus market is less cost sensitive and failed taillights require an immediate repair. As a result, the US truck market made a quick and nearly complete conversion of incandescent to LEDs several years ago. The very high brightness white LEDs are already beginning to replace conventional automotive headlamps in luxury model, which will definably segue into the other models in time. Halogen (55 W) and high-intensity discharge (HID) (35 W) lamps, which are the conventional automotive lamps, can be replaced by several thin-film flip-chip LEDs (~12–44 W). Moreover, the use of LEDs not only allows a more compact auto headlamp design but also a precisely defined emitting area owing to sharper far-field radiation patterns, which improve visibility while reducing glare for the oncoming traffic [100] (Figure 1.63).

Decorative lighting is an area where not only savings occur but also the design flexibility is gained, with the use of LEDs. For example, multicolor landscape lighting with programmable and decorative color might someday soon be very popular. There are other applications as well, for example, the Australian branch of the McDonald's restaurant chain started to outline the rooflines of its buildings with a chain of red LEDs. LEDs are significantly more energy efficient than the competing neon technology. Red LEDs are already at cost parity with neon lights and expectations are that similar cost parity will emerge for yellow, green, and blue LEDs in the not so distant future. There are three major groups of commercial enterprises that are

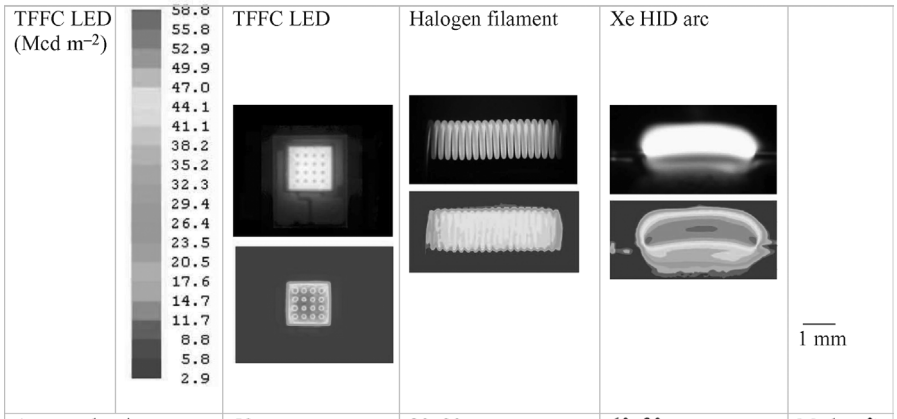

Average luminance	50	20–30	60–80	Mcd m^{-2})
Flux out (power in)	158 (<4) each	1500 (55)	3400 (35)	lm(W)
Flux on road (%)	90–130 each (~60–80%)	400–600 (~25–40%)	800–1000 (~25–40%)	lm

Figure 1.63 Comparison of a thin-film flip-chip (TFFC) white LED to conventional halogen and HID lamps used for low-beam automotive forward lighting (headlight) applications. The top row is the lit visual image each of the three technologies compared. The lower top row represents the color-scaled luminance image. The scales for the halogen filament and HID arc are the same. The scale for the LED is different and is indicated at the left. The table lists average luminance, source flux, input power, and useful flux (utilization percentage) in the application. Courtesy of Lumileds/Philips. (Please find a color version of this figure on the color tables.)

interested in decorative lighting: fast food chains, gas stations, and hotels. It is a form of advertising and presentation, and all these groups wish to get the attention of potential customers driving by.

Other target applications for LEDs are the large outdoor video screens and changeable displays for advertising. For instance, a 600 m^2 video screen uses 3 million 5 mm LEDs. The LEDs are arranged in end-stackable tiles. The LED density is one lamp per 2 cm^2 of board space. The 5 mm lamp itself has a cross section of 0.2 cm^2, thus leaving 90% of the space empty. The LED is the technology of choice for large video screens because it is the technology with the lowest cost for the empty space between the pixels, basically, the cost of a two-sided printed circuit board, which is far less than any glass-based display technology. Additionally, LEDs are directly viewed and unfiltered, which makes LEDs more competitive than other display technologies, an advantage that is more appealing when it comes to monochrome applications. In these cases, there are no color-mixing losses for the LEDs, but there are additional filtering losses for incandescent lamps.[2)]

2) Variability in efficiency of the color filters used to produce various colors is of special interest. For example, the filter used in a red traffic light absorbs 90% of the white light. Roughly, the same is true for blue filters. However, the red filter of an automobile taillight has a wider transmission band and results in an orange–red color. Yellow and green filters are fairly efficient and transmit a large fraction of the white spectrum. LEDs are inherently monochrome and do not suffer from filtering losses, as they do not need them.

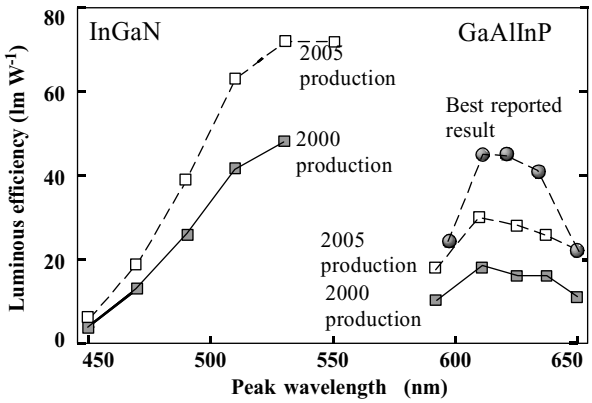

Figure 1.64 LED efficiency at 85 °C junction temperature as a function of wavelength for the two dominant material systems (GaAlInP and AlGaInN). The best estimate for year 2005 production is also shown, which has been met since then, if not exceeded.

LEDs of reasonable efficiencies span almost the entire visible spectrum, with the exception of a narrow window in the yellow–green, paving the way for white-light sources. The improvements in materials quality and device design and packaging have led to LED efficiencies (in photometric terms ($\mathrm{lm\,W^{-1}}$)) at 85 °C junction temperature, which is shown in Figure 1.64. The efficiency of the GaAlInP material system (from red to amber) follows the luminous efficacy response. The same is true, albeit with lower efficiencies for the InGaN system. The long-wavelength end for the InGaN system (amber/yellow) and the short-wavelength end for the AlGaInP system fall short of the luminous efficacy curve.

As shown in Table 1.3, LED efficiencies exceed those of filtered incandescent lamps by a large margin over the entire visible wavelength range except for yellow, where the two technologies are close to parity .

1.14
Luminescence Conversion and White-Light Generation with Nitride LEDs

Availability of violet and blue compact LED emitters has paved the way for alternative approaches to generate blue, green, and red primary colors. A blue or a violet LED can be used to pump a medium containing the desired color centers, dyes in organic and phosphors in inorganic materials, to generate the color(s) desired including white. For white LEDs to be accepted for indoor illumination, the CRI, see Section 1.14.2, must conform to the CIE standards. While the color temperature requirements can be met with phosphor-pumped LEDs, the strict CRI as well as the very high luminous efficacy is nearly impossible to meet. The former is due to very close adherence to produce the Planckian spectrum and the latter is due to the Stokes shift (loss in this

Table 1.3 LED efficiencies in broad color ranges as compared to those of filtered long-life incandescent lamps.

Color[a]	Filtered long-life incandescent efficiency (lm W^{-1})	Year 2000 LED production (lm W^{-1})	Year 2006 (lm W^{-1})
Red (627 nm)	1–6	16	58 (LumiLED's K2 @350 mA)
Yellow (580 nm)	4–8	10	40 (Cree's Xlamp @350 mA)
Green (528 nm)	3–10	48	110 (Osram's Golden Dragon @100 mA
Blue (470 nm)	1–4	13 at low drive I	20 (Osram's Golden Dragon @100 mA)
White	12	20	100 (developmental, Cree/Nichia @20 mA)[b]

For nitride LED, see the results for high-current operation [128]. The lifetime is defined as the time when a reduction to 70% of the original flux is reached. The data from LumiLEDs are associated with its K2 emitter; data from Cree are represented by the Xlamp3 7090 and from Nichia by the i-LED, which emit at red, yellow, and white, respectively. None of the three companies produce a violet (400–420 nm) LED commercially (Table 1.2).

[a]Wavelengths above for the year 2006 LEDs indicated.

[b]LED lamps with above 75 lm W^{-1} are seen to be commercially available in 2006 and are produced by Cree, Lumileds, and Nichia. Values of 100 lm W^{-1} are beginning to appear. These high flux lamps feature in some cases photonic crystals for top mount and darkened emitting surface for flip-chip mount varieties.

case) associated with phosphor downconversion. LED bandwidth and in particular the wavelength of emission in the multiple-color LED approach must be precisely controlled, which is very stringent, as will be discussed soon.

With broad bandwidth associated with green LEDs (in addition to the much reduced power available in the so-called green gap) and to a lesser extent for blue LEDs, it may not be quite feasible for a while to use a three- or four-LED approach to achieve white light meeting the CIE indoor illumination standards. If so, an inexpensive and attainable method for white-light generation may be to pump tricolor phosphors, which are known to have sharp emission linewidths, with LEDs. Alternatively, a blue source could pump two-color or three-color phosphors for white-light generation. However, if one were to limit the phosphors to what has traditionally been available, one needs deep UV LEDs with high power (which would not lead to high luminous efficacy because of losses associated with Stokes shift during down-conversion) or develop efficient phosphors that can be excited efficiently with blue LEDs then the less desirable UV LED approach that is accessible by the GaN system. The phosphors that can be pumped by GaN-based LEDs are under development and seem to be progressing well. When LED-based white light with very good CRIs (in the 90 percentile) is achieved, some estimates are that LEDs will be direct replacement for point sources such as incandescent lamps, while OLEDs might eventually replace area sources such as fluorescent lamps for back illumination although LEDs have captured this market in at least the mobile devices where brightness is a key issue.

Both LEDs and OLEDs have been under development for special segments of the illumination/display markets.

Solid-state lighting based on inorganic LEDs has the potential to fundamentally change the nature of lighting that human kind has experienced over the last century [129]. Since the introduction of the incandescent lamp in 1879, there has been a drive for brighter, cheaper, smaller, and more reliable light sources. In the United States, about 30% of all generated electricity is used for lighting, with about 40% of this being incandescent lighting and 60% being fluorescent lighting. This is representative of the global trend; consequently, significant improvements in lighting efficiency would have a major impact on worldwide energy consumption. Unfortunately, none of the conventional light sources (incandescent, halogen, and fluorescent) have improved significantly in the past several decades in terms of efficiency. Because an average of about 70% of the energy consumed by these conventional light sources is wasted as heat, which in many cases ends up only increasing the cooling required and consuming additional energy in the process, there is clearly room for improvement. With increasing demand and declining reserves for natural means of generating energy, such as gas and fossil fuel, the future for efficient solid-state lighting is very bright indeed, despite commercial interests and policy makers' infatuation with Hg containing compact fluorescent bulbs.

The relatively recent developments in LEDs, in terms of range of wavelengths, efficiency, and lifetime, are proving to have significant impact in the low-flux lighting technology, with the projection that the same will also be true for general lighting. In this fluidic environment, it may be that lighting applications may even encompass lasers, particularly vertical cavity surface emitting lasers (VCSELs) when developed in conjunction with phosphors. VCSELs emit light perpendicular to the p–n-junction plane, as compared to emission in the plane of the junction for edge emitters, and provide wall-plug efficiencies as high as 50%, albeit at 850 nm [130]. As far as nitrides are concerned, current injection VCSELs are not yet available, but its forbearer, the optically pumped variety operating at the near-UV wavelength of 384 nm, has been reported [131].[3)]

With SSL, anticipated improvements to the quality of white lighting for general illumination include steady output color at all levels of illumination, ability to continuously vary output color, simplified and flexible design for mounting and fixtures, ease of integration, advanced building controls including daylighting, and low-voltage and *safe* power distribution. Developments of efficient and reliable blue and green LEDs using nitride-based alloys are significant for the realization of efficient white-light LEDs with excellent quality (high color rendering index).

1.14.1
Color as Related to White-Light LEDs

In order for LEDs to be used for general lighting, it is imperative that they have appropriate white color with good color rendering characteristics when illuminating objects. Needless to say, color rendering and efficacy represent the two most

3) Low temperature injection VCSELs have been reported during the interim period.

important criteria for light sources used for general lighting. The US Energy Policy Act (EPACT 1992 [132]) specifies the minimum color rendering indices, which are discussed in the next section, and the minimum efficacy for common lamps.

Color rendering depends solely on the spectrum of the source. Thus, the white-light spectrum generated from LEDs needs to meet requirements of efficacy and color rendering. Desirable color rendering is best achieved by broadband spectra distributed throughout the visible region, uniformly as perceived by eye. However, the efficacy is best achieved by a monochromatic radiation at 555 nm (green), the wavelength where the human eye response reaches its maximum for daylight vision as discussed in Section 1.6. To a first extent, it appears that there is a trade-off between the two important criteria for white light: high-quality color rendering and high efficacy. For example, a low-pressure sodium lamp used in some highways and parking lots, having a light orange color, has an efficacy of about 200 lm W^{-1}, which is the highest among the available discharge lamps, but colors of objects are not distinguishable. Objects such as a red car not having orange pigments would appear gray. However, a xenon arc lamp, having a very similar spectrum as daylight and exhibiting excellent color rendering, has an efficacy of only 30 lm W^{-1}.

The evaluation method for color rendering of light sources is well established by CIE, and since 1965, the color rendering index [133] has been widely used in the lighting industry.

A succinct description of the fundamentals of the CIE colorimetric system [36] including the color rendering index is given along with a discussion of applications to white-light generation. The definitions of the terms in photometry and colorimetry used in this section follow those found in Ref. [134]. For further details of colorimetry, an overview of the CIE system of colorimetry is available in an article by Ohno [135].

1.14.2
Color Rendering Index

Color rendering of a light source is characterized by comparing the appearance of various object colors under illumination by the particular light source versus that under reference illumination, daylight for correlated color temperature (CCT), > 5000 K, and Planckian radiation for correlated color temperature (CCT), < 5000 K. The smaller the color differences of the object colors from those determined under reference source, the better the color rendering. The standardized method, the CRI, is very well outlined by the CIE [133]. In this method, 14 Munsell [136, 137] samples of various colors, spectra for eight are given in Figure 1.65, including several saturated colors, are carefully selected and the color differences, denoted as ΔE_i, of these color samples under the test illumination and under the reference illumination are calculated on the 1964 $W*U*V*$ uniform color space [133]. The process incorporates corrections for chromatic adaptation. Then, the *special color rendering index*, R_i, for each color sample is calculated using $R_i = 100 - 4.6\Delta E_i$. Here, a figure of 100 represents the best color rendering index.

The R_i value is an indication of color rendering for each particular color. The *general color rendering index*, R_a, is given as the average of R_i for the first eight color samples that have medium color saturation. With the maximum value of 100, R_a gives a scale

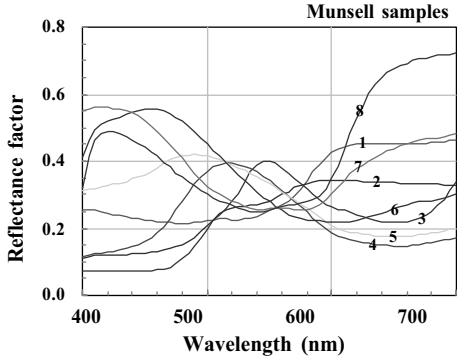

Figure 1.65 Munsell samples spectra for determining the color rendering index. Courtesy of M. E. Coltrin of Sandia National Laboratory. (Please find a color version of this figure on the color tables.)

that matches well with the visual impression of color rendering of illuminated scenes. For example [135], lamps having R_a values greater than 80 may be considered to be high quality and suitable for interior lighting, and R_a values greater than 95 may be suitable for visual inspection purposes. Thus, the spectral distribution of white-light-generating LEDs should be designed to achieve the R_a value required for the application in mind. For comparison with conventional light sources, the CRI values (R_a values) of several common types of fluorescent lamps and HID lamps are tabulated in Table 1.4.

To gain an insight about the extent of color saturation, the LED output is generally indicated on the chromaticity diagram, as depicted in Figure 1.66 (see also Figure 1.20). The oval near the center indicates various grades of "white light." The line

Table 1.4 General CRI of common lamps.

Source type	CCT	General color rendering index (R_a)
Daylight	6430	76
Cool White	4230	64
White	3450	57
Warm white	2940	51
Cool white deluxe	4080	89
Warm white deluxe	2940	73
Metal halide	4220	67
Metal halide, coated	3800	70
Mercury, clear	6410	18
Mercury, coated	3600	49
High-pressure sodium	2100	24
Xenon	5920	94

The first six entries represent various types of incandescent bulbs listed here for comparison [129].

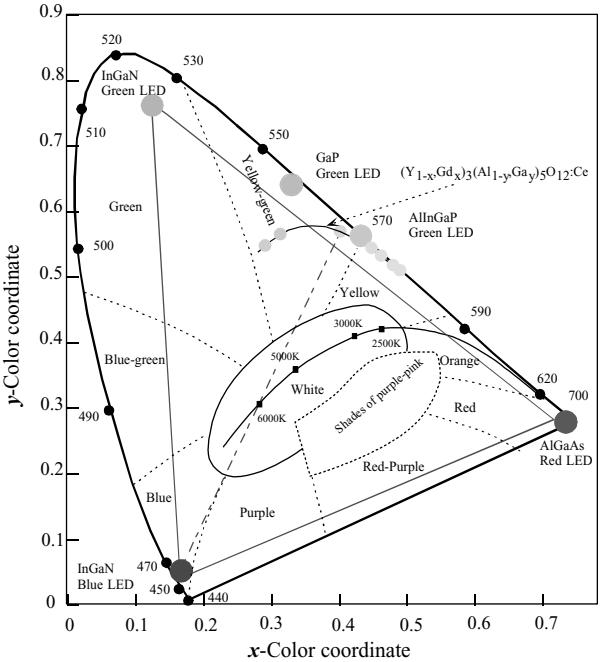

Figure 1.66 The chromaticity diagram along with available commercial LED performance data. Clearly, blue and green InGaN LEDs constitute the two important legs of the triad, the three primary colors that are needed for full-color displays. Moreover, the output of an optically pumped YAG medium doped for yellow emission is shown with data points indicative of various Gd concentrations. The broken line that connects the blue LED to one particular composition of the YAG medium indicates the range of warm white colors that can be obtained. (Please find a color version of this figure on the color tables.)

through the white-light region indicates the color diagram for white light with the accompanying color temperature (Planckian locus). The narrower the output spectrum of an LED, the closer its color is to the outer periphery. As the spectrum gets wider, the corresponding color on the chromaticity diagram is pulled toward the center, reducing the range of colors that can be obtained by the color-mixing scheme. Moreover, the output of a commercially available white LED constructed from a blue InGaN LED overcoated with a yellow light under blue photoexcitation emitting cerium (Ce)-doped yttrium aluminum garnet (YAG:Ce) [$Y_3Al_5O_{12}$:Ce^{3+} (4f′)] inorganic phosphor (YAG) is marked with data points indicative of various Gd concentrations (see Section 1.15.3).

The blue and red LEDs available commercially are almost saturated while the same cannot yet be said for green ones. The spectral broadening observed for green LEDs is attributed to compositional inhomogeneities, which get larger with increasing InN mole fraction. When used in conjunction with the available red and blue LEDs, present InGaN green LEDs provide the means for achieving some 70–80% of all the color possible.

1.15
Approaches to White-Light Generation

An advantage of LEDs is that they are available in most wavelengths in the visible region of the electromagnetic spectrum, and the output spectrum from LEDs may be more flexible than that for the traditional discharge light sources whose output spectra depend on available phosphors and emissions from gas. In the case of multiple-chip LEDs, white light can be achieved by a mixture of one or more LEDs, with the aid of phosphors when needed, with different emission wavelengths. Combining the spectra from three-LED, particularly, four-LED chips could provide the best color rendering index, making the multicolor approach quite acceptable for general lighting. But the downside of this approach, in addition to the cost, is that it requires absolute control over the wavelengths of all the LEDs, relative power levels, and also the spectral width of emission. For example, in the four-LED approach, the relative intensities provided by blue, green, yellow, and red LEDs would have to be 14, 23, 22, and 41%, respectively, for a color rendering index in the high 90 percentile range. The red color power needs to be the highest because of the much reduced eye sensitivity to red color.

The width of the emission spectra and the control of the emission wavelength that are available from many of the LEDs may not be sufficiently narrow in many cases when the wavelength accuracy to a fraction of a nanometer and bandwidth to a nanometer might be needed. White light generated by LED/phosphor combination is the least expensive and can also have reasonable color rendering (in the 70 percentile range) because the phosphors generally produce broadband radiation. Let us delve into generation of white light using what is dubbed the SSL-LEDs suitable for high-quality general illumination.

To summarize, for a CCT of 3000 K CRI values of 85, 97, and 99 can be obtained with three-, four-, and five-LED approaches, respectively. It should be noted, however, that there is a trade-off between the color rendering index and luminous efficacy in that the higher the color rendering index desired the lower the efficacy. This means that while the approaches with more color sources provide better color rendering index, the efficacy is lower. In addition, to attain very high color rendering index, wavelength accuracy to a fraction of nanometers and linewidths of about 1 nm are required. The narrower linewidths give slightly better luminous efficacy without a penalty in CRI.

1.15.1
White Light from Three-Chip LEDs

The three primary colors, red, green, and blue with identical intensities perceived by the eye, can be mixed together to generate white light. With currently available LEDs, the generation of white light can have luminous efficacies of approximately $45\,\mathrm{lm\,W^{-1}}$. An example of a white-light spectrum produced by combining the outputs from a three-color multiple LED is shown in Figure 1.67. Note that because the human eye's reduced response to the red color, the intensity of the red color LED

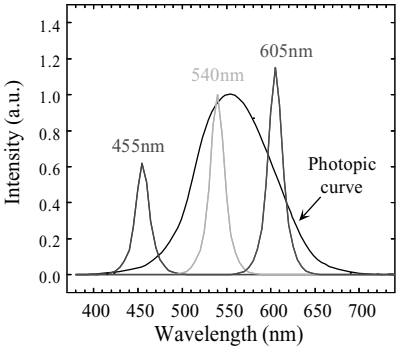

Figure 1.67 White-light output emission spectrum from a three-color multichip LED. Courtesy of M. E. Coltrin of Sandia National Laboratory. (Please find a color version of this figure on the color tables.)

must be higher to generate white light with acceptable color rendering index. LED-based white-light sources have been in commercial production and consist of collectively housed LED chips, or arrays of different colored LED lamps, that is, multiple-chip LEDs. This three-color approach is a potentially very efficient, high-quality white lighting approach, but the cost is expected to be high as it involves InGaN and AlInGaP technologies with each LED requiring different drives.

This particular approach has a few problems. The perceived color may change with viewing angle due to the discrete wavelengths of light used. Multiple-LED chip requirements make this approach relatively expensive. Obtaining a consistent color across an array of such white pixels could also be a source of problem because the light intensity of LEDs and driving voltages tend to vary from diode to diode, and color-tuning individual diodes is likely to be difficult. Temperature dependence of wavelength shift for each of the three diodes used may be different, causing color variation with temperature. Another consideration is the variation in operating life and/or degradation rate of different color LEDs. Because the intensity variations also lead to overall color change, uneven degradation of the three LEDs would lead to color change over time. For example, the light output level of AlGaAs-based LEDs is found to decrease by about 50% after 15 000–40 000 h of operation. This effect represents a serious challenge for multiple-chip LEDs where the white-light color rendering is critically dependent on the relative intensities of the separate red, green, and blue colors. However, multichip SSL-LEDs could offer the greatest versatility and the largest efficacies of all the approaches that are discussed here. When and if perfected, these approaches could potentially produce any color and any color temperature with as high a color rendering index as desired. The advantages can be summarized as follows: long-term and the most efficient, dynamic tuning of color temperature, excellent color rendering, and very large range of colors are available. The challenges include the following: vintage 2002 LEDs require color feedback to account for LED degradation with temperature and time (three different color LEDs respond differently), color mixing is somewhat involved, and there may be a little gap in the

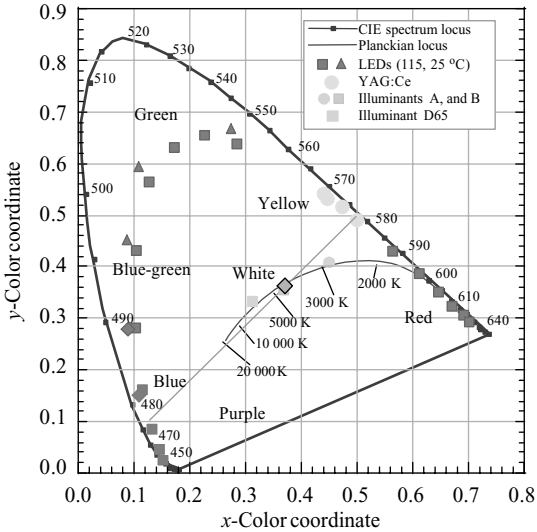

Figure 1.68 Mixture of two LEDs at 485 and 580 nm each with a half-maximum width of 20 nm. The (x, y) chromaticity coordinates of the resulting white light is shown as a solid diamond [129].

yellow–green region. In time, with further advances in LED technology, this issue would be mitigated.

The chromaticity coordinates (x, y), CCT, CRI, and the luminous efficacy of radiation can be calculated if the spectral power distribution of a light source is known [129]. The CRI (R_a) of the white light produced by mixing the outputs from two 20 nm half-bandwidth LEDs shown in Figure 1.68 is calculated to be only about 4, which is very small. Consequently, standard two-chip LEDs with any combination of wavelengths cannot produce white light with an R_a value that is acceptable for general lighting applications. As discussed later in this section, the three-LED chip approach and in particular the four-LED approach (discussed in Section 1.15.2) are capable of producing much better color rendering, but the selection of peak wavelengths is critical in order to produce a CRI acceptable for general lighting. Simulations of three LEDs having peak wavelengths of 450, 550, and 650 nm, with their relative power adjusted to create white light with a color temperature of 4000 K, result in a color rendering index value that is not acceptable. Each LED is modeled using a Gaussian line shape function [138], with a half-bandwidth of 20 nm. In this case, the CRI (R_a) is only 37 with luminous efficacy of 228 lm W^{-1} (theoretical maximum). Again, a value of $R_a = 37$ is not acceptable for use in general lighting, except for limited outdoor use [129].

In terms of the three-LED solution, when the wavelengths of each of the three LEDs in the three-LED chip set are optimized and controlled precisely, general color rendering index can be improved substantially [129]. Figure 1.69 shows the result of a simulation of a three-LED chip set with peak wavelengths of 459.7, 542.4, and 607.3 nm leading to $R_a = 80$ and a luminous efficacy of 400 lm W^{-1}, which represents

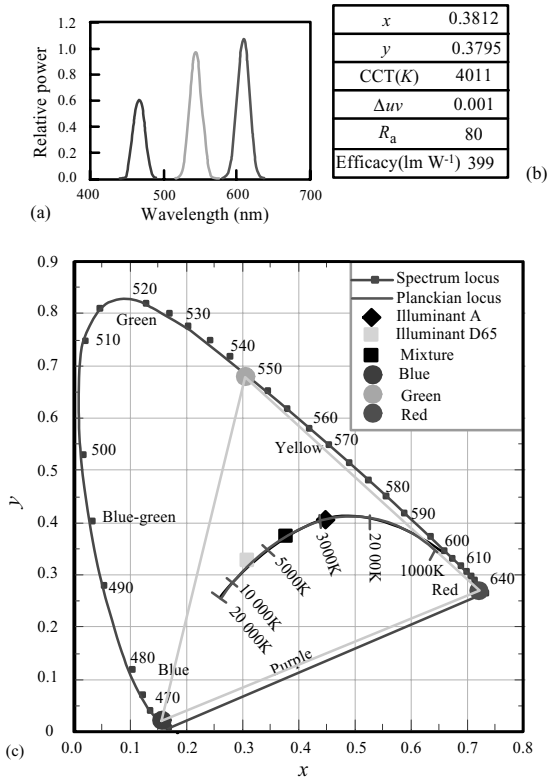

Figure 1.69 The effect of optimizing the wavelengths of a three-chip white-light LED. (a) The spectral response of the three LEDs used for mixture. (b) Correlated color temperature, color rendering index (R_a), efficacy, and (c) the chromaticity coordinates (x, y) for the white light are shown as the solid square near 4000 K. Because of the CRI, R_a of about 80, this is an example of white light with good color rendering [129]. (Please find a color version of this figure on the color tables.)

the theoretical maximum. A 20% LED chip efficiency leads to a total efficacy of 80 lm W^{-1}, comparable to typical fluorescent lamps [129]. This combination is acceptable for general lighting including indoor applications.

Continuing on with the three-LED solution, the LE and CRI values for a wide range of wavelength combinations from GaInN blue and green LEDs and AlGaInP red LED (the trichromatic approach) have also been calculated by Chhajed *et al.* [139] in order to find the best wavelengths for a trichromatic source. These values in the form of contour plots for a trichromatic Gaussian white-light source with linewidth of 5 and 8 kT at 300 K for different wavelength combinations are shown in Figures 1.70 and 1.71. The 5 and 8 kT linewidth examples are shown to make the point how sensitive this approach is to not only the control of the wavelength of sources but also their linewidths. If the linewidth (ΔE) of emission in each LED is assumed to be 5 kT at 300 K, a luminous efficacy of 318 lm W^{-1} and a CRI of 86 with the wavelength

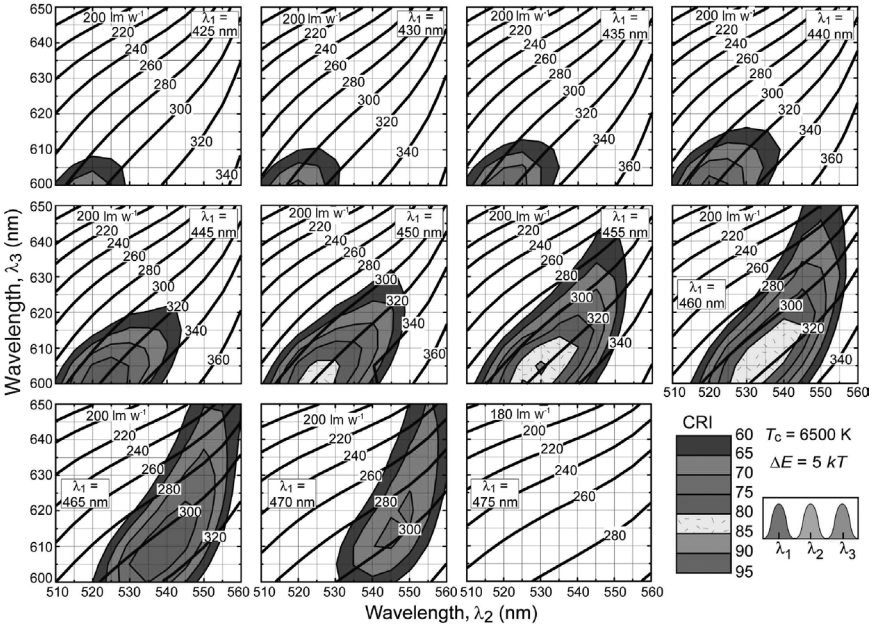

Figure 1.70 Contour plots for LE of radiation and CRI of a trichromatic Gaussian white-light source with linewidth of 5 kT at 300 K for different wavelength combinations. Courtesy of E. F. Schubert [139]. (Please find a color version of this figure on the color tables.)

combination (455, 530, and 605 nm for blue, green, and red, respectively) can be realized. If, however, a light source linewidth of $\Delta E = 8\,\mathrm{kT}$ is assumed, a luminous efficacy of $300\,\mathrm{lm\,W^{-1}}$ and a CRI of 93 can be obtained using the wavelength combination (455, 530, and 610 nm). In addition, the calculation showed a rapid decrease of the CRI value for even small deviations from the optimum wavelengths. Therefore, the control of the high luminous efficacy together with high-CRI white light requires an extremely precise degree of control over the wavelengths and the linewidths of the three LEDs forming the backbone of the trichrome approach.

In reality, however, the efficiency of an LED is different for different wavelengths, and the availability of various wavelength-emitting LEDs is restricted. Despite these restrictions, optimum designs of white-light LEDs with available color LEDs for any desired CCT can be made. A four-LED chip set should give even better color rendering.

Setting difficulties aside, if progress in other approaches is not made, this method may be interesting for producing white light with acceptable color rendering index. First, use of more colors leads to better control of white light with a high color rendering index in addition to being able to obtain millions of colors. Second, photons from each of the LEDs contribute directly to the white-light intensity, eliminating the need for photon conversion media and associated conversion losses.

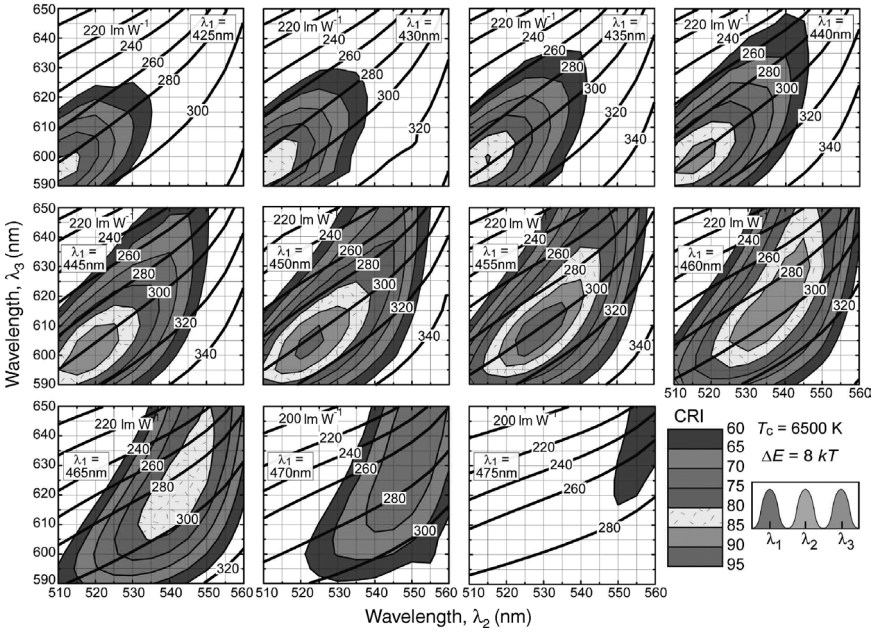

Figure 1.71 Contour plots for LE of radiation and CRI of a trichromatic Gaussian white-light source with linewidth of 8 kT at 300 K for different wavelength combinations. Courtesy of E. F. Schubert [139]. (Please find a color version of this figure on the color tables.)

Third, by changing the relative intensity of the different color LEDs, it is relatively easy to change the color and hue of this kind of light source for different applications. To reiterate, for this method to work well, the separate colors from the individual components must be mixed appropriately to achieve uniform white light keeping human eye response in mind. Substantial effort is required for the multichip solution to achieve over 200 lm W^{-1} white light and a power conversion efficiency of approximately 50% inclusive of color-mixing losses, which is formidable.

Despite the difficulties, consideration of this approach continues to the system level as graphically depicted in Figure 1.72 under a study for the US Department of Energy by Navigant Consulting, Inc. for the year 2005 with projected targets. The diagram assumes a correlated color temperature target of 4100 K (the equivalent CCT of a cool white fluorescent lamp), and a CRI of at least 80. The year 2005 LEDs typically had color temperatures in the range of 5000–6000 K, and usually a lower CRI that assumed. Attaining the stated target values (goals) will require more efficient LEDs across the most efficacious part of the spectrum (particularly green emitters) and greater improvements elsewhere in the system than those indicated.

To reiterate, further complications arise as three or more different color components required have different voltage requirements, degradation characteristics and temperature dependencies both of which would change the color, necessitating

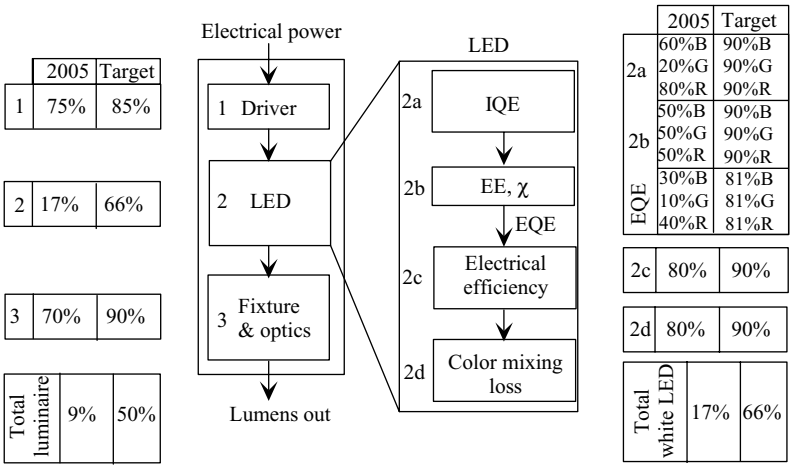

Figure 1.72 The year 2005 and target system efficiencies using the trichrome LED color-mixing approach in which the target assumes a CCT of 4100 K and CRI of 80. The year 2005 CCT and CRI used are 5000–6000 K and 75, respectively. IQE, internal quantum efficiency; χ, extraction efficiency; EQE, external quantum efficiency, which is a product of the internal quantum efficiency and the extraction efficiency; B, G, and R are for blue, green, and red, respectively. Patterned after NGLIA LED Technical Committee report prepared for the US Department of Energy "Solid-State Lighting Research and Development Portfolio," March 2006.

sophisticated control systems. Although on the surface this looks like an approach that could provide very good color rendition, in practice it would be very tricky.

For demonstration purposes, LED solutions to replicate the spectrum of a lighting industry standard CIE D65 illuminant have been developed, in particular by Lumileds/Philips Lighting with the nomenclature of "light box." In all LED approaches, RGB, amber, and white LEDs were used together to reproduce a spectrum closely matching that of the D65 illuminant in the spectral range of 420–650 nm. A correlated color temperature of 6705 K and a color rendering index of $R_a = 96$ have been obtained. The spectra of the D65 standard illuminant and LED set are shown in Figure 1.73.

In short, this method requires narrow FWHMs from each of the three LEDs, which are not available with nitride LEDs, particularly green, yet. The voltage requirements for the three LEDs are widely different, making the control system complicated. Furthermore, the aging characteristics for each of the three LEDs may be different. Consequently, a single UV LED pumping a tricolor phosphor option is preferable providing that phosphors for two or three primary colors, which can be efficiently pumped by a near UV or blue GaN LED, can be developed. Good progress is being made along these lines both on the LED front and on the phosphor front.

1.15.2
White Light from Four-Chip LEDs

It is clear by now that the higher the number of LEDs employed, the better the color rendering index and/or the luminous efficacy as they are related. Let us now discuss

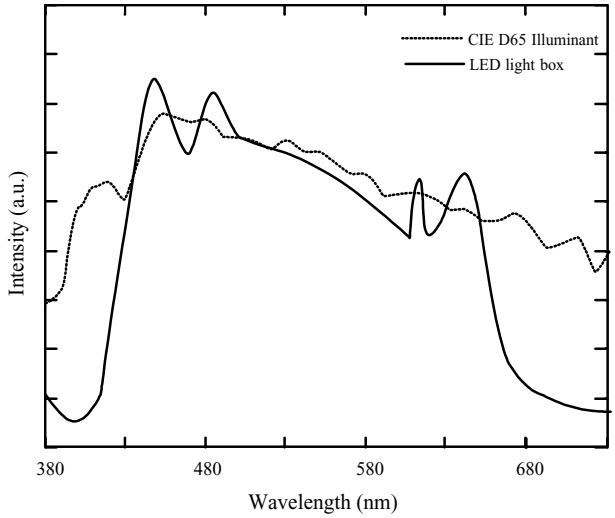

Figure 1.73 Spectra of the CIE standard D65 illuminant and RGB, amber, and white LED set showing good representation in terms of the correlated color temperature (6705 K) and a color rendering index of $R_a = 96$. Courtesy of Lumileds/Philips.

the four-LED approach for white-light generation as shown in Figure 1.74a. Also shown, Figure 1.74b, are the wavelengths of four LEDs required for a range of luminous efficacy and CRI combinations covered in Figure 1.74a.

As Figure 1.74a indicates, the maximum luminous efficacy drops with increasing CRI as expected. Also, 408 lm W^{-1} is the maximum luminous efficacy that can be expected for a four-color SSL with CRI = 90 (assuming 100% wall-plug efficiency for

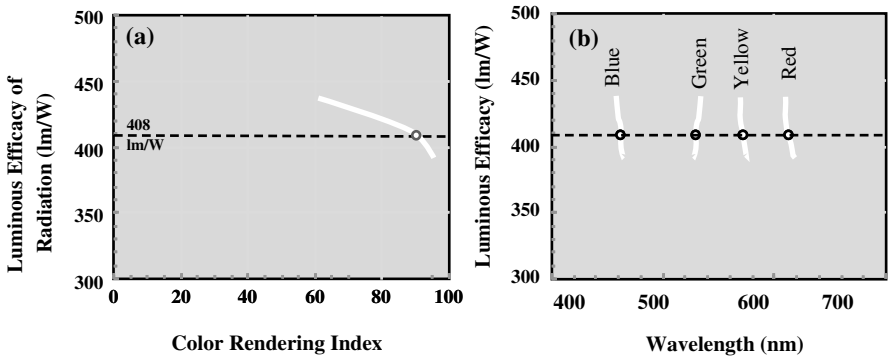

Figure 1.74 The luminous efficacy and color rendering index compromise (a) and the wavelength requirements for each of the four LEDs (b). Courtesy of M. E. Coltrin, Sandia National Laboratories.

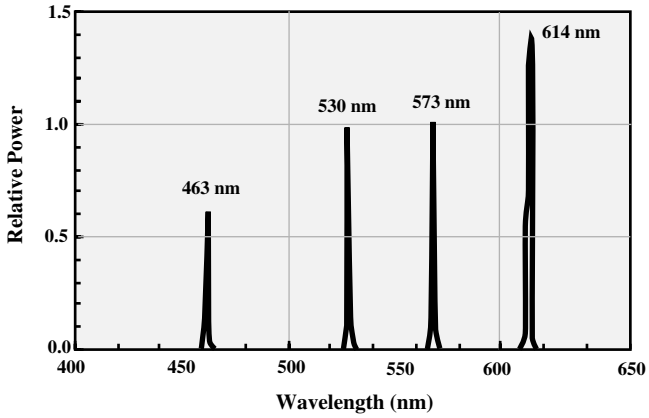

Figure 1.75 The wavelengths and relative power levels required from each of the LEDs for the four-LED white-light generation with high color rendering index and luminous efficacy. Courtesy of M. E. Coltrin, Sandia National Laboratories.

semiconductor sources). The wavelengths required for the blue, green, yellow, and red LED sources in this scheme are 463 nm (B), 530 nm (G), 573 nm (Y), and 614 nm (R), as shown in Figure 1.75, with the relative required power level from each LED. Small differences in the wavelength of LED source can result in large changes in power fractions needed from each of the four LEDs. For example, for a CRI of 60, the power fractions for green and yellow need to be 15% (G) and 33% (Y). Increasing the CRI to 90 changes the power fractions to 23% (G) and 22% (Y).

Clearly the wavelengths of the four LEDs are widely spaced across the visible wavelengths, 463 nm (B), 530 nm (G), 573 nm (Y), and 614 nm (R). In addition, the relative watt fractions for the LEDs are as follows: B, 14%; G, 23%; Y, 22%; and R, 41%. Such a premium demand on the red LED is due to the lackluster eye response to that particular color. Furthermore, the linewidths required are very narrow compared to the broadly varying Munsell samples (basis of CRI). The 1 nm linewidths (or 20 nm linewidths characteristic of LEDs) are nearly "δ-functions" as compared to the Munsell sample spectra shown in Figure 1.65.

The red wavelength is very important in the white-light generation in that shorter wavelengths improve luminous efficacy, as they are closer to peak eye sensitivity. However, a CRI of 90 is impossible for red LED wavelength $\lambda < 615$ nm, as shown in Figure 1.76. Conversely, the longer wavelength improves CRI, but a luminous efficacy $>286\,\mathrm{lm\,W^{-1}}$ is impossible for $\lambda > 654$ nm. If 100% efficient primary semiconductor LED sources are assumed, the 614 nm red corresponds to an efficacy of $408\,\mathrm{lm\,W^{-1}}$, and 654 nm corresponds to an efficacy of $286\,\mathrm{lm\,W^{-1}}$. If a more realistic 70% efficient primary semiconductor source is assumed, the 615 nm red is needed to reach an efficacy of $286\,\mathrm{lm\,W^{-1}}$, but the AlInGaP efficiency drops as λ gets shorter. We should mention that attaining blue, green, and yellow at >70% efficiency is a challenge, particularly the green.

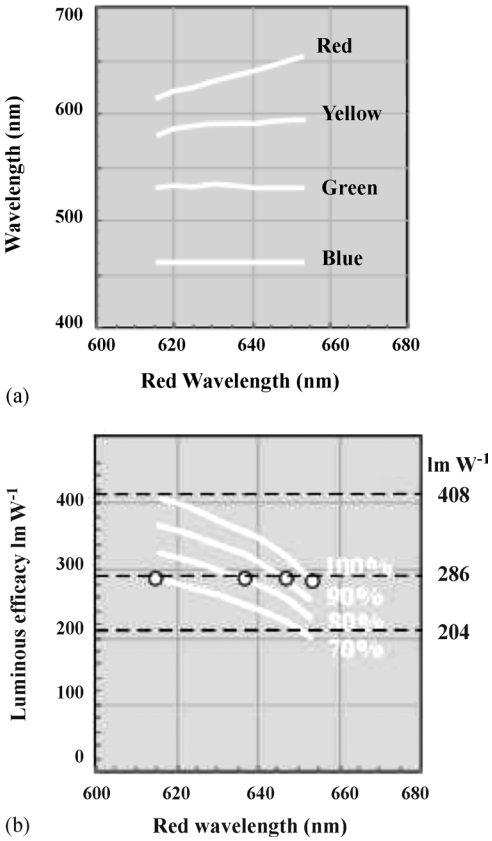

Figure 1.76 The sharp dependence of luminous efficacy on the wavelength of the red LED used in the four-color LED approach to white-light generation for a CRI of 90 and CCT of 3000 K. Courtesy of M. E. Coltrin, Sandia National Laboratories.

1.15.3
Combining LEDs and Phosphor(s)

This method for white-light generation from multiple-chip LEDs involves the use of one or more phosphors, such as the combined use of a blue LED and a yellow phosphor, which represents the least expensive solution and has seen considerable activity. This method is favored in that the technology already exists, is low cost, and requires small space. Already cool white with a color temperature of 5500 K and CRI of 70, and warm white with a color temperature of 3200 K and CRI of 90 have been reported to be available.

In the approach called the RG_GB, the red and blue primary semiconductor sources are used in conjunction with a green phosphor pumped by blue. An efficiency of 95%

is assumed for the green phosphor (less the 15.4% Stokes loss), which is a very challenging goal. Narrower ranges of red wavelengths can be used with efficiencies of 80% (615 nm red) or 90% (626 nm red) to reach 286 lm W^{-1}. Broad linewidths are needed for the green phosphor (50–75 nm) as the red wavelength increases; the CRI improves to makeup for the "missing" short-wavelength red. The broad green phosphor used in this approach replaces the green and yellow LEDs in the four-LED approach.

In the R_RG_GB approach, the blue primary semiconductor source is used to pump the green and red phosphors. An efficiency of 95% is typically assumed for both phosphors with Stokes losses: 24.2% (red) and 15.4% (green). Owing to the properties of the red phosphor, a very narrow range of red wavelengths is allowed for >286 lm W^{-1}. However, one needs a blue efficiency of 90% (if 615 nm red is used) or 100% (if 625 nm red is used) to reach the 286 lm W^{-1} luminous efficacy mark. The broad linewidths are needed for green phosphor (50–70 nm) as red wavelength increases. Narrow linewidths (1–20 nm) are needed for red phosphor pumped by blue. The irony is that no phosphor system meeting these specifications is available with developments reportedly in place. Figure 1.77 shows the interrelationship between the linewidth, wavelength, and luminous efficacy, underscoring again the importance of the red wavelength. We discuss the details, particularly in terms of the phosphors, later in this section following the discussion of the BY_Y approach in which a blue LED source is used to pump a yellow phosphor.

A more simplified approach wherein a blue LED source is used to pump a yellow phosphor (as opposed to green and red phosphors shown in Figure 1.77), termed the BY_Y approach, has gained considerable interest despite its low color rendering index for outdoor lighting in particular. Commercially available white LEDs are constructed from a blue InGaN LED overcoated with a yellow light emitting (under blue photoexcitation) cerium (Ce)-doped yttrium aluminum garnet (YAG:Ce) [$Y_3Al_5O_{12}$:Ce^{3+} (4f′)] inorganic phosphor. These are called the white pcLEDs. In this approach, the InGaN LED generates blue light at a peak wavelength of about 460–470 nm, which excites the trivalent cerium Ce^{3+}:YAG phosphor that emits pale-yellow light, centered at about 580 nm with a full-width-at-half-maximum linewidth of 160 nm.

The combination of the blue light from the LED, which is transmitted through the phosphor, and the pale-yellow light from the Ce^{3+}:YAG results in soft white light with a color temperature of, for example, 4600 K, as shown in Figure 1.78 for several drive currents. The emission spectrum of the YAG phosphor can be modified (tuned) by substituting some or all the yttrium sites with other RE elements such as gadolinium (Gd) or terbium (Tb). The RE^{3+}:YAG emission and absorption spectrum can be further engineered by replacing some or all of the aluminum sites by gallium. Instead of illuminating inorganic phosphors such as RE^{3+}:YAG, the blue-light emission from the InGaN LED can also be used to generate luminescence from organic polymers that are coated on the domed epoxy encapsulate of an InGaN LED lamp, but this approach has not made it to the marketplace yet and may never do so, owing to the success of the approach using solid phosphors.

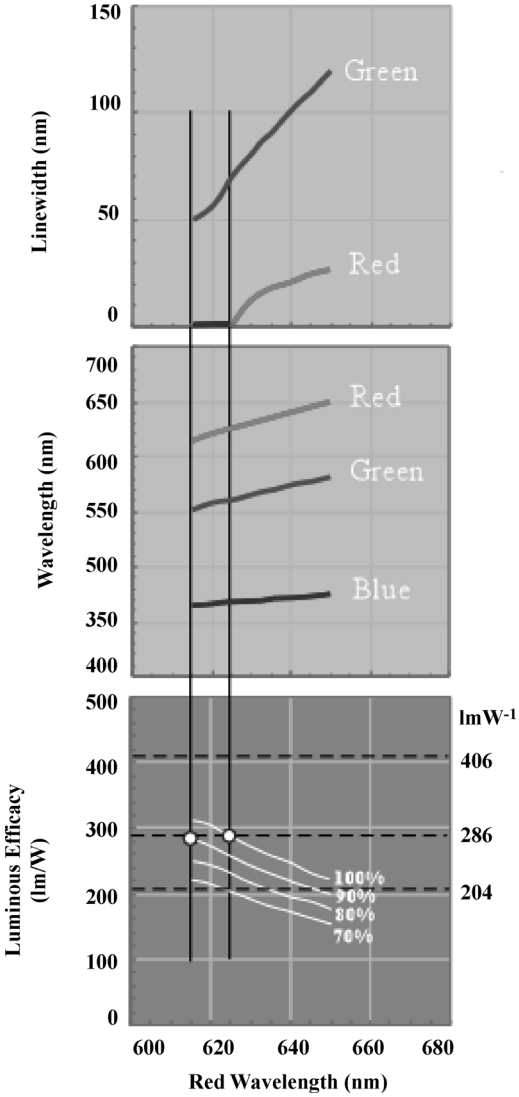

Figure 1.77 The relationship between the linewidth (top), wavelength (center), and luminous efficacy (bottom) in the BG_CR_R approach wherein a blue LED source with a halfwidth of 1 nm is used to pump green and red phosphors to achieve white light. Courtesy of M. E. Coltrin, Sandia National Laboratories. (Please find a color version of this figure on the color tables.)

The efficacy of the properly packaged (for heat removal as well as light extraction) production of phosphor-white LEDs was around 60 lm W^{-1} with half lifetimes of 100 000 h in the year 2005 (the figures improved considerably by a factor of nearly 3 for efficacy by the year 2008). When compared to multiple-chip LEDs for red, green,

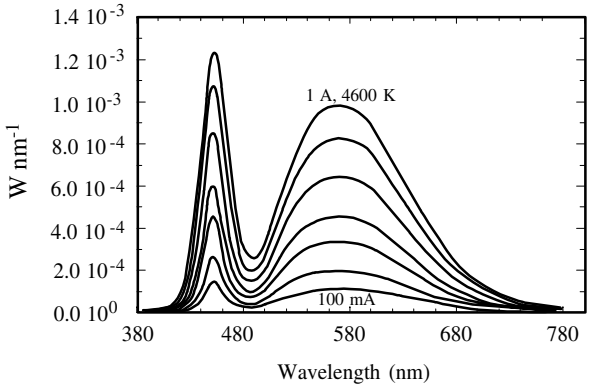

Figure 1.78 Emission spectrum of a white single-phosphor conversion LED, pcLED, (blue + YAG:Ce) showing the blue peak of light leaking through the phosphor and the broader yellow peak from the phosphor. In a well-designed pcLED, the spectrum changes negligibly with drive current. The color temperature (CCT) stays at 4600 K perfectly dimmable. Courtesy of Lumileds/ Philips.

and blue color outputs, an advantage of the phosphor-white or hybrid-white phosphor conversion LED is that it only requires one blue LED (or ultraviolet, in which case the blue light must be emitted by another phosphor which would lower the efficiency). Also, conversion efficiencies of about 90% are possible in inorganic YAG-based converters without the bounds imposed on the active layer composition. In addition, white-light LEDs based on phosphors have been shown to be relatively insensitive to temperature, which is very desirable.

While simple, there are several technological problems with this approach, at least with early designs. Among them is a halo effect of blue/yellow color separation due to the different emission characteristics of the LED (directional) and the phosphor (isotropic). Moreover, as mentioned above, the color rendering index is low, only about 75–85 for the cool white, and broad color "bins" are necessary to ensure reasonable product yields. Finally, most lamps have color points that do not lie on the blackbody curve, which is undesirable and eventually a color shift from blue to yellow with aging and variation in drive current is noted. In addition to the aforementioned challenges that mainly deal with the excitation source, there are other challenges associated with the phosphor material.

White pcLEDs with blue LED and yellow phosphor for solid-state illumination have seen considerable advances of late, so much so that they are beginning to be competitive in some areas of not so stringent lighting. We already displayed the emission spectra of the yellow phosphor and blue LED combination versus the drive current in Figure 1.78. Note that the wavelength for the LED up to a current drive of 1 A remains unchanged. Shown in Figure 1.79 is the lumen output of a single-chip pcLED together with its efficiency versus drive current under pulsed (duty cycle of 1%) and CW conditions [104]. Color parameters of 4200 K for CCT and 75 for

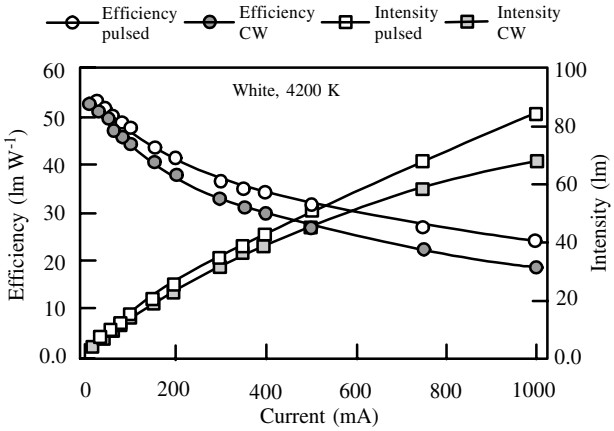

Figure 1.79 Injection current dependence in a white phosphor conversion LED, pcLED, (blue + YAG:Ce) of photometric flux (lm) and luminous efficiency (lm W^{-1}) under 1% duty cycle pulsed and CW (DC) drive have reached values, which surpass incandescent and halogen sources. Courtesy of Lumileds/Philips.

R_a have been obtained. At the nominal operation point of 350 mA (50 A cm^{-2}), more than 32 and 35 lm/device have been achieved. This compares favorably with figures of 6–15 lm W^{-1} offered by incandescent lamps, and 25–30 lm W^{-1} offered by small halogen lamps.

In standard one LED/one phosphor solution (pcLED), the thickness of the yellow phosphor through which the blue LED light travels changes the tint by changing absorption and therefore the yellow emission. This means that the tint depends on the viewing angle for the construct shown in Figure 1.80a. Conformal coating of the LED die with the yellow die shown in Figure 1.80b is designed to mitigate the "tint" change problem. The viewing angle dependence of the normalized CCT, with respect to on axis, for the phosphor slurry method of Figure 1.80a and conformal phosphor coating method of Figure 1.80b is shown in Figure 1.81, where a change of as large as 700 K in the CCT for the slurry case as opposed to 80 K for the conformal coating case is noted.

The flux that can be obtained in the pcLED combination is given as

$$\phi = \eta_{\text{int}} \cdot \eta_{\text{extr}} \cdot \eta_{\nu} \cdot \varepsilon_{0,\text{ph}} \cdot \eta_{\text{QD}} \cdot \eta_{\text{ph}} \cdot \eta_{\text{pkg}} \cdot P, \tag{1.35}$$

where η_{int} is the internal quantum efficiency, η_{extr} is the photon extraction efficiency (% photons extracted per photon generated), η_{ν} is the electrical efficiency (photon energy divided by the injection energy), $\varepsilon_{0,\text{ph}}$ is the luminous efficacy of phosphor/LED combination in terms of lm W^{-1}, η_{QD} is the quantum deficit due to Stokes shift (in terms of %), η_{ph} is the phosphor quantum efficiency, η_{pkg} is the package photon extraction efficiency, and P is the electrical power applied (W). Improvement of the internal quantum efficiency depends on the materials quality and quantum well design. The extraction efficiency depends on the use of generated photons and can be

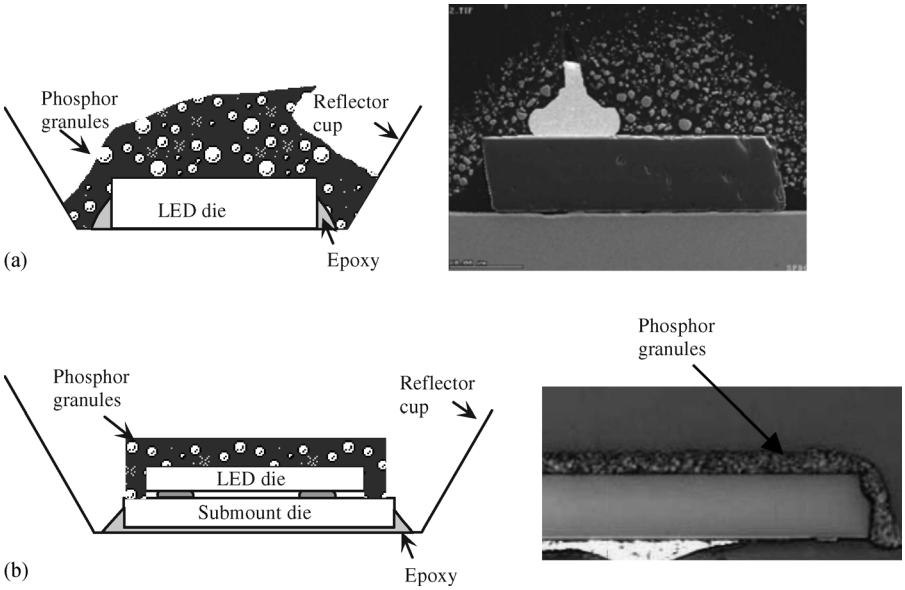

Figure 1.80 (a) Conformal coating of the yellow die (b) versus the standard coating to avoid color tint dependence on the viewing angle. Courtesy of Lumileds/Philips.

improved by chip and package design. The phosphor quantum efficiency is dependent on the phosphor material and can be improved by progress in the phosphor science. Finally, the level of electrical power that can be applied depends on the chip and package design. All of these components are on the table for improvement for

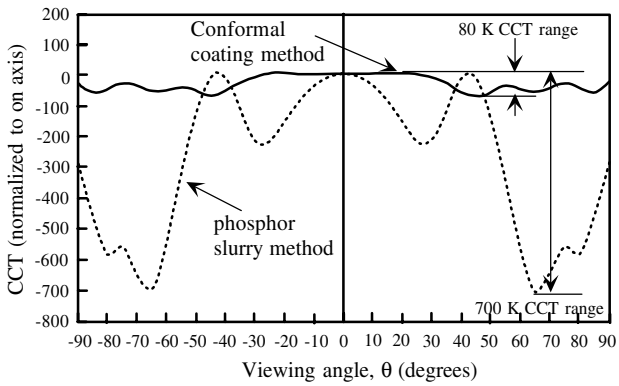

Figure 1.81 Normalized (with respect to on axis) viewing angle dependence of the CCT in LED + phosphor slurry construct and LED + phosphor conformal coating construct. A viewing angle dependence by as much as 700 K in CCT in the slurry design versus only 80 K in the conformal coating method is noted. Courtesy of Lumileds/Philips.

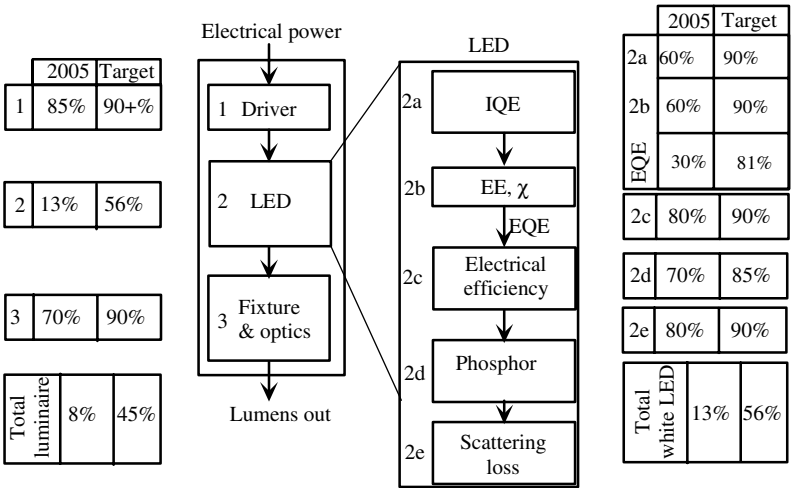

Figure 1.82 The year 2005 and target system efficiencies using the phosphor conversion LED color-mixing scheme in which the year 2005 CCT and CRI used are 5000–6000 K and 75, respectively, and the target CCT and CRI used are 4100 K and 80, respectively. IQE, internal quantum efficiency; χ, extraction efficiency; EQE, external quantum efficiency, which is a product of the internal quantum efficiency and the extraction efficiency; B, G, and R are for blue, green, and red, respectively. Patterned after NGLIA LED Technical Committee report prepared for the US Department of Energy "Solid-State Lighting Research and Development Portfolio," March 2006.

increasing the flux obtainable from white LEDs based on the phosphor/LED combination.

Consideration of the phosphor LED approach continues to the system level as graphically depicted in Figure 1.82 under a study for the US Department of Energy by Navigant Consulting, Inc. for the year 2005 with projected targets. The diagram assumes a correlated color temperature target of 4100 K (the equivalent CCT of a cool white fluorescent lamp) and a CRI of 75 for the target data. In the scenario, the driver (1) is assumed to have an efficiency of 85% for the year 2005. Ultimately, this can potentially be improved to a value greater than 90%. The other components in the system have more room for improved efficiency. Among them, the 2005 extraction efficiency of the LED chip was about 50%. The ultimate goal is to raise the extraction efficiency of the mounted, encapsulated chip to 90% with the use of thin-film vertical and flip-chip mounted LEDs. The areas with the greatest potential for improvement are the internal quantum efficiency, IQE (2a), and extraction efficiency, χ (2b), of the LED chip, and the fixture and optics (3). In the year 2005, the phosphor conversion LED luminaire/system was approximately 8% efficient at converting electrical power into visible white light. If all targets stipulated in the projections are attained, the LED device (lamp) would be expected to have an efficiency of 56%, with a system efficiency of 45%. Similar to the trichromatic color-mixing approach, the electrical luminous efficacy (in $\mathrm{lm\,W_e^{-1}}$) of the phosphor conversion LED approach can be calculated by multiplying the wall-plug efficiency (W_o/W_e) by the *optical* luminous efficacy

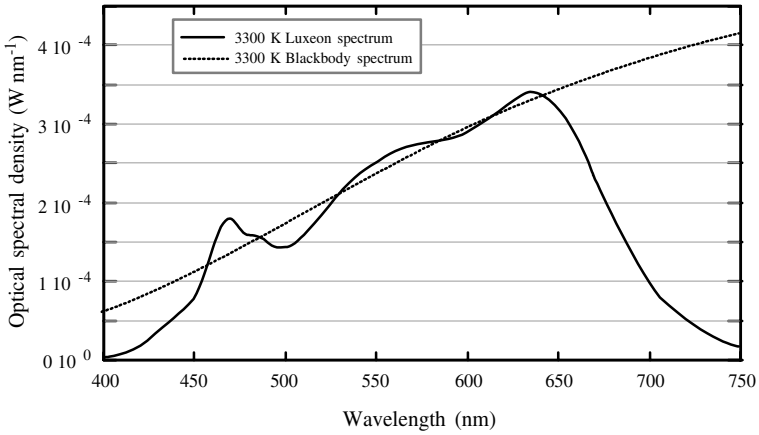

Figure 1.83 Spectra of 3300 K blackbody radiation as well as that from a 3300 K Lumileds Luxeon white pcLED indicating close replication. Courtesy Lumileds/Philips.

(useful light out (lm)/optical power in W_o) of a phosphor. Similar to the trichromatic color-mixing LED approach, a practical goal for a phosphor converting LED lamp would be about 160 lm W_e^{-1}. Improving the phosphor efficiency and temperature performance could improve the efficacy even more.

Various pcLED solutions replicating the blackbody radiation have been demonstrated. To reiterate, nominally white pcLEDs with 3200–3500 K correlated color temperature and color rendering indices greater than 90% have been attained. Shown in Figure 1.83 are the spectra of 3300 K blackbody radiation and those provided by 3300 K Luxeon lamp. Clearly, the replication of the blackbody radiation for this warm white is very good.

Packaging has a sizeable effect on the operative lifetime of pcLEDs. For example, the white LEDs constructed in a 5 mm package exhibit degradation of more than 60% in the output power after 10 000 h of operation, whereas higher power Luxeon LEDs packaged in a high-power package with good heat sinking display much more gradual degradation. Some 80% of the output power is retained after 20 000 h of operation. As the materials' quality is improved for better quantum efficiency, rugged fabrication procedures developed and employed along with packages with more efficient heat removal capability are being implemented, one would expect much longer lifetimes for a given degradation. Simply, as the lumens/W efficiency of the LED is improved along with advances in packaging, better lifetimes would result.

Let us now discuss illumination based on a near-UV emitting chip (380–410 nm peak wavelength), and a blend of downconversion phosphors where the optical pump does not really form the blue primary color. A plethora of prior work in relation to fluorescent lamps is already available. Consequently, the white light generated by UV excitation should closely follow that of available fluorescent lamps, which utilize a triphosphor (red, green, and blue) blend with one important exception. Because there is a dearth of phosphor materials that are efficiently excited by a 380–410 nm source,

particularly red- and green-emitting phosphors, it will be necessary to develop these materials.

The human eye's response to visible light (discussed in Section 1.6) suggests a lamp design departing from the traditional methodology of commercial incandescent lamps. The incandescent lamps try to replicate daylight as a continuum. Strong visual effects, such as higher perceived brightness per watt and better color rendering, can be attained if white light more closely resembles the three pure spectral colors while leaving the rest of the visible spectrum nearly empty, as in fluorescent lamps.

Fluorescent lamps utilize phosphors as converters of UV emission from rare gas/mercury discharge plasma into visible white light. In the 1970s, a blend of three phosphors called triphosphor or tricolor blend, which emits in the blue, green, and red spectral regions, paved the way for a new generation of white-light fluorescent lamps that simultaneously provided markedly high color rendering and high efficacy.

The role of the phosphors in the triphosphor blend of the fluorescent lamp is to generate photons at wavelengths near the "three-peaked" spectral response of the human eye. The three narrow emission bands centered near 450 nm (blue component), 550 nm (green component), and 610 nm (red component) are the ideal "prime colors" for this purpose. The resulting white light has high efficacy and excellent color rendering. The individual phosphors used in the tricolor blend of a typical fluorescent lamp are listed in Table 1.5, while their respective emission spectra are shown in Figure 1.84. Note that the color temperature can be varied by changing the ratio of the power in the three components while restricting any changes in the peak wavelength emission of the three components

The question here is whether a corresponding triphosphor blend, excitable at 380–410 nm, can be used to develop a phosphor-assisted white-light LED with high efficacy and good color rendering, as in the case of fluorescent lamps. Furthermore, with such a blend, when available, it should be possible to design white-light LEDs with a variety of color temperatures and with very high color rendering index. As indicated earlier, pumping schemes employing a source so far from the visible spectrum lead to high Stoke shift-related losses, degrading the luminous efficacy considerably. For this reason, the method described earlier wherein a blue source is used to pump green and red (not yet available) phosphors would be desirable.

Table 1.5 Phosphors used in the triphosphor blend of typical fluorescent lamps.

Phosphor	Color	Emission bandwidth	Emission peak (nm)
Eu^{2+}:(Sr, Ba, Ca)$_5$(PO$_4$)$_3$Cl	Blue	Broad	450
Eu^{2+}:$BaMg_2Al_{16}O_{27}$	Blue	Broad	450
(Ce, Tb)$^{3+}$:$LaPO_4$	Green	Narrow	543
Eu^{3+}:Y_2O_3	Red	Narrow	611

Here, "Broad" and "Narrow" are defined loosely and intended to give a flavor of comparison. Phosphors get excited by 254 nm wavelength radiation [129].

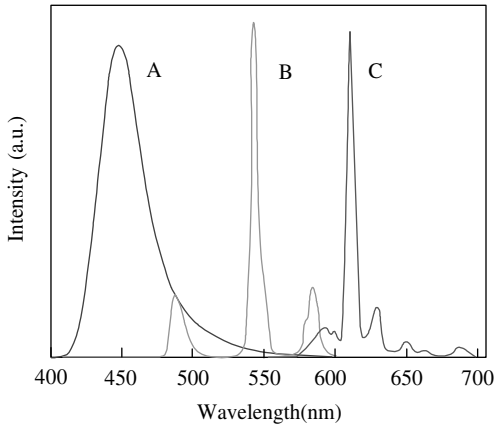

Figure 1.84 Emission spectra of phosphors of the triphosphor blend: A is Eu^{3+}:(Sr, Ba, Ca)$_5$(PO$_4$)$_3$Cl (blue); B is (Ce^{3+}, Tb^{3+}): LaPO$_4$ (green); and C is Eu^{3+}:Y_2O_3 (red) [129]. (Please find a color version of this figure on the color tables.)

Unlike the triphosphor blend used in fluorescent lamps, one of the issues with existing phosphors, excited by blue LEDs, is that the absorption in the blue by the available rare earth ions such as Ce^{3+} is low. This situation is reminiscent of the early days of the solid-state laser research using Nd^{3+}:YAG, where Nd^{3+}:YAG had a similar absorption problem when pumped by flash lamps, that is, not much absorption in the blue. It was later discovered that adding Cr to YAG increased the blue-light absorption and thus, through excited-state energy-transfer processes, energy is transferred from the Cr^{3+} ion to the Nd^{3+} ion, thereby increasing the overall efficiency. Similar ideas for increasing the blue absorption process for the triphosphor blend and/or other phosphors should be explored. Phosphors must strongly absorb at the wavelength of the LED radiation with absorption exceeding 90%; the intrinsic phosphor efficiency defined by the ratio of the emitted photons to absorbed photons must be high to lead to a quantum efficiency of 85% or higher; the phosphors should be compatible with operation in the LED and be easily manufactured; and the phosphors should display excellent lumen retention, which is defined as the change in lumens/brightness with time.

It is imperative that the *red phosphor* employed displays an emission spectrum that has a narrow linewidth centered at or near 614 nm, requirements that are well met by trivalent europium Eu^{3+}:Y_2O_3, as shown in Figure 1.84. The quantum efficiency of the Eu^{3+}:Y_2O_3 phosphor for excitation wavelengths below 254 nm is close to unity and is the highest of all known phosphors used in lighting. However, photons with wavelengths of 380–410 nm are very poorly absorbed by this phosphor, which preclude this phosphor being used in a UV LED-based white-light source unless advances are made. Any future discovery of red emitters based on the Eu^{3+} luminescence for UV LED applications will invariably require sensitization of the medium for the following reason. The absorption of UV photons by the Eu^{3+} ion is via a charge-transfer transition involving the Eu^{3+}ion and the surrounding anions.

It is known that the quantum efficiency of Eu^{3+} activated phosphors is low when the charge-transfer transition is centered at wavelengths longer than about 300 nm. Hence, for UV LED applications, where the phosphor is expected to absorb 380–410 nm radiation, sensitization of the Eu^{3+} luminescence is imperative.

The particulars for *green phosphors* are different from those of red-emitting phosphors. Because the eye response to green light is of relatively higher luminosity, the narrowness requirement of the spectral emission in the green is relaxed. This relaxation allows for the identification of several candidates for green-emitting phosphors. The broadband emission of divalent europium ions (Eu^{2+}), which is via the $4f^6\ 5d \rightarrow 4f^7$ optical transitions, is extensively tunable with emission wavelengths extending from the UV to red wavelength spectral regions. Moreover, the absorption by $4f^7 \rightarrow 4f^6\ 5d$ optical transitions usually extends throughout the ultraviolet.

Although not favored because of large Stokes shift related losses, let us discuss the particulars surrounding blue phosphors as well for completeness. The Eu^{2+}-based *blue phosphors* absorb the UV LED radiation and emit at the required wavelength of 450 nm. However, the absorption for 380–410 nm radiation needs to be further improved by increasing the europium content in the phosphor formulation (recall that the phosphor composition has been optimized for absorption of the 254 nm radiation). The increase in europium concentration is limited by the efficiency loss arising from concentration quenching and by the high cost of europium. Nevertheless, for the specific application in UV LEDs, there are numerous subtle trade-off possibilities that require reoptimization of the phosphor composition.

The advantages of white-light generation in the scheme where a UV LED is used to pump RGB phosphor(s) are as follows: white light is determined by the phosphors only and not subject to variation in the LEDs; they are simple to manufacture, at least in theory; they have a decent color rendering index ($R_a = 75$); and the temperature stability of various phosphors is excellent. However, damaging UV leakage is of concern, the fundamental limit of conversion efficiency is determined by phosphors, there is a Stokes shift, and self-absorption is an issue. There are also challenges in that color uniformity is dependent on the angle at which the source is viewed, and packaging must be robust to UV radiation.

In short, this approach uses output from a UV LED to pump several phosphors to simultaneously generate multiple colors. High color rendering indices, which are comparable to standard fluorescent lamps, can be realized. This approach also has the advantage of limited "tint" variation besetting the blue LED/yellow phosphor approach (unless conformal coating is used that mitigates the problem to some extent, see Figure 1.81). In addition, the ballast driver requirement is simple. Because the UV light is not used directly, it requires that the UV emitter efficiency be higher to account for conversion losses. In order to achieve 200 lm W^{-1} white light, a power conversion efficiency of over 70% might be required for the UV LED. Other disadvantages include lower efficacy, need for new phosphor development, and potential UV packaging requirements, as alluded to below.

Packaging is the holy grail of LEDs in general, and white lighting applications are no exception. Emulating the phosphor-coated fluorescent lamp glass tube application

of a phosphor layer directly to the LED can be an efficient manner to enhance conversion. The individual phosphors may be dry blended and then added to a liquid suspension medium or they can be added to a liquid suspension, such as a nitrocellulose/butylacetate binder and solvent solution used in commercial lacquers. Other liquids including water with a suitable dispersant and thickener or binder such as polyethylene oxide can also be used. The phosphor-containing suspension can then be painted, or coated, or otherwise applied to the LED and dried. Alternatively, the phosphors can be combined to suitable liquid polymer systems, such as polypropylene, polycarbonate, or polytetrafluoroethylene, or, more commonly, epoxy resin or silicone, which is then coated or applied to the LED and dried, solidified, hardened, or cured. For optimum brightness, it is imperative that high-quality coatings with minimum defects are developed and that the phosphor blend about the chip is arranged in such a manner as to convert as much of the chip's radiation into visible light as possible. Moreover, the absorption and reflection of the binder materials and the overall conversion efficiency have to be taken into account. Naturally, methods to minimize intrinsic efficiency loss are important.

Packaging would not be complete unless it addressed the issues related to LED drive electronics, LED addressing, and "on-board" controllers for multichip LED systems. Before any commercial production implementation, circuit and electronic designs must be stable and possible to produce at low costs. Thus, if a low-cost replacement for fluorescent or incandescent lights is to be realized, the packaging issues must be addressed satisfactorily.

In short, the issue dealing with the viewing angle can be addressed as has been done for the single-LED yellow-phosphor case by controlling the thickness of the phosphor. With progress in the phosphor technology, the UV light leakage may not be of a serious concern. Furthermore, UV LEDs are improving in their efficiency very well. It could be very likely that one LED/trichrome phosphor approach will end up being used for white light, with color temperature and rendering index that are acceptable providing, however, that conversion efficiencies of over 70% is achieved in the pump LED. Otherwise, the blue pumped two phosphor approach would be desirable as it does not suffer from as much stokes loss.

1.15.4
Other Photon Conversion Schemes

There are other photon conversion schemes for white-light generation. Among them are photon energy conversion techniques based on quantum effects using aggregates of small-sized (nanometer scale) semiconductor materials [140], photon-recycling semiconductor LEDs (PRS-LEDs), where a blue InGaN LED is joined to an AlGaInP top layer generating two complementary colors and hence white light [141], and exploitation of the high-power-narrow-bandwidth light output produced by UV lasers [142]. Another approach, in which the phosphor converter is eliminated, is to construct an integrated one-chip white LED by incorporating two InGaN epilayers emitting two wavelengths (blue and yellow) [143, 144]. Although not seriously considered, we discuss these approaches as well for the sake of completeness.

Quantum size effects can be used to tune the wavelength of visible light with high quantum yields by manipulating nanometer-size semiconductor structures whose bandgap energy depends on the size of the nanoparticle due to the effect of quantum confinement of the electron–hole pair. This is an advantage for inorganic semiconductors as compared to traditional organic phosphors for lighting applications in that they are less likely to suffer degradation during electron or hole injection in electroluminescent displays. Many semiconductors have been used in the form of QDs to shift the wavelength of emission and GaN is no exception. However, II–VI semiconductors lend themselves to synthesis processes that are not expensive.

A variety of techniques are available for producing quantum dots. One method is by molecular beam epitaxy (MBE), which can form the dots as well as coat them with a larger bandgap material. Due to the control and precision afforded by MBE, the early developments of quantum dots more or less had to be fabricated by MBE, but now that a good deal of understanding exists regarding the optical properties of quantum dots, other and less expensive techniques are gaining momentum. The most common approach to the synthesis of colloidal QDs is the controlled nucleation and growth of particles in a solution of chemical precursors containing the metal and the anion sources (controlled arrested precipitation) [145].

The controlled nucleation methods are easy to employ, do not require expensive capital equipment, and offer the quality needed for imaging [146]. As can be garnered, nanocrystals can be prepared at relatively modest temperatures [147]. Assuaging the process is the fact that the melting temperature drops with size as $1/r$ [148, 149]. The decrease in melting temperature with small sizes allows the synthesis of highly crystalline and faceted nanoparticles at temperatures compatible with wet chemical processing. Consequently, extremely high-quality inorganic nanoparticles have been prepared as colloids. Recent successes in the preparation of II–VI [150, 151] and III–V [152–154] (which are more difficult than II–VI dots) quantum dots illustrate the strengths of the colloidal preparation techniques.

A common method for II–VI colloidal QD formation is rapid injection of a solution of chemical reagents containing the group-II and group-VI species into hot and vigorously stirred solvent containing molecules that can coordinate with the surface of the precipitated QD particles [145, 155]. As a result, a large number of nucleation centers are initially formed, and the coordinating ligands in the hot solvent prevent or limit particle growth via Ostwald ripening. Further improvement of the resulting size distribution in the QD particles can be achieved through selective precipitation [155], whereby slow addition of a nonsolvent to the colloidal solution of particles causes precipitation of the larger sized particles. This process can be repeated several times to narrow the size distribution of II–VI colloidal QDs to a small percentage of the mean diameter [155].

The II–VI semiconductors such as CdS have direct bandgaps and are of particular interest. Because high quantum yields of visible light are possible. For example, light emission intensities have been demonstrated from 3.0 nm CdS nanoparticles similar in photoluminescence intensity and position to those obtained from laser dyes such as Coumarin 500. Furthermore, the peak of the light emission can be shifted from about 430 nm to ~700 nm by variation of both the size and the interface characteristics. The effect of the latter is demonstrated in Figure 1.85, where a coplot of the

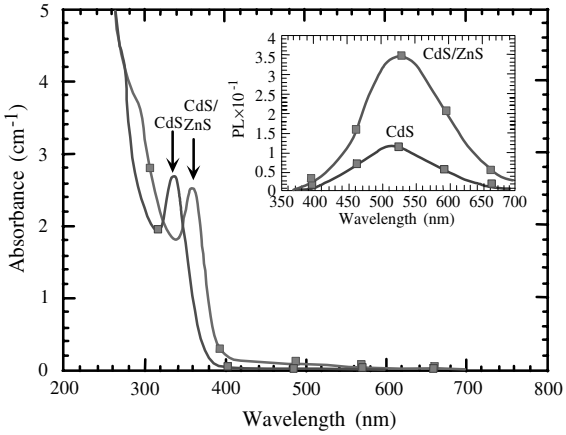

Figure 1.85 Plot of the UV absorbance and green photoluminescence spectra (inset) of nanosized CdS with and without a ZnS coating [129].

absorbance and fluorescence (inset) from a solution of CdS nanoparticles coated with a layer of ZnS to reduce nonradiative surface recombination (ZnS by itself has emission at ~420 nm and is transparent to CdS emission) was shown. A redshift and enhancement of over a factor of 3 in the light emitted occurs due to the coating. The redshift is due to reduced confinement caused by ZnS, which does not provide an infinitely large energy barrier to electrons and holes, and increases in intensity are due to reduction of nonradiative processes.

It is also possible to alter the peak energy and quantum efficiency by varying the excess ions at the nanoparticle interface. For example, intense blue–green emission at ~488 nm occurs with an excess of Cd at the interface, while weaker red emission at 590 nm is observed with excess S at the nanoparticle surface. Thus, by variation of both size and interface chemistry, it is possible to obtain a wide range of output colors even with only a single semiconductor material. A critical challenge with these kinds of nanoparticles for LEDs is to improve the quantum efficiency. To date, an absolute determination of the energy conversion efficiency has not been made, but studying this phenomenon is attractive and may have a long-term payoff. While these dots have already found a niche in biological fluorescence labeling, and so on, LED applications using these dots have not yet been realized and their utility has not been demonstrated in the marketplace.

As for the photon-recycling semiconductor LED approach, the maximum theoretical white-light efficacies using a blue InGaN LED wafer bonded to a sapphire substrate and a photon-recycling wafer (AlGaInP) are estimated [156] to be about 300 lm W^{-1}, with laboratory models exhibiting about 10 lm W^{-1} of white light.

Light generation using semiconductor lasers for excitation source of phosphors rather than LEDs may be advantageous. In one approach, remotely located UV lasers may excite phosphors that are painted on a wall to produce unusual lighting effects without any power connections in the wall. Unlike an LED, all of the 380 nm pump beam can easily be directed to the phosphor for photon conversion due to

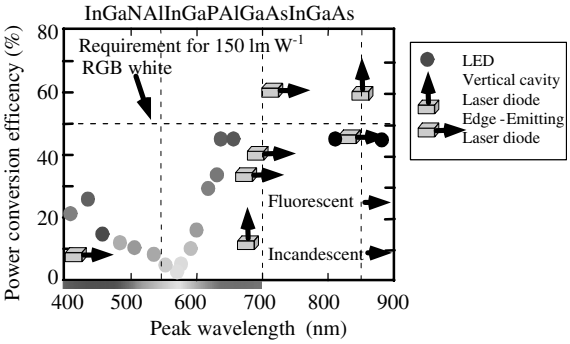

Figure 1.86 Best power conversion efficiencies reported for laser LEDs across the visible spectrum. For comparison and benchmarking, the efficiencies of unfiltered incandescent light bulbs and fluorescent light bulbs are also indicated. The vertical arrows indicate vertical emitters while the horizontal ones indicating edge emitters. Courtesy of Lumileds/Philips. (Please find a color version of this figure on the color tables.)

directionality of the beam. The best power conversion efficiencies reported for laser LEDs across the visible spectrum are shown in Figure 1.86. For comparison and benchmarking, the efficiencies of unfiltered incandescent light bulbs and fluorescent light bulbs are also indicated. The vertical arrows indicate vertical emitters while the horizontal ones indicate edge emitters.

Again, in the quest to generate white light without the use of phosphor conversion, Huang *et al.* [157] achieved white light InGaN/GaN quantum wells LED structures using the prestrained MOCVD technique. This technique enhanced indium incorporation in InGaN/GaN QWs by generating a tensile strain in the barrier above the QW. White light emitted by the LED comprised two wavelengths (460 and 576 nm) from blue QW and yellow QWs. The color temperature at 50 mA injection was reported to be 5600 K. In yet another phosphorless approach, Wang *et al.* [158] used a strained relaxed InGaN underlying layer (UL) for white-light emission. This UL-enhanced indium phase separation resulted in the formation of large-radius In-rich QDs in the InGaN QWs. These QDs emitted yellow light (570 nm) while blue light (440 nm) came from the rest of the same QWs. We should caution, however, that approaches of this kind do not lend themselves to the production environment due to poor reproducibility.

1.16
Toward the White-Light Applications

While the LED manufacturers are gunning for conventional illumination and they are not too far away, many lighting applications, which can be served by low-power incandescent or halogen lamps, can be served by LEDs as available or without much further improvement [128]. For instance, a 15 W incandescent bulb generates 120 lm,

Table 1.6 White-LED efficiencies (and lifetimes) including those that are of "50+" lm W^{-1} expected for year 2010.

Lamp type	Power (W)	Efficiency (lm W^{-1})	Lifetime (h)
Standard incandescent	15	8	1000
Standard incandescent	100	15	1000
Long life incandescent	135	12	5000
Halogen	20	12	3000
Halogen	300	24	3000
Compact halogen	50	12	2500
Compact halogen	11	50	10 000
Standard fluorescent	30	80	20 000
White LED 2000	Any	20	50–100 kh
White LED 2002	Any	30	50–100 kh
White LED 2005	Any	45	50–100 kh
Warm white LED 2005		20	50 000 kh
White LED 2010	Any	100+	50–100 kh
Green LED 2005		53	50 000 kh
Blue LED 2005		16	50 000 kh
Red LED 2005		42	50 000 kh
Amber LED 2005		42	50 000 kh

Efficiency figures over 100 lm W^{-1} have been reported for low injection levels with about 100 lm W^{-1} being available at high injection levels in the development circles. This calls for better and defining standards of efficiency in place, as it is clear that higher efficiencies are obtained in smaller devices at lower injection levels. Courtesy of Lumileds/Philips.

while a 50 W compact halogen lamp generates 600 lm. In this low-flux range from 100 to 600 lm, incandescent and halogen lamps are relatively inefficient and the energy saving from using LEDs can be significant, particularly in cases when they are on during a significant portion of each day. Among these applications are shelf lighting, theater and stair lighting, accent lighting, landscape and path lighting, flashlights, and some aspects of underwater lighting.

Let us briefly review the history of technologies developed for white-light generation to gain an understanding of the relevance of LEDs to the field. Just observing what goes on around us would immediately indicate that the last century of lighting has, by and large, been dominated by incandescent, fluorescent, and HID light sources (the latest performance of which are tabulated in Table 1.6).

The first electrically powered light was discovered by Thomas Edison and Joseph Swan independently in 1879. The Edison incandescent light bulb utilized a carbonized sewing thread. The first commercial product, though, used carbonized bamboo fibers and operated at about 60 W for about 100 h and an efficacy of approximately 1.4 lm W^{-1}. The improvements that followed over time have raised the efficacy of the current 120 V, 60 W incandescent lamp to about 15 lm W^{-1} for products with an average lifetime of 1000 h.

Peter Cooper Hewitt patented the first low-pressure mercury vapor (MV) discharge lamp in 1901, which marked the first prototype of today's modern fluorescent lamp. General Electric improved the original design and created the first practical

fluorescent lamp, introduced at the New York and San Francisco World's Fairs in 1939. Ever since that time, the efficacy of fluorescent lighting has improved and reached a range of approximately 65–100 lm W^{-1}, depending on lamp type and wattage, but the technology is very mature.

Sir Humphry Davy obtained a glow from platinum strips by passing an electric current through them in 1801, and in 1810, he demonstrated a discharge lamp to the Royal Institution Britain by creating a small arc between two charcoal rods connected to a battery. This paved the way to the development of HID lighting. However, the first high-pressure MV lamp was not sold until 1932. Gilbert Reiling patented the first metal halide (MH) lamp in 1961. This particular lamp achieved an increase of lamp efficacy and color properties over the MV variety, which made it more suitable for commercial and street lighting. As in the case of the fluorescent bulb, the MH lamp was introduced at the 1964 World's Fair. The first HPS lamp soon followed in 1965. The efficacy of HID lighting since that time has reached a range of approximately 45–150 lm W^{-1}, being highly dependent on lamp type and wattage.

Getting back to the discussion on low-level lighting applications of LEDs and focusing on shelf lighting, nominally hot and bulky incandescent and halogen lamps are traditionally used on the underside of shelves to illuminate merchandise in many retail outlets. Fluorescent lamps require protection against the inherent high operating voltage. An LED-based solution is nearly ideal for this application with its cool, compact, efficient, dimmable, long operating life, and low-voltage lighting capability. Similar arguments can be made about theater and stair lighting, where the LED can effectively illuminate flights of stairs and gangways. The LEDs can be mounted into the stair steps or on walls. Wall-mounted units require a very directional beam, which is consistent with the superior directionality of LED-based designs, as a large fraction of the light from an incandescent light bulb in these kinds of applications is wasted. Accent lights are used in retail shops to highlight merchandise, while in homes the main application is decorative ceiling lighting or highlighting artwork. LED-based solutions in place of incandescent and halogen lamps will lower energy and maintenance cost, as well as reduce fire hazard. Directionality of LEDs is again desirable here. Landscape lighting provides esthetics or orientation in public places such as parks, gardens, or office grounds. Low-voltage operation and efficient operation by LEDs should reduce installation, maintenance, and operation costs. Flashlights are a perfect example of LED replacement for incandescent lamps in flashlights, which have chronically poor shock resistance, and many flashlights are discarded due to incandescent filament breakage let alone insatiable battery consumption by incandescent bulbs. The 40–60 lm that are needed for flashlights can easily be provided by an LED source adding only \$0.05 lm^{-1}, which is quickly compensated for by extended battery life.

Many applications of white LEDs, in fact in rapidly growing numbers particularly in handheld portable electronics, are in back-displayed illumination, which requires different packaging. A typical backlighting system consists of a light guide plate, into which the light is allowed to go in from the bottom side. The light guide plate is equipped with optical extraction features and/or a taper and a reflector on the backside to reflect the light from the light plate toward, for example, the liquid crystal

display (LCD) panel. If, however, an RGB all-LED array is considered, the light from the LEDs is mixed in the light guide plate to generate the white light. If LEDs of each color are connected serially and each type of LED is controlled, the color of the backlight can be changed by changing the respective intensities of each color element. The system can be operated in either open-loop or closed-loop configuration with the aid of sensors, which allow measurement of color white point and color temperature [159].

In the open-loop configuration, the color points of all the LEDs must be known a priori, as well as inclusion in the system control of the predetermined LED color shift with temperature and drive current. This would include having to take into account flux degradation of the LEDs over time. The closed-loop system relies on an optical feedback sensor, which in its most simple form consists of three Si diodes, each having a separate color filter. The color filters ideally would have the transmission curves of the *X*, *Y*, and *Z* color matching functions. In this scenario, the signals from the three diodes can be directly related to the actual white point of the backlight.

In the backlight configuration depicted in Figure 1.87, R, G, and B LEDs are situated directly at the side of the light guide plate, with the drawback that the backlight region close to the edge has poor color and luminance uniformity [159]. This deficiency can be mitigated by employing a separate mixing light guide [160], as illustrated in Figure 1.88. In this configuration, the mixing light guide is positioned behind the main light guide plate, and an elliptical U-turn mirror is employed to reflect the light from the mixing plate to the extraction plate. The color uniformity of the light after mixing depends on the length of the mixing plate and the size of the white cluster in the RGB sequence. In Ref. [160], an LED pitch of 9 mm was employed, with a mixing plate length of 75 mm, to attain good uniformity. The slim

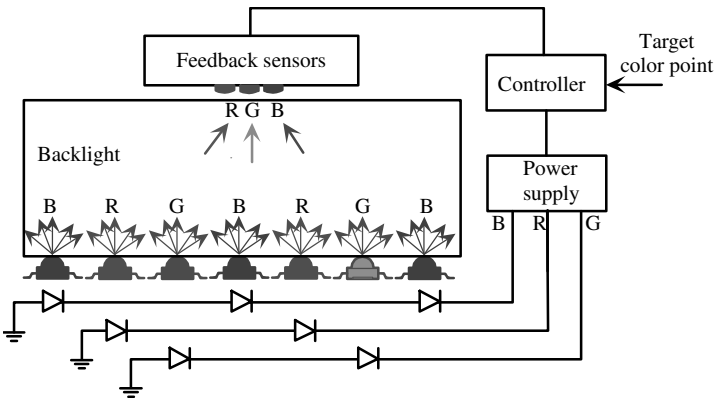

Figure 1.87 White point control in a backlight with R, G, and B LEDs. The LEDs inject the light into the backlight, where the light is mixed to create white. The color point of the white is measured using three sensors with approximate the *X*, *Y*, and *Z* color matching functions. A controller is used to compare the signals from the color sensors with those from the target white point. Courtesy of Lumileds/Philips. (Please find a color version of this figure on the color tables.)

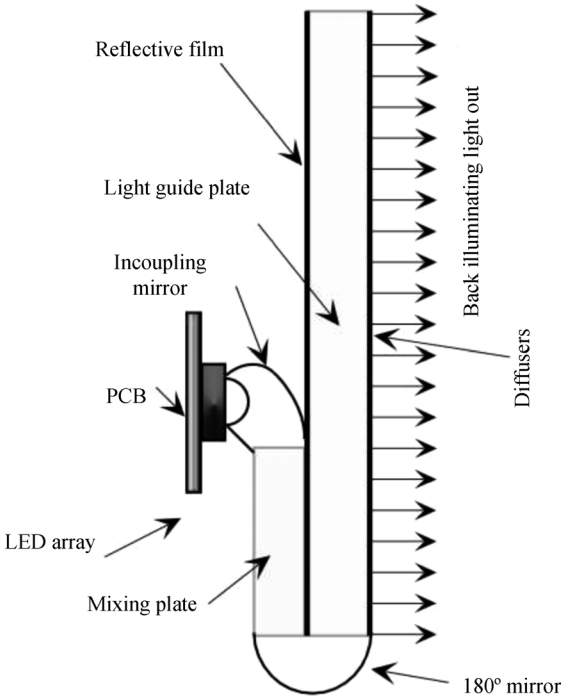

Figure 1.88 RGB LED backlighting configuration used, for example, in computer monitors and small LCD displays such as those found in handheld portable devices (handsets). A separate mixing plate is used to mix the light emanating from LEDs with the aid of a mixing plate placed behind the main light guiding plate the purpose of which is to spread the light over the LCD panel. Moreover, a 180° U-turn mirror is used to reflect the light from the mixing plate out into the main light guide plate. Courtesy of Lumileds/Philips.

LED technology for LCD backlighting to produce very thin handset displays for office automation devices, and consumer electronics. The side-emitting microside LEDs stand 0.6 mm high and high-intensity surface-mount LEDs have been developed for larger backlight applications [161].

Due to production variables (tolerances), LEDs vary in color, linewidth, efficiency, and forward voltage required for a given current necessitating auto testing and sorting (grouping) of all LEDs. The sequence of placement of sorted LEDs must to be optimized for attaining high luminance and color uniformity, as discussed in a patent on the topic [162]. In the U-turn configuration shown in Figure 1.88, a color uniformity with color variation $u'v' < 0.01$ (depicting the maximum distance between the color points in the 1976 CIE diagram) can be achieved, with a total efficiency of 50% (the ratio of light out from the backlight over to the light out from the LEDs). The efficiency is limited due to the light guide plates, inevitably with absorption losses, and the losses involved in coupling the light into the plate. If thickness is less of a concern, which is not the case in handsets, it is advantageous to avoid using light guide plates all together. An example of this, called a direct backlight, is shown in

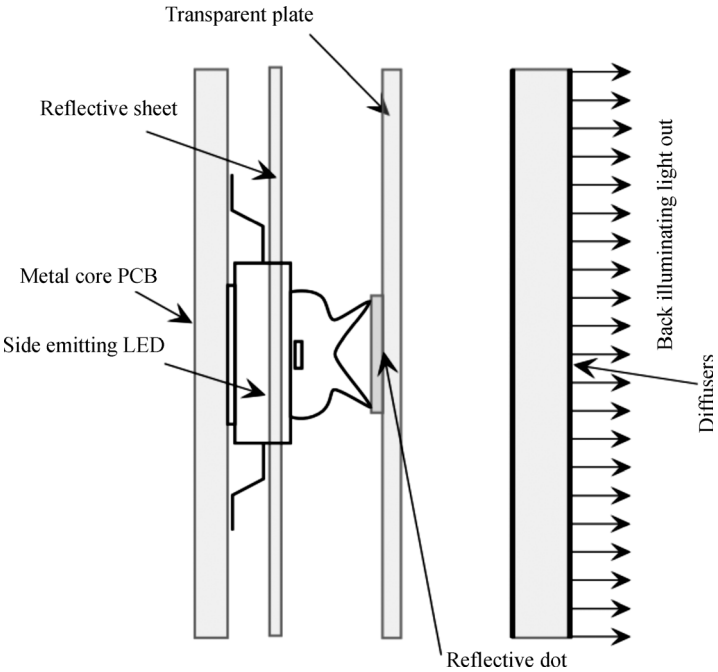

Figure 1.89 An example of a direct LED backlighting configuration where the LEDs are placed in a highly reflective cavity that consists of highly reflective walls and a diffuser on the front side. For good color and illuminance uniformity, the LEDs must have a broad intensity profile. In the example shown, the light from the top surface of LED is blocked by a white reflective dot. Courtesy of Lumileds/Philips.

Figure 1.89. Two of these units are then used to illuminate the backplate from both sides. A series of diffuser sheets and other electronics are also at the end of the LCD panel.

As implied, these types of backlights are used in large displays, for example, LCD TVs [163]. The LUXEON backlight module designed specifically for this purpose features a flux density of 60–75 lm in^{-1} in a standard LED array and 125 lm in^{-1} at its best, which will become the standard shortly. The pitch distance between LEDs in the one-dimensional array is 9 mm. The LEDs are binned and matched to produce a CCT of 9000 K. The lifetime of the backlight module is over 50 000 h and requires about 3 W in^{-1} drive power. Since the light guide plates have absorption losses and light coupling losses into the plates, direct backlight is more efficient if the thickness of the panel is a less important factor. This direct backlight is used in large display, as for example, LCD TVs [159]. As an alternative to a side emitter (also a regular Lambertian emitter can be used), a secondary lens to spread the light is used [164]. In an effort to achieve a high color and brightness uniformity, side emitters have been employed.

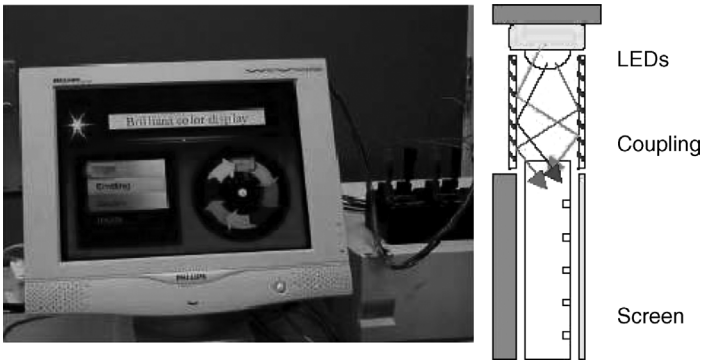

Figure 1.90 LED backlighted 18 in flat panel computer screen and a schematic representation of illumination. Courtesy of Lumileds/ Philips. (Please find a color version of this figure on the color tables.)

A side-emitting LED, for example, the LUXEON side emitter, has peak intensity at an approximate angle of 80° with the surface normal [165].

In the simplest sense, a white LED or a combination of white LEDs can be used in a glass waveguide. From the get go, flat panels of the size either 40×136 or $102 \times 126\,\text{mm}^2$ became available for background lighting. But color parameters such as color rendition and dimming without color shift are not sufficient. Consequently, more elaborate schemes had to be developed for the LED approach to be viable and compete with fluorescent-based and also organic LED-based backlighting schemes. Fortuitously, advanced designs incorporating three-color LEDs have been developed with excellent color stability through active feedback and infinite dimming without color shift. The advances are such that flat panel color displays of 18 in size have been produced with three-color LEDs. The advances are such that flat panel color displays of 18 in size have been produced with three-color LEDs as shown in Figure 1.90.

The Luxeon backlight module built for this purpose features a flux density of 60–75 lm in^{-1} in a standard LED array and 125 lm in^{-1} at its best, which has the potential to become the standard, at least a derivative of this. The pitch distance between LEDs in the one-dimensional array is 9 mm. The LEDs are binned and matched to produce a CCT of 9000 K. The lifetime of the backlight module is over 50 000 h and requires about 3 W in^{-1} drive power. Since the light guide plates have absorption losses and light coupling losses into the plates, direct backlight is more efficient if the thickness of the panel is a less important factor. This direct backlight is used in large displays, as, for example, in LCD TVs [159].

Last but not least, these modules are free of Hg used in cold cathode fluorescent light bulbs (CCFLs), each LED module replacing four CCFL bulbs. In addition, simulated images that can be produced by CCFLs for back illumination and RGB LEDs for the same indicate the RGB solution producing much more vivid and pleasant colors.

The penetration of LEDs into the signaling market provided the impetus for the development of higher power LEDs and lower cost. This performance/price

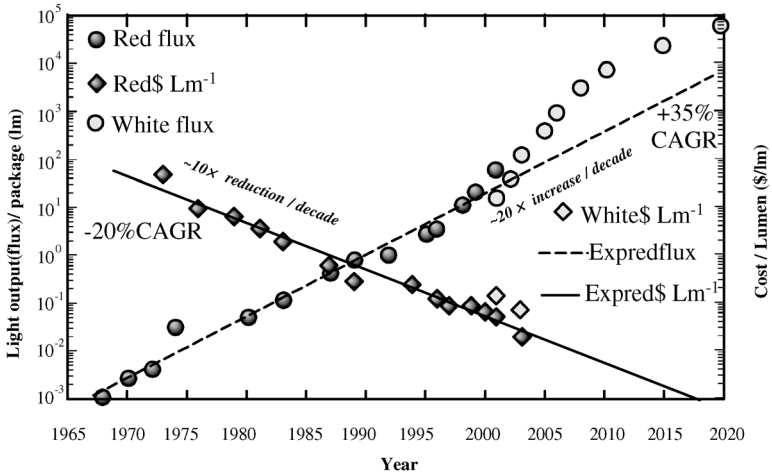

Figure 1.91 Historical and projected evolution of the performance (lm package^{-1}) and cost ($ lm^{-1}) for commercially available red LEDs. *Note*: CAGR = compound annual growth rate. Both lines on the same numerical scale, but with different units. These data were compiled by R. Haitz from HP historical records [128].

evolution for red- and white-light LEDs is illustrated in Figure 1.91, covering the period from first LED sales in 1965 to a projected year 2020. As the figure indicates, flux per unit increased 20-fold per decade for the past 40 years and crossed the 10 lm level in 1998. While during the same period, the cost per unit flux ($ lm^{-1}) decreased by 10-fold per decade and reached 6 cents lm^{-1} in 2000. At this price, the LEDs in a typical 20–30 lm center high-mount stop lights in automobiles contributes only $1.50 to the cost of the complete unit.[4)]

The success of LED-based white-light sources suitable for general illumination critically depends on improving LED efficacies across the visible spectrum from 30 to 50 lm W^{-1} to the desired 200 lm W^{-1}. For phosphors and other energy conversion methods, further research and development is required in order to understand and improve photon conversion efficiencies and output wavelengths. Moreover, improved packaging strategies have to be developed for all approaches, and applications exploiting the unique properties of lasers have to be explored. Putting it in other words, to produce 150 lm W^{-1} of white light, which is necessary to compete with fluorescent lamps, SSL devices producing red, green, and blue light must operate with a power conversion efficiency of about 50%. Already red LEDs are nearly operative at these efficiencies, but nitride-based LEDs producing green light need to be improved

4) Although this cost is higher than that of an incandescent light bulb, it is low enough that desired compactness, styling freedom, and absence of warranty cost easily make up the difference.

by a factor of 5–10, and those producing blue light need to improve by a factor of 2–3. The challenge to increase nitride efficiencies to 50% is formidable, but it is doable.

In pursuit of progress along these lines, Lumileds (formerly Agilent that in turn formerly Hewlett Packard) obtained a 592 nm (amber) LED producing 480 lm W^{-1} outputs. Furthermore, green and blue InGaN-based LEDs having efficacies in the range of 70 lm W^{-1} are being reported by Cree Research, Inc. Estimates for successfully demonstrating a 200 lm W^{-1} white-light levels range from 3 to 6 years. A second goal, in many ways more applicable, is taking laboratory-produced LEDs (producing 200 lm W^{-1} white light) and commercializing at competitive costs.

Table 1.6 compares current and projected efficiencies of white LEDs with those of the most widely used conventional white-light sources. The most popular incandescent lamps with a power rating of 60–100 W have an efficiency of around 15 lm W^{-1} and a rated life of 1000 h, the efficiency of which drops off at lower power ratings or for lamps with a longer, 3000–6000 h, rated lifetimes. A similar pattern is in effect for halogen sources covering the range of 12–24 lm W^{-1}. Fluorescent lamps at 80 lm W^{-1} are the most efficient white-light sources and dominate commercial and industrial lighting applications. Nichia achieved an efficacy of 150 lm W^{-1} in a white-light lamp-type LED having the CCT of 4600 K in 2006, but this efficacy was obtained at an extremely low injection current of 20 mA in a laboratory setting (one can deduct that this high efficacy did not hold up at high current drives). Commercial products showing 75 lm W^{-1} and CCR of 6000 K at 350 mA are available by Cree as of 2007. Semi-LEDs, a California-based company with manufacturing facilities in Taiwan, also achieved luminous intensities ranging from 92 to 96 lm from LEDs driven at 350 mA of injection current. These efficiencies significantly exceed the standard 60–100 W incandescent lamps performance. The leveling off is based on the understanding and expectations based on the time of predictions and one should not be surprised if the actual performance turns out to be different.

1.17 Organic/Polymeric LEDs (OLED, PLED)

Application areas of nitride-based emitters and organic emitters overlap when it comes to indoor uses, background lighting, large-area illumination, and display screens, and in the past decade, a good amount of research has been dedicated to the organic emitters' understanding [166, 167]. This overlap in application areas provided the impetus to provide some basics related to OLEDs/PLEDs. As there is a multitude of organic compounds with varying electrical and optical properties, the organic materials used in various layers of an OLED device are classified according to their physical structure. OLEDs have been made with small organic molecules and organic polymers [168, 169]. Although the two types of OLEDs are produced differently, in both cases, the organic layers are highly disordered, which opens up the possibility that they can be produced inexpensively in large areas. Systems employing small organic molecular compounds are typically deposited by vacuum deposition [170], although developments in an organic vapor-phase deposition (OVPD) technique show promise

for high-definition features to be deposited, which are critical in terms of production if the molecular system is to be the method of choice for thin OLED displays [171]. For polymer-based OLEDs, the organic medium can be sprayed onto a substrate along with a carrier that must be evaporated, and techniques such as those in spin coating, screen printing [172], and ink-jet printing [173] have been used to produce polymer films; the result is a low-cost method of production, suitable for large-scale manufacture. Dendrimers, due to their lower degree of disorder and ability to efficiently transfer energy from a singlet state on its surface to a housed phosphorescing metal within them, also show much promise in OLED applications. It should also be noted here that this use of dendritic molecular architectures has been successfully utilized to produce "molecular" systems in the same fashion as the polymeric systems (i.e., low-cost spin coating techniques) [174]. This compromise appears promising for electrophosphorescent (a method of increasing efficiencies in OLEDs that has had more success in molecular systems over polymeric systems, see Section 1.17.3) OLEDs that are additionally efficient and easily fabricated devices.

Fabrication techniques originally required that the organic materials be deposited onto a glass substrate in a batch process; however, advances are bringing to life one of the advantages of utilizing an organic material over an inorganic in its ability to be deposited on mechanically flexible substrates [175, 176]. The prospects in terms of devices possible when flexible substrates are used include not only illumination and display screens but also novel applications such as furniture, wallpaper, clothing, books, and so on. To demonstrate the agility and flexibility of OLEDs, a flexible display produced by Sony Corp. is shown in Figure 1.92.

A difficulty with using flexible substrates, as compared to glass, stems from the fact that films are unacceptably permeable to water and oxygen, which degrade the organic layers of the OLEDs and cause delamination of the electrodes [177]. Reasons

Figure 1.92 A flexible, full-color organic electroluminescent display (OLED) built using organic thin-film transistor (TFT) technology with a plastic substrate. The 2.5 in prototype display, which is 0.3 mm thick and weighs 1.5 g without the driver, supports 16.8 million colors at a 120 × 160 pixel resolution (80 ppi, 0.318 mm pixel pitch). Press release by Sony Corp., http://www.sony.co.jp/SonyInfo/News/Press/200705/07-053/index.html. (Please find a color version of this figure on the color tables.)

for the degradation are that oxygen will often attack bonds in the film, forming nonradiative recombination sites, and that efficient devices employ low work function cathode metals, such as calcium, which are highly susceptible to oxidation [178]. OLEDs typically made on glass substrates are covered with a second piece of glass to keep water and oxygen out. But for the flexible substrates, solutions include building hermetic barrier layers onto the films, designing efficient devices that do not require reactive electrodes, and designing organic layers that are inherently resistant to photooxidation.

OLED displays have now entered the market in portable imaging products such as cellular phones, digital cameras, and car audio systems: applications that are currently served by traditional LCDs and vacuum fluorescent displays (VFDs). Because OLEDs are self-luminous, backlights are not required as in LCDs. OLEDs have very low power requirements and are thin, bright, and efficient. Some other attractive characteristics of these displays are emission wavelengths tunable by incorporation of suitable dyes in the emissive layers, low forward voltage compared to some other fluorescent displays (under 10 V), high emission efficiencies, which result in high brightness coupled with low power consumption, wide viewing angles, fast response (10 μs), thin and lightweight display construction, potential for low-cost manufacturing, low-temperature processing technology, compatibility with flexible substrate displays, and environment-friendly features in the form of reduced power consumption and lack of need for mercury-containing backlight assemblies [166]. Disadvantages, which are formidable, are chemical instability and degradation by UV light. As such, requirements of lowered cost, storage lifetimes of at least 5 years, and operating lifetimes of >20 000 h are to be met. To meet these goals, significant activity is being undertaken to optimize the emitting structure, improve encapsulation, and develop materials that are more resistant to chemical degradation, such as oxidation.

Similar to the case of inorganic LED inclusive of performance projections into the future, Figure 1.93 presents a diagram for an OLED system and compares the current typical efficiency values for the individual system elements to a set of suggested program targets. The projected target values in some categories are highly optimistic, some reaching the perfect value of 100%, which would be the first time ever. Furthermore, it is not clear if these projected values would hold up at high intensities and if so for how long. If the target values were to come true, OLED look much better than the nitride-based white LEDs for illumination.

1.17.1
OLED Structures

In what follows, the intent is to be introductory. As such, references to specific schemes, molecular or polymeric will be limited. Although Figures 1.94 and 1.95 show a number of widely used π-conjugated small molecules and polymers, respectively [179], the trials involved within each of the schemes lie outside the scope of this book. The reader interested in detailed information, specific to particular schemes, can refer to Ref. [179].

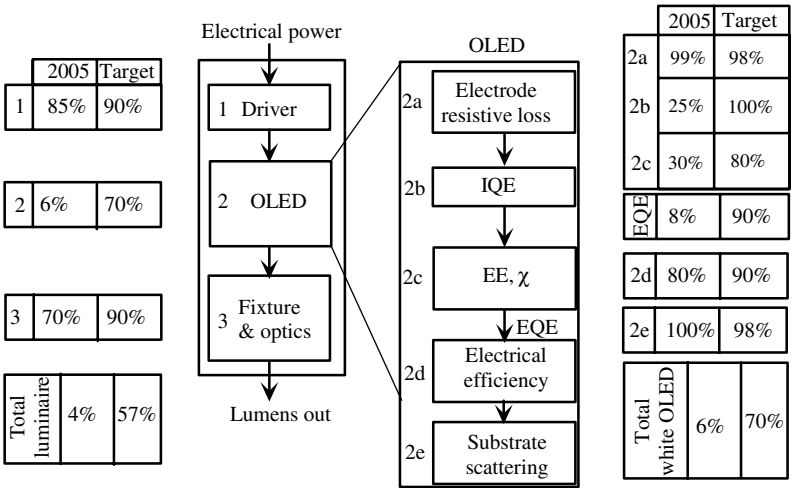

Figure 1.93 OLED system efficiencies and projections into the future. The target CCT and CRI used are 3000–6000 K and 80, respectively, with 1000 cd m^{-2}. IQE, internal quantum efficiency; χ, extraction efficiency; EQE, external quantum efficiency, which is a product of the internal quantum efficiency and the extraction efficiency; B, G, and R are for blue, green, and red, respectively. Note that target efficiencies in some categories are perfect, which is very optimistic. In addition, whether these target values would hold up at light intensities and, if so, for how long remain to be seen. Patterned after NGLIA LED Technical Committee report prepared for the US Department of Energy "Solid-State Lighting Research and Development Portfolio," March 2006. *Note 1*: Electrode electrical loss – negligible for small devices, possible issue for large-area devices. *Note 2*: Includes substrate and electrode optical loss – negligible for glass and very thin electrodes but may be important for plastic or thicker electrodes. NGLIA OLED Technical Committee.

Although tris-(8-hydroxyquinoline)aluminum (Alq_3) OLEDs or LEPs performance is noteworthy, OLEDs represented not much more than a scientific curiosity prior to the early work of Tang and Van Slyke [168]; however, their work with Alq_3 is more or less responsible for the creation of the field. In the wake of rapid scientific progress, particularly in the operation lifetime, a bright future is now seen for organic emitters, indoor displays, background panels, and night-lights built around relatively large organic molecules. The large area, the physical flexibility, and the low cost are the attractive features offered by the organic technology. There are also efforts to fabricate transistors based on polymers with the hope of constructing displays having built-in control circuitry in much the same way as liquid crystal displays.

Originally, devices were constructed simply by sandwiching an organic emissive layer between two electrodes. The organic material inevitably had vastly different mobilities for electrons and holes, and thus, recombination often occurred near one of the electrodes, resulting in considerable nonradiative recombination due to conformational defects. By incorporating multiple organic layers as transport layers for holes or electrons, recombination was effectively moved away from the electrodes, resulting in higher quantum efficiencies (multiple layers were initially difficult to achieve in the polymeric systems). By choosing the hole transport layer (HTL) or

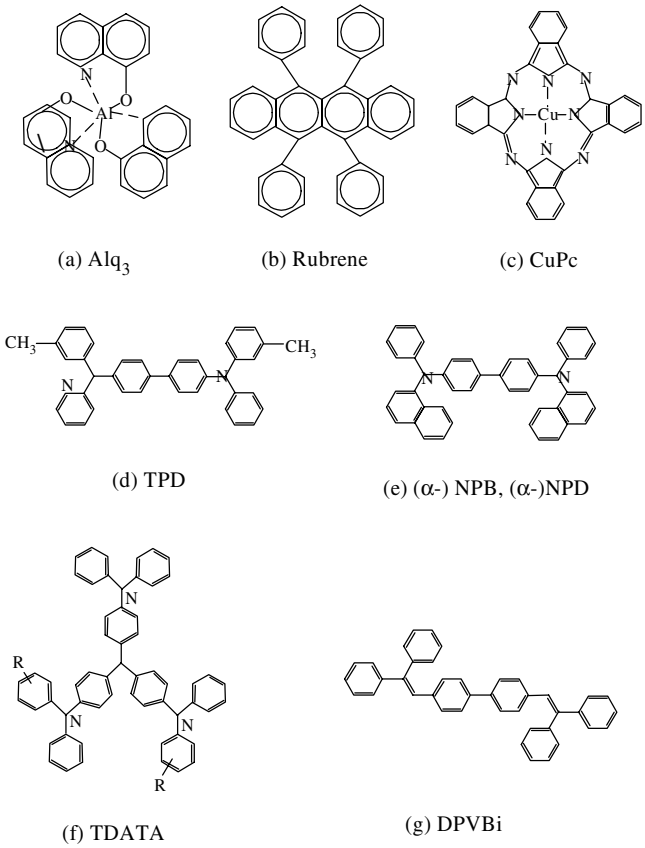

Figure 1.94 Structures of widely used π-conjugated small molecules: (a) tris-(8-hydroxy quinoline Al) (Alq_3); (b) rubene (5,6,11,12-tetraphenyl tetracene or 5,6,11,12-tetraphenyl naphthacene); (c) copper phthalocyanine (CuPc); (d) *N*,*N*′-diphenyl-*N*,*N*′-bis(3-methyphenyl)-1,1′-biphenyl-4,4′diamine (TPD); (e) *N*,*N*′-diphenyl-*N*,*N*′-bis(1-naphthylphenyl)-1,1′-biphenyl-4,4′-diamine (NPB, α-NPB, NPD, or α-NPD); (f) 4,4′,4″-(tris(diphenyl amino) triphenylamines (TDATAs); and (g) 4,4′-bis(2,2′-diphenylvinyl)-1,1′-biphenyl (DPVBi) [179].

electron transport layer (ETL) appropriately (i.e., mismatching the energy bands so that the HTL's highest occupied molecular orbital (HOMO) corresponds to the work function of the anode or the ETL's lowest unoccupied molecular orbital (LUMO) corresponds to the work function of the cathode), the layers can be made to serve as hole- or electron-blocking layers, increasing the likelihood of radiative recombination within the emitting layers. Similarly, due to the unavailability of high work function metals, electrons are easier to inject, but the number of holes must be matched with the number of electrons that are injected, for a mismatch will contribute to current but not emission. The typical multilayer OLED device is shown in Figure 1.96a along with an energy level diagram for a bilayer OLED in Figure 1.96b, and schematic representation of the charge-carrier injection (1), exciton formation (2), and radiative

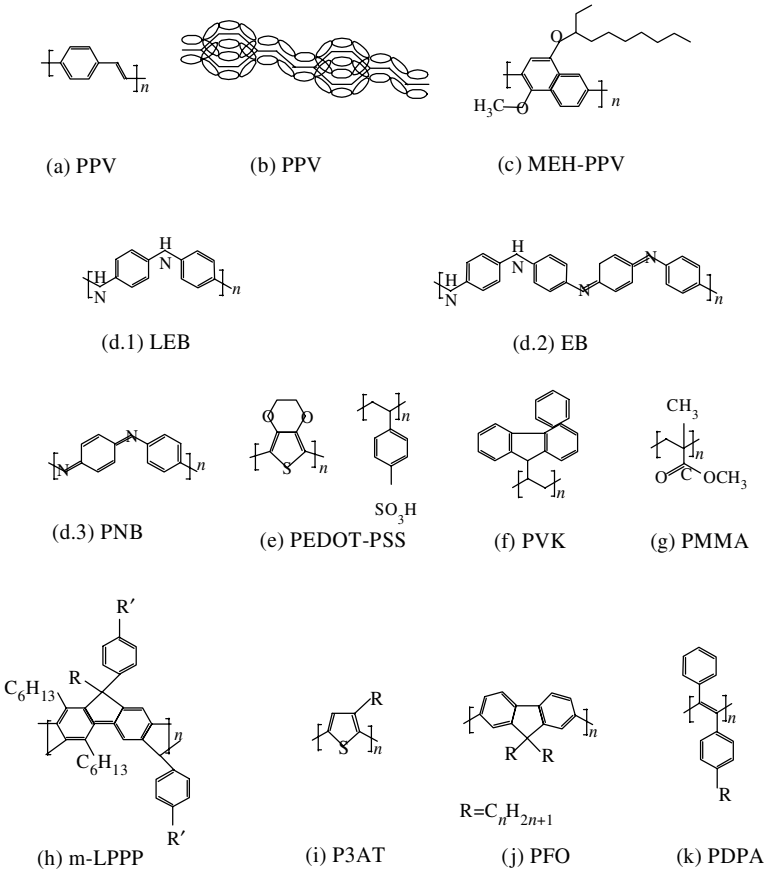

Figure 1.95 Structures of widely used π-conjugated and other polymers: (a) poly(*para*-phenylene vinylene) (PPV); (b) s (solid line along backbone) and p ("clouds" above and below the s line) electron probability densities in PPV; (c) poly(2-methoxy-5-(2-ethyl)-hexoy-1,4-phenylene vinylene) (MEH-PPV); (d) polyaniline (PANI): (d.1) leucoeneraldine base (LEB), (d.2) emeraldine base (EB), (d.3) pernigraniline base (PNB); (e) poly(*N*-vinyl carbazole) (PVK); (g) poly(methyl methacrylate) (PMMA); (h) methyl-bridged ladder type poly(*p*-phenylene) (m-LPPP); (i) poly(3-alkyl thiophenes) (P3Ats); (j) polyflorenes (PFOs); (k) diphenyl-substituted *trans*-polyacetylenes (*t*-$(CH)_x$) or poly(diphenyl acetylene) (PDPA) [179].

recombination (3) in organic LEDs in Figure 1.96c [180]. The choice of suitable energy band mismatch, as well as the ability to get light out of the device once it is emitted, is the key to realizing efficient OLEDs; the latter applies to LEDs of all types. The device consists of an anode, a high work function metal to inject holes (usually ITO), a hole transport layer, an emissive layer (or layers – this could also possibly be the same layer as the HTL or ETL and could possibly be doped with fluorescent or phosphorescent dyes) [181], an electron transport layer, and a low work function cathode, usually a reflective thin-film metal to inject electrons (typically aluminum, calcium, or magnesium or metal alloys such as magnesium–silver and

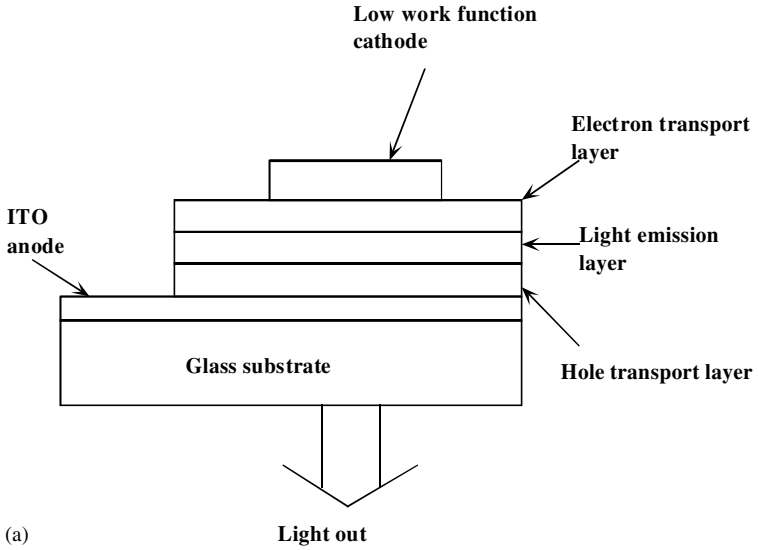
Low work function cathode
Electron transport layer
ITO anode
Light emission layer
Glass substrate
Hole transport layer
Light out

(a)

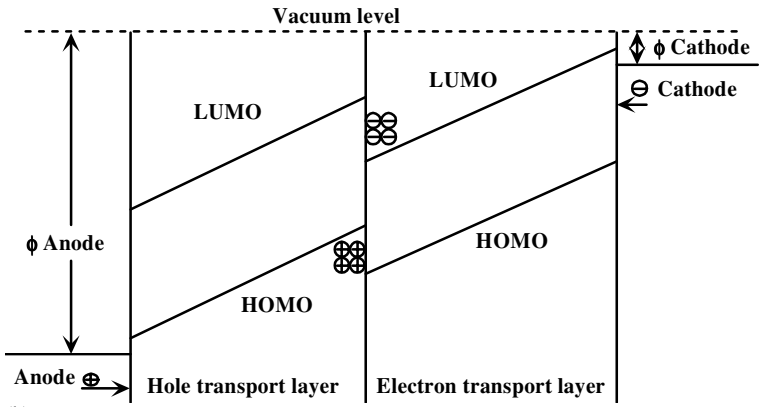
Vacuum level
ϕ Cathode
Cathode
LUMO
LUMO
ϕ Anode
HOMO
HOMO
Anode
Hole transport layer
Electron transport layer

(b)

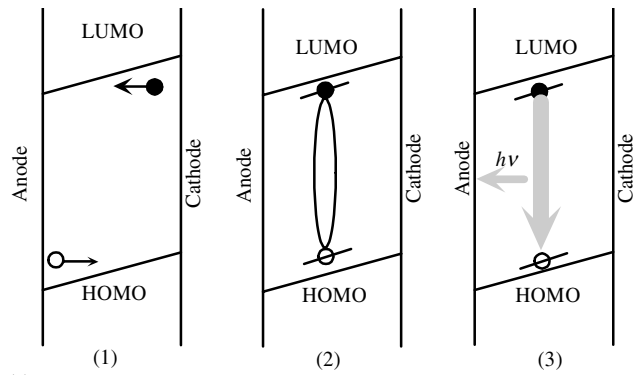
LUMO
Anode
Cathode
HOMO
(1)
LUMO
Anode
Cathode
HOMO
(2)
LUMO
Anode
hν
Cathode
HOMO
(3)

(c)

lithium–aluminum). Note here that one of the electrodes must be transparent in order for the light to escape – this is typically the ITO anode; however, progress is being made in the vein of making completely transparent OLEDs [182, 183]. In this case, a thin layer (~10 nm) of electron injecting material is typically placed next to the organic layers, and the cathode is capped with ITO. Transparent OLEDs (TOLEDs) are also suitable for additional applications over traditional OLEDs such as helmet or windshield-mounted displays, "smart" windows that double as nightlights, or other novel sources of light.

In order to maximize device performance, each of the organic films must be specially optimized for each color desired. The overall thickness of the device is less than 200 nm, so it cannot support itself and as such is often fabricated on a glass substrate, though flexible substrates are being developed. The more flexible substrates are improved, the less susceptible they become to atmospheric permeation, a lingering problem for the earlier versions.

It has been estimated that the permeability of an OLED package should be less than $5 \times 10^{-6}\,\mathrm{g\,m^{-2}\,day^{-1}}$ at room temperature, in order to achieve a lifetime of 10 000 h, or organic materials will have to be engineered to be unaffected by the presence of water or oxygen [184]. Langowski [185] discussed the barrier, against oxygen and water vapor, requirements for various product sectors (defined by dotted lines) and performance of polymer-based flexible structures (defined by shaded areas) as depicted in Figure 1.94.

Developments have resulted in a barrier coating that can be put over a plastic substrate that significantly retards the diffusion of oxygen and water, called Barix. This is a multilayer coating consisting of alternating layers of inorganic oxide to impede the diffusion of the water and oxygen, and a polyacrylate film that planarizes the oxide and impedes the propagation of defects through this barrier. The surface roughness of the coated sample is less than 10 Å, and testing showed that this barrier allowed only $2 \times 10^{-6}\,\mathrm{g\,m^{-2}\,day^{-1}}$ of water or oxygen through it. The OLEDs that were built on Barix-coated polyethylene terephthalate (PET) were shown to have half lives of 3800 h from an initial luminance of $425\,\mathrm{cd\,m^{-2}}$, when driven at $2.5\,\mathrm{mA\,cm^{-2}}$ [186].

As there is a plethora of available organic compounds from which to choose suitable layers from, OLEDs being produced are of many varieties and are classified according to the physical structure's organization: molecule, oligomer, or polymer. The most important differences in the types are the methods that are used to fabricate them, and again polymers are more attractive in that they can be made at room temperature using spin coating, screen printing, or ink-jet printing techniques. The radiative recombination methods of each type of organic device are essentially the same. The relaxation of singlet states, although excitations leading to them are

Figure 1.96 (a) A typical OLED multi-layer device structure.
(b) Schematic energy level diagram of a bilayer OLED device,
(c) Schematic of the charge carrier injection (1), exciton formation
(2) and radiative recombination (3) in organic LEDs [191].

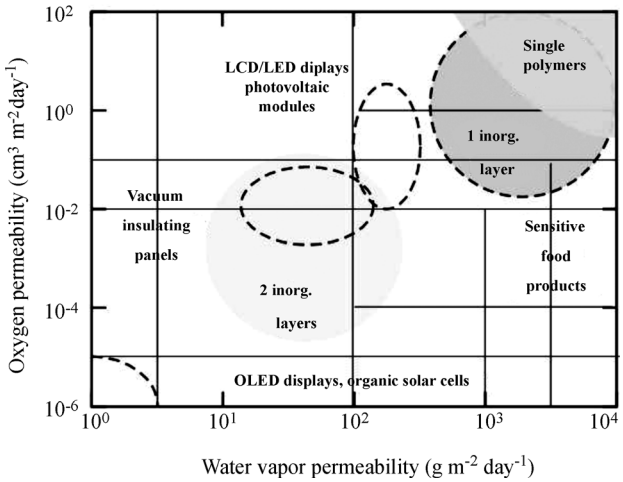

Figure 1.97 Barrier requirements against oxygen and water vapor, for various product sectors (dotted lines) and performance of flexible polymer based structures (shaded areas). Patterned after [185].

limited by spin to statistics to occur ~25% of the time at best, were the original method of harvesting photons from organic LEDs. More recently, by using dyes (molecules or on-chain ligands for polymers) that allow phosphorescence to occur from the relaxation of excited triplet states, efficiencies have been brought up.

Conjugated molecular systems, polymers and oligomers, have attracted considerable attention for their applications to OLEDs [187, 188]. Conductive polymers have also been explored for electronics applications, primarily FETs [189], and a detailed treatment has been presented by Christos and Dimitrakopoulos [190]. A review of conjugated polymers, particularly of their optical properties can be found in Ref. [191]. While discrete emitters based on organic molecules and polymers have been attained, the impact of these devices is expected to be in the region of large-area displays. In this vein, flat panel displays promise to offer good value to electronic products that incorporate displays for viewing information, and manufacturers have already demonstrated active-matrix displays as large as 40 in [192].

Aside from problems with efficiency and lifetime, which would be ameliorated by employing hole transport and electron transport layers, the first organic polymers to be shown to have light-emitting properties were not feasible for employment in the production of white light due to their inability to produce short wavelengths (blues). The ability to shorten the conjugation length by addition of acceptor side chains on the polymer was soon discovered, and this was used to engineer the wavelength of the emitted light to the desired length; similarly, molecules have been found that produce the shorter blue wavelength necessary for white-light emission.

For practical applications, it is important to operate the devices at low voltages, consuming little power, and polymers have been more successful in reducing

their operating voltages than their molecular competitors. One widely used electron transport material in OLEDs is Alq_3; however, the effective mobility of electrons in Alq_3 is reported to be as low as $1.4 \times 10^{-6}\,cm^2\,V^{-1}\,s^{-1}$ at an electric field of $4 \times 10^5\,V\,cm^{-1}$ [193]. When both the cathode and anode are perfectly injecting, low electron mobility in Alq_3 becomes a limiting factor on voltage reduction. One can reduce the thickness of the Alq_3 layer for lowering the operating voltage. However, the thickness reduction unavoidably results in high leakage current and low quantum efficiency.

Hamada *et al.* [194] reported that bis(5-hydroxy flavonato) beryllium had better electron transport property than Alq_3, whereas a bias of 8 V was still required to generate a luminance of 2000–3000 cd m^{-2}. Hung and Mason [195] reported that the use of copper phthalocyanine (CuPc) as the ETL combined with an ultrathin LiF/Al bilayer between the ETL and the emitting Alq_3 layer resulted in a reduction in the operating voltage by about 40%: from 8 V required to generate a current density of 100 mA cm^{-2} when Alq_3 was used as the ETL to 5–5.5 V. Another ETL composed of a Cs:phenyldipyrenylphosphine oxide ($POPy_2$) layer with an atom:molar ratio of 1 : 2 has been employed by Oyamada *et al.* [196], which resulted in a current conduction of 100 mA cm^{-2} at 3.9 V. The formation of a CsAl alloy layer of Cs:$POPy_2$/Al cathode interface and the charge-transfer complex between the Cs and $POPy_2$ contributed to attaining enhancement of the efficiency of electron injection and transport. An extremely low driving voltage of 2.9 V at a current density of 100 mA cm^{-2} and very high luminance at a low driving voltage have been demonstrated in an OLED: 1000 cd m^{-2} at 2.4 V, 10 000 cd m^{-2} at 2.8 V, and 920 000 cd m^{-2} at 4.5 V. In the OLED, the use of p-doped alpha-sexithiophene and n-doped phenyldipyrenylphosphine oxide carrier transport layers generated free charge carriers by charge transfer from matrix to dopant molecules, resulting in an increase in electrical conductivities and formation of Ohmic contacts at metal/organic interface [197].

As stated earlier, an imbalance of charge injection will contribute to current but not emission. Due to the unavailability of high work function metals, electrons are easier to inject. Thus, the number of holes injected is the limiting factor in terms of excitons formed. Along these lines, but in an attempt to decrease the number of excimer complexes formed between polymer chains, Sainova *et al.* [198] introduced several different hole-transporting materials into a single-layer OLED. The OLEDs were prepared from poly(2,7-(9,9-bis(2-ethylhexyl))-*co*-(9,9-bis((3S)-3,7-dimethyloctyl)) fluorine) (PF C26) blended with several low molecular weight hole-transporting molecules (HTMs) – a triphenylamine derivative (TPTE), starburst amine (ST 755)) and *N*,*N*8-diphenyl-*N*,*N*8-bis-α-naphthylbenzidide (ST 16/7) at weight ratio 1–0.03. Due to the differing oxidation potentials (electron affinity), the HTMs acted as hole traps, as was evidenced by thermoluminescence (TL). A shift to a higher temperature (by ~50 K) of the peak of the TL clearly indicates the existence of deep trapping sites. The sites effectively reduced hole mobility as well as established a space charge field, which allowed both increased quantum efficiency and a reduction in long-wavelength emission. Obviously, a similar approach could be employed in molecular-based systems.

Because the internal quantum efficiencies of phosphorescent OLEDs can now reach ~100% [199], the natural direction that much of the current research is going is toward increasing the external quantum efficiencies, η_{ex}, because this figure has been typically estimated to be as low as 0.17–0.5 [200, 201]. This substantial loss arises due to light incident to the substrate–air interface or the organic–substrate interface at angles greater than the critical angles, that is, total internal reflection occurs (Figure 1.98).

Various methods have been used to increase the external efficiencies of OLED devices (Figure 1.98b–f) including surface roughening [203], introduction of an aerogel layer [204], an integrated distributed feedback gratings [205], scattering microspheres [206], microlenses [207], mesa structures on which to build [208], or by use of microcavities [209–211]. Each of these methods have their own advantages and disadvantages in terms of cost, production feasibility, polarization effects, dispersion effects, changes in spectral linewidth, and of course extraction efficiency, and as such a method for use in an illumination application may not be feasible for a display application. For details on these and other mechanisms refer to Ref. [202] and the corresponding literature.

1.17.2
Charge and Energy Transport Fundamentals

Unlike the inorganic LEDs, where high degrees of crystallinity and close-packed atomic structure favor higher electronic conductivity, strong exchange interactions often do not exist in the disordered organics. Intermolecular separations are large as compared to separations of atoms in the inorganic's lattices, because the organics interact by weak van der Waals or London type forces. This implies that molecular orbitals weakly overlap and intermolecular electron exchange is small. Hence, electron orbitals are localized (except in the case of the fully conjugated polymers) making some argue that hopping or tunneling are the favored methods of charge migration in the organics [212].

In organic materials with localized energy states, energy can be transferred without the transport of mass or charge. Fortuitously, energy transfer within an organic material is less sensitive than charge transport to structural disorders (traps). This stems from the fact that unlike the inorganics, organics do not exhibit conventional Mott–Wannier excitons. The more localized, mobile Frenkel excitons are the energy-transfer mechanisms, and due to their strong Coulombic interactions, they can be thought of as essentially neutral and hence not subject to the all of the trapping mechanisms inherent in the quasiamorphous system [212].

Unlike the inorganic semiconductors, where thermal excitation can lead to substantial dark conductance, the dark conductivity of organic systems that are not intentionally doped varies vastly from family to family of organic solids. This could arise from intrinsic excitation ($\Delta E < 2$ eV) or defect excitations ($\Delta E > 2$ eV). From this stems the long debate of whether the band model (often under Bloch's one-electron potential approximation) or a nonband model (hopping or tunneling) is appropriate for the discussion of carrier transport. Either way, charge carriers often suffer from

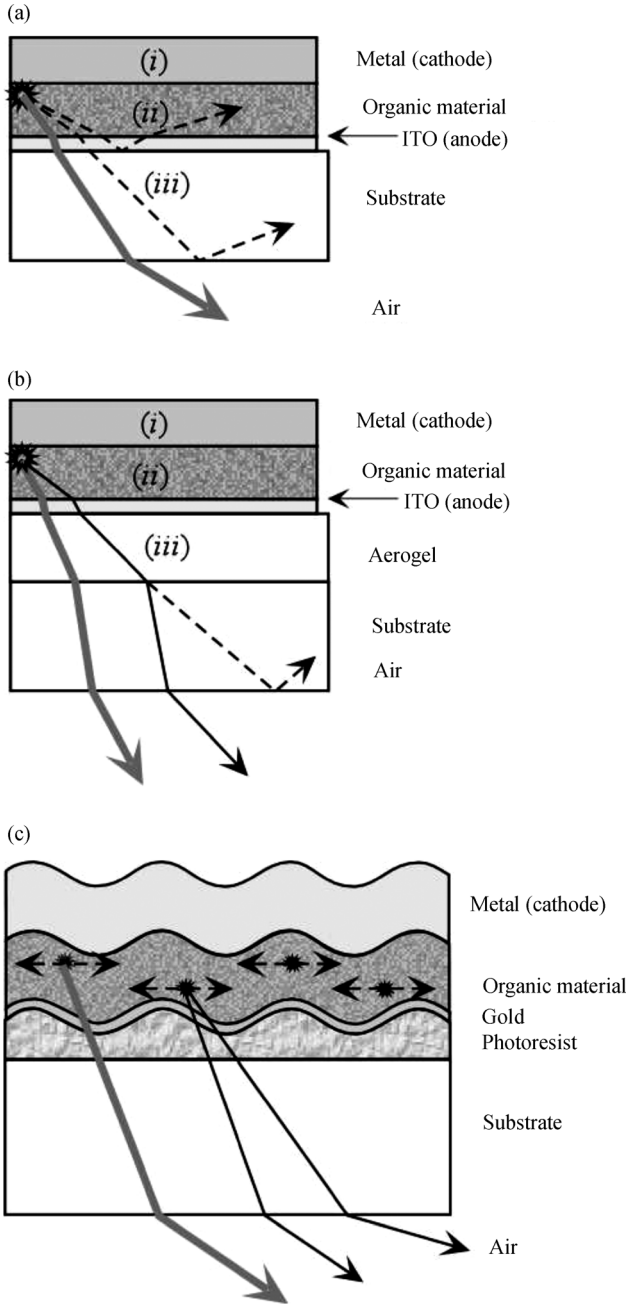

Figure 1.98 (a) Schematic of losses reducing extraction efficiency; (b–f) various methods utilized to extract light from OLED device [202].

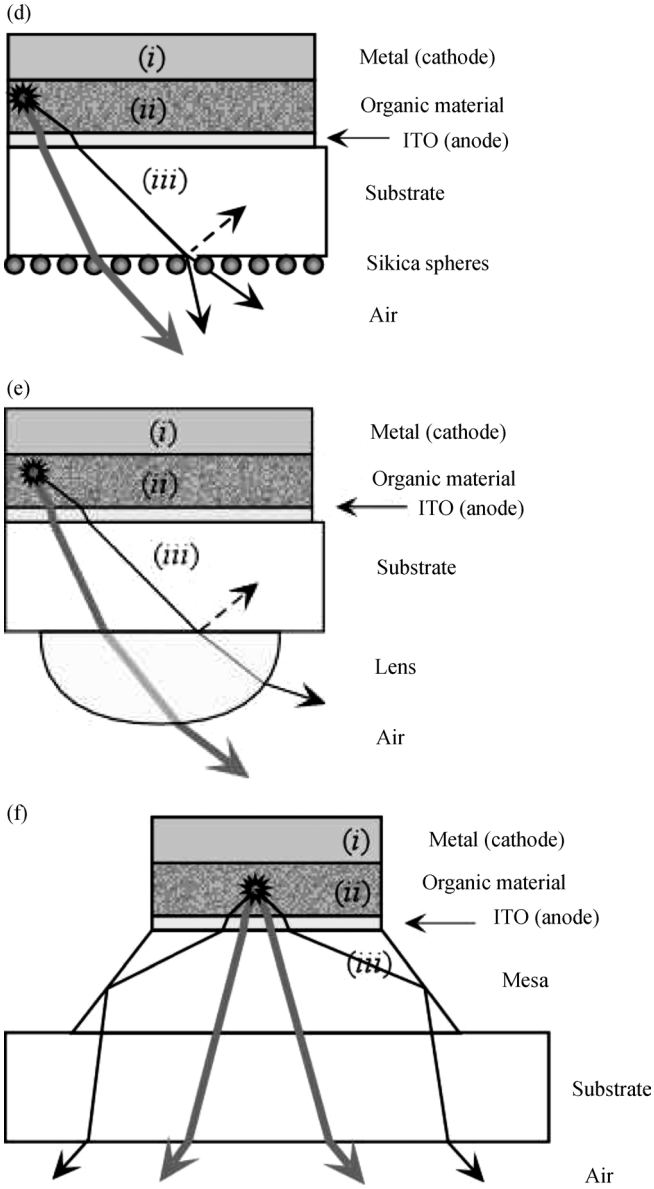

Figure 1.98 (*Continued*)

very low mobilities. The inherent disorder of the system causes interaction between free carriers and the surrounding "lattice" via polarization effects including charge-induced dipole interactions, dipole-induced dipole interactions, charge–dipole interactions, charge–quadrupole interactions, superpolarization effects, charge-induced

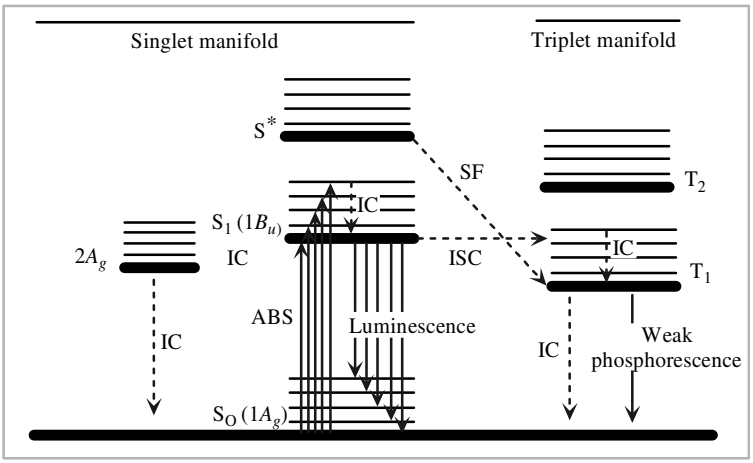

Figure 1.99 Schematic of the radiative and nonradiative recombination processes [191].

quadrupole interactions, and energy contributions from higher order multipoles. Chemical impurities, whether intentional or not, affect the electrical properties in that trapping occurs as differing electron affinities (ionization potentials) behave as traps or antitraps.

This brings us to the issue of recombination. The goal here for the LED is for the recombination to be radiative. Once the charges are injected into a device, depending on the relative alignment of the spins, phonon interaction, orbital overlap, and long-range order, electrons and holes form negative and positive polarons, as they are coupled with the lattice. These polarons migrate across the electron transport or hole transport layer to the emissive layer and form singlet or triplet excitons as they meet. In turn, either electroluminescence occurs due to the fluorescent decay of singlet excitons from the first excited state (S_1) to the ground state (S_0) or eventual phosphorescent decay of triplet excitons takes place, as shown in Figure 1.99.

1.17.3
Properties of Organic Crystals

Not only the organic emissive layers must convert energy to useful amounts of light but also the device must be built in such a manner that the emitted light gets out of the OLED device. Investigations are moving from a focus on increasing the brightness and optimizing the efficiency of emission within the organic layer of the LEDs to optimizing the out-coupling of light from the device structure by incorporation of microcavities, shaped substrates, or index matching mediums [213].

Conjugated polymers are semiconducting owing to alternating single and double carbon–carbon bonds. Single bonds are called σ-bonds and double bonds include a σ-bond and a π-bond. While the σ-bonds can be found in all conjugated polymers, the π-bonds are formed from the remaining out-of-plane p_z orbitals on the carbon atoms overlapping with neighboring p_z orbitals. The π-bonds are the source of the

semiconducting properties of these polymers. First, the π-bonds are delocalized over the entire molecule, and then, the overlap of p_z orbitals actually produces two orbitals, a bonding (π) orbital and an antibonding (π^*) orbital.

In terms of the electronic structure, the optical properties are related to the frontier orbitals: the HOMO produced by the lower energy π-orbitals and the LUMO produced by the higher energy π^*-orbitals. The energy difference between the two levels is equivalent to the bandgap that determines the optical properties of the material such as photon absorption and emission. The bandgaps for most conjugated polymers are between HOMO and LUMO in the range of 1.5–3 eV, and the absorption coefficient is $\sim 10^5\,\mathrm{cm}^{-1}$.

Ab-initio and semiempirical calculations have been undertaken and attribute the HOMO to the bonding π and LUMO to the antibonding π^* molecular orbitals determined by the overlapping of p_z orbitals [214, 215]. The body of knowledge of molecular orbitals indicates that any variation in overlap, such as geometrical modifications induced by the presence of substituent groups in polymers, interactions with solvents, and thermal effects, leads to modifications in the electronic structure, and thus optical properties [191].

Bathochromic (hypsochromic) shifts are observed in both the absorption and emission bands as a result of positive (negative) solvatochromism in organic materials. Similar to the inorganic class of LEDs, intensity can be related to temperature, with reduced vibrations at low temperatures causing an increase. Also, torsion of the chain in a polymer-based system reduces the overlap of p_z orbitals and increases the gap between π and π^* orbitals, which results in shorter conjugation lengths and that in turn causes a hypsochromic absorption shift [216].

Optical transitions in solid-state mode crystals are well known to be due to Frenkel excitons [217–219]. Properties resemble those of the isolated molecules because excitons are strongly confined in a molecule and only the weak interaction with the surrounding molecules takes place, which leads to biexcitation formation. The main effect of intermolecular interactions is to split each molecular state into different crystalline states, termed Davydov splitting [217]. These are characterized by different symmetries, as shown in Figure 1.100. If there is more than one molecule per unit cell, and the molecules are related by symmetry operations, the crystal wave functions are constructed out of the subsets of nonequivalent molecules. This exercise leads to representation of the crystal states, which are either symmetric or antisymmetric combinations of the subset wave functions [219]. This splitting of molecular states in crystalline states with well-defined symmetry strongly affects the relaxation processes of molecular excitations.

The electronic structure and transition levels between occupied and unoccupied excited states of molecules can be determined from various optical techniques (ultraviolet photoemission spectroscopy (UPS), X-ray photoemission spectroscopy (XPS) [220], and so on). An interesting feature found in the oligothiophenes is the crossing of states, with different symmetries, as a function of the chain length. The states of interest within the C_{2h} symmetry possess $1B_u$ and $2A_g$ symmetry. As the chain length and the number of double bonds are increased, the lowest optical transition changes from an allowed (B_u) to a forbidden transition (A_g) [191]. Another

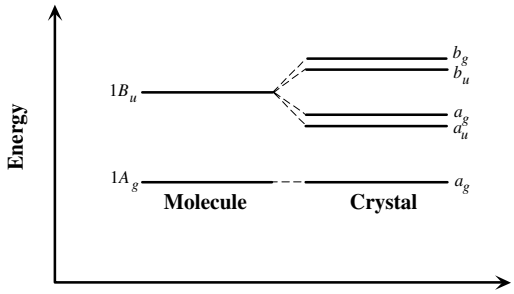

Figure 1.100 Energy diagram (calculated by semiempirical methods) of the electronic states for an isolated molecule (left) and in solid state (right). The presence of intermolecular interactions determines a splitting of the molecular states in a number of crystalline states depending on the number of equivalent molecules in the unit cell [191].

feature of interest in unsubstituted oligothiophenes is the linear dependence of the $S_0 \rightarrow S_1$ transition energy on the inverse number of rings forming the chain [221] (Figure 1.101). Intuitively, a substantial redshift of the lowest electronic transition occurs as the chain length is increased, which is a result of the progressive extension of the π-delocalized states. Instead, the change in size of the singlet–triplet $S_0 \rightarrow T_1$ transition energies with chain length is much weaker than that for the $S_0 \rightarrow S_1$ excitation [221]. The singlet–triplet excitation is only lowered by ~0.2 eV when going from the dimer to the hexamer, whereas a bathochromatic shift of ~1.4 eV is observed for the singlet–singlet transition $S_0 \rightarrow S_1$. Such behavior, in fact, reflects the stronger confinement of the triplet exciton with respect to those associated with singlets. This trend is consistent with optically detected magnetic resonance (ODMR) data for polythiophenes, which indicate that the T_1 triplet state barely extends more

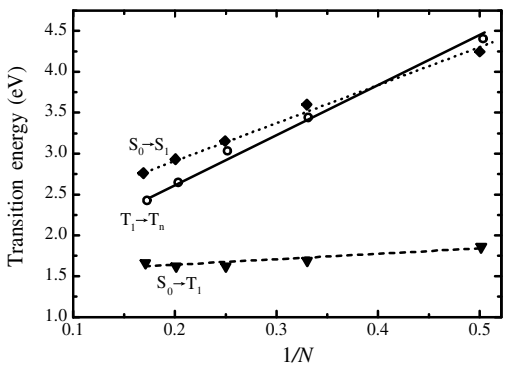

Figure 1.101 Chain size dependence of the $S_0 \rightarrow S_1$ transition energy between the ground state (S_0) and the first excited singlet state (S_1), of the singlet–triplet transition energy $S_0 \rightarrow T_1$, and of the triplet–triplet transition energy $T_1 \rightarrow T_n$ [191].

than a single thiophene unit [222]. A larger delocalization of the higher lying triplet state, T_n, leads to a more noticeable redshift of the $T_1 \rightarrow T_n$ transition versus $1/N$ as shown in Figure 1.101.

The exciton binding energy of the conjugated polymers has been the subject of debate in the literature over the past decades. Reporters have proposed the values between a few k_bT (k_bT in the order of 10^{-5} eV) and 1 eV for the binding energy [223–225]. It seems that people accept that most conjugated polymers have a binding energy of about 0.3 eV–0.4 eV [224, 226]. Also relevant is the diffusion length of singlet excitons, which is in the range of 5–15 nm, and the radiative decay associated with them in a timescale of 100–1000 ps [227].

At first, the efficiencies of OLEDs were limited due to the materials used; radiation only resulted from singlet relaxations, relaxations conserving spin symmetry. These extremely rapid (~1 ns) transitions are typically from singlet excited states to ground states, and the resulting photon emission is called fluorescence. Based on a spin statistics, the singlet excitation efficiency η_s was believed to have a maximum value of 25%. In other words, only 25% of excitons were supposed to be singlets, which was the only mechanism for producing photons. The remaining 75% of the excitons would therefore have resulted in triplet states, which do not lead to fluorescence. Consequently, this was thought to impose a 25% fundamental limit on the internal quantum efficiency of electroluminescence. However, further studies showed that the 25% figure was no longer valid in that singlet excitation could be as high as 50% in some π-conjugated polymers. This was attributed to a higher cross section for an electron–hole pair to form a singlet state versus a triplet, due to the delocalized nature of charged particles in π-conjugated polymers [228]. Nonetheless, in any organic system, it has become common to introduce phosphorescing materials, which can produce optical emission from triplets, into emissive layers in order to take advantage of the large majority of excitons that are triplets. By obtaining radiation from both singlet and triplet excitons, internal quantum efficiency can theoretically reach 100%. It should be noted that this technique has found more success in the molecular rather than the polymeric LEDs.

The problem with polymeric systems that include phosphorescing chromophores is that aggregation quenching reduces the quantum efficiency. The polymer systems are too disordered, and including chromophores on all chains yields a chromophore-rich system. Interchain interactions, especially the formation of excited states (exciplexes), lead to reduced radiative recombination as well as a bathromic shift in the spectrum.

By utilizing phosphorescing materials (dyes) in the emitting layers, luminous phosphorescence arises from the forbidden transitions that do not conserve spin symmetry. A sample of some of the molecules that have been used to achieve phosphorescence from triplet states is shown in Figure 1.102. Baldo *et al.* [229] showed that a phosphorescent yield of approximately <25% could be obtained with a 6% doping concentration of PtOEP in Alq_3. This corresponds to a >90% transfer of energy from Alq_3 to PtOEP, which means that both singlets and triplets must participate in energy transfer. They went on to suggest that the transfer was due to the

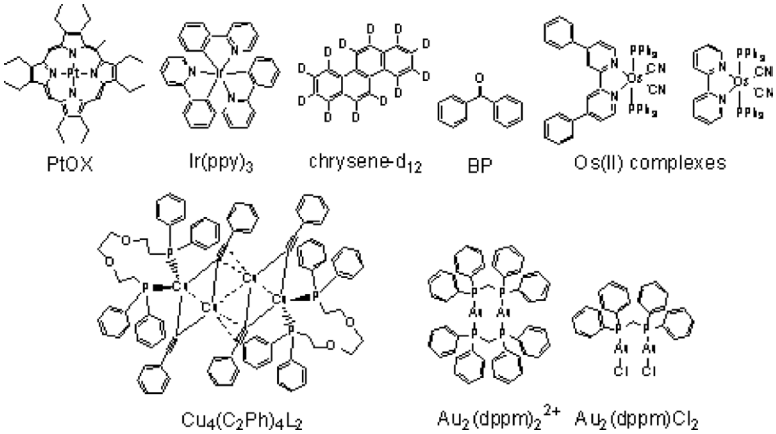

Figure 1.102 Chemical structure of important degenerate and nondegenerate conjugated polymers, reported to have been used to get phosphorescence from triplet states. The PtOX and the Ir $(ppy)_3$ are the most successful and produce red and green light, respectively.

Dexter process (short range, <4 nm) because of the high doping levels of PtOEP required to obtain high quantum efficiencies.

This suggestion was corroborated when the group introduced PtOEP into Alq_3 ~20 nm away from a recombination zone doped with DCM2, a fluorescent with efficient energy transfer from Alq_3. It was shown that the intensity of emission in the spectra attributed to the DCM2 was not reduced when the PtOEP was introduced, solidifying the Dexter transfer argument [229]. It has also been suggested that the emitting triplet state of a dye can be excited by an energy transfer from a singlet state of the host via Foerster transfer followed by a fast intersystem crossing (ISC) [230].

The group obtained the highest quantum efficiency for a red-emitting OLED in its time, 4% with a dopant concentration of 6%. However, the quantum efficiency decreased as current densities increased when a lower dopant concentration was used. Further, they found that this trend in quantum efficiency could be reversed by increasing the dopant concentration, which implied that the PtOEP sites were being saturated. This was attributed to the long lifetime of the PtOEP triplet exciton. Moreover, at doping concentrations above 6%, the quantum efficiency decreased no matter what current density was used, a limit to doping concentration. This was attributed to bimolecular quenching [230].

1.17.4
Light Emission Dynamics

As stated before, in order to achieve high efficiencies at high illumination levels, singlet relaxation (which occurs rapidly, $\sim 10^{-9}$ s) must be coupled with rapid relaxation of triplets. Light emission arising from triplet relaxation (phosphorescence) occurs at room temperature more strongly, that is, rapid relaxation occurs, when electron

spin–orbit coupling is most prominent, specifically in heavy transition metal complexes. Lanthanide as well as transition metal complexes have been successfully used in organic molecular as well as polymeric systems for phosphorescent light emission. In general, phosphorescent relaxation takes much more time to occur than fluorescence, typically on the order of >100 μs, and thus saturation of emitting sites will occur at high drive currents when the doping levels are low. High drive currents, additionally, render the phosphors prone to nonradiative recombination mechanisms: triplet–triplet annihilation, triplet–charge carrier interactions, and electric field induced triplet dissociation phenomena, and so the phosphorescing materials employed in the emitting layers should have the shortest lifetimes available.

In order to understand the dynamics of triplet relaxations, Baldo and Forrest [231] used transient electrophosphorescence to observe either the diffusion of triplets through a conductive host material or evidence of exciton trapping or direct formation of excitons on phosphorescing guest materials.

Let us first assume that triplet states are created. Now there are four processes that determine the overall efficiency of energy transfer between host and guest molecules: relaxation rates k_G and k_H of excitons from guest and host, respectively, and forward and reverse transfer rates of triplets from host to guest, k_F and k_R (Figure 1.103). The rate equations are then.

$$\frac{dG}{dt} = -k_G G - k_R G + k_F H$$

and

$$\frac{dH}{dt} = -k_H H - k_F H + k_R G, \tag{1.36}$$

where G and H are the densities of triplets in the guest and host. The solutions to these are biexponential decays of the form

$$G, H = A_1 \exp[-k_1 t] + A_2 \exp[-k_2 t], \tag{1.37}$$

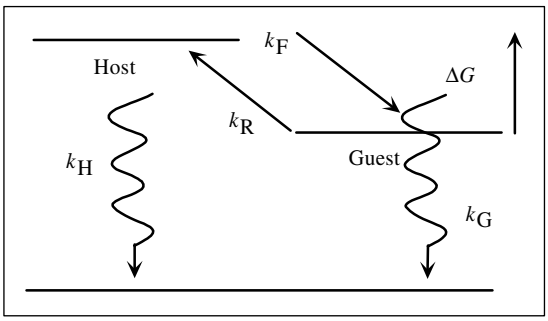

Figure 1.103 Triplet dynamics in a guest–host system: the rates of forward and back transfer k_F and k_R are determined by the Gibbs free energy change (ΔG) and molecular overlap; also of interest are the rates of decay from the host and guest (k_H and k_G), respectively [231].

where A_1 and A_2 are determined from initial conditions and the characteristic decay rates:

$$k_1, k_2 = \frac{k_F + k_R + k_H + k_G}{2} \times \left(1 \pm \sqrt{\frac{4(k_G + k_R)(k_H + k_F) - 4k_F k_R}{(k_F + k_R + k_H + k_G)^2}}\right). \quad (1.38)$$

Apparently, to maximize guest phosphorescence, we first seek $k_G \gg k_H$. This means that the host material has a very large triplet lifetime, allowing guest triplet relaxation even if the energy of the guest triplets is higher than that of the host triplets. Secondly, we seek $k_F \gg k_R \gg k_H$, which maximizes the population of guest triplets, thus reducing nonradiative losses from triplets in the host.

At low temperatures (high temperatures enhance the rate of nonradiative triplet decay), $k_H + k_G$ can be determined using the transient phosphorescent decay. The terms k_F and k_R can be understood after one considers the processes that are occurring. Dexter interactions permit exciton hops from molecule to molecule when there is no change in spin. In this manner, triplet hopping can be thought of as simultaneous transfer of an electron and a hole. With correction of the reorganization energy and comparison of the rates of triplet transfer with those of electron and hole transfer, the triplet transfer rate has been demonstrated [232] to be related to the electron and hole transfer rates predicted by Marcus theory. Marcus theory reflects the Franck–Condon principle: electron motion is so rapid during an electronic transition that the atomic configuration of the reactant and product states is unchanged. Marcus theory recognizes that the rate of transfer is not limited by the electron transfer itself, but rather the formation of the activated complex that precedes the transfer. These lead one to reason that the most probable activated complex is the one with minimal energy of formation (G, Figure 1.103), under the restriction that the total energy of the complex remains unchanged during the transfer. Transfer probability then takes the form

$$k = \sqrt{\frac{4\pi^3}{h^2 \lambda k_B T}} |M_{DA}|^2 \exp\left[\frac{(\Delta G + \lambda)^2}{4\lambda k_B T}\right], \quad (1.39)$$

where M_{DA} is the matrix element mixing donor and acceptor states. Measuring the phosphorescent spectra for the relaxed triplet state energies for both the donor and acceptor molecules gives ΔG, and if $\Delta G = 0$. Then the energy barrier in the forward and reverse directions is given by λ. For small changes in the free energy, Marcus transfer via an activated complex behaves similar to an Arrhenius barrier of $\sim\lambda/4$. As ΔG increases, the rate does as well until resonance, and with further increases in ΔG, the rate decreases yielding the so-called "Marcus inverted region."

Dexter transfer additionally requires of the molecules that combined spin be conserved during energy transfer. As an example,

$$^3D^* + {}^1A \rightarrow {}^1D + {}^3A^*. \quad (1.40)$$

Note that the singlet states in the host may be passed to the guest via the Dexter transfer, but if the spectral overlap is sufficient, long-range dipole–dipole or Foerster

energy transfer dominates. When the donor is phosphorescent, Foerster transfer from triplet of acceptor to singlet of donor molecules can be a very efficient energy-transfer method.

$$^3D^* + {}^1A \rightarrow {}^1D + {}^1A^*. \tag{1.41}$$

This is useful in transferring triplet states to singlets of the acceptor, or by employing a phosphorescing guest in a phosphorescing host. Unlike triplet–triplet transfer, donor and acceptor molecules are well coupled in Foerster transfer; hence, the rate depends on the overlap of donor emission and acceptor absorption [231].

Baldo and Forrest [231] used the following materials: (a) *N,N′*-diphenyl-*N,N′*-bis(3-methylphenyl)-[1,1′-biphenyl]-4,4′-dimine (TPD) (hole transport), (b) 2,9-dimethyl-4,7-diphenyl-1,10-phenanthroline (bathocuproine or BCP) (electron transport), (c) 4,4′-*N,N′*-dicarbazole-biphenyl (CPB) (hole transport), and (d) Alq_3 (electron transport) as host materials and (e) *fac* tris(2-phenylpyridine) iridium [$Ir(ppy)_3$] and (f) 2,3,7,8,12,13,17,18-octaethyl-21*H*,23*H*-porphine platinum(II) (PtOEP) as guest materials. The phosphor guests emit at ~510 nm with a phosphorescent lifetime of ~0.4 μs [229] and at 650 nm with a phosphorescent lifetime of 100 μs [233] for $Ir(ppy)_3$ and PtOEP, respectively.

The phosphorescent spectra of each of these materials were examined first to determine their triplet energy levels (Table 1.7). Films with a thickness of 2000 Å were subjected to 500 ps pulse at 1 Hz excitations from a N_2 laser emitting at a wavelength of 337 nm, and transient analyses using a streak camera separated delayed fluorescence from phosphorescence.

Turning now to diffusion of triplets in a host, Baldo and Forrest [231] intentionally left areas undoped between the phosphorescing zones and the exciton formation zones, forcing excitons to travel lengths of several hundred angstroms. By applying a short pulse, singlet and triplet excitons are created at the HTL/ETL interface. Then after excitation, the delay between fluorescence and phosphorescence is measured. Knowing that the delay must be attributed to either charge diffusion or triplet diffusion, a reverse bias is applied, effectively turning the charge diffusion to zero.

Table 1.7 Material triplet energies and room-temperature lifetimes.

Material	Triplet energy (±0.1 eV)	Triplet lifetime
PtOEP	1.9	110 ± 10 μs[a]
$Ir(ppy)_3$	2.4	0.8 ± 0.1 μs[b]
CBP	2.6	>1 s
BCP	2.5	<10 μs
TPD	2.3	200 ± 50 μs
Alq_3[c]	2.0	25 ± 15 μs

[a]6% PtOEP doped in CBP, photoexcitation density $<10^{17}$ cm^{-3}.
[b]6% $Ir(ppy)_3$ doped in BCP, photoexcitation density $<10^{17}$ cm^{-3}.
[c]The Alq_3 triplet energy is inferred from the phosphorescent spectra of related hydroquinoline complexes of Pb, Bi, Rb, and Ir [234]. The triplet lifetime is calculated from diffusion measurements.

By observing which systems exhibit phosphorescence in the presence of the reverse bias, they were able to determine whether triplet diffusion occurs or charge trapping and the formation of excitons directly on the phosphorescent molecule dominate the system.

Continuing, 8%PtOEP:Alq_3 and 6%$Ir(ppy)_3$:TPD exhibited energy transfer, while 8%PtOEP:CBP and 6%$Ir(ppy)_3$:CBP did not retain their phosphorescence in the presence of strong negative bias. It was assumed that the deep HOMO level of CBP that makes hole trapping likely on its guests. Furthermore, by utilizing several areas of differing widths, the triplet diffusion coefficients and lifetimes of the triplets were found (Table 1.7) and could be fitted to the diffusion equation:

$$\frac{d\varphi}{dt} = \frac{\varphi}{\tau} + D_T \frac{d^2\varphi}{dx^2}. \tag{1.42}$$

1.17.4.1 Nonradiative Recombination

As in the case of other materials, competing nonradiative processes reduce the quantum efficiency. Nonradiative decay channels can be intramolecular, such as internal conversion (IC), ISC, and singlet fission (SF), or intermolecular, such as the formation of aggregates and charge-transfer excitons (CTEs). Additionally, in the solid state, quenching of the singlet excitons may occur due to extrinsic or conformational defects [235] (see Figure 1.99).

1.17.4.2 Internal Conversion

Internal conversion depicts relaxation from a highly excited state into a state of lower energy, within the same manifold, either in the singlet form or in the triplet form, by emission of phonons. This process is quite fast, generally, on the order of a femtosecond. Internal conversion can provide a nonradiative decay channel if the transition from the high energy state into the ground state is forbidden by the symmetry of the wave function of the relaxing state. If the lowest singlet excited state is, for instance, a $2A_g$ singlet state, radiative transitions to the ground state are symmetry forbidden and the coupling with the ground state is possible only via phonon emission, which precludes radiative recombination.

1.17.4.3 Intersystem Crossing

Intersystem crossing describes energy transfer between the singlet and triplet manifolds. Subsequent internal conversion usually leads to the decay into the lowest triplet state (T_1), which is nonradiative [236]. The rate of intersystem crossing is governed by the spin–orbit coupling term [237], which is enhanced in the presence of heavy atoms. As stated above, however, given the proper system, this can be a method of harnessing electroluminescence when the crossing is done in a material suited to phosphoresce from triplet excitons.

1.17.4.4 Singlet Fission

Singlet fission consists of the generation of two triplet excitons from the fission of one singlet excited state. The excited singlet state may be the lowest excited singlet state

S_1, or a higher excited singlet produced by singlet–singlet fusion under intense irradiation. In order for singlet fission to be an energetically allowed process, the energy of the singlet excited state undergoing fission must be at least twice that of the triplet excited state. Considering the case of the lowest singlet state S_1, which may play a role in the nonradiative decay of oligomers, it must be $E(S_0 - S_1) \geq 2E(S_0 - T_1)$. Belijonne *et al.* [221] showed that this condition is satisfied for short oligomers, but it is not for longer oligomers.

1.17.4.5 Aggregation and Davydov Splitting

Aggregation and Davydov splitting Davydov splitting is the emergence of additional electronic levels due to vibrational couplings between molecules once they are brought together. The effect of different crystalline structures on the electronic states has been accounted for by considering a simple one-dimensional model in which an infinite number of molecules are ordered and located at distance a (Figure 1.104) from one another. If only the first neighbor interactions are taken into account, the energy of an excited state can be expressed as [191].

$$E^e(0) \approx \Delta E^e + D^e + L^e(\vec{k}) = \Delta E^e + D^e + 2d^2 \frac{1-3\cos^2(\alpha)}{a^3} \cos(\vec{k}\, a),$$

where d is the yield of the dipole transition and α is the angle between the dipole and the straight line a. In Figure 1.105, the $k = 0$ exciton energy versus the angle α is shown. For $\alpha > 54.7^\circ$ (H-aggregates), the resonance interaction $L^e(\vec{k})$ is positive and the excitonic state energy is larger than that for the single molecule. For values of $\alpha < 54.7^\circ$ (J-aggregates), the resonance interaction is instead negative and the excitonic state energy is lower than that for single molecule. The energy of the $k = \pi/a$ excitonic state (all the other $k \neq 0$ excitonic states are not optically allowed) is also shown. If the supramolecular structure is that of an H-aggregate, the lowest energy state where thermalization occurs is optically forbidden, determining a quenching of the PL efficiency. Actually, this selection rule is strictly valid only for

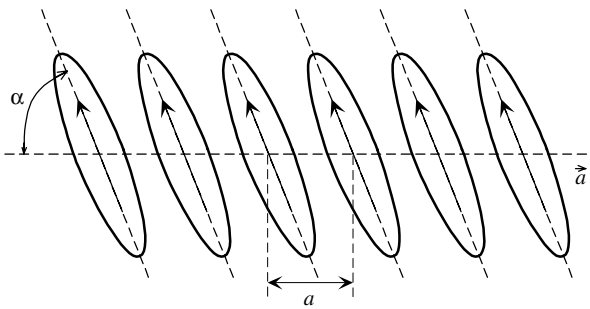

Figure 1.104 One-dimensional crystal model. An infinite number of molecules, forming an angle α with the $\hat{a}$ axis, are periodically located at distance a [191].

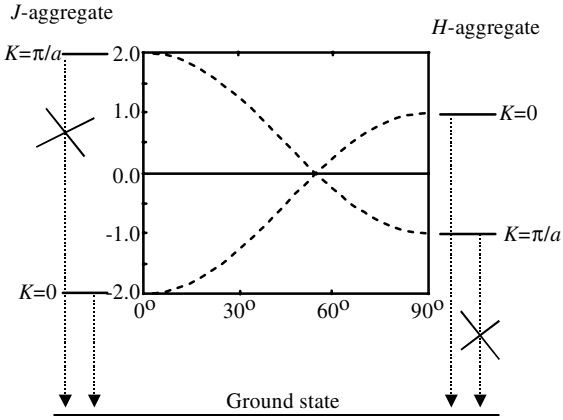

Figure 1.105 Evolution of the $k = 0$ excitonic state energy with the angle α. For values of $\alpha < 54.7°$ (*H*-aggregates), the resonance interaction is negative and the excitonic state energy is lower than that of the single molecule. For values of $\alpha > 54.7°$ (*J*-aggregates), the resonance interaction is positive and the excitonic state energy is larger than the single molecule one. The energy of the $k = \pi/a$ excitonic state (as all the other $k \neq 0$ excitonic states are not optically allowed) is also shown. If the supramolecular structure is that of an *H*-aggregate, the lowest energy state is optically forbidden [191].

an ideal infinite single crystal. The dipole selection rules are relaxed when the crystalline size is reduced or in the presence of disorder, meaning otherwise forbidden transitions may be allowed, albeit not very efficiently.

1.17.4.6 **Charge-Transfer Excitons**

The focus has so far been on neutral excitations where the charges are not separated, but localized on the same oligomer unit (Frenkel excitons). Excitations where a separation of charges occurs are termed as CTE) and consist of a weakly bound electron–hole pair localized over two or more adjacent oligomers (Figure 1.106). CTE represents the intermediate step between excitons and carrier separation. If the weakly bound electron–hole pair recombines readily, it can in fact form the intramolecular singlet exciton before charge separation occurs, which leads to a new nonradiative channel. In order to establish how efficient this nonradiative channel is, the energy separation between the intramolecular Frenkel excitons and CTE must be taken in account. This depends on the oligomer chain length, the first ionization energy, the electron affinity, and the intermolecular distance. An increase of the oligomer chain length leads to a larger π-electron delocalization and a stronger π–π van der Walls force, which increases the electron affinity and reduces the intermolecular distances as well as the first ionization potentials. All of these factors tend to reduce the energy separation between the intermolecular charge-transfer excitons and the intramolecular Frenkel excitons and determine a competing nonradiative decay channel.

Charge-transfer excitons are not easily observed in the linear absorption spectrum due to the poor overlap between the wave function of the ground state, localized on a

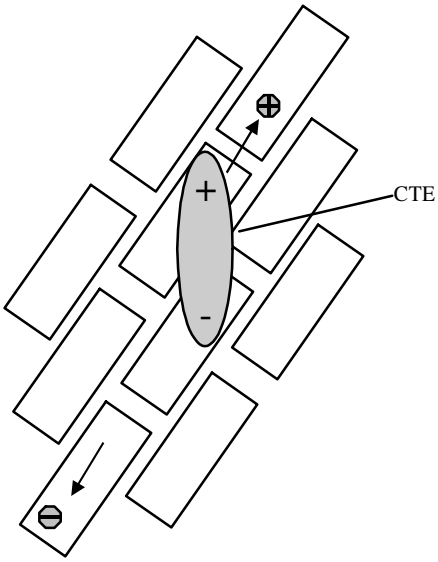

Figure 1.106 Excitations where a separation of charges occurs are termed as CTE. They consist of a weakly bound electron–hole pair localized over two or more neighboring oligomers. The CTE is the intermediate step toward carrier separation and transport [191].

single oligomer, and excited states spread over two or more adjacent oligomers. However, they can be observed in electric field modulated spectroscopy [238]. This method exploits the large dipole moment of the excited states, which generates an electroabsorption signal proportional to the second derivative of the absorption spectrum. Nevertheless, CTE have been identified for many conjugated molecules and the corresponding energies are much higher than those of the respective first singlet absorption bands [239]. The interested reader can find details on these nonradiative channels as well as quenching mechanisms in Refs [191, 240] and the references therein.

1.17.5
OLED Devices

It is curious to note that iridium complexes can be utilized in the production of all colors, because the strong spin–orbit coupling induces short triplet lifetimes (typically on the order of 1–14 μs [241]) in many of the molecules employing iridium as the heavy metal. The reduced lifetime also translates into sustained efficiency at high current drives.

Red, green, and blue polymer- and molecular-based systems using metalorganic phosphorescing complexes utilizing Pt or Ir heavy metals have been developed, pushing internal quantum efficiencies to nearly 100%, which cannot yet be realized externally. Increasing the ability to out-couple the light is a major challenge to be faced

Table 1.8 Performance in terms of efficiency and lifetime for organic emitters [260].

Color	Red	Green	Blue [242]
CIE (x, y)	0.64, 0.36 or 0.65, 0.35	0.38, 0.59 or 0.36, 0.61	0.16, 0.37
Luminous efficiency ($cd\,A^{-1}$)	28 at 1000 $cd\,m^{-2}$ or 24 at 1000 $cd\,m^{-2}$	67 at 1000 $cd\,m^{-2}$ or 56 at 1000 $cd\,m^{-2}$	22
Lifetime (h)	330 000 at 1000 $cd\,m^{-2}$ or 300 000 at 1000 $cd\,m^{-2}$	250 000 at 1000 $cd\,m^{-2}$ or 75 000 at 1000 $cd\,m^{-2}$	15 000 at 200 $cd\,m^{-2}$

[a] *Source*: http://www.universaldisplay.com.

in both molecular and polymeric systems. Molecular systems currently enjoy external efficiencies of 20–40%, while the polymeric systems only achieve 2–10% external quantum efficiencies. The data shown in Table 1.8 represent some of the best results in terms of efficiency and lifetime for red, green, and blue phosphorescent small molecule-based OLED devices from Universal Display Corp.

1.17.5.1 White OLEDs

Similar to the approach to white light with the inorganic LEDs, the organic molecules or polymers can be simultaneously stimulated so that the overall emission spectrum of the device appears white to the eye. This is commonly done by segregating the red-emitting molecule from the green-emitting molecule and the blue-emitting molecule in the formation of a multilayered structure, which would usually be done by sequential evaporations. Obviously, this is a more costly way of producing white light than if the different molecules or polymers could be blended together and then simply spun on a substrate, but combining them into one emitting structure has a problem in that the emission band of the molecule with the higher energy emission will typically overlap the absorption band of the other molecule, resulting in Foerster transfer and, say, only red light emitted. In addition to the cost of segregating the emitting layers, further problems in terms of balancing the injection of carriers into each layer and trapping the excitons within each layer are problematic [243]. Although some groups have fabricated white LEDs from only two emission bands and still had good color rendering, the complexity with respect to charge injection and exciton confinement problems still resides [244].

In a different, much more cost-effective approach by Thompson *et al.* [245], four molecules whose individual spectrums all lie in the blue were blended together in every possible combination of two. Because of the significant overlap in the LUMO of the blue species, exciplex (a complex formed between the excited state of a molecule and the ground state of a different molecule, as shown in Figure 1.107) formation becomes likely. Excitation of the molecule with the lowest electron affinity, the donor, is followed by electron transfer to the other molecule, the acceptor, and results in a complex electron–hole pair, which can then decay via photon emission, considerably redshifted compared to that from either of the individual molecules. The donor molecule can be identified from the photoluminescence excitation (PLE) spectrum.

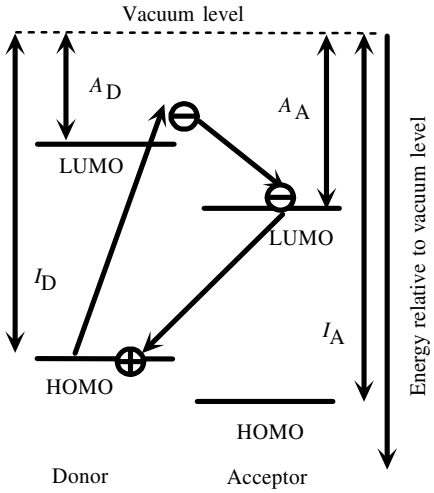

Figure 1.107 Energy band diagram showing the mechanism of exciplex formation. A_D, I_D, and A_A, I_A are the electron affinities and ionization potentials of the donor and acceptor molecules, respectively [245].

Photoluminescence spectra of five of the six sets showed broadband radiation with no peaks attributable to any individual molecule. UV–visible absorption spectroscopy of the spin-coated films showed the absence of any new chemical species that might give rise to redshifted emission. This phenomenon is characteristic of exciplex formation. Because highly demoralized π orbitals are characteristic of the LUMO of conjugated organics, it follows that it is indeed exciplex formation that causes the broadband white light [245]. In general, exciplex emission is inefficient, however, because its transition dipole moment is lower than that of fluorescence, that is, transition from the singlet excited state to the ground state of the individual component(s) [246]. Typical efficiencies of these devices are very low, often $<\sim 0.6$ lm W^{-1}, and therefore are not suitable [243].

Kawamura *et al.* [247] employed sensitizers and multiple dopants to improve the quantum efficiency of polymer OLEDs, which have been less successful in terms of brightness and efficiency. The group used sensitizing phosphors with triplet-state energies between those of the host and the emitting dopant. To examine sensitized phosphorescent energy transfer, the group fabricated devices employing $Ir(ppy)_3$ as a sensitizer for $Btp_2Ir(acac)$ codoped in PVK. Two series of devices were investigated: one with 5 wt% $Ir(ppy)_3$ and 0.5–4 wt% $Btp_2Ir(acac)$, and the other with 1–5 wt% $Ir(ppy)_3$ and 5 wt% $Btp_2Ir(acac)$. As inferred from the spectra and CIE coordinates of the several devices, the emission color changed from greenish yellow (for 5% $Ir(ppy)_3$ in 0.5% $Btp_2Ir(acac)$) to reddish orange (for 5% $Ir(ppy)_3$ in 4% $Btp_2Ir(acac)$). This spectral change with the proportional decrease of the green emission as the concentration of $Btp_2Ir(acac)$ increases indicates the existence of energy transfer between the two phosphors. Here, a maximum efficiency for the red device,

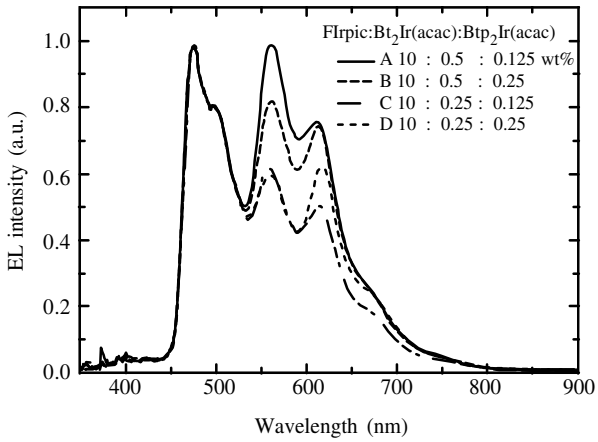

Figure 1.108 EL spectra of white-emitting FIrpic:Bt_2Ir(acac): Btp_2Ir(acac) PHOLEDs at a current density of $J = 10\,mA\,cm^{-2}$ (doping in wt% of device A: 10 : 0.5 : 0.125; device B: 10 : 0.5 : 0.25; device C: 10 : 0.25 : 0.125; device D: 10 : 0.25 : 0.25) [247].

corresponding to 5% $Ir(ppy)_3$ in 4% Btp_2Ir(acac) is $\eta_{ext} = 3.3 \pm 0.2\%$, or approximately 1.5 times higher than that obtained for the unsensitized device. Furthermore, at $\eta_p = 1.2\,lm\,W^{-1}$, the power efficiency is approximately doubled. This is a result of the increased quantum efficiency of the sensitized device, coupled with its lower operating voltage that is due to the improved hole-transporting characteristics of Ir (III) complex doped devices.

To further test the mechanism of sensitization and energy transfer, the PVK emissive region was triply doped with FIrpic for blue, Bt_2Ir(acac) for yellow, and Btp_2Ir(acac) for red emission. Doping concentrations of FIrpic, Bt_2Ir(acac), and Btp_2Ir(acac) were 10, 0.25 or 0.5, and 0.125 or 0.25 wt%, respectively. The EL spectra at $10\,mA\,cm^{-2}$ for devices with different combinations of dopant concentrations are shown in Figure 1.108. As expected, each device exhibits white luminescence due to mixed emission from the three constituent phosphors. The CIE coordinates of devices with 0.5 wt% Bt_2Ir(acac) (devices A and B) are (0.37, 0.42), whereas the 0.25 wt% Bt_2Ir (acac) device has closer to an "ideal" white emission at (0.33, 0.41). The 0.25 wt% Btp_2Ir (acac) devices (B and D) exhibited a higher CRI = 77 as the result of the enhancement of red peak than that of the 0.125 wt% devices (A and C) with CRI = 72 and 71, respectively.

Figure 1.109 shows the current dependence of both η_{ext} and η_p for the white PHOLEDs in Figure 1.108. The current characteristics of the devices were categorized into two types by the concentration of the red dopant, Btp_2Ir(acac). The maximum $\eta_{ext} = 2.1 \pm 0.1\%$ was achieved in device D, also having the closest to ideal CIE and CRI for white emission. When compared with the peak efficiencies obtained using these dopants in monochromatic devices, this high η_{ext} indicates very efficient energy transfer from the host to the several dopants in the blended luminescent layer. Note that the sensitization due to the blue dopant is minimal

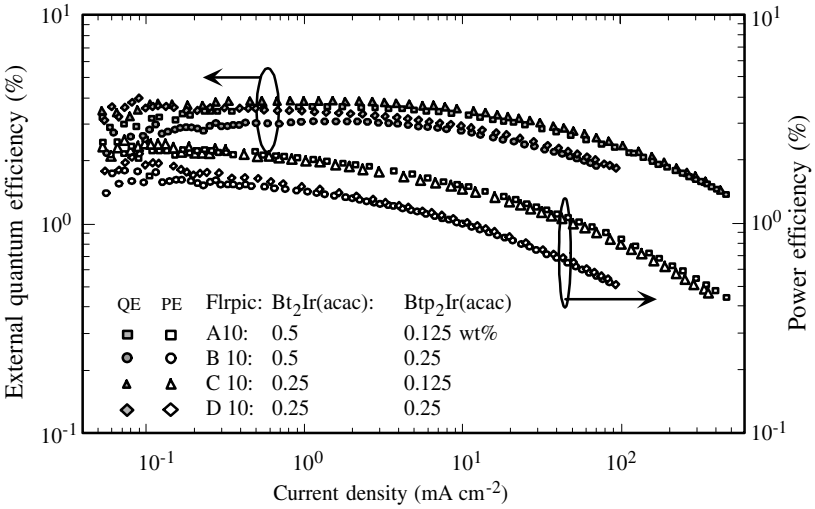

Figure 1.109 Dependence of η_{ext} and η_p on current density for the white-emitting PHOLEDs in Figure 1.108 (squares, device A; circles, device B; triangles, device C; diamonds, device D) [247].

because its energy levels are more displaced from those of the red and yellow dopants by a larger energy than the host, PVK. Indeed, given the range of low trap energies available to the polymer backbone, the most likely energy-transfer mechanism is via direct hopping from the polymer to the three individual dopants, with little interaction between the dopants themselves. The maximum power efficiency obtained was $\eta_p = 1.4 \pm 0.1\,\mathrm{lm\,W^{-1}}$ at 10 V for device A. Further, the maximum brightness was $L = 6800\,\mathrm{cd\,m^{-2}}$, which was achieved at $J = 295\,\mathrm{mA\,cm^{-2}}$ for device C. These results for nonoptimized OLEDs show the advantage of phosphorescence compared with previous reports for fluorescent polymer white devices having $\eta_p = 0.83\,\mathrm{lm\,W^{-1}}$ at 10 V, and for polymer blends where $\eta_{ext} = 1.2\%$

Adamovich *et al.* [243] have demonstrated a remarkably efficient OLED utilizing only one dopant. By exploiting a series of platinum(II) [2-(4,6-difluorophenyl)pyridinato-N,$C^{2'}$] β-diketonates, the group was able to extract photons from both the monomer and aggregate species codoped in an emissive layer of either *N,N′*-dicarbazolyl-4,4′-biphenyl (CBP) or *N,N′*-dicarbazolyl-3,5-benzene (mCP). Optimizations of the systems include ensuring that the light renders well and keeping quantum efficiency as high as possible. The spectra of the emitted light are dependent on the ratio of emission of monomer to aggregate states, and the concentration of dopant introduced plays a role in the carrier transport, and thus the quantum efficiency. By modifying the configuration of the dopant, and introducing an electron-blocking material, fac-tris(1-phenylpyrazole)iridium(III) (Irppz) to confine charge and energy in the emitting area, the group obtained very efficient white OLEDs. Doping the CPB with 10% of the single dopant resulted in a peak brightness of $8000\,\mathrm{cd\,m^{-2}}$. The maximum QE was $3.3 \pm 0.3\%$ ($7.3 \pm 0.7\,\mathrm{lm\,W^{-1}}$) at $0.5\,\mathrm{cd\,m^{-2}}$,

with this dropping to $2.3 \pm 0.2\%$ ($5.2 \pm 0.3\,\mathrm{lm\,W^{-1}}$) at $500\,\mathrm{cd\,m^{-2}}$; however, CIE coordinates and a CRI of 67 were unchanged as the brightness changed.

The record for the largest white OLED (WOLED) is held by researchers at GE, who presumably are utilizing a blue-light-emitting polymer along with several downconverting phosphors. The press release [248] in March 2004 of a $24 \times 24\,\mathrm{in^2}$ white OLED emitting at $15\,\mathrm{lm\,W^{-1}}$ came with no indication of how the group realized the large emitter, of lifetime, or of CRI, but a previous report when the group achieved their $1 \times 1\,\mathrm{in^2}$ (operating at $3.8\,\mathrm{lm\,W^{-1}}$) prototype indicated the use of a polyfluorene-based light-emitting polymer and the downconverting layers consisted of organic molecules (perylene orange and perylene red) and inorganic phosphor particles (Y(Gd)AG:Ce) [249].

Konica Minolta developed the most efficient WOLED with power efficiency of $64\,\mathrm{lm\,W^{-1}}$ at $1000\,\mathrm{cd\,m^{-2}}$ – a brightness that is appropriate for low-level lighting applications. Applying Konica Minota's own highly efficient and long-life blue phosphorescent material, along with multilayer design technology and innovative optical design technology, developing an OLED having a practical light emission level of approximately 10 000 h was succeeded.[5)] A fluorescent blue, a phosphorescent green, and a phosphorescent red emitter stack with a CRI of 95 (CIE coordinates: 0.35, 0.37) has also been reported. In addition, the efficiency is quite high at $16.3\,\mathrm{lm\,W^{-1}}$ emitting at $1000\,\mathrm{cd\,m^{-2}}$ [250].

The significant improvements in the lifetime of WOLEDs were achieved by Novaled with a white OLED emitting at $1000\,\mathrm{cd\,m^{-2}}$ and having a lifetime of 100 000 h and a power efficiency of $35\,\mathrm{lm\,W^{-1}}$. The device exhibits CIE color coordinates of $x, y = 0.43/0.44$ with a CRI of 90. The OLED features a stacked setup with blue fluorescent and red/green phosphorescent emitter materials (hybrid approach). For the stacking layer and transport layer, Novaled proprietary materials have been used. The OLED device is equipped with a standard outcoupling enhancement film. At a higher brightness level of $4000\,\mathrm{cd\,m^{-2}}$, the efficiency was $31\,\mathrm{lm\,W^{-1}}$, with no significant changes in color and CRI value.[6)]

1.17.5.2 **Displays**

Early attempts at producing polymer-based displays included using broadband emission followed by red, blue, or green filtering [251] or use of pixilated microcavities [252]. As the technology evolved, polymer-based displays have been typically fabricated by either screen printing techniques [172], which have problems in terms of the deposition accuracy of pixels for high-resolution systems, or ink-jet techniques [173], which often become difficult when subsequent depositions each require the wetting of the substrate in order for the correctly positioned polymers (red, green, and blue) to connect. Tedious laser-induced thermal imaging (material transfer from one substrate to another via local heating) [253] and reductive

5) The press release by Phillips, June 2006: http://konicaminolta.jp/about/release/2006/0630_01_01.html.

6) The press release, Lumileds/Philips, December 2007: http://www.novaled.com/news/2007_11_05_pr.html).

laser-induced bleaching (mixing red and green emitters in a blue host and tuning by local photoinduced process) [254] have also been applied to colored OLED fabrication. Synthesizing red, green, and blue poly(spirobifluorene-*co*-fluorene) polymers with oxetane side chains, Muller *et al.* [255] showed a promising method in which standard photolithography techniques can be used. The oxetane side chains effectively cross-link, when photostimulated, resulting in insoluble polymer networks in desired areas. Performance in terms of η_{max} was 3.0, 6.5, and 1.1 cd A^{-1}, for the blue, green, and red cross-linked polymers, respectively. The excitement revolving around these so-called spiro compounds is because they allow multiple "polymer" layers to be fabricated with ease (spin coating) and have high morphologic stability [256].

Molecular systems are somewhat the same in that methods to manufacture flat displays require red, green, and blue pixels positioned in such a way as to provide a high-resolution screen. Attempting to simply place red, green, and blue emitters side by side is not feasible considering the comparative cost of vacuum deposition versus spinning on a polymer, not to mention quasiphotolithography steps that must be developed. It seems unreasonable to use filters because this requires the output of the LED to be not only inclusive of red, blue, and green, but also because up to 90% of optical power would be used to saturate a red pixel, and the OLED would have to be driven at up to 10 times the brightness required, inevitably ruining the lifetime of the OLED. Downconversion of blue light is somewhat feasible because the conversion quantum efficiency could be 100%. A low-resolution display based on downconverting layers was reported as early as 1996 [252]. A tunable system where differing voltages are used to drive the emitting layer to different energy light output was proposed, but would require a costly drive system, not to mention that it must independently control color and brightness [170]. Wu *et al.* [257] developed a novel method of a "programmable" system in which the three colors are all deposited atop one another in the emitting layer. The layers are chosen such that each of the blue, green, and red layers is a hole-blocking layer, and each has successively increasing glass transition temperatures. As fabricated, the device emits blue light; however, by increasing the temperature to above the glass transition temperature of the first layer (which could be done with a bias voltage), the layer becomes green emitting. Similarly, the device could be made to emit red. It is interesting to note here that, similar to the "fuzzy junction" work done by Chen *et al.* [258] in which an organic–organic abrupt heterojunction is replaced by a graded, interdiffused non-abrupt junction, drive voltage was reduced along with enhanced efficiency in the green and red devices.

Due to the low cost of manufacture and the small currents required to drive them, thin displays built on OLED technology are poised to capture a share of that $20 billion market. As in the case of thin-film transistor liquid crystal-based displays (TFT-LCDs) such as those in laptops, there are two primary types of OLED displays depending on the addressing scheme utilized, namely, passive-matrix and active-matrix displays. The passive-matrix OLED displays have a simpler structure and are well suited for low-cost and low-information-content applications such as alphanumeric displays. The active-matrix OLED displays have an integrated electronic backplane as their substrate

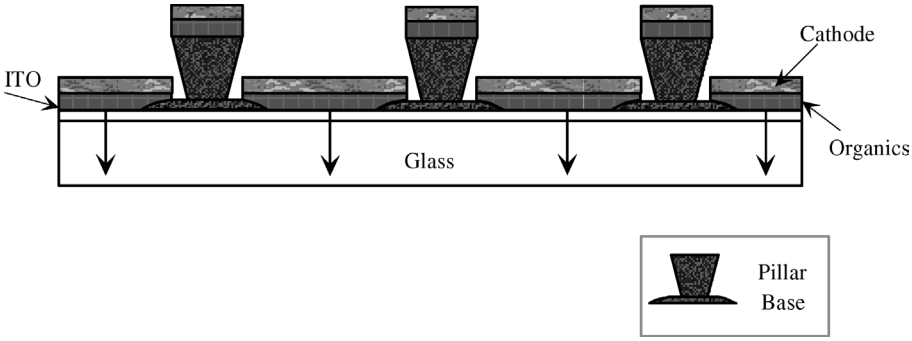

Figure 1.110 Typical patterning method for passive-matrix OLED displays. Advantages include the ability to perform photolithography prior to organics/cathode deposition and scalability to large area.

and lend themselves to high-resolution, high-information-content applications including videos and graphics.

A passive display is composed of an array of OLED pixels connected by intersecting anode and cathode conductors. A relatively simple but unique method is used for the fabrication of the passive-matrix OLED displays, as shown in Figure 1.110. The "base and pillar" structure is preformed on patterned ITO anode lines. As the organic materials and cathode metal are deposited, the "base and pillar" structure automatically produces an OLED display panel with the desired electrical isolation for the cathode lines. The fact that all patterning steps are based on conventional photolithography manufacturing processes is a major advantage of this approach.

A passive display works as follows: to drive a passive-matrix OLED display, electrical current is passed through selected pixels by applying a voltage to the corresponding rows and columns from drivers attached to each row and column. An external controller circuit provides the necessary input voltage, video data signal, and multiplex switches. The data signal is normally supplied to the column lines and synchronized to the scanning of the row lines. When a particular row is selected, the column and row data lines determine which pixels are powered and lit up. Unfortunately, response times for such matrixing schemes are often on the order of 100–250 ms, which prohibits its usefulness as video displays; also, because all the elements in, say, a row are connected, high contrast cannot be achieved as the number of multiplexed lines increases. Also, because all pixels are not lit simultaneously, the brightness requirements of each pixel are significantly increased, thereby requiring higher drive currents and decreasing the lifetime of the device. Considering the brightness requirements for LCD displays, those required of OLED are 27 000 cd m^{-2} for red and blue and 85 000 cd m^{-2} for green [259]. Also, resistive losses become an issue as the display size increases.

The more complicated active-matrix OLED displays include an electronic backplane in the display panel. This type of display is made possible by the development of

low-temperature polysilicon (LT-pSi) technology used for TFTs. Because of its high carrier mobilities, which for n-type is $100\,cm^2\,V^{-1}\,s^{-1}$ and for p-type is about $60\,cm^2\,V^{-1}\,s^{-1}$, this technology provides TFTs with higher current carrying capability and high switching speed. Several key advantages in active-matrix OLED displays are low power consumption, high resolution, large area, fast response time (1–10 μs), robust pixel design, and available integrated drivers.

In an active-matrix OLED display, each individual pixel can be independently addressed through the associated TFTs and capacitors in the electronic backplane. In principle, each pixel element can be selected to stay "on" during the entire frame time. Therefore, there are no intrinsic limitations to the pixel count, resolution, or size in the case of an active-matrix OLED display. Moreover, current drivers for OLEDs and the necessary scanning circuitry based on LT-pSi technology can be built directly on the substrate, which eliminates the need for high-density and expensive interconnects and discrete peripheral drivers.

It should be noted that the use of relatively low-mobility ($0.5–1\,cm^2\,V^{-1}\,s^{-1}$) amorphous silicon (a-Si) as a substrate for OLED displays has some potential benefits over the more conventional (higher mobility $\sim$50–200 $cm^2\,V^{-1}\,s^{-1}$) LT-pSi. Most important is the potential reduction in manufacturing costs that is available with the use of a-Si – fewer processing steps, fewer masks, and less equipment are required. The LT-pSi requires the use of excimer laser annealing (ELA) for the poly-Si crystallization, an ion implanter, and for activation, a rapid thermal annealer. This initial capital is not required by a-Si. It has been estimated that a-Si backplanes will cost one-half as much as a comparable LT-pSi one [260]. Second, the uniformity of the TFTs is better and OLEDs on a-Si typically have higher yields. Because the LT poly-Si crystallization is done via ELA, the difficulty in achieving uniform crystallization means that differences in mobility and threshold voltage are existent across the substrate. This affects the output current and ultimately the brightness across the final display: the display is nonuniform.

However, issues with a-Si are considerable. The threshold voltage can change by as much as 2 V over time, resulting in a different output current, meaning that the current is not as stable, which is crucial to an OLED whose luminance is a function of the drive current. Also the a-Si technology is only capable of making n-type TFTs, so the benefits of a fully integrated drive system in the substrate are lost. Finally, a-Si TFTs inherently have a larger width-to-length ratio (W/L), meaning that the effective size of a pixel is smaller in a bottom emitting structure. This ultimately will preclude the use of a-Si as the substrate of choice in small-area displays, but the lower cost of a-Si along with the unavailability of quality LT-pSi substrates larger than $1\,m^2$ will probably cause a-Si to be the winner for OLED substrate for large-area displays [261].

The intrinsic quality of OLED emissive technology is superb – high brightness and efficiency, low drive voltage, and fast response. Low-cost manufacturing methods are already in use for passive-matrix OLED displays and the advance of the complementary low-temperature polySi technology has enabled fabrication of high-resolution, full-color, active-matrix OLED displays. Kodak and Sanyo Electric Co., Ltd produced the first full-color 2.4 in active-matrix OLED display in 1999.

Since then they have displayed 5.5 and 15 in AM displays, as well as brought to market in March 2003 the first widely accessible consumer product employing a full-color active-matrix OLED (Kodak EasyShare LS633 digital camera; display specifications: 521 × 218 dots, displayed 55.9 mm (2.2 in) diagonally, displaying 24 frames per second). More devices such as cell phones, PDAs, DVD players, and later televisions with beautiful AM OLED displays will soon make their way to the consumer market if the staggering pace of development continues as it indubitably will.

An exciting recent development: despite the issues mentioned above with respect to a-Si, Samsung displayed at the May 2005 SID International Symposium a 40 in full-color active-matrix display, emitting at WXGA resolution (1280 × 800) constructed on a-Si.

1.17.6
Lighting with OLEDs

Today, the OLED's performance is not yet adequate for general illumination. During the past few years, OLED technology has progressed enormously. Efficacies have increased by about two orders of magnitude and the operating lifetime at display brightness levels has increased from less than 1 h to tens of thousands of hours. The lifetime of the OLED tends to decrease with increasing brightness, and understanding and eliminating degradation mechanisms will take a great deal of effort.

Several major issues stand in the way of successful commercialization of OLEDs for general lighting. Solving each of these issues will require a series of incremental improvements and inventions. The major issues with existing OLED devices are low efficiency, insufficient operating life, and high cost [262].

Substantial advances in technology, most of them requiring inventions, remain to be made even though *fundamental* roadblocks may not exist. Substantial research would have to be devoted to the fundamentals and development of OLEDs and particularly to the design and synthesis of a vast array of novel high-performance materials before this approach could be considered for general lighting. The lack of high-performance small molecules and polymers that transport charge and singlet and triplet emitters with the right emission spectrum is the major obstacle in achieving the devices for general lighting. Their use in displays could be a stepping stone for OLEDs. The companies that develop displays may focus their effort toward OLEDs for general lighting, only after commercial success in displays.

For two identical devices, it is well known that the device driven at the higher current will degrade more rapidly. However, actually defining lifetime is rather involved in that as the OLEDs reach the end of their life, their brightness fades away; failure is not catastrophic. The consensus, which is being applied to OLEDs, is the point where a drop of 50% in initial luminance at a constant current occurs [263]. Given this definition, a desired lifetime has been set at a minimum of 10 000 h, so that OLEDs would be competitive with fluorescent light bulbs.

Many theories exist with regard to the mechanism of degradation in the OLEDs; however, most agree that the primary cause of degradation is the exposure of the device to atmosphere, especially when considering that the devices degrade, though slower, even when they are not operated. The dark spots in OLEDs are attributable to cathode delamination and reactions with atmosphere at the cathode/organic interface [264].

The OLEDs fabricated on glass, where hermetic barriers can be used to keep (mostly) O_2 and H_2O out, already have reached tens of thousands of hours of life when driven at display levels of current [265]. This may simply be because the brighter device needs all of the emission sites the device offers, and as contaminants permeate the device, these areas are no longer radiative recombination sites [263, 266].

There is no single cause limiting the useful life of the OLEDs. Among the factors are reactions with the ambient (oxygen, CO_2, and moisture) involving the electrode metals, charge-transporting small molecules and polymers, excitons, and dopants. Moreover, electrochemical degradation, such as reduction or oxidation, involving the electrode transport interface, charge-transporting small molecules and polymers, excitons, emitters, and dopants are also causes for degradation. The list does not end there. Other causes, such as spontaneous (thermal) statistical conversions/decay of the charged species (charge-transporting small molecules and polymers) and excitons, must also be dealt with. As in the case of inorganic emitters, the OLED emitters of different colors age at different rates, which means that the quality of the white color will deteriorate with time, unless the aging rates are brought to the same level.

While it may seem that the display market is competitive, the lighting market is much more so, as the bulbs that are available have been around for quite some time and manufacturing processes are very well streamlined. This makes it necessary for OLEDs in lighting applications to cut down manufacturing costs by a factor of some 10–20. It may be that the flat glass platform may have to be abandoned in favor of some sort of roll-to-roll production including the electrode deposition, encapsulation, and any required patterning. But this would mean that lifetime issues made more difficult with this approach would have to be worked out. The key issues to be addressed are the organic deposition technology and encapsulation when the devices are built on webs and scaled up to a 36 in wide web that is running at 200 ft min^{-1}.

Reiterating, the advantages in using organic materials compared to inorganic materials are in the ease of their synthesis, high processability, and easy tuning of relevant electronic properties and hence optical properties. All of these characteristics make them excellent candidates for low-cost, large-area devices eventually employing flexible substrates [267]. In the near future, we shall see the further penetration of OLEDs in the display market, either as an individual player or in some LCD-OLED hybrid device. The push for solid-state lighting for general illumination may also bring the efficient OLEDs into direct competition with the fluorescent tube. In the end though, as the time and time again tested adage goes, time will tell!

References

1 Özgür, Ü., Alivov, Ya.I., Liu, C., Teke, A., Reshchikov, M., Doğan, S., Avrutin, V., Cho, S.-J. and Morkoç, H. (2005) A comprehensive review of ZnO and related devices. *Journal of Applied Physics Review*, **98**, 041301-1–041301-103.

2 Lee, T.P. and Dentai, A.G. (1978) *IEEE Journal of Quantum Electronics*, **14**, 150.

3 Wang, S. (1989) *Fundamental of Semiconductor Theory and Device Physics*, Prentice-Hall, Englewood Cliffs, NJ.

4 Evans, D., Hodapp, M., Sorensen, H., Jamison, K. and Krause, B. (1981) *Optoelectronics/Fiber-Optics Applications Manual*, 2nd edn, McGraw-Hill, New York, Chapter 2.

5 Thompson, G.H.B. (1980) *Physics of Semiconductor Laser Devices*, John Wiley & Sons, Ltd, Chichester, p. 307.

6 Žukauskas, A., Shur, M.S. and Gaska, R. (2002) *Introduction to Solid-State Lighting*, John Wiley & Sons, Inc., New York, p. 75.

7 See, for example, Nakamura, S. and Fasol, G. (1997) *The Blue Laser Diode*, Springer, Berlin.

8 Eliashevich, I., Li, Y., Osinsky, A., Tran, C.A., Brown, M.G. and Karlicek, R.F., Jr (1999) *Proceedings of SPIE*, **3621**, 28.

9 Kim, H., Park, S.J., Hwang, H. and Park, N.M. (2002) *Applied Physics Letters*, **81**, 1326.

10 Krames, M.R., Christenson, G., Collins, D., Cook, L.W., Craford, M.G., Edwards, A., Fletcher, R.M., Gardner, N., Goetz, W., Imler, W., Johnson, E., Kern, R.S., Khare, R., Kish, F.A., Lowery, C., Ludowise, M.J., Mann, R., Maranowski, M., Maranowski, S., Martin, P.S., O'Shea, J., Rudaz, S., Steigerwald, D., Thompson, J., Wierer, J.J., Yu, J., Basile, D., Chang, Y.L., Hasnain, G., Hueschen, M., Killeen, K., Kocot, C., Lester, S., Miller, J., Mueller, G., Mueller-Mach, R., Rosner, J., Schneider, R., Takeuchi, T. and Tan, T.S. (2000) *Proceedings of SPIE*, **3938**, 2.

11 Guo, X. and Schubert, E.F. (2001) *Applied Physics Letters*, **78**, 3337.

12 Jeon, S.-R., Song, Y.-H., Jang, H.-J., Yang, G.M., Hwang, S.W. and Son, S.J. (2001) Lateral current spreading in GaN-based light-emitting diodes utilizing tunnel contact junctions. *Applied Physics Letters*, **78**, 3265.

13 Chang, S.J., Chang, C.S., Su, Y.K., Chuang, R.W., Lin, Y.C., Shei, S.C., Lo, H.M., Lin, H.Y. and Ke, J.C. (2003) Highly reliable nitride-based LEDs with SPS + ITO upper contacts. *IEEE Journal of Quantum Electronics*, **39**, 1439.

14 Chen, C.H., Chang, S.J. and Su, Y.K. (2004) InGaN/AlGaN near-ultraviolet multiple quantum well light-emitting diodes with p-InGaN tunneling contact layer. *Journal of Vacuum Science & Technology A: Vacuum Surfaces and Films*, **22**, 1020.

15 Wang, H.X., Jiang, N., Hiraki, H., Nishimura, K., Sasaoka, H., Hiraki, A. and Sakai, S. (2004) Fabrication of high-performance 407 nm violet light-emitting diode. *Journal of Crystal Growth*, **270**, 57.

16 Chen, C.-H. (2006) InGaN/GaN blue light emitting diodes with modulation-doped AlGaN/GaN heterostructure layers. *Journal of Vacuum Science & Technology A: Vacuum Surfaces and Films*, **24**, 1001.

17 Guo, X., Li, Y.L. and Schubert, E.F. (2001) *Applied Physics Letters*, **79**, 1936.

18 Krames, M.R., Bhat, J., Collins, D., Gardner, N.F., Götz, W., Lowery, C.H., Ludowise, M., Martin, P.S., Mueller, G., Mueller-Mach, R., Rudaz, S., Steigerwald, D.A., Stockman, S.A. and Wierer, J.J. (2002) *Physica Status Solidi a: Applied Research*, **192**, 237.

19 Wierer, J.J., Steigerwald, D.A., Krames, M.R., O'Shea, J.J., Ludowise, M.J., Christenson, G., Shen, Y.-C., Lowery, C., Martin, P.S.,

Subramanya, S., Gotz, W., Gardner, N.F., Kern, R.S. and Stockman, S.A. (2001) High-power AlGaInN flip-chip light-emitting diodes. *Applied Physics Letters*, **78** (22), 3379–3381.

20 Bhat, J.C., Kim, A., Collins, D., Fletcher, R., Khare, R. and Rudaz, S. (2001) High efficiency monochromatic and white InGaN flip-chip dice. International Symposium on Compound Semiconductors, September 2001, Japan.

21 Fujii, T., Gao, Y., Sharma, R., Hu, E.L., DenBaars, S.P. and Nakamura, S. (2004) Increase in the extraction efficiency of GaN-based light-emitting diodes via surface roughening. *Applied Physics Letters*, **84**, 855.

22 Shchekin, O.B., Epler, J.E., Trottier, T.A., Margalith, T., Steigerwald, D.A., Holcomb, M.O., Martin, P.S. and Krames, M.R. (2006) High performance thin-film flip-chip InGaN–GaN light-emitting diodes. *Applied Physics Letters*, **89**, 071109.

23 Tran, C.A. (2007) SemiLEDs. Presented at Challenges Facing ZnO and GaN: Facts and Myths, October 18–19, Virginia Crossing Resort.

24 Jeon, H. (2007) Seoul National University. Presented at Challenges Facing ZnO and GaN: Facts and Myths, October 18–19, Virginia Crossing Resort.

25 Kim, D.-H., Cho, C.-O., Roh, Y.-G., Jeon, H. and Park, Y.S. (2005) *Applied Physics Letters*, **87**, 203508.

26 Lee, J.-S., Lee, J., Kim, S. and Jeon, H. (2006) *IEEE Photonics Technology Letters*, **18**, 1588.

27 Kolb, H. (2003) How retina works. *American Scientist*, **91** (1), 28–35.

28 Kolb, H. and Famiglietti, E.V. (1974) Rod and cone pathways in the inner plexiform layer of the cat retina. *Science*, **186**, 47–49.

29 MacAdam, D.L. (1985) *Color Measurement*, 2nd edn, *Springer Series in Optical Sciences*, Vol. 27, Springer, Berlin.

30 Morkoç, H. and Mohammad, S.N. (1995) *Science*, **267**, 51.

31 Craford, M.G. (1992) *IEEE Circuits and Devices Magazine*, **8**, 24.

32 Bhargava, R.M. (1992) *Optoelectronics – Devices and Technologies*, **7**, 19.

33 See, for example, Berg, A.A. and Dean, P.J. (1976) *Light-Emitting Diodes*, Clarendon, Oxford, pp. 11–35.

34 CIE Publication 18.2 (1983) The Basis of Physical Photometry.

35 IESNA Lighting Handbook (2000) 9th edn, p. 26-3.

36 CIE Publication 15.2 (1986) Colorimetry, 2nd edn.

37 CIE/ISO 10527 (1991) CIE Standard Colorimetric Observers.

38 CIE/ISO 10526 (1991) CIE Standard Colorimetric Illuminants.

39 IESNA Lighting Handbook (2000) 9th edn, p. 4-24.

40 Kendall, M. and Scholand, M. (2001) Energy Savings Potential of Solid State Lighting in General Lighting Applications. Prepared by Arthur D. Little, Inc. for US Department of Energy, April 2001. Available to the public from National Technical Information Service (NTIS), US Department of Commerce, 5285 Port Royal Road, Springfield, VA 22161, USA, Phone: 1-800-553-6847, Office of Building Technology Website www.eren.doe.gov/buildings/documents/.

41 Pankove, J.I., Miller, E.A. and Berkeyheiser, J.E. (1971) *RCA Review*, **32**, 383.

42 Mukai, T., Nagahama, S., Iwasa, N., Senoh, M. and Yamada, T. (2001) Nitride light-emitting diodes. *Journal of Physics: Condensed Matter*, **13**, 7089–7098.

43 Amano, H., Kito, M., Hiramatsu, K. and Akasaki, I. (1989) *Japanese Journal of Applied Physics*, **28**, L2112.

44 Nakamura, S., Mukai, T. and Senoh, M. (1991) *Japanese Journal of Applied Physics*, **30**, L1998.

45 Amano, H., Kito, M., Hiramatsu, K. and Akasaki, I. (1989) *Japanese Journal of Applied Physics*, **28**, L2112.

46 Akasaki, I. and Amano, H. (1994) *Journal of the Electrochemical Society*, **141**, 2266.

47 Amano, H., Hiramatsu, K. and Akasaki, I. (1988) *Japanese Journal of Applied Physics*, **27**, L1384.

48 Nakamura, S., Senoh, M., Isawa, N. and Nagahama, S. (1995) *Japanese Journal of Applied Physics*, **34**, L797.

49 Pankove, J., Berkeyheiser, J.E., Maruska, H.P. and Wittke, J. (1970) *Solid State Communications*, **8**, 1051.

50 Narendran, N., Maliyagoda, N., Bierman, A., Pysar, R. and Overington, M. (2000) *Light-Emitting Diodes: Research, Manufacturing, and Applications IV* (eds W. Yao, I.T. Ferguson and E.F. Schubert), SPIE, Bellingham, WA.

51 Kim, A.Y., Götz, W., Steigerwald, D.A., Wierer, J.J., Gardner, N.F., Sun, J., Stockman, S.A., Martin, P.S., Krames, M.R., Kern, R.S. and Steranka, F.M. (2001) Performance of high-power AlInGaN light emitting diodes. *Physica Status Solidi a: Applied Research*, **188** (1), 15–21.

52 Mukai, T., Narimatsu, H. and Nakamura, S. (1998) *Japanese Journal of Applied Physics*, **37**, L479.

53 Kish, F.A. and Fletcher, R.M. (1997) *AlInGaP Light-Emitting Diodes*, Vol. 48, Academic Press, San Diego, CA, p. 149.

54 Kneissl, M., Treat, D.W., Teepe, M., Miyashita, N. and Johnson, N.M. (2003) Advances in InAlGaN laser diode technology towards the development of UV optical sources. *Proceedings of SPIE*, **4995**, 103–107.

55 Mukai, T., Yamada, M. and Nakamura, S. (1999) Characteristics of InGaN-based UV/blue/green/amber/red light-emitting diodes. *Japanese Journal of Applied Physics*, **38**, 3976–3981.

56 Mukai, T. and Nakamura, S. (1999) Ultraviolet InGaN single quantum well structure light-emitting diodes grown on epitaxially laterally overgrown GaN substrates. *Japanese Journal of Applied Physics*, **38**, 5735–5739.

57 Tadatomo, K., Okagawa, H., Ohuchi, Y., Tsunekawa, T., Imada, Y., Kato, M. and Taguchi, T. (2001) High output power InGaN ultraviolet light-emitting diodes fabricated on patterned substrates using metalorganic vapor phase epitaxy. *Japanese Journal of Applied Physics, Part 2: Letters*, **40**, L583–L585.

58 Nishida, T., Saito, H. and Kobayashi, N. (2001) *Applied Physics Letters*, **79**, 711–712.

59 Wang, T., Liu, Y.H., Lee, Y.B., Ao, J.P., Bai, J. and Sakai, S. (2002) *Applied Physics Letters*, **81**, 2508–2510.

60 Nishida, T., Kobayashi, N. and Ban, T. (2003) *Applied Physics Letters*, **82**, 1–3.

61 Chitnis, A., Zhang, J.P., Adivarahan, V., Shuai, W., Sun, J., Shatalov, M., Yang, J.W., Simin, G. and Kahn, M.A. (2002) *Japanese Journal of Applied Physics*, **41**, L450–L451.

62 Zhang, J.P., Chitnis, A., Adivarahan, V., Wu, S., Mandavilli, V., Pachipulusu, R., Shatalov, M., Simin, G., Yang, J.W. and Kahn, M.A. (2002) *Applied Physics Letters*, **81**, 4910–4912.

63 Mukai, T., Morita, D. and Nakamura, S. (1998) *Journal of Crystal Growth*, **189–190**, 778.

64 Adivarahan, V., Chitnis, A., Zhang, J.P., Shatalov, M., Yang, J.W., Simin, G. and Khan, M.A. (2001) *Applied Physics Letters*, **79**, 4240.

65 Hirayama, H., Kinoshita, A. and Ayoagi, Y. (2001) Proceedings of the 4th International Conference on Nitride Semiconductors (ICNS-4), Denver, CO, *Physica Status Solidi a: Applied Research*, **188**, 83–89.

66 Nishida, T., Saito, H. and Kobayashi, N. (2001) Efficient and high-power AlGaN-based ultraviolet light-emitting diode grown on bulk GaN. *Applied Physics Letters*, **79** (6), 711–712.

67 Nishida, T., Saito, H. and Kobayashi, N. (2001) Milliwatt operation of AlGaN-based single-quantum-well light emitting diode in the ultraviolet region. *Applied Physics Letters*, **78** (25), 3927–3928.

68 Hirayama, H., Kinoshita, A., Yamabi, T., Enomoto, Y., Hirata, A., Araki, T., Nanishi, Y. and Aoyagi, Y. (2002) Marked enhancement of 320–360 nm ultraviolet emission in quaternary $In_xAl_yGa_{1-x-y}N$ with In-segregation effect. *Applied Physics Letters*, **80** (2), 207–209.

69 Kinoshita, A., Hirayama, H., Ainoya, M., Aoyagi, Y. and Hirata, A. (2000) *Applied Physics Letters*, **77**, 175.

70 Kipshidze, G., Kuryatkov, V., Zhu, K., Borisov, B., Holtz, M., Nikishin, S. and Temkin, H. (2003) AlN/AlGaInN superlattice light-emitting diodes at 280 nm. *Journal of Applied Physics*, **93** (3), 1363–1366.

71 Salvador, A., Sverdlov, B., Lehner, T., Botchkarev, A., Houng, F. and Morkoç, H. (1994) Resonant cavity enhanced InP/InGaAs photodiode on Si using epitaxial liftoff. *Applied Physics Letters*, **65**, 1880–1882.

72 Song, Y.-K., Diagne, M., Zhou, H., Nurmikko, A.V., Schneider, R.P., Jr and Takeuchi, T. (2000) Resonant cavity InGaN quantum well blue light emitting diodes. *Applied Physics Letters*, **77** (12), 1744–1746.

73 Margalith, T., Buchinsky, O., Cohen, D.A., Abare, A.C., Hansen, M., DenBaars, S.P. and Coldren, L.A. (1999) *Applied Physics Letters*, **74**, 3930.

74 Ozden, I., Diagne, M., Nurmikko, A.V., Han, J. and Takeuchi, T. (2001b) A matrix addressable 1024 element blue light emitting InGaN QW diode array. *Physica Status Solidi a: Applied Research*, **188** (1), 139–143.

75 Lee, T.-X., Kao, K.-F., Chung, T.-Y. and Sun, C.-C. (2007) Light extraction analysis for GaN-based LEDs. Proceedings of SPIE Opto 2007, Gallium Nitride Materials and Devices II, January 27, 2007.

76 Bergh, A., Craford, G., Duggal, A. and Haitz, R. (2001) The promise and challenge of solid-state lighting, Physics Today Online, http://www.physicstoday.org/pt/vol-54/iss-12/p42.html.

77 Dadgar, A., Poschenrieder, M., Bläsing, J., Fehse, K., Diez, A. and Krost, A. (2002) Thick, crack-free blue light-emitting diodes on Si(1 1 1) using low-temperature AlN interlayers and *in situ* Si_xN_y masking. *Applied Physics Letters*, **80** (20), 3670–3672.

78 Kipshidze, G., Kuryatkov, V., Borisov, B., Holtz, M., Nikishin, S. and Temkin, H. (2002) AlGaInN-based ultraviolet light-emitting diodes grown on Si(1 1 1). *Applied Physics Letters*, **80** (20), 3682–3684.

79 Steckl, A.J., Garter, M., Lee, D.S., Heikenfeld, J. and Birkhahn, R. (1999) *Applied Physics Letters*, **75**, 2184.

80 Garter, M.J., Scofield, J., Birkhahn, R. and Steckl, A.J. (1999) *Applied Physics Letters*, **74**, 182.

81 Heikenfeld, J., Garter, M.J., Lee, D.S., Birkhahn, R. and Steckl, A.J. (1999) *Applied Physics Letters*, **75**, 1189.

82 Wang, Y.Q. and Steckl, A.J. (2003) *Applied Physics Letters*, **82**, 502.

83 Torvik, J.T., Qiu, C.H., Feuersteun, R.J., Pankove, J.I. and Namavar, F. (1997) *Journal of Applied Physics*, **81**, 6343.

84 Perlin, P., Iota, V., Weinstein, B.A., Wisniewski, P., Suski, T., Osinski, M. and Eliseev, P. (1997) *Applied Physics Letters*, **70**, 2993.

85 Perlin, P., Osinski, M. and Eliseev, P.G. (1997) *III–V Nitrides* (eds F.A. Ponce, T.D. Moustakas, I. Akasaki and B.A. Monomar), Materials Research Society, Pittsburgh, PA, *Materials Research Society Symposium Proceedings*, **449**, 1173.

86 Lester, S.D., Ponce, F.A., Craford, M.G. and Steigerwald, D.A. (1995) *Applied Physics Letters*, **66**, 1249.

87 Osamura, K., Naka, S. and Murakami, Y. (1975) *Journal of Applied Physics*, **46**, 3422.

88 Nakamura, S., Senoh, M., Nagahama, S., Iwasa, N., Yamada, T., Matsushita, T., Kiyoku, H. and Sugimoto, Y. (1996) *Japanese Journal of Applied Physics*, **35**, L74.

89 Zolina, K.G., Kudryashov, V.E., Turkin, A.N., Yunovich, A.E. and Nakamura, S. (1996) *MRS Internet Journal of Nitride Semiconductor Research*, **1**, 11.

90 Chichibu, S., Azuhata, T., Sota, T. and Nakamura, S. (1996) *Applied Physics Letterss*, **69**, 4188.

91 Narukawa, Y., Kawakami, Y., Funata, M., Fujita, S., Fujita, S. and Nakamura, S. (1997) *Applied Physics Letters*, **70**, 981.

92 Osinski, M., Zeller, J., Chiu, P.C., Phillips, B.S. and Barton, D.L. (1996) AlGaN/InGaN/GaN blue light emitting diode degradation under pulsed current stress. *Applied Physics Letters*, **69**, 898.

93 Barton, D., Zeller, J., Phillips, B., Chiu, P., Askar, S., Lee, D., Osinski, M. and Malloy, K. (1995) Proceedings of the 33rd Annual IEEE International Reliability Physics Symposium, IEEE, New York, pp. 191–199.

94 Barton, D. and Osinski, M. (1997) private communication.

95 Barton, D.L., Osinski, M., Perlin, P., Eliseev, P.G. and Lee, J. (1999) Single-quantum well InGaN green light emitting diode degradation under high electrical stress. *Microelectronics Reliability*, **39**, 1219.

96 Stafford, L., Voss, L.F., Pearton, S.J., Wang, H.T. and Ren, F. (2007) Improved long-term thermal stability of InGaN/GaN multiple quantum well light-emitting diodes using TiB_2- and Ir-based p-Ohmic contacts. *Applied Physics Letters*, **90**, 242103.

97 Osinski, M., Barton, D.L., Perlin, P. and Lee, J. (1998) *Journal of Crystal Growth*, **189–190**, 808.

98 Meneghesso, G., Levada, S., Pierobon, R., Rampazzo, F., Zanoni, E., Cavallini, A., Castaldini, A., Scamarcio, G., Du, S. and Eliashevich, I. (2002) Degradation mechanisms of GaN-based LEDs after accelerated DC current aging. Digests of IEEE IEDM 2002, p. 103.

99 Narendran, N., Gu, Y., Freyssinier, J.P., Yu, H. and Deng, L. (2004) Solid-state lighting: failure analysis of white LEDs. *Journal of Crystal Growth*, **268**, 449.

100 Krames, M.R., Shchekin, O.B., Mueller-Mach, R., Mueller, G.O., Zhou, L., Harbers, G. and Craford, M.G. (2007) Status and future of high-power light-emitting diodes for solid-state lighting. *Journal of Display Technology*, **3**, 160.

101 Huang, W., Zhang, Y., Yu, Y. and Yuan, Y. (2007) Studies on UV-stable silicone–epoxy resins. *Journal of Applied Polymer Science*, **104**, 3954.

102 Egawa, T., Ishikawa, H., Jimbo, T. and Umeno, M. (1996) Optical degradation of InGaN/AlGaN light-emitting diode on sapphire substrate grown by metalorganic chemical vapor deposition. *Applied Physics Letters*, **69**, 830.

103 Meneghini, M., Trevisanello, L.-R., Levada, S., Meneghesso, G., Tamiazzo, G., Zanoni, E., Zahner, T., Zehnder, U., Härle, V. and Strauß, U. (2005) Failure mechanisms of gallium nitride LEDs related with passivation. IEDM Technical Digest, p. 1009.

104 Mueller-Mach, R., Mueller, G.O., Krames, M.R. and Trottier, T. (2002) High-power phosphor-converted light-emitting diodes based on III-nitrides. *IEEE Journal of Selected Topics on Quantum Electronics*, **8** (2), 339–345.

105 Narendran, N., Maliyagoda, N., Bierman, A., Pysar, R. and Overington, M. (2000) Characterizing white LEDs for general illumination applications, in *Light-Emitting Diodes: Research, Manufacturing, and Applications IV* (eds H.W. Yao, I.T. Ferguson and E.F. Schubert), SPIE, Bellingham, WA, *Proceedings of SPIE*, **3938**, 240.

106 Krames, M.R., Shchekin, O.B., Mueller-Mach, R., Mueller, G.O., Zhou, L., Harbers, G. and Craford, M.G. (2000) *Proceedings of SPIE*, **3938**, 2.

107 Mukai, T., Yamada, M. and Nakamura, S. (1999) *Japanese Journal of Applied Physics, Part 1: Regular Papers, Short Notes & Review Papers*, **38**, 3976.

108 Harbers, G. and Bierhuizen, S. (2006) *Society for Information Display (SID) International Symposium Digest of Technical Papers*, **37**, 2007.

109 Pope, I.A., Smowton, P.M., Blood, P., Thomson, J.D., Kappers, M.J. and Humphreys, C.J. (2003) *Applied Physics Letters*, **82**, 2755.

110 Rozhansky, I.V. and Zakheim, D.A. (2007) *Physica Status Solidi a: pplied Research*, **204**, 227.

111 Okamoto, K., Kaneta, A., Kawakami, Y., Fujita, S., Choi, J., Terazima, M. and Mukai, T. (2005) *Journal of Applied Physics*, **98**, 064503.

112 Chichibu, S.F., Sota, T., Wada, K. and Nakamura, S. (1998) *Journal of Vacuum Science & Technology B: Microelectronics and Nanometer Structures*, **16**, 2204.

113 Vasconcellos, A.R., Luzzi, R., Rodrigues, C.G. and Freire, V.N. (2003) *Applied Physics Letters*, **82**, 2455.

114 Kim, M.-H., Schubert, M.F., Dai, Q., Kim, J.K., Schubert, E.F., Piprek, J. and Park, Y. (2007) Origin of efficiency droop in GaN-based light-emitting diodes. *Applied Physics Letters*, **91**, 183507.

115 Shen, Y.C., Mueller, G.O., Watanabe, S., Gardner, N.F., Munkholm, A. and Krames, M.R. (2007) Auger recombination in InGaN measured by photoluminescence. *Applied Physics Letters*, **91**, 141101.

116 Gardner, N.F., Müller, G.O., Shen, Y.C., Chen, G., Watanabe, S., Götz, W. and Krames, M.R. (2007) Blue-emitting InGaN–GaN double-heterostructure light-emitting diodes reaching maximum quantum efficiency above 200 A/cm^2. *Applied Physics Letters*, **91**, 243506.

117 Li, Y.-L., Huang, Y.-R. and Lai, Y.-H. (2007) Efficiency droop behaviors of InGaN/GaN multiple-quantum-well light-emitting diodes with varying quantum well thickness. *Applied Physics Letters*, **91**, 181113.

118 Piprek, J. (2003) *Semiconductor Optoelectronic Devices: Introduction to Physics and Simulations*, Academic Press, San Diego, CA.

119 Jang, D.-J., Lin, G.-T., Hsiao, C.-L., Tu, L.W. and Lee, M.-E. (2008) Auger recombination in InN thin films. *Applied Physics Letters*, **92**, 042101.

120 Beattie, A.R. and Landsberg, P.T. (1958) Auger effect in semiconductors. *Proceedings of the Royal Society of London. Series A, Mathematical and Physical Sciences*, **249**, 16–29.

121 Beattie, A.R. and Landsberg, P.T. (1960) One-dimensional overlap functions and their application to Auger recombination in semiconductors. *Proceedings of the Royal Society of London. Series A, Mathematical and Physical Sciences*, **258**, 486–495.

122 Landsberg, P.T. (1972) On detailed balance between Auger recombination and impact ionization in semiconductors. *Proceedings of the Royal Society of London. Series A, Mathematical and Physical Sciences*, **331**, 103–108.

123 Landsberg, P.T. and Adams, M.J. (1973) Theory of donor–acceptor radiative and Auger recombination in simple semiconductors. *Proceedings of the Royal Society of London. Series A, Mathematical and Physical Sciences*, **334**, 523–539.

124 Pankove, J.I. (1971) *Optical Processes in Semiconductors*, Prentice-Hall. Englewood Cliffs, NJ.

125 Chen, Y.K., Wu, M.C., Kuo, J.M., Chin, M.A. and Sergent, A.M. (1991) Self-aligned InGaAs/GaAs/InGaP quantum well lasers prepared by gas source molecular beam epitaxy with two growth steps. *Applied Physics Letters*, **59** (23), 2929–2931.

126 Morkoç, H., Sverdlov, B. and Gao, G.B. (1993) Strained layer heterostructures and their applications to MODFETs, HBTs and lasers. *Proceeding of IEEE*, **81** (4), 492–556.

127 Amano, H. (2007) Meijo University. Presented at Challenges Facing ZnO and GaN: Facts and Myths, October 18–19, Virginia Crossing Resort.

128 Haitz, R., Kish, F., Tsao, J. and Nelson, J. (1999) The case for a national research program on semiconductor lighting. A white paper first presented publicly at the 1999 Optoelectronics Industry

Development Association (OIDA) Forum in Washington, DC, on October 6.

129 Jones, E.D. (2000) Inorganic light emitting diodes for general illumination. An Optoelectronics Industry Development Association Technology Roadmap, October 26–27.

130 Lear, K.L., Kilcoyne, S.P., Schneider, R.P., Jr, Choquette, K.D. and Hadley, G.R. (1995) LEOS '95, IEEE Lasers and Electro-Optics Society 1995 Annual Meeting, 8th Annual Meeting, Conference Proceedings, October 30–31, San Francisco, CA.

131 Hailong, Z., Diagne, M., Makarona, E., Nurmikko, A.V., Han, J., Waldrip, K.E. and Figiel, J.J. (2000) *Electronics Letters*, **36**, 1777.

132 Energy Policy Act of 1992. U.S. Public Law 486, 102nd Congress, October 24, 1992.

133 CIE Publication 13.3 (1995) Method of Measuring and Specifying Colour Rendering Properties of Light Sources.

134 CIE 17.4/IEC 50 (845) (1987) International Lighting Vocabulary.

135 Ohno, Y. (2000) CIE fundamentals for color measurements. Proceedings of the IS&T NIP16 International Conference on Digital Printing Technologies, October 15–20, Vancouver, Canada.

136 Munsell, A.H. (1905) *A Color Notation*, 1st edn, Munsell Color Company, Baltimore, MD.

137 Munsell, A.H. (1915) *Atlas of the Munsell Color System*, Wadsworth–Howland & Company, Malden, MA.

138 Jones, C.F. and Ohno, Y. (1999) Colorimetric accuracies and concerns in spectroradiometry of LEDs. Proceedings of the CIE Symposium'99 – 75 Years of CIE Photometry, Budapest, pp. 173–177.

139 Chhajed, S., Xi, Y., Li, Y.-L., Gressmann, Th. and Schubert, E.F. (2005) Influence of junction temperature on chromaticity and color-rendering properties of trichromatic white-light sources based on light-emitting diodes. *Journal of Applied Physics*, **97**, 054506.

140 Broderick, J. (2001) Photonics West Workshop on SSL, San Jose, CA.

141 Guo, X., Graff, J.W. and Schubert, E.F. (1999) *1999 IEDM Technical Digest*, **IEDM-99**, 600 and also *Compound Semiconductors*, issue 6, no. 4 (May/June 2000).

142 Johnson, N.M., Nurmikko, A.V. and DenBaars, S.P. (2000) *Physics Today*, **53**, 31.

143 Huang, C.-F., Lu, C.-F., Tang, T.-Y., Huang, J.-J. and Yang, C.C. (2007) Phosphor-free white-light light-emitting diode of weakly carrier-density-dependent spectrum with prestrained growth of InGaN/GaN quantum well. *Applied Physics Letters*, **90**, 151122.

144 Wang, X.H., Jia, H.Q., Guo, L.W., Xing, Z.G., Wang, Y., Pei, X.J., Zhou, J.M. and Chena, H. (2007) White light-emitting diodes based on a single InGaN emission layer. *Applied Physics Letters*, **91**, 161912.

145 Weller, H. and Fychmiiller, A. (1996) *Semiconductor Nanoclusters*, Vol. 103 (eds P.V. Kamat and D. Meisel), Elsevier, New York, p. 5.

146 Hines, M.A. and Guyot-Sionnest, P. (1996) Synthesis and characterization of strongly luminescing ZnS-capped CdSe nanocrystals. *The Journal of Physical Chemistry*, **100**, 468.

147 Alivisatos, A.P. (1998) Electrical studies of semiconductor–nanocrystal colloids. *MRS Bulletin*, **23** (2), 18–23.

148 Buffat, Ph. and Borel, J.P. (1976) Size effect on the melting temperature of gold particles. *Physical Review A*, **13** (6), 2287.

149 Goldstein, A.N., Echer, C.M. and Alivisatos, A.P. (1992) Melting in semiconductor nanocrystals. *Science*, **256**, 1425.

150 Murray, C.B., Norris, D.J. and Bawendi, M.G. (1993) Synthesis and characterization of nearly monodisperse CdE (E = S, Se, Te) semiconductor nanocrystallites. *Journal of the American Chemical Society*, **115** (19), 8706.

151 Katari, J.E.B., Colvin, V.L. and Alivisatos, A.P. (1994) X-ray photoelectron spectroscopy of CdSe nanocrystals with applications to studies of the nanocrystal surface. *The Journal of Physical Chemistry*, **98** (15), 4109.

152 Olshavsky, M.A., Goldstein, A.X. and Alivisatos, A.P. (1990) Organometallic synthesis if GaAs crystallites exhibiting quantum confinement. *Journal of the American Chemical Society*, **112** (25), 9438.

153 Mićić, O.I. and Nozik, A.J. (1996) Synthesis and characterization of binary and ternary III–V quantum dots. *Journal of Luminescence*, **70**, 95.

154 Nozik, A.J. and Mićić, O.I. (1998) Colloidal quantum dots of III–V semiconductors. *MRS Bulletin*, **23** (2), 24–30.

155 Murray, C.B., Norris, D.J. and Bawendi, M.G. (1993) *Journal of the American Chemical Society*, **115**, 8706.

156 Wilcoxon, J.P. and Samara, G.A. (1996) *Applied Physics Letters*, **74**, 3164.

157 Huang, C.-F., Lu, C.-F., Tang, T.-Y., Huang, J.-J. and Yang, C.C. (2007) Phosphor-free white-light light-emitting diode of weakly carrier-density-dependent spectrum with prestrained growth of InGaN/GaN quantum well. *Applied Physics Letters*, **90**, 151122.

158 Wang, X.H., Jia, H.Q., Guo, L.W., Xing, Z.G., Wang, Y., Pei, X.J., Zhou, J.M. and Chena, H. (2007) White light-emitting diodes based on a single InGaN emission layer. *Applied Physics Letters*, **91**, 161912.

159 See for example Harbers, Gerard., Bierhuizen, S.J. and Krames, M.R. (2007) Performance of high power light emitting diodes in display illumination applications. *IEEE Journal of Display Technology*, **3**, 98.

160 Martynov, Y., Konijn, H., Pfeffer, N., Kuppens, S. and Timmers, W. (2000) High-efficiency slim LED backlight system with mixing light guide. Society for Information Display (SID) 03 Digest, 1259–1261.

161 Roos, G. (2006) LEDs slim down for LCD backlights. *Electronic Engineering Times*, **1452**, 51–60.

162 Martynov, Y., Sillevis-Smitt, J.W.H., Abrahamse, G.J. and Timmers, W.A.G. (2004) Illumination system and display device. U.S. Appl. US 2004/0227869 (November 18, 2004).

163 West, R.S. *et al.* (2003) High brightness direct LED backlight for LCD-TV. Society for Information Display (SID) 03 Digest, 1262–1265.

164 Zeiler, M., Hüttner, J., Plötz, L. and Ott, H. (2000) Optimization parameters for LED backlighting solutions. Society for Information Display (SID) 06 Digest, 1524–1527.

165 Luxeon Emitter, Tech Datasheet DS25. Available at http://www.philipslumileds.com.

166 Friend, R.H., Gymer, R.W., Holmes, A.B., Burroughes, J.H., Marks, R.N., Taliani, C., Bradley, D.D.C., Dos Santos, D.A., Bredas, J.L., Logdlund, M. and Salaneck, W.R. (1999) *Nature*, **397**, 121.

167 Forrest, S.R., Burrows, P.E. and Thompson, M.E. (1995) *Laser Focus World*, **31**, 99.

168 Tang, C.W. and Van Slyke, S.A. (1987) *Applied Physics Letters*, **51**, 913.

169 Burroughes, J.H., Bradley, D.D., Brown, A.R., Marks, R.N., Mackay, K., Frien, R.H., Burns, P.L. and Holmes, A.B. (1990) *Nature*, **347**, 539.

170 Burrows, P.E., Gu, G., Bulovic, V., Shen, Z., Forrest, S.R. and Thompson, M.E. (1997) *IEEE Transactions on Electron Devices*, **44**, 1188.

171 Sheitn, M., Peumans, P., Benziger, J. and Forrest, S. (2003) *Journal of Applied Physics*, **93**, 4005.

172 Pardo, D.A., Jabbour, G.E. and Peyghambarian, N. (2000) *Advanced Materials*, **12**, 1249.

173 Haskal, E.*et al.* (2002) *Society for Information Display (SID) Digest of Technical Papers*, **33**, 776.

174 Markham, J.P.J., Lo, S.-C., Magennis, S.W., Burn, P.L. and

Samuel, I.D.W. (2002) *Applied Physics Letters*, **80**, 2645.

175 Gustafsson, G., Cao, Y., Treacy, G.M., Klavetter, F., Colaneri, N. and Heeger, A.J. (1992) *Nature*, **357**, 477.

176 Gu, G., Burrows, P.E., Vendatesh, S., Forrest, S.R. and Thompson, M.E. (1997) *Optics Letters*, **22**, 172.

177 Liew, Y.-F., Aziz, H., Hu, N.-X., Chan, H., Xu, G. and Popovic, Z. (2000) *Applied Physics Letters*, **77**, 2650.

178 Sheats, J., Antoniadis, H., Hueschen, M., Leonard, W., Miller, J., Moon, R., Roitman, D. and Stocking, A. (1996) *Science*, **273**, 884.

179 Shinar, J. and Savvateev, V. (2004) *Organic Light Emitting Devices: A Survey* (ed. J. Shinar), Springer, New York, p. 2

180 Kelly, S.M. (2000) *Flat Panel Displays: Advanced Organic Materials* (ed. J.A. Connor), The Royal Society of Chemistry, Cambridge.

181 Kido, J., Kimura, M. and Nagai, K. (1995) *Science*, **267**, 1332.

182 Gu, G., Bulovi, V., Burrows, P.E., Forrest, S.R. and Thompson, M.E. (1996) *Applied Physics Letters*, **68**, 2606.

183 Parthasarathy, G., Adachi, C., Burrows, P.E. and Forrest, S.R. (2000) *Applied Physics Letters*, **76**, 2128.

184 Burrows, P.E., Graff, G.L., Gross, M.E., Martin, P.M., Hall, M., Mast, E., Bonham, C., Bennet, W., Michalski, L., Weaver, M.S., Brown, J.J., Fogarty, D. and Sapochak, L.S. (2001) *Proceedings of SPIE*, **4105**, 75.

185 Langowski, H.C. (2003) 46th Annual Technical Conference Proceedings of the Society of Vacuum Coaters, San Francisco, CA, p. 559.

186 Weaver, M.S., Michalski, L.A., Rajan, K., Rothman, M.A., Silvernail, J.A., Brown, J.J., Burrows, P.E., Graff, G.L., Gross, M.E., Martin, P.M., Hall, M., Mast, E., Bonham, C., Bennett, W. and Zumhoff, M. (2002) *Applied Physics Letters*, **81**, 2929.

187 Sheats, J.R., Antoniadis, H., Hueschen, M., Leonard, W., Miller, J., Moon, R., Roitman, D. and Stocking, A. (1996) *Science*, **273**, 884.

188 Friend, R.H., Gymer, R.W., Holmes, A.B., Burroughes, J.H., Marks, R.N. *et al.* (1999) *Nature*, **397**, 121.

189 Garnier, F., Hajlaoui, R., Yassar, A. and Srivastava, P. (1994) *Science*, **265**, 1684.

190 Dimitrakopoulos, C.D. (2003) Organic field effect transistors for large area electronics, in *Recent and Evolving Advanced Semiconductor and Organic Nanotechnologies*, 3 Vols (ed. H. Morkoç), Academic Press, London.

191 Gigli, G., Barbarella, G., Anni, M. and Cingolani, R. (2003) Organic optoelectronics: the case of oligothiophenes, in *Recent and Evolving Advanced Semiconductor and Organic Nanotechnologies*, 3 Vols (ed. H. Morkoç), Academic Press, London.

192 Samsung's press release can be found at http://www.samsung.com/PressCenter/PressRelease/PressRelease.asp?seq=20050519_0000123644 (accessed July 2005).

193 Kepler, R.G., Beeson, P.M., Jacobs, S.J., Anderson, R.A., Sinclair, M.B., Valencia, V.S. and Cahill, P.A. (1995) *Applied Physics Letters*, **66**, 3618.

194 Hamada, Y., Sano, T., Fujii, H., Nishio, Y., Takahashi, H. and Shibata, K. (1997) Organic light-emitting diodes using 3- or 5-hydroxyflavone–metal complexes. *Applied Physics Letters*, **71** (23), 3338–3340.

195 Hung, L.S. and Mason, M.G. (2001) Voltage reduction in organic light-emitting diodes. *Applied Physics Letters*, **78** (23), 3732–3734.

196 Oyamada, T., Sasabe, H., Adachia, C., Murase, S., Tominaga, T. and Maeda, C. (2005) Extremely low-voltage driving of organic light-emitting diodes with a Cs-doped phenyldipyrenylphosphine oxide layer as an electron-injection layer. *Applied Physics Letters*, **86**, 033503.

197 Matsushima, T. and Adachi, C. (2006) Extremely low voltage organic light-emitting diodes with p-doped alpha-sexithiophene hole transport and n-doped

phenyldipyrenylphosphine oxide electron transport layers. *Applied Physics Letters*, **89**, 253506.

198 Sainova, D., Miteva, T., Nothofer, H.G., Scherf, U., Glowacki, I., Ulanski, J., Fujikawa, H. and Neherb, D. (2000) Control of color and efficiency of light-emitting diodes based on polyfluorenes blended with hole-transporting molecules. *Applied Physics Letters*, **76** (14), 1810–1812.

199 Adachi, C., Baldo, M.A., Thompson, M.E. and Forrest, S.R. (2001) *Journal of Applied Physics*, **90**, 5048.

200 Kim, J.-S., Ho, P.K.H., Greenham, N.C. and Friend, R.H. (2000) *Journal of Applied Physics*, **88**, 1073.

201 Lu, M.H. and Sturm, J.C. (2002) *Journal of Applied Physics*, **91**, 595.

202 Meerholz, K. and Muller, D. (2001) Outsmarting waveguide losses in thin-film-light-emitting diodes. *Advanced Functional Materials*, **11**, 251–253.

203 Windisch, R., Heremans, P., Knobloch, A., Kiesel, P., Döhler, G.H., Dutta, B. and Borghs, G. (1999) *Applied Physics Letters*, **74**, 2256.

204 Tsutsui, T., Yashiro, M., Yokogawa, H., Kawano, K. and Yokoyama, M. (2001) *Advanced Materials*, **13**, 1149.

205 (a)Lupton, J.M., Matterson, B.J., Samuel, I.D.W., Jory, M.J. and Burns, W.L., (2000) *Applied Physics Letters*, **77**, 3340. (b) Matterson, B.J., Lupton, J.M., Safonov, A.F., Salt, M.G., Burns, W.L. and Samuel, I.D.W. (2001) *Advanced Materials*, **13**, 123.

206 Yamasaki, T., Sumioka, K. and Tsutsui, T. (2000) *Applied Physics Letters*, **76**, 1243.

207 Madigan, C.F., Lu, M.H. and Sturm, J.C. (2000) *Applied Physics Letters*, **76**, 1650.

208 Gu, G., Garbuzov, D.Z., Burrows, P.E., Vendakesh, S., Forrest, S.R. and Thompson, M.E. (1997) *Optics Letters*, **22**, 396.

209 Takada, N., Tsutsui, T. and Saito, S. (1993) *Applied Physics Letters*, **63**, 2032.

210 Tsutsui, T., Takada, N., Saito, S. and Ogino, E. (1994) *Applied Physics Letters*, **65**, 1868.

211 Jordan, R.H., Rothberg, L.J., Dodabalapur, A. and Slusher, R.E. (1996) *Applied Physics Letters*, **69**, 1997.

212 Simon, J. and Andre, J. (1985) *Molecular Semiconductors: Photoelectrical Properties and Solar Cells* (eds J.M. Lehn and Ch.W. Rees), Springer, New York.

213 Kohler, A., Wilson, J.S. and Friend, R.H. (2002) *Advanced Engineering Materials*, **4**, 453.

214 Bredas, J.L., Elsembaumer, R.L., Chance, R.R. and Silbey, R. (1983) *Journal of Chemical Physics*, **78**, 5656.

215 Champagne, B., Mosley, D.H. and Anré, J.-M. (1994) *Journal of Chemical Physics*, **100**, 2034.

216 Gigli, G., Lomascolo, M., Cingolani, R., Barbarella, G., Zambianchi, M., Antolini, L., Della Sala, F., Di Carlo, A. and Lugli, P. (1998) *Applied Physics Letters*, **73**, 2414.

217 Davydov, A.S. (1971) *Theory of Molecular Excitons*, Plenum Press, New York.

218 Craig, D.P. and Walmsley, S.H.W. (1968) *Excitons in Molecular Crystal*, W.A. Benjamin, Inc., New York.

219 Pope, M. and Swenberg, C.E. (1982) *Electronic Processes in Organic Crystals*, Clarendon Press, Oxford.

220 Fichou, D. (ed.) (1999) *Handbook of Oligo and Poly-Thiophenes*, Wiley-VCH Verlag GmBH, Weinheim.

221 Belijonne, D., Cornil, J., Friend, R.H., Janssen, R.A. and Bredas, J.L. (1996) *Journal of the American Chemical Society*, **118**, 6453.

222 Swanson, L.S., Shinarand, J. and Yoshino, K. (1990) *Physical Review Letters*, **65**, 1140.

223 Chandross, M., Mazumdar, S., Jeglinski, S., Wei, X., Vardeny, Z.V., Kwock, E.W. and Miller, T.M. (1994) Excitons in poly(*para*-phenylenevinylene). *Physical Review B: Condensed Matter*, **50**, 14702.

224 Marks, R.N., Halls, J.J.M., Bradley, D.D.C., Friend, R.H. and Holmes, A.B. (1994) The photovoltaic response in poly(*p*-phenylene vinylene)

thin-film devices. *Journal of Physics: Condensed Matter*, **6**, 1379.

225 Lee, C.H., Yu, G., Moses, D. and Heeger, A.J. (1994) Picosecond transient photoconductivity in poly(*p*-phenylenevinylene). *Physical Review B: Condensed Matter*, **49**, 2396.

226 Barth, S. and Bassler, H. (1997) Intrinsic photoconduction in PPV-type conjugated polymers. *Physical Review Letters*, **79**, 4445.

227 Greenham, N.C., Peng, X. and Alivisatos, A.P. (1997) A CdSe nanocrystal/MEH–PPV polymer composite photovoltaic. Proceedings of Future Generation Photovoltaic Technologies: First NREL Conference, Denver, CO, p. 295.

228 Cao, Y. *et al.* (1999) *Nature*, **397**, 414.

229 Baldo, M.A., Lamansky, S., Burrows, P.E., Thompson, M.E. and Forrest, S.R. (1999) *Applied Physics Letters*, **75**, 4.

230 Blumstengel, S., Meinardi, F., Tubino, R., Gurioli, M., Jandke, M. and Strohriegl, P. (2001) Long-range energy transfer of singlet and triplet excitations in dye-doped tris(phenylquinoxaline). *Journal of Chemical Physics*, **115** (7), 3249–3255.

231 Baldo, M.A. and Forrest, S.R. (2000) Transient analysis of organic electrophosphorescence. I. Transient analysis of triplet energy transfer. *Physical Review B: Condensed Matter*, **62** (16), 10958–10966.

232 Closs, G.L., Johnson, M.D., Miller, J.R. and Piotrowiak, P. (1989) *Journal of the American Chemical Society*, **111**, 3751.

233 Baldo, M.A., O'Brian, D.F., You, Y., Shoustikov, A., Sibley, S., Thompson, M.E. and Forrrest, S.R. (1998) *Nature*, **395**, 151.

234 Ballardini, R., Varani, G., Indelli, M.T. and Scandola, F. (1986) *Inorganic Chemistry*, **25**, 3858.

235 Yang, A., Kuroda, M., Shiraishi, Y. and Kobayashi, T. (1998) *Journal of Chemical Physics*, **109**, 8442.

236 Becker, R.S., de Melo, J.S., Macanita, A.L. and Elisei, F. (1995) *Pure and Applied Chemistry*, **67**, 9.

237 Bixon, M. and Jortner, J. (1968) *Journal of Chemical Physics*, **48**, 715.

238 Sebastian, L., Weiser, G. and Bassler, H. (1981) *Journal of Chemical Physics*, **61**, 125.

239 Sillinsh, E.A. and Capek, V. (1994) *Organic Molecular Crystals, Interaction, Localization and Transport Phenomena*, AIP Press, Woodbury, NY.

240 Kalinowski, J., Stampor, W., Mezyk, J., Cocchi, M., Virgili, D., Fattori, V. and Di Marco, P. (2002) *Physical Review B: Condensed Matter*, **66**, 235321.

241 Lamansky, S., Djurovich, P., Murphy, D., Abdel-Razzaq, F., Lee, H.-E., Adachi, C., Burrows, P.E., Forrest, S.R. and Thompson, M.E. (2001) *Journal of the American Chemical Society*, **123**, 4304.

242 Universal Display Press Release, http://www.physorg.com/news4887.html (accessed July 2005).

243 Adamovich, V., Brooks, J., Tamayo, A., Alexander, A.M., Djurovich, P.I., D'Andrade, B.W., Adachi, C., Forrest, S.R. and Thompson, M.E. (2002) *New Journal of Chemistry*, **26**, 1171.

244 Cheon, K.O. and Shinar, J. (2002) *Applied Physics Letters*, **81**, 1738.

245 Thompson, J., Blyth, R.I.R., Mazzeo, M., Anni, M., Gigli, G. and Cingolani, R. (2001) White light emission from blends of blue-emitting organic molecules: a general route to the white organic light-emitting diode? *Applied Physics Letters*, **79**, 560.

246 Gebler, D.D., Wang, Y.Z., Fu, D.-K., Swager, T.M. and Epstein, A.J. (1998) *Journal of Chemical Physics*, **108**, 7842.

247 Kawamura, Y., Yanagida, S. and Forrest, S. (2002) Energy transfer in polymer electrophosphorescent light emitting devices with single and multiple doped luminescent layers. *Journal of Applied Physics*, **92**, 87.

248 GE's press release can be found at http://www.ge.com/cgi-bin/cnn-storydisplay_nu.cgi?story=/www/bw/webbox/bw.030404/240644365.htm (accessed June 2004).

249 Duggal, A., Shiang, J.J., Heller, C.M. and Froust, D.F. (2002) *Applied Physics Letters*, **80**, 3470.

250 Birnstock, J., Hofmann, M., Murano, S., Vehse, M., Blochwitz-Nimoth, J., Huang, Q., He, G., Pfeiffer, M. and Leo, K. (2005) Society for Information Display (SID) 05 Digest, 4.4L, 40.

251 Kido, J., Kimura, M. and Nagai, K. (1995) *Science*, **267**, 1332.

252 Dodabalapur, A., Rothberg, L.J. and Miller, T.M. (1994) *Electronics Letters*, **30**, 1000.

253 Seong, T.L., Lee, J.Y., Kim, M.H., Suh, M.C., Kang, T.M., Baetzold, Y.J.J., Bellmann, E., Savvateev, V., Wolk, M. and Webster, S. (2002) A new patterning method for full-color polymer light-emitting devices: laser induced thermal imaging (LITI). *Society for Information Display (SID) Symposium Digest of Technical Papers*, **33** (1), 784–787.

254 Trattnig, G., Pogantsch, A., Langer, G., Kern, W. and Zojer, E. (2002) Polymer-based red, green, and blue emitting devices fabricated by reductive photopatterning. *Applied Physics Letters*, **81**, 4269.

255 Muller, C.D., Falcou, A., Reckefuss, N., Rojahn, M., Wiederhirn, V., Rudati, P., Frohne, H., Nuyken, O., Becher, H. and Meerholz, K. (2003) Multi-colour organic light-emitting displays by solution processing. *Nature*, **421**, 829.

256 Salbeck, J., Yu, N., Bauer, J., Weissortel, F. and Bestgen, H. (1997) *Synthetic Metals*, **91**, 209.

257 Wu, C.-C., Chen, C.-W. and Cho, T.-Y. (2003) Three-color reconfigurable organic light-emitting devices. *Applied Physics Letters*, **83**, 611.

258 Chen, C.-W., Cho, T.-Y., Wu, C.-C., Yu, H.-L. and Luh, T.-Y. (2002) Fuzzy-junction organic light-emitting devices. *Applied Physics Letters*, **81**, 1570.

259 Bolink, H., Buechel, M., Jacobs, B., de Kok, M., Ligter, M., Meulenkamp, E.A., Vulto, S. and van da Weijer, P. (2003), Status of red, green, and blue light emitting polymers for passive matrix displays, *Proceedings of SPIE*, **4800**.

260 Hack, M. and Brown, J.J. (2004) *Society for Information Display (SID) Digest of Technical Papers*, **20**, 12.

261 Lih, J.-J. (2004) *Society for Information Display (SID) Digest of Technical Papers*, **20**, 18.

262 The Promise of Solid-State Lighting for General Illumination Light-Emitting Diodes (LEDs) and Organic Light-Emitting Diodes (OLEDs). Published by Optoelectronic Industry Development Association (OIDA), 1133 Connecticut Avenue, NW, Suite 600, Washington, DC 20036, USA, Phone: 1-202-785-4426, Fax: 1-202-785-4428, Web: http://www.OIDA.org.

263 Weaver, M.S., Michalski, L.A., Rajan, K., Rothman, M.A., Silvernail, J.A., Brown, J.J., Burrows, P.E., Graff, G.L., Gross, M.E., Martin, P.M., Hall, M., Mast, E., Bonham, C., Bennett, W. and Zumhoff, M. (2002) *Applied Physics Letters*, **81**, 2929.

264 Liew, Y.-F., Aziz, H., Hu, N.-X., Sze-On Chan, H., Xu, G. and Popovic, Z. (2000) *Applied Physics Letters*, **77**, 2650.

265 Kwong, R.C., Nugent, M.R., Michalski, L., Ngo, T., Rajan, K., Tung, Y.-J., Weaver, M.S., Zhou, T.X., Hack, M., Thompson, M.E., Forrest, S.R. and Brown, J.J. (2002) *Applied Physics Letters*, **81**, 162.

266 Chwang, A.B., Rothman, M.A., Mao, S.Y., Hewitt, R.H., Weaver, M.S., Silvernail, J.A., Rajan, K., Hack, M., Brown, J.J., Chu, X., Moro, L., Krajewski, T. and Rutherford, N. (2003) *Applied Physics Letters*, **83**, 413.

267 Kallinger, C., Hilmer, M., Haugeneder, A., Perner, M., Spirkl, W., Lemmer, U., Feldmann, J. *et al.* (1998) *Advanced Materials*, **10**, 920.